(2)

Bulletin 53
(Part 3 of 4 Parts)

THE SHOCK AND VIBRATION BULLETIN

Part 3
Vehicle Dynamics and
Vibration: Test and Criteria

MAY 1983

A Publication of
THE SHOCK AND VIBRATION
INFORMATION CENTER
Naval Research Laboratory, Washington, D.C.

Office of
The Under Secretary of Defense
for Research and Engineering

DISCLAIMER NOTICE

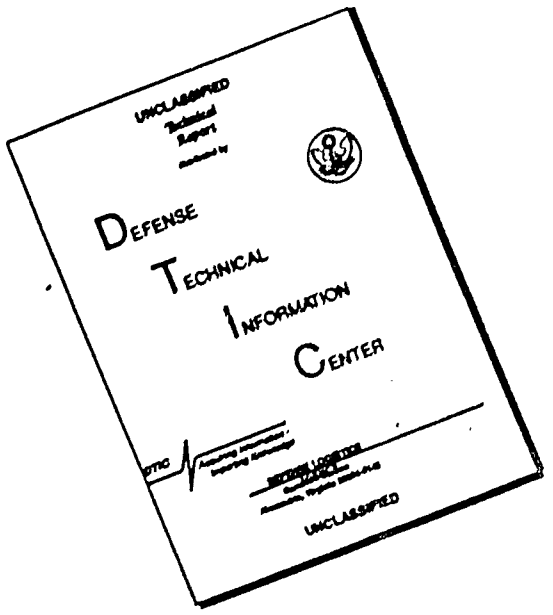

THIS DOCUMENT IS BEST QUALITY AVAILABLE. THE COPY FURNISHED TO DTIC CONTAINED A SIGNIFICANT NUMBER OF PAGES WHICH DO NOT REPRODUCE LEGIBLY.

SYMPOSIUM MANAGEMENT

THE SHOCK AND VIBRATION INFORMATION CENTER

Henry C. Pusey, Director
Rudolph H. Volin
J. Gordan Showalter
Jessica Hileman
Elizabeth A. McLaughlin
Mary K. Gobbett

Bulletin Production

Publications Branch, Technical Information Division,
Naval Research Laboratory

Bulletin 53
(Part 3 of 4 Parts)

THE SHOCK AND VIBRATION BULLETIN

MAY 1983

A Publication of
THE SHOCK AND VIBRATION
INFORMATION CENTER
Naval Research Laboratory, Washington, D.C.

The 53rd Symposium on Shock and Vibration was held at the Radisson Ferncroft Hotel, Danvers, MA on October 26-28, 1982. The U.S. Army Materials and Mechanics Research Center, Watertown, MA, was the host.

Office of
The Under Secretary of Defense
for Research and Engineering

CONTENTS

PAPERS APPEARING IN PART 3

Vehicle Dynamics

RESEARCHING THE MAN-MACHINE SYSTEM AS A FUNCTION OF SOIL-ENVIRONMENT SYSTEM 1
A. Massinas, University of Patras, Patras, Greece, and P. Drakatos, Visiting Professor, M.I.T., Cambridge, MA

A STOCHASTIC MODEL FOR THE MAN-MACHINE-SOIL-ENVIRONMENT SYSTEM (MMSES) AND THE INFLUENCE OF VIBRATIONS 9
A. Massinas, University of Patras, Patras, Greece, and P. Drakatos, Visiting Professor, M.I.T., Cambridge, MA

AN OPTIMUM SEAT-SUSPENSION FOR OFF-ROAD VEHICLES 19
S. Rakheja and S. Sankar, Concordia University, Montreal, Canada

FREQUENCY AND TIME DOMAIN ANALYSES OF OFF-ROAD MOTORCYCLE SUSPENSION 35
M. van Vliet, S. Sankar and C. N. Bapat, Concordia University, Montreal, Canada

BRAKING-TURNING-MANEUVERING STABILITY OF HEAVY TRANSPORTERS 51
P. Woods, Martin Marietta Corporation, Denver, CO

ACOUSTIC ENVIRONMENTS FOR JPL SHUTTLE PAYLOADS BASED ON EARLY FLIGHT DATA 63
M. R. O'Connell and D. L. Kern, Jet Propulsion Laboratory, California Institute of Technology, Pasadena, CA

COMPUTER-AIDED SYNTHESIS OF A SATELLITE ANTENNA STRUCTURE WITH PROBABILISTIC CONSTRAINTS 79
V. K. Jha, SPAR Aerospace Limited, Ste. Anne de Bellevue, Quebec, Canada, and
T. S. Sankar and R. B. Bhat, Concordia University, Montreal, Quebec, Canada

DYNAMIC BEHAVIOUR OF A SATELLITE ANTENNA STRUCTURE IN RANDOM VIBRATION ENVIRONMENT ... 91
V. K. Jha, SPAR Aerospace Limited, Ste. Anne de Bellevue, Quebec, Canada, and
T. S. Sankar and R. B. Bhat, Concordia University, Montreal, Quebec, Canada

INVESTIGATION OF THE ACOUSTIC CHARACTERISTICS OF AIRCRAFT/ENGINES OPERATING IN A DRY-COOLED JET ENGINE MAINTENANCE TEST FACILITY 105
V. R. Miller, G. A. Plzak, J. M. Chinn, Air Force Wright Aeronautical Laboratories, Wright-Patterson AFB, OH, and
R. J. Reilly, Independent Consultant, St. Paul, MN

Vibration: Test and Criteria

CRITERIA FOR ACCELERATED RANDOM VIBRATION TESTS WITH NON-LINEAR DAMPING 115
R. G. Lambert, General Electric Company, Utica, NY

VIBRATION TEST ENVIRONMENTS FOR ELECTRONICS MOUNTED IN A REMOTELY PILOTED VEHICLE 125
V. R. Beatty, Harris Corporation, Melbourne, FL

VIBRATION TEST SOFTWARE FOR ELECTRONICS MOUNTED IN A REMOTELY PILOTED VEHICLE 135
S. M. Landre, Harris Corporation, Melbourne, FL

AUTOMATED VIBRATION SCHEDULE DEVELOPMENT FOR WHEELED AND TRACKED VEHICLES AT ABERDEEN PROVING GROUND 143
W. H. Connon, III, Materiel Testing Directorate, Aberdeen Proving Ground, MD

TESTING FOR SEVERE AERODYNAMICALLY INDUCED VIBRATION ENVIRONMENTS 155
H. N. Roos and G. R. Waymon, McDonnell Douglas Corporation, St. Louis, MO

EVALUATION OF MODAL TESTING TECHNIQUES FOR SPACECRAFT STRUCRURES 161
K. Shiraki and H. Mitsuma, National Space Development Agency of Japan, Tokyo, Japan

A FREE-FREE MODAL SURVEY SUSPENSION SYSTEM FOR LARGE TEST ARTICLES 171
R. Webb, Martin Marietta Corporation, Denver, CO

PAPERS APPEARING IN PART 1

WELCOME
Dr. Edward Wright, Director, U.S. Army Materials and Mechanics Research Center, Watertown, MA

Keynote Address

KEYNOTE ADDRESS – AVRADCOM RESEARCH IN HELICOPTER VIBRATIONS
Major General Story C. Stevens, Commanding General, U.S. Army Aviation Research and Development Command, St. Louis, MO

Invited Papers

TECHNICAL INFORMATION SUPPORT FOR SURVIVABILITY
Henry C. Pusey, Rudolph H. Volin and J. Gordan Showalter, Shock and Vibration Information Center, Naval Research Laboratory, Washington, DC

AIRCRAFT SURVIVABILITY
Dale B. Atkinson, Chairman, Joint Technical Coordinating Group on Aircraft Survivability, Naval Air Systems Command, Washington, DC

UNITED STATES FLEET SURVIVABILITY OF U.S. NAVAL COMBATANT SHIPS
Captain F. S. Hering, USN, Director, Survivability and Readiness Subgroup, Naval Sea Systems Command, Washington, DC

ELIAS KLEIN MEMORIAL LECTURE –
VIBRATION CHALLENGES IN MICROELECTRONICS MANUFACTURING
Dr. Eric Ungar, Bolt Beranek and Newman, Inc., Cambridge, MA and
Colin G. Gordon, Bolt Beranek and Newman, Inc., Canoga Park, CA

MAURICE BIOT 50TH ANNIVERSARY LECTURE –
THE EVOLUTION OF SPECTRAL TECHNIQUES IN NAVY SHOCK DESIGN
Gene M. Remmers, David Taylor Naval Ship Research and Development Center, Bethesda, MD

MATERIALS IMPLICATIONS OF ADVANCED THERMAL AND KINETIC ENERGY THREATS
Robert Fitzpatrick and John Mescall, U.S. Army Materials and Mechanics Research Center, Watertown, MA

SUMMARY OF MIL-STD-810D PANEL SESSION

Pyrotechnic Shock and Shock Testing and Analysis

PYROTECHNIC SHOCK TEST AND TEST SIMULATION
M. E. Hughes, Martin Marietta Corporation, Orlando, FL

STRAIN HISTORIES ASSOCIATED WITH STAGE SEPARATION SYSTEMS USING LINEAR SHAPED CHARGE
D. R. Powers, McDonnell Douglas Astronautics Company, Huntington Beach, CA

SHOCK SPECTRAL ANALYSIS BY PERSONAL COMPUTER, USING THE IFT ALGORITHM
C. T. Morrow, Consultant, Encinitas, CA

AN EXPLOSIVE DRIVEN SHOCK TUBE FOR VERIFYING SURVIVAL OF RADIOISOTOPE HEAT SOURCES DURING SPACE SHUTTLE LAUNCH ACCIDENT
F. H. Mathews, Sandia National Laboratories, Albuquerque, NM

CALCULATION OF THE SHOCK WAVE FROM A PENTOLITE TAPERED CHARGE
J. T. Gordon and D. K. Davison, Physics International Company, San Leandro, CA

EFFECT OF MEASUREMENT SYSTEM PHASE RESPONSE ON SHOCK SPECTRUM COMPUTATION
P. L. Walter, Sandia National Laboratories, Albuquerque, NM

EFFICIENT ALGORITHMS FOR CALCULATING SHOCK SPECTRA ON GENERAL PURPOSE COMPUTERS
F. W. Cox, Computer Sciences Corporation, Houston, TX

EVALUATION AND CONTROL OF CONSERVATISM IN DROP TABLE SHOCK TESTS
T. J. Baca, Sandia National Laboratories, Albuquerque, NM

ICE IMPACT TESTING OF SPACE SHUTTLE THERMAL PROTECTION SYSTEM MATERIALS
P. H. DeWolfe, Rockwell International, Downey, CA

PROCEDURES FOR SHOCK TESTING ON NAVY CLASS H. I. SHOCK MACHINES
E. W. Clements, Naval Research Laboratory, Washington, DC

EQUIVALENT NUCLEAR YIELD AND PRESSURE BY THE RESPONSE SPECTRUM FIT METHOD
J. R. Bruce and H. E. Lindberg, SRI International, Menlo Park, CA

PAPERS APPEARING IN PART 2

Fluid Structure Dynamics

EXPERIMENTAL VALIDATION OF THE COMPONENT SYNTHESIS METHOD FOR PREDICTING VIBRATION OF LIQUID—FILLED PIPING
F. J. Hatfield and D. C. Wiggert, Michigan State University, East Lansing, MI, and
L. C. Davidson, David Taylor Naval Ship Research and Development Center, Annapolis, MD

ACOUSTIC RESPONSES OF COUPLED FLUID-STRUCTURE SYSTEM BY ACOUSTIC-STRUCTURAL ANALOGY
Y. S. Shin, Naval Postgraduate School, Monterey, CA and
M. K. Chargin, NASA Ames Research Center, Moffett Field, CA

FLUID-STRUCTURE INTERACTION BY THE METHOD OF CHARACTERISTICS
F. D. Hains, Naval Surface Weapons Center, White Oak, Silver Spring, MD

A SOLUTION TO THE AXISYMMETRIC BULK CAVITATION PROBLEM
F. A. Costanzo and J. D. Gordon, David Taylor Naval Ship Research and Development Center, Underwater Explosions Research Division, Portsmouth, VA

A SOLUTION TO THE ONE DIMENSIONAL BULK CAVITATION PROBLEM
B. M. Stow and J. D. Gordon, David Taylor Naval Ship Research and Development Center, Underwater Explosions Research Division, Portsmouth, VA

Dynamic Analysis

DYNAMIC SIMULATION OF STRUCTURAL SYSTEMS WITH ISOLATED NONLINEAR COMPONENTS
L. Minnetyan, Clarkson College of Technology, Potsdam, NY, J. A. Lyons, Niagara Mohawk Power Corporation, Syracuse, NY, and T. G. Gerardi, AFWAL/FIX, Wright-Patterson AFB, OH

EXPERIMENTAL AND ANALYTICAL INVESTIGATION OF ACTIVE LOADS CONTROL FOR AIRCRAFT LANDING GEAR
D. L. Morris, Air Force Wright Aeronautical Laboratories, Wright-Patterson AFB, OH, and
J. R. McGehee, NASA Langley Research Center, Hampton, VA

ON THE MODAL IDENTIFICATION OF MULTIPLE DEGREE OF FREEDOM SYSTEMS FROM EXPERIMENTAL DATA
D. I. G. Jones, Materials Laboratory, AFWAL/MLLN, Wright-Patterson AFB, OH, and
A. Muszynska, Bently Nevada Corporation, Minden, NV

AN APPLICATION OF THE KINETIC ENERGY CALCULATION AS AN AID IN MODE IDENTIFICATION
J. J. Brown and G. R. Parker, Hughes Helicopters, Inc., Culver City, CA

DYNAMICS OF A SIMPLE SYSTEM SUBJECTED TO RANDOM IMPACT
T. T. Soong, State University of New York, Amherst Campus, Buffalo, NY

APPROXIMATE NUMERICAL PREDICTIONS OF IMPACT-INDUCED STRUCTURAL RESPONSES
R. W. Wu, Lockheed Missiles and Space Co., Inc., Sunnyvale, CA

ON THE FACE-SHEAR VIBRATIONS OF CONTOURED CRYSTAL PLATES
S. De, National Research Institute, W. Bengal, India

DYNAMIC BEHAVIOR OF COMPOSITE LAYERED BEAMS BY THE FINITE ELEMENT METHOD
P. Trompette, R. Gaertner I.N.S.A., Laboratoire de Mecanique des Structures, Villeurbanne, France

PAPERS APPEARING IN PART 4

Damping

EXPERIMENTAL INVESTIGATION OF CONTROLLING VIBRATIONS USING MULTI-UNIT IMPACT DAMPERS
C. N. Bapat and S. Sankar, Concordia University, Montreal, Quebec, Canada, and
N. Popplewell, University of Manitoba, Winnipeg, Manitoba, Canada

AS EXPERIMENTAL HYBRID MODEL FOR A BILINEAR HYSTERETIC SYSTEM
K. R. McLachlan, Department of Civil Engineering, N. Popplewell and W. J. McAllister, Department of Mechanical Engineering, University of Manitoba, Winnipeg, Manitoba, Canada, and
C. S. Chang, Institute of Mechanics, Peking, People's Republic of China

MEASUREMENT AND ANALYSIS OF PLATFORM DAMPING IN ADVANCED TURBINE BLADE RESPONSE
T. J. Lagnese and D. I. G. Jones, Air Force Wright Aeronautical Laboratories, AFWAL/MLLN, Wright-Patterson AFB, OH

A VIBRATION DAMPING TREATMENT FOR HIGH TEMPERATURE GAS TURBINE APPLICATIONS
A. D. Nashif, Anatrol Corporation, Cincinnati, OH, W. D. Brentnall, Solar Turbines, Inc., San Diego, CA, and D. I. G. Jones, Air Force Wright Aeronautical Laboratories, AFWAL/MLLN, Wright-Patterson AFB, OH

EXPERIMENTAL MEASUREMENT OF MATERIAL DAMPING USING DIGITAL TEST EQUIPMENT
P. W. Whaley and P. S. Chen, University of Nebraska, Lincoln, NB

ELECTRONIC DAMPING OF A LARGE OPTICAL BENCH
R. L. Forward, Hughes Research Laboratories, Malibu, CA, C. J. Swigert, Hughes Aircraft Company, Culver City, CA, and M. Obal, Air Force Weapons Laboratory, Kirtland AFB, NM

MEASUREMENT OF STRUCTURAL DAMPING USING THE RANDOM DECREMENT TECHNIQUE
J. C. S. Yang, N. G. Dagalakis, University of Maryland, College Park, MD, and
G. C. Everstine, Y. F. Wang, David Taylor Naval Ship Research and Development Center, Bethesda, MD

DAMPED PNEUMATIC SPRING AS SHOCK ISOLATOR: GENERALIZED ANALYSIS AND DESIGN PROCEDURE
M. S. Hundal, University of Vermont, Burlington, VT

Machinery Dynamics

ANALYTICAL AND EXPERIMENTAL INVESTIGATION OF ROTATING BLADE RESPONSE DUE TO NOZZLE PASSING FREQUENCY EXCITATION
J. S. Rao, Indian Institute of Technology, New Delhi, H. M. Jadvani, Regional Engineering College, Surat, and
P. V. Reddy, Escorts Scientific Research Centre, Faridabad

PREDICTION OF CRITICAL SPEEDS, UNBALANCE AND NONSYNCHRONOUS FORCED RESPONSE OF ROTORS
P. Berthier, G. Ferraris, and M. Lalanne, I.N.S.A., Laboratoire de Mechanique des Structures, Villeurbanne, France

UNBALANCE RESPONSE OF A SINGLE MASS ROTOR MOUNTED ON DISSIMILAR HYDRODYNAMIC BEARINGS
R. Subbiah, R. B. Bhat and T. S. Sankar, Concordia University, Montreal, Quebec, Canada

NONLINEAR COUPLING RESPONSES TO VARIABLE FREQUENCY EXCITATIONS
F. H. Wolff and A. J. Molnar, Engineering-Analytical Dynamics Corporation, Trafford, PA

SIMPLE APPROXIMATE MODELS FOR A CLASS OF STRUCTURES
A. J. Molnar and F. H. Wolff, Engineering-Analytical Dynamics Corporation, Trafford, PA

SOURCE SIGNATURE RECOVERY IN REVERBERANT STRUCTURES
R. H. Lyon, Massachusetts Institute of Technology, Cambridge, MA

COMPARISON OF STATISTICAL ENERGY ANALYSIS AND FINITE ELEMENT ANALYSIS VIBRATION PREDICTION WITH EXPERIMENTAL RESULTS
L. K. H. Lu, W. J. Hawkins, and D. F. Downard, Westinghouse Electric Corporation, Sunnyvale, CA, and
R. G. Dejong, Cambridge Collaborative, Cambridge, MA

TITLES AND AUTHORS OF PAPERS PRESENTED IN THE SHORT DISCUSSION TOPICS SESSION

NOTE: These papers were only presented at the Symposium. They are not published in the Bulletin and are only listed here as a convenience.

THE DEVELOPMENT OF A VISCOELASTIC AEROSPACE STRUCTURES TECHNOLOGY DAMPING DESIGN GUIDE
J. Soovere, Lockheed-California Co., Burbank, CA, M. Drake, University of Dayton Research Institute, Dayton, OH, L Rogers and V. Miller, Air Force Wright Aeronautical Laboratories, Wright Patterson AFB, OH

APPROXIMATE RELAXATION MODULUS FROM THE FRACTIONAL REPRESENTATION OF COMPLEX MODULUS
L. Rogers, Air Force Wright Aeronautical Laboratories, Wright Patterson AFB, OH

DEVELOPMENT OF HIGH FREQUENCY ISOLATION SYSTEM
F. J. Andrews, Barry Controls, Watertown, MA

A RECENT APPLICATION EMPLOYING ELASTOMERIC TECHNOLOGY TO ISOLATE A HIGH RESOLUTION AERIAL RECONNAISSANCE CAMERA
D. F. Reynolds, Barry Controls, Watertown, MA

MERCURY ISOLATION SYSTEM/DESIGN, DEVELOPMENT MANUFACTURE AND TEST
M. Peretti, Barry Controls, Watertown, MA

LOOSENING OF BOLTED JOINTS DURING VIBRATION TESTING
J. J. Kerley, Jr., Goddard Space Flight Center, Greenbelt, MD

BOLTS AND FASTENER TIGHTENING TO BROCHURE IDEALNESS THROUGH VIBRATION SIGNATURES
A. S. R. Murty, Indian Institute of Technology, Kharagpur, India

DEVELOPMENT OF A MATERIAL TESTING MACHINE CAPABLE OF HIGH CYCLE LOADINGS SUPERIMPOSED ONTO LOW CYCLE LOADINGS
R. C. Goodman, University of Dayton Research Institute, Dayton, OH

PREDICTION OF STRUCTURAL RELIABILITY FROM VIBRATION MEASUREMENTS
P. Mlakar, U.S. Army Engineer Waterways Experiment Station, Vicksburg, MS

PROGRESS REPORT ON U.S. STATE OF THE ART ASSESSMENT OF MOBILITY MEASUREMENTS PROGRAM
D. J. Ewins, Imperial College of Science and Technology, London, England

UNDERWATER SHOCK ANALYSIS OF A MISSILE LAUNCH TUBE
K. C. Kiddy, Naval Surface Weapons Center, Silver Spring, MD

THE VIBRATION OF SLIGHTLY CURVED RECTANGULAR PLATES UNDER COMPRESSION
S. M. Dickinson and S. Ilanko, University of Western Ontario, London, Ontario, Canada and S. C. Tillman, University of Manchester, Manchester, England

SHOCK ANALYSIS OF DICED DISK TRANSDUCER USING ANSYS
A. Haecker and H. Mitson, Gould, Inc., Cleveland, OH

SESSION CHAIRMEN AND COCHAIRMEN

Date	Session Title	Chairmen	Cochairmen
Tuesday, 26 Oct. A.M.	Opening Session	Mr. Richard Shea, U.S. Army Materials and Mechanics Research Center, Watertown, MA	Mr. Henry C. Pusey, Shock and Vibration Information Center, Naval Research Laboratory, Washington, DC
Tuesday, 26 Oct. P.M.	Elias Klein Memorial Lecture Plenary A	Mr. Henry C. Pusey, Shock and Vibration Information Center, Naval Research Laboratory, Washington, DC	
Tuesday, 26 Oct. P.M.	Machinery Dynamics	Dr. Ronald L. Eshleman, The Vibration Institute, Clarendon Hills, IL	Mr. Samuel Feldman, NKF Engineering Associates, Inc., Vienna, VA
Tuesday, 26 Oct. P.M.	Pyrotechnic Shock-Measurement/ Simulation	Mr. C. Douglas Hinckley, TRW Systems, Ogden, UT	Mr. Peter Bouelin, Naval Weapons Center, China Lake, CA
Tuesday, 26 Oct. P.M.	MIL-STD-810D Panel Session	Mr. Preston Scott Hall, Air Force Wright Aeronautical Laboratories, Wright Patterson Air Force Base, OH	Mr. Rudolph H. Volin, Shock and Vibration Information Center, Naval Research Laboratory, Washington, DC
Wednesday, 27 Oct. A.M.	Maurice Biot 50th Anniversary Lecture Plenary B	Mr. George J. O'Hara, Naval Research Laboratory, Washington, DC	
Wednesday, 27 Oct. A.M.	Vibration: Test and Criteria	Mr. John Wafford, Aeronautical Systems Division, Wright Patterson Air Force Base, OH	Mr. Howard D. Camp, Jr., U.S. Army Electronic Research and Development Command, Ft. Monmouth, NJ
Wednesday, 27 Oct. A.M.	Shock Testing and Analysis	Mr. Edwin Rzepka, Naval Surface Weapons Center, Silver Spring, MD	Mr. Ami Frydman, Harry Diamond Laboratories, Adelphi, MD
Wednesday, 27 Oct. P.M.	Damping	Dr. Frederick C. Nelson, Tufts University, Medford, MA	Dr. Lynn Rogers, Air Force Wright Aeronautical Laboratories, Wright Patterson Air Force Base, OH
Wednesday, 27 Oct. P.M.	Fluid-Structure Dynamics	Dr. Anthony J. Kalinowski, Naval Underwater Systems Center, New London, CT	Dr. Martin W. Wambsganss, Argonne National Laboratory, Argonne, IL
Thursday, 28 Oct. A.M.	Plenary C	Mr. Richard Shea, U.S. Army Materials and Mechanics Research Center, Watertown, MA	
Thursday, 28 Oct. A.M.	Dynamic Analysis I	Lt. Col. John J. Allen, Air Force Office of Scientific Research, Washington, DC	Dr. Robert L. Sierakowski, University of Florida, Gainesville, FL
Thursday, 28 Oct. A.M.	Vehicle Dynamics	Dr. Richard A. Lee, U.S. Army Tank-Automotive Command, Warren, MI	Dr. Grant R. Gerhart, U.S. Army Tank-Automotive Command, Warren, MI
Thursday, 28 Oct. P.M.	Dynamic Analysis II	Dr. James J. Richardson, U.S. Army Missile Command, Redstone Arsenal, AL	Mr. Brantley R. Hanks, NASA Langley Research Center, Hampton, VA
Thursday, 28 Oct. P.M.	Short Discussion Topics	Mr. R. E. Seely, Naval Weapons Handling Center, Earle, Colts Neck, NJ	Mr. E. Kenneth Stewart, U.S. Army Armament, Research and Development Command, Dover, NJ

VEHICLE DYNAMICS

RESEARCHING THE MAN-MACHINE SYSTEM AS A FUNCTION OF SOIL-ENVIRONMENT SYSTEM

A. Massinas
Mechanical and Electrical Engineer
University of Patras, Patras, Greece

P. Drakatos
Visiting Professor, M.I.T.,
Cambridge MA

The present work is concerned with the determination of a stochastic model which describes the functional relationship between man-machine system (MMS) and Soi-Environment system(SES) with respect to the earth moving equipment.

The Vashy-Buchingham theorem was applied and non-dimensional P_i terms resulted.

This model has been approved by means of a lot of experiments that is valid for a large range of values.

INTRODUCTION

In the last years, many efforts have been taken to control the interaction of man-machine system, as Parsons [8] experiments carried out.

Olson and Woods [7] studied the similitude for structural modeling of Rollover protective structure under dynamic loading.

Swain [12], Rebideav [9] studied the human performance in man-machine systems and Shoenberger [11] the psycholphysical assessment on whole-body vibration.

Richards [10] has carried out different experiments to determine passenger models for buses and trains.

Many experiments have been carried out by Drakatos [43], [2], [3], [4] [5] to investigate the performance of earth-moving machines as a function of soil parameters.

At present there is no mathematical model that describes in general the man-machine system (MMS)as a function of Soil-Environment system (SES), especially introducing cost and cost related values among the indepedent variables of the MMS.

METHODS

In the present work an effort is made to determine the function between MMS and SES as a model that would describe the behaviour of the systems and the different interactions of the various dependent and independent variables which are involved in the systems.

The parameters that affect the function between the above systems are too many. The selection of the independent variables of the MMS as well as those of the SES was based on the characteristics and properties of those that affect the operation and independence of each system.

The variables that were taken into consideration for the determination of the function of MMS and SES are shown in table 1. On table 1 we chose the variables and parameters that there are

concerned with excavation work only, and for this reason we chose the blade capacity.

TABLE 1

Dependent and Independent Variables of man-machine system and Soil-Environment system.

1. INDEPENDENT VARIABLES

a. MAN-MACHINE SYSTEM

Man (operator)

Level of wage factor	W_a	[Dol/month]
Fatigue	f_g	[Kcal/h]
Work load	W_d	[%]
Reaction Time	T_r	[sec]

Machine

Age	J_p	[years]
Reliability	R	[%]
RPM	N_s	[rpm]
Velocity	V_s	[m/s]
Towing Power	F	[kp]
Blade capacity	V_L	[m^3]
Initial value of machine	C_s	[Dol.]
Remaining value of machine	S	[Dol.]
Operating cost	b_o	[Dol/h]
Maintenance cost	K_s	[Dol/h]

b. SOIL-ENVIRONMENT SYSTEM

Soil

Angle of friction	φ_m	[degree]
Cohesion	C	[kp/cm^2]
Wet. density	ρ	[$Fl.T^{-4}L^2$]
Shearing stress	τ	[kp/cm^2]
Relative humidity	W_s	[%]
Elasticity value	E	[kp/cm^2]
Coefficient of uniformity	U	[%]

Environment

Temperature	θ_e	[°C]
Barometric pressure	W_e	[kp/cm^2]
Relative humidity	W_{es}	[%]

2. DEPENDENT VARIABLES

Machine power	N	[HP]
Performance of the machine	$\dot{V}$	[m^3/h]
Operators Skill factor	t_d	[%]
Acceleration of vibration	b_v	[m/s^2]
Noise level	P_c	[db]

Using the Vaschy-Buckingham theorem, or theorem of P_i terms Murphy [6], the 24 dimensional terms resulted.

Using Numerical Analysis and substituting the functions of P_i terms in the equation form

$$\Phi(P_1, P_2, P_3, \ldots P_{24}) = 0 \qquad (1)$$

We get the functional relationship that gov the MMS and SES as follows:

$$\Phi\left(\frac{\tau\cdot\dot{V}}{N}, \frac{N_s \dot{V}^{1/5}}{b_v^{3/5}}, \frac{F\,\dot{V}^{1/5}\,b_v^{2/5}}{N}, \frac{V_L\, b_v^{3/5}}{\dot{V}^{6/5}}, \frac{J_p}{\dot{V}}, \right.$$

$$\frac{f_g}{N}, W_d, \frac{T_r\, b_v^{3/5}}{\dot{V}^{1/5}}, \varphi_m, \frac{C\,\dot{V}}{N}, \frac{\rho\, b_v^{4/5}\, V^2}{N},$$

$$R, W_s, \frac{E\,\dot{V}}{N}, U, \theta_e, \frac{W_e \dot{V}}{N}, \frac{C_s\, b_v^{3/5}}{\dot{V}^{1/5} W_a}, \frac{S\, b_v^{3/5}}{V^{1/5} W_a},$$

$$\left.\frac{b_o}{W_a}, \frac{K_s}{W_a}, t_d, \frac{P_c\,\dot{V}}{N}, \frac{V_s}{\dot{V}^{1/5}\, b_v^{2/5}}\right) = 0 \qquad (2)$$

The whole study is based on experimental data obtained during a five years period and on data gathered from various relevant experiments using five different types of soil (table 3), three machines (caterpilar-Allis Chalmers-Comatsu) and six operators aged 22-45 (table 2) with different experience, under different environmental conditions (table 4).

TABLE 2

Characteristics of men (operators) used to carry out different experiments of MMS as a function of SES.

Nº	Age (years)	Weight (Kg)	Height (m)	Experience in years
1	36	78	1.75	10
2	41	76	1.73	1
3	45	73	1.70	18
4	22	65	1.67	2
5	32	66	1.65	9
6	28	72	1.71	4

TABLE 3

Samples of soil using in researching of man-machine system as a function of soil-environment system.

Composition % \ Sample	№1	№2	№3	№4	№5
Clay	22	10	10	14	16
Silt	74	42	64	36	46
Sand	4	30	26	50	38
Gravel		18			

TABLE 4

Environmental conditions of experiments

№	Barometric Pressure Kp/cm.	Temperature dry$_{o}$C bulb	Temperature wet$_{o}$C bulb	Relative Humidity %
1	0.9993	8.43	5.92	68.8
2	1.0028	10.96	8.81	75.0
3	1.0037	11.21	9.05	74.8
4	1.0034	16.08	13.84	78.2
5	1.0010	21.57	17.02	63.6
6	1.0006	23.18	18.52	64.8
7	1.0001	25.60	19.35	57.5
8	0.0003	24.02	19.87	68.3
9	1.0012	21.56	18.08	71.3
10	1.0038	17.71	14.53	70.4
11	1.0017	15.04	12.55	74.2
12	0.9979	11.47	9.22	73.2

According to the experimental conditions, for a particular soil, for the same time, same operator and machine the parameters $\varphi_m, W_s, U, \theta_e$ $f_g, W_d, T_r, J_p, V_L, C_s, S$ were considered to be constant, and the solution of equation (2) can be achieved through a special computer prigram Fig.1.

The model (eq.2) describes the MMS as a function of SES and contains all the variables which are considered (table 1) without any restriction.

In general the problem which is being studied e.g. the MMS as a function of SES, is complicated and has a large variability with deterministic or stochastic variables-parameters in time (e.g. vibrations, noise, reliability e.t.c).

EXPERIMENTAL PROCEDURE

The experimental procedure which has been used in order to define the values of different parameters involved in the P_i terms is as follows:

1st Stage: Determination of the number of samples which have to be taken from different soils, as well as the instrumentation.

2nd Stage: Determination of the positions for vibration measurements which are:

a. On the floor of the operators cabinet
b. On the seat of the operator
c. On the head, shoulders, legs, and abdominal area of the operator.

3rd Stage: Performance of the experiments and analysis of the experimental results. For each sample of soil the following tests and analyses were made:

a. Grain size analysis
b. Compaction test
c. Q test
d. Shear test
e. Triaxial compression test
f. Consolidation test
g. Pressure-compression diagram

The vibration and noise measurements were made in the range of frequency 0÷ 200 HZ under the conditions of real situations.

Bruel and Kjaer instruments were used for vibration, noise measurements and analyses (e.g. tape record 7003, accelerometer 4370, charge amplifier 2635, real time analyzer model 2031 B & K e.t.c.).

RESULTS

Table 5 shows the results of the experiments carried out to determine the soil characteristics and table 6 the vibrations of man-machine system.

Table 7 shows the mean values of vibration of acceleration of each operator for different samples of soil for a specific machine under different environmental conditions.

The number of experiments that have been carried out for researching the MMS as a function of SES was 4.860. (the number 4860 results from the combination 6 operators X 5 types of soil X3 types of

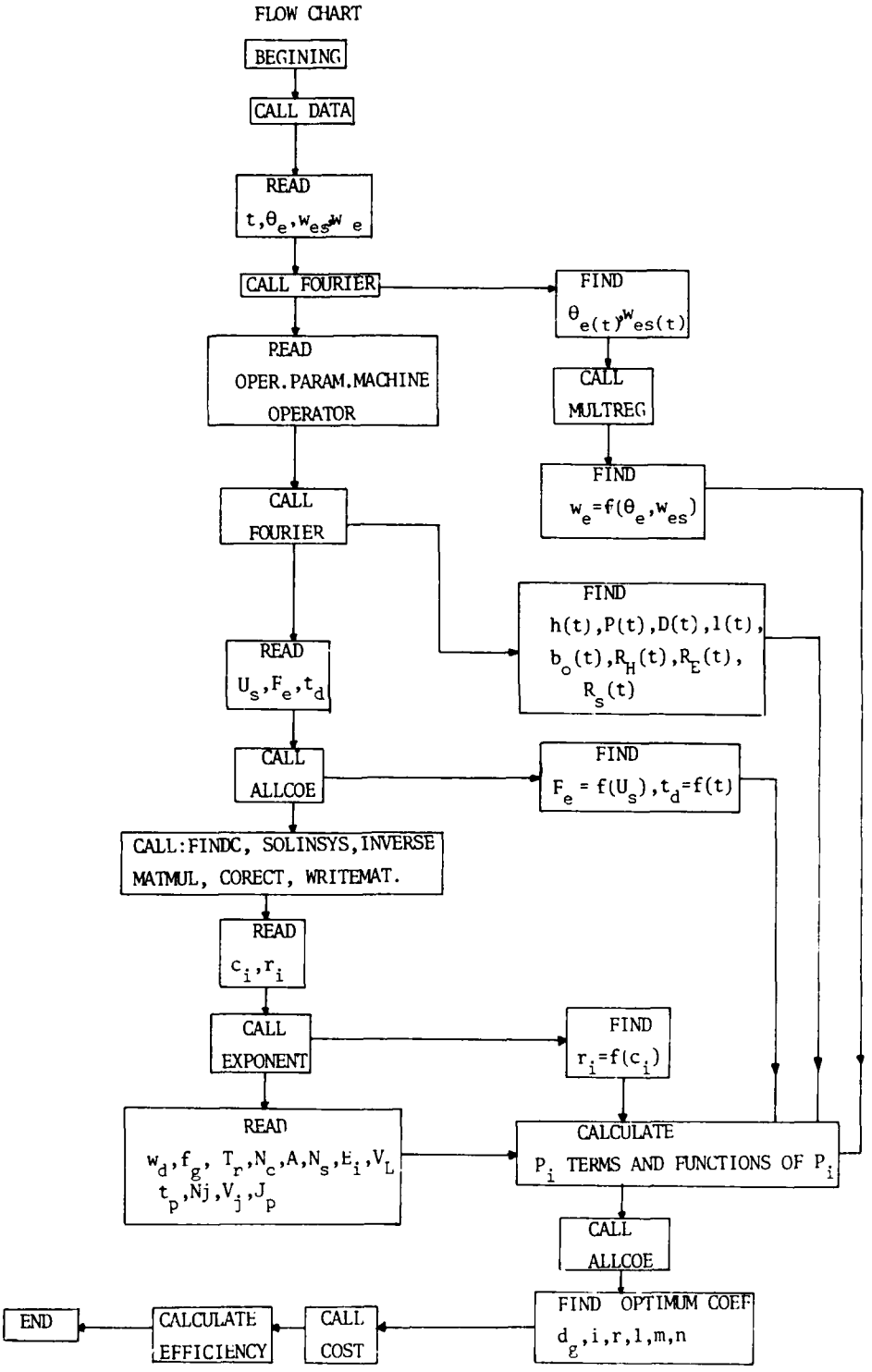

Fig.1 Flow Chart

TABLE 5

Summary of experimental results of soil

№	Parameters \ Sample soil	№1	№2	№3	№4	№5
1	Angle of friction φ_m	35°	40°	22°	27°	35°
2	Cohesion $\left[\frac{Kp}{cm^2}\right]$ c	0.60	0.50	0.90	0.68	0.36
3	Wet density $\left[\frac{Kp}{cm^4 s^2}\right]$ ρ	0.19	0.17	0.178	0.18	0.18
4	Shearing stress $\left[\frac{Kp}{cm^2}\right]$ τ	2.60	2.97	1.98	2.14	2.71
5	Relative humidity % w_s	14.8	14.3	16.6	14.5	14.5
6	Elasticity value $\left[\frac{Kp}{cm^2}\right]$ E	163	103	137	134	146
7	Factor of uniformity % U	92	94	90	94	96

TABLE 6

Summary of experimental results. Maximum values of the vibration acceleration on man (operator) in different positions for machine type D854A-12 and soil No5. (reference level $0db=10^{-2}mms^{-2}$)

No	POSITION	1000 RPM		1300 RPM		1600 RPM	
		HZ	ACCELERATION (db)	HZ	ACCELERATION (db)	HZ	ACCELERATION (db)
1	FLOOR	37.5	104.5	80.5	101.5	52	104.4
2	SEAT	45.5	101.5	136	105.9	56.5	98.6
3	HEAD	14	75.4	3	74.3	81	68.3
4	SHOULDERS	3.5	76.3	29	78	6.5	79.4

Continues table 6

No	POSITION	1000 RPM		1300 RPM		1600 RPM	
		HZ	ACCELERATION (db)	HZ	ACCELERATION (db)	HZ	ACCELERATION (db)
5	ABDOMINAL AREA	5.75	94.4	5.75	89.9	1.75	97.8
6	LEGS	7.25	96.1	6.5	86.9	8.25	99

TABLE 7

Mean values of vibrational acceleration of each operator for different samples of soil, for machine type D854 A-12(db)

Operator (man) \ Sample of soil	№ 1	№ 2	№ 3	№ 4	№ 5
№ 1	58	59	59.5	57.5	61
№ 2	57.8	59.4	59.2	56.9	60.2
№ 3	58.1	59.1	59	57.3	61.1
№ 4	57.9	58.9	59.3	57.1	59.8
№ 5	58.2	59.5	59.1	57.4	60.3

machines X 6 measurement positions X 3 level of rpm X (1 displacement level velocity level acceleration level)

The analysis of variance of the experimental results showed that there is no important difference between men (operators) and significant difference between soils and machines under several environmental conditions.

Using the above values of soil characteristics and vibrational acceleration together with equation 2 and the values of the parameters (table 1) of the men, machine, soil, environment, the mean performance of the MMS per hour per month is derived (table 8)

TABLE 8

The mean performance per hour per month of machine type D8 and Soil N°1 for excavation

J Months	$\dot{V}$ (m^3/h)	J Months	$\dot{V}$ (m^3/h)	J Months	$\dot{V}$ (m^3/h)
1	33.58	9	37.45	17	40.88
2	34.19	10	37.75	18	41.39
3	34.8	11	38.05	19	41.83
4	35.39	12	38.40	20	42.15
5	35.93	13	38.81	21	42.35
6	36.40	14	39.27	22	42.35
7	35.81	15	39.79	23	42.20
8	37.15	16	40.34	24	41.89

APPLICATION

Given a man-machine system and a soil-environment system with the following characteristics the monthly production rate or the mean performance of MMS is to be determined.

Man-machine System

Man (operator)

Level of wage factor	:	$ 215/month
Fatigue	:	4.5 Kcal/min
Work load	:	Normal
Reaction time	:	0.17 sec
Operators skill factor	:	0.90
Maximum acceleration of vibration in the operator	:	75.1 db

Machine

Age	:	first year
Reliability	:	1st year 0.90, 2nd year 0.80
Revolution	:	2000 RPM
Velocity	:	0.67 m/s
Towing Power	:	17.000 Kp
Blade capacity	:	2.5 m^3
Initial value of machine	:	$ 125.000
Remaining value of machine	:	$ 12.500
Operating cost	:	$ 9/hour
Maintenance cost	:	$ 0.3/hour
Machine power	:	270 HP

Soil Environmental System

Soil

Angle of friction	:	35°
Cohesion	:	0.60 KP/cm^2
Unit weight	:	1.90 X 10^{-3} KP/cm^3
Shearing Stress	:	2.6 KP/cm^2
Relative humidity	:	0.148
Elasticity value	:	163 KP/cm^2
Coefficient of uniformity	:	0.92

Environment

Temperature	:	18°C
Barometric pressure	:	1.01 KP/cm^3
Relative humidity	:	0.50
Noise level	:	72.2 db

The mean performance of MMS can be achieved by solving equation (2) via a special computer program (fig.1) which results the 24 predicted values of $\dot{V}$ (table 9)

TABLE 9

Mean performance per hour per month of MMS (operator No 1, machine- D-8) for different shearing stress and operator's fatigue under different environmental conditions.

N°	Shearing Stress of Soil in (KP/cm^2)	Performance of MMS $\dot{V}$ (m^3/h)	
		fatigue fg=180 Kcal/h	fatigue fg=240 Kcal/h
1	1	25	36
2	1.19	22	32.2
3	1.4	18	28.2
4	1.58	15.5	25
5	1.8	12	22
6	2	10	19.8
7	2.2	8	18
8	2.4	6.1	16.2
9	2.6	6.5	15
10	2.8	4	13

DISCUSSION

Comparing the values of table 9, which have resulted from the MMS as a function of SES, with the actual ones it can be seen that there is no great difference.

From the solution of the model (eq.2) that governs the MMS and SES we have the performance of MMS in different soils under several environmental conditions.

The performance of the MMS was based on the final results of the machine (m^3/h) that resulted from real time situations.

Based on the results shown on table 9 we see that as the shearing stress of the soil increases the performance of the MMS decreases.
This occurs in practice and the performance depends on the efforts of the man(operator).

CONCLUSIONS

The resultant stochastic model that describes the functional relationship between MMS and SES without restrictions in the use of the number of variables can be solved with respect to any variable.

REFERENCES

1. P. A. Drakatos , "The application of similarity methods during the Experimental Researvh on soil compaction Machines",Ph.D.thesis
2. P. A. Drakatos, "The vibration in construction equipment",46th Shock and Vibration bulletin, Washington.
3. P.A. Drakatos, etc. A.S. Massinas, "Com - puterised method of constructions equipment cost estimating", AACE Transactions 1978.
4. A.S. Massinas, G. Masouros, P.A. Drakatos "Cost depreciating in Construction equipment" IMSA, 6th Interest Congress, 24-29 Oct.1979, Garmischparten Kirchen.
5. A.S. Massinas, P.A. Drakatos, "Human factors in Equipment Construction", VII International Congress of Biomechanics, Warsaw, Sept.18-21 1979.
6. G. Murphy, "Similitude in Engineering", N.York, Ronald Press.,1950
7. D.L. Olson, T.W. Woods, "Similitude for structural modeling of Rollover Protective structurs under dynamic loading", SESA Spring meeting, Chicago, May 11-16,1975.
8. H. M. Parsons, "Man-Machine system experiments", John Hopkins Pres.London.
9. G.F. Rabideav, "Field measurement of Human performance in man-machine systems", Human Factors Vo.6, N№6, 1964.
10. L.G. Richards, I.D. Jacobson, "Ride quality evaluation in ground based vehicles:Passenger comfort models for buses and trains", Ergonomics 1978, Vol.21,N№6.
11. R.W. Shoeberger, H. Stanley, "Psychophysical assessment on wholebody vibration"Human Factors Vol.13, N№1, 1971.
12. A.D Swain, "Some problems in the measurement of Human performance in man-machine systems", Human Factors, Vol.6, N№6,1964.

DISCUSSION

Voice: Do you think that the stochastic model that you have been using can be expanded to be used on aircraft or pilot-aircraft interaction?

Mr. Drakatos: Yes, in my opinion, because I used the stochastic model. The characteristic of the stochastic model is that the behavior of the involved parameters and variables are very changeable because, as you know, the soil is a non-continued material with a very intensive stochastic element. We have a different problem in air. For example, the pressure is changed in a deterministic way, as is the humidity. But I believe that stochastic model will probably do that with acceptable boundaries. It is valid, but we must carry out some experiments first.

A STOCHASTIC MODEL FOR THE MAN-MACHINE-SOIL-ENVIRONMENT SYSTEM (MMSES) AND THE INFLUENCE OF VIBRATIONS.

A. Massinas
Mechanical and Electrical Engineer
University of Patras, Greece
P. Drakatos
Visiting Professor, M.I.T.,
Cambridge, MA

The present work is concerned with the determination of a stochastic model which describes the interaction of different parameters involved in the man-machine-soil-environment system (MMSES), with respect to the efficiency of the earth moving equipment.

There is a large number of dependent and independent variables that affect the systems however, only those which were thought to be influencial in the operation of the system were taken into consideration.

The Vashy-Buckingham theorem was applied and non dimensional Pm terms were resulted. Employing the general form of curvilinear Regression equation and the method of least squares through the use of a spesial computer program the functional relationships that govern the MMSE system were determined.

Experiments using six operators, five types of soil and three different machines under different environmetal conditions were carried out and various results obtained.

The effects of vibrational acceleration were also taken into consideration.

The validity of the model was justified by experimental results gathered from various sources during a five year period and also from the data obtained from various experiments made ad hoc.

INTRODUCTION

The need to study the role of the human factor into various systems is due to the large usage of technological means and the great advances of the technology during the past years.

Today one of the most interesting problems of the construction industry is the examination of the behaviour and efficiency of the man-machine-soil-environment system (MMSES).

In the last three decades many experiments and studies have been carried out to examine the interaction of man-machine in simple and complicated systems. The main purpose being either the examination of the recrewtment of machines or the examination of the behaviour of operators because of the systems environmental conditions.

Parsons [9] gives a record of studies and experiments that have been carried out with respect to a simple man-machine system. These studies are mainly concerned with the examination

of the efficiency of a man in a determined system and the identification of the operational procedures of the machine.

Repperger & Smiles [10] proved that in a closed system there are many important variations in the input and output characteristics when the operator is under various thermal conditions.

Captain and Wormley [2] using simulating techniques determined the machine's vibrations due to the soil abnormalities in surface.

To improve the working conditions and to avoid accidents, various studies such as those of Bloomquist [1] and Huston [5] concerned with the determinations of the properties and abilities of a man in a system have also been carried out.

Parsons and Griffing [8] studied the influence of sinusoidal, horizontal and vertical vibrations, with respect to the positioning of the seat (short or tall) in the feeling of comfortable sensation.

The studies of man-machine systems that have been carried out up today are mainly concerned with the determination of the parameters of man or environment, one separated from each other. No study up to now explains the interaction of various variables in the MMSES.

At present there is no mathematical model that describes in general the variations and interactions of all the various parameters-variables involved in a man-machine-soil-environment system, eg. to determine the performance of a machine (earth moving equipment) in productional units with respect to its conditions (age, power, speed e.t.c.), operator characteristics (experience, stress, psychological conditions, vibrations etc) and working conditions (soil environment).

METHODS

In this work an effort is made to determine a stochastic model that would describe the behaviour of a real MMSE system and also examine the influence and interaction of the various dependent and indepentent variables of the system in its performance.

Analytical methods of research i.e. operational research, information theory etc. are valuable tools in the study of the man-machine system especially in cases in which usual methods cannot be applied or give deficient results.

The behaviour of the MMSE system is governed by many factors most of which are known but some of them remain unspecified.

The parameters (factors) that influence the operation of a MMSE system and consequently influence its performance i.e. the overal efficiency coefficient, are too many. They were seperated into the following four large categories.

Category I (Xm) It includes the characteristics of the earth moving equipment (e.g.type-power-speed-vibration etc).

Category II(Xo) It includes the characteristic of the operator (e.g. age-experience-stress-response-vibration etc).

Category III (Xs) It includes soil resistance and main soil characteristics due to its properties (i.e. angle of friction, cohesion, shearing stress etc).

Category IV (Xe) It includes the characteristics of the environment (i.e. temperature-humidity-noice etc).

The interaction and dependance of the various variables (parameters) in a MMSE system are shown in a schematic form below.(Fig.1).

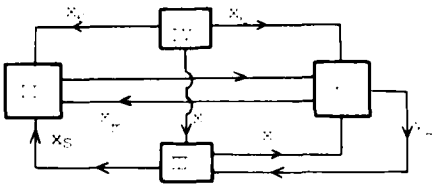

Fig.1. Variables interaction of MMSE system

The selection of the independent variables of the machine as well as those of the operator, soil and environment in which the whole system operates, was based on the characteristics and properties of those that were thought to be more influencial for the operation and independence of system. The parameters that thought to be

most influencial for the system are shown on table 1.

TABLE 1

Physical Parameters Governing the MMSES

1. INDEPENDENT VARIABLES	Symbol	Dimensions
a. Machine		
(1) Age	Jp	$F^oL^oT\ D^o$
(2) Reliability	R	$F^oL^oT^oD^o$
(3) RPM	Ns	$F^oL^oT^{-1}D^o$
(4) Velocity	Vs	$F^oL\ T^{-1}D^o$
(5) Towing Power	F	$F\ L^oT^oD^o$
(6) Blade Capacity	VL	$F^oL^3T^oD^o$
b. Man(operator)		
(1) Level of wage factor	Wa	$F^oL^oT^{-1}D$
(2) Fatique	f_g	$F\ L\ T^{-1}D^o$
(3) Work load	Wd	$F^oL^oT^oD^o$
(4) Reaction Time	Tr	$F^oL^oT\ D^o$
c. Soil		
(1) Angle of Friction	φ_m	$F^oL^oT^oD^o$
(2) Cohesion	c	$F\ L^{-2}T^oD^o$
(3) Wet density	ρ	$F\ L^{-4}T^2\ D^o$
(4) Shearing Stress	τ	$F\ L^{-2}T^oD^o$
(5) Relative Humidity	Ws	$F^oL^oT^oD^o$
(6) Elasticity value	E	$F\ L^{-2}T^oD^o$
(7) Factor of uniformity	U	$F^oL^oT^oD^o$
d. Environment		
(1) Temperature	θ_e	$F^oL^oT^1D^o$
(2) Barometric pressure	We	$F\ L^{-2}T^oD^o$
(3) Relative Humidity	Wes	$F^oL^oT^oD^o$
e. Cost		
(1) Initial value of machine	Cs	$F^oL^oT^oD^1$
(2) Remaining value of machine	S	$F^oL^oT^oD^1$
(3) Operating cost	bo	$F^oL^oT^{-1}D$
(4) Maintenance cost	ks	$F^oL^oT^{-1}D$
2. DEPENDENT VARIABLES		
(1) Machine Power	N	$F\ L\ T^{-1}D^o$
(2) Efficiency of the machine	$\dot{V}$	$F^oL^3T^{-1}D^o$
(3) Operators skill factor	td	$F^oL^oT^oD^o$
(4) Acceleration of vibration	bv	$F^oL\ T^{-2}D^o$
(5) Noise	Pc	$F\ L^{-2}T^oD^o$

The whole study is based on experimental data obtained during a five year period and on data gathered from various experiments made ad hoc using five different types of soil, three machines (Caterpilar-Allis Chalmers-Comatsu) and six operators, 22-45 years old. Vibration measurements were taken for the following positions.

a. On the floor of the operators cabinet
b. On the seat of the operator
c. On the head, shoulders, legs and abdominal area of the operator

Using the Vaschy-Buckingham theorem, or theorem of Pm terms [7] the listing in table 2, dimensionaless terms resulted.

TABLE 2

Nondimensional Pm terms of Man-Machine-Soil-Environment system.

$P_1=\frac{r\cdot\dot{V}}{N}$	$P_9=\varphi_m$	$P_{17}=\frac{W_e\dot{V}}{N}$
$P_2=\frac{N_s\cdot\dot{V}^{1/5}}{b_v^{3/5}}$	$P_{10}=\frac{C\cdot\dot{V}}{N}$	$P_{18}=\frac{C_s\cdot b_v^{3/5}}{\dot{V}^{1/5}\cdot W_\alpha}$
$P_3=\frac{F\cdot\dot{V}^{1/5}\cdot bv^{-2/5}}{N}$	$P_{11}=\frac{\rho\cdot bv^{4/5}\cdot\dot{V}^{7/5}}{N}$	$P_{19}=\frac{S\cdot bv^{3/5}}{\dot{V}^{1/5}\ Wa}$
$P_4=\frac{V_L\cdot bv^{3/5}}{\dot{V}^{6/5}}$	$P_{12}=R$	$P_{20}=\frac{b_o}{W_\alpha}$
$P_5=\frac{J_p\cdot bv^{3/5}}{\dot{V}^{1/5}}$	$P_{13}=Ws$	$P_{21}=\frac{Ks}{W_\alpha}$
$P_6=\frac{f_g}{N}$	$P_{14}=\frac{E\cdot\dot{V}}{N}$	$P_{22}=t_d$
$P_7=W_d$	$P_{15}=U$	$P_{23}=\frac{P_c\cdot\dot{V}}{N}$
$P_8=\frac{T_r\cdot bv^{3/5}}{\dot{V}^{1/5}}$	$P_{16}=\theta_e$	$P_{24}=\frac{U}{\dot{V}^{1/5}bv^{2/5}}$

Using Numerical Analysis the functional relationship that governs the above system will take the form. [6]

$$\Phi(P_1P_2P_3.....P_{24})=0 \text{ or}$$

$$\Phi_1(V,r,N_s,F,V_L,J_p,f_g,W_d,T_r,\varphi_m,C,\rho,R,W_s,E,V,\theta_e,W_e,C_s,S,b_o,K_s,t_d,P_c,V_s,N,bv,W_\alpha)=0 \quad (1)$$

According to the experimental conditions, for a particular soil for the same time and same operator, if the general form of curvilinear Regression equation and the method of least squares equation are employed by means of a special computer program equation (2) can be derived.

$$Piijrenv = \sum_{q=0}^{q_1} a_{qimrenv} \left[\prod_{\substack{m-nm \\ nm<m}}^{m_1} P_{mijrenv} \right]^q \quad (2)$$

The number of parametric equations($n_{\delta s}$) of equation (2) is given by equation (3).

$$n_\delta = \prod_{\substack{i=1\\r=1\\e=1\\n=1\\v=1}}^{i_1 r_1 e_1 n_1 v_1} i.r.e.n.v. \sum_{n_4=0}^{m} \frac{m!}{(m-n_4)!} \quad (3)$$

Where:

$a_{qimrenv}$:Factors determinedby least squares equation.

i=1 ; i_1:Type of soil

j=1 ; j_1:Time in months

r=1 ; r_1:Level of vibration

e=1 ; e_1:Level of noise

n=1 ; n_1:Level of operator's weight

m=1 ; m_1:Number of nondimensional Pm terms which are involved in the polynomial

v=1 ; v_1:Magnitude of Towing Power

q=0 ; q_1:Power of polynomial

n_m=m-1, m-2,...,m_1-1:Number of nondimensional terms multiplied.

The variables in the P_m terms are generally considered to be mathematical functions of the polynomial form

$$Y_i = \sum_{q=0}^{V} aq\ Xi^q$$

or Fourier series form:

$$f(t) = a_o + \sum_{n=1}^{V} \left(a_n \cos\frac{2n\pi}{T} t + b_n \sin\frac{2n\pi}{T} t\right)$$

e.g.

Function of operator skill factor [4]

$$t_d(t) = 0.25 + 1.22\frac{t}{100} + 11.5\left(\frac{t}{100}\right)^2 - 20\left(\frac{t}{100}\right)^3 \quad (4)$$

Function of machine operating hours per month

$$h(t) = a_{10} + \sum_{n=1}^{V} a_{1n} \cos(0.523n\ t) \quad (5)$$

Function of Human operating hours per machine operating hours.

$$P(t) = a_{20} + \sum_{n=1}^{V} b_{2n} s\ in\ (0.48\ t + 4.35)n \quad (6)$$

ıction of system Reliability

$$R_s(t) = \frac{P(t)}{3} \left[\frac{\int_o^t h(t)dt}{200t}\right]^{\cdot} \quad (7)$$

Inserting all the functions of the variables those appearing in table 1 in the terms of table 2 and subsequently in equation (2) we get the general form, which governs the man-machine-soil-environment system, equation (8).

$$\dot{V}ijrenv = \frac{Nij}{ri} \sum_{q=0}^{q_1} a_{qimrenv} \left[\prod_{--n_m K=1}^{m_1 Vis} \cdot \left(\sum_{s=1}^{s1} ks\, b_{qimrenv} \sum_{ksijmrenv}^{Fks} Z + C_{kimrenv} \right) \right]^{q_i} \quad (8)$$

where: $a_{qimrenv}$:Factors determined by least squares

$b_{ksqirmenv}$:Factors arising from the product of the Pm terms

s=1:s_1 :Number of terms of series

k=1:V_{s1} :Number of multiplied sums

$Z_{ksijmrenv}$:Function of the form $f(u_s,t,c,E,K,\cos(va),\sin(va))$

$F_{k,s}$:A function that gives the exponent of variable Z depending on the Pm terms employed, at the variable function relationships.

$C_{kimrenv}$:Constant depending on the polynomial forms.

The number of nondimensional Pm terms in equation (2) and subsequently the parameters in equation (8) are determined by a special computer program under different conditions in order to obtain in maximum efficiency. In other words the function (8) is maximized.

RESULTS

TABLE 3

Maximum value of the vibration acceleration in various frecuency bands - RPM - position - Soil (Clay 16% - silt 45% - sand 38%) -operator No 1 - Machine type D854A - 12 as Percentage of g.

Revol	Rang Freq.	Pos Val.	Fl.	Seat	Head	Shoul	Abdom.	Leg.
1000 RPM	0÷30HZ	HZ	12.5	2.5	14	3.5	5.75	7.25
		bv	0.098	0.093	0.006	0.0066	0.054	0.065
	30÷60HZ	HZ	37.5	45.5	35	58	43	30.25
		bv	0.17	0.123	0.001	0.0064	0.011	0.017
	60÷90	HZ	78.5	63	89.5	87		
		bv	0.04	0.056	0.002	0.0017		
	90÷120	HZ	110	91.5	105.5	96.5		
		bv	0.08	0.114	0.0007	0.0014		
	120÷150	HZ	147.5	137	120.5	135.5		
		bv	0.058	0.143	0.003	0.0006		
	150÷180	HZ	178	171.5	164	157		
		bv	0.076	0.06	0.0004	0.0006		
	180÷210	HZ	184	183	193	182		
		bv	0.05	0.082	0.0003	0.0005		
1300 RPM	0÷30	HZ	23	7	3	5	5÷75	3
		bv	0.061	0.121	0.0053	0.004	0.032	0.025
	30÷60	HZ	32.5	60	30.5	36.5	30	35
		bv	0.082	0.128	0.0015	0.002	0.007	0.01
	60÷90	HZ	80.5	73	62.5	68		
		bv	0.12	0.161	0.0002	0.0014		
	90÷120	HZ	110	105	100	100		
		bv	0.073	0.071	0.0002	0.001		
	120÷150	HZ	134	136	122.5	127		
		bv	0.081	0.201	0.0001	0.001		
	150÷180	HZ	170.5	164	174	158		
		bv	0.07	0.083	0.0001	0.0014		
	180÷210	HZ	188	181	183	188		
		bv	0.73	0.083	0.0001	0.0017		
1600 RPM	0÷30	Hz	10	14	3.5	6.5	1.75	8.25
		bv	0.113	0.0076	0.0017	0.0095	0.079	0.1
	30÷60	HZ	31.5	56.6	35	34	33.12	31.87
		bv	0.20	0.087	0.0008	0.0016	0.029	0.0096
	60÷90	HZ	62.5	89.5	81	66.5		
		bv	0.134	0.054	0.0026	0.0008		
	90÷120	HZ	94	113.5	108	113		
		bv	0.091	0.043	0.0009	0.0009		
	120÷150	HZ	123.5	136.5	121	138.5		

Continues tabl3 3

Revol	Rang Freq.	Pos Val.	Fl.	Seat	Head	Shoul	Abdom.	Leg.
		bv	0.092	0.067	0.002	0.0009		
	150÷180	HZ	156	161	155	151		
		bv	0.075	0.042	0.0003	0.0011		
	180÷210	HZ	188.5	193.5	200	180.5		
		bv	0.114	0.058	0.0004	0.0011		

Table 3 shows the results of the experiments that carried out to determine the vibrations of the operator. These results are for a particular machine, operator and soil.

Same type experimental results were also obtained for different machines-weather conditions-soil-operators.

The analysis of variance of the results showed that there is no important difference in the vibrations (displacement-velocity-acceleration) for different operators, however, there is a difference of vibration for different types of soil-machine and speed of machine.

The largest values of the vibrational acceleration that appeared in the various measuring positions in various frequency bands are shown on fig.2,3,4,5 and 6.

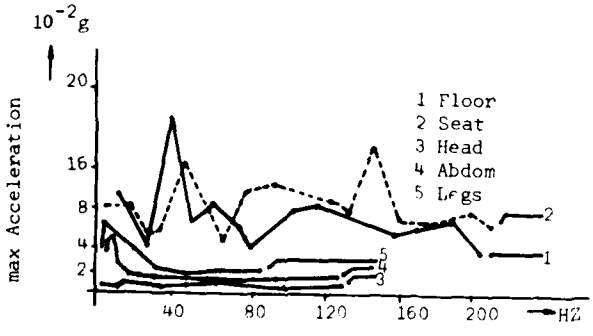

Fig.2 Max. Acceleration for 1000 RPM

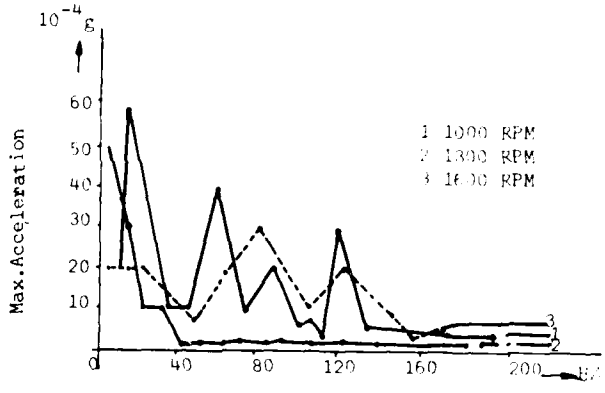

Fig.3. Maximum Acceleration of Head

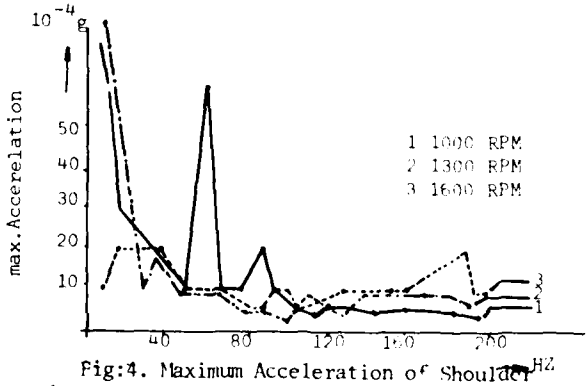

Fig:4. Maximum Acceleration of Shoulder

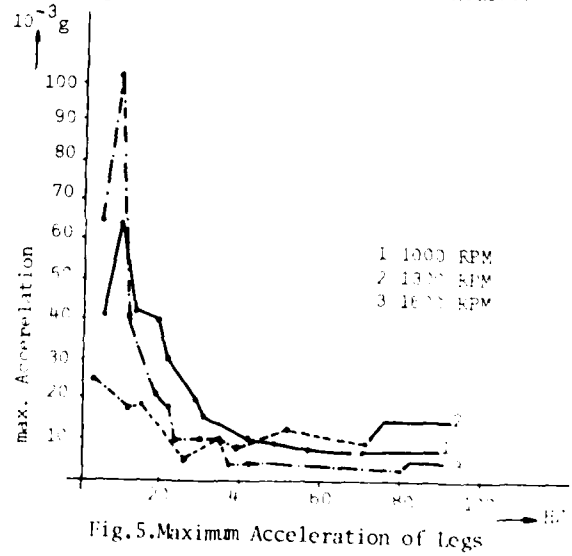

Fig.5.Maximum Acceleration of Legs

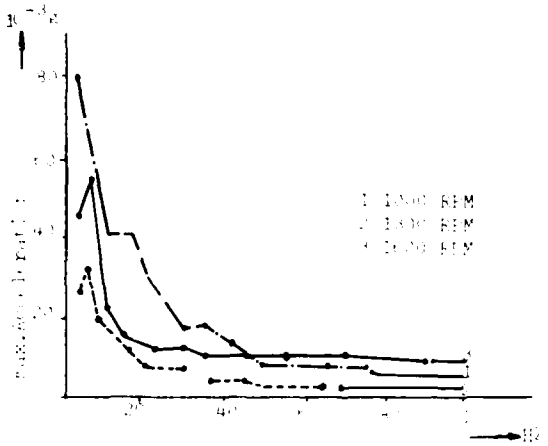

Fig.6. Maximum Acceleration of Abdominal Area

Using the above values of vibrational acceleration together with equation (8) and the values of the parameters of the machine operator, soil and environment shown on table 4 the mean performance of the system per hour per month is derived (Fig.7.8.9.10).

Comparing these results with the actual ones it can be seen that there is no large difference (table 5)

TABLE 4

Values of the parameters of the machine, operator, soil and environment who have used in order to define the mean efficiency of the MMSES.

Machine type D-7	Man operator	Soil	Environment
Jp=1 year	Wa=$200/month	Jm=35°	θc=16°C
N=160 HP	fg=240Kcal/h	c=0.12Kp/cm^2	We=1.0034 $\frac{Kp}{cm^2}$
η=0.80	Wd=1	p=1.91.10^{-3} $\frac{Kp}{cm^4 \cdot S^2}$	W_{es}=78.2%
R_S=2000 rpm			
V_s=0.67m/s	Tr=0.175 sec	τ=1.19Kp/cm^2	P_C=70.9db
F=16.000Kp	t_d=0.80	W_S=14.8%	
V_L=2.52m^3	bv=75.9db	E=24Kp/cm^2	
C_S=$ 10^5		U=5	
S=$ 75.10^3			
b_o=$10/h			
K_S=$0.4/h			

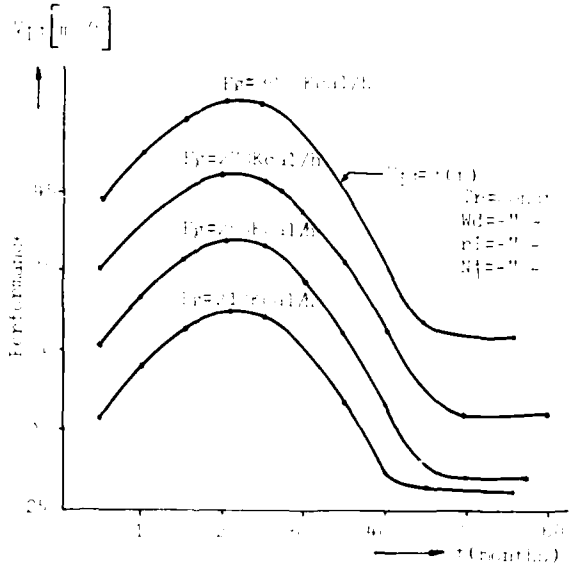

Fig.7. Performance as a function of time

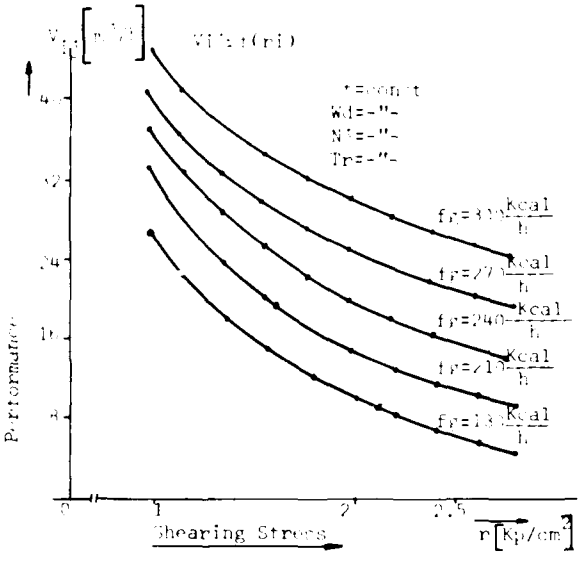

Fig.8. Performance as a function of shearing stress.

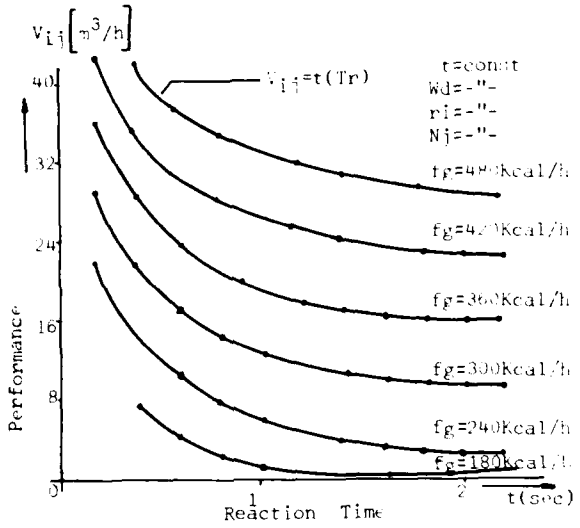

Fig.9 Performance as a function or reaction time

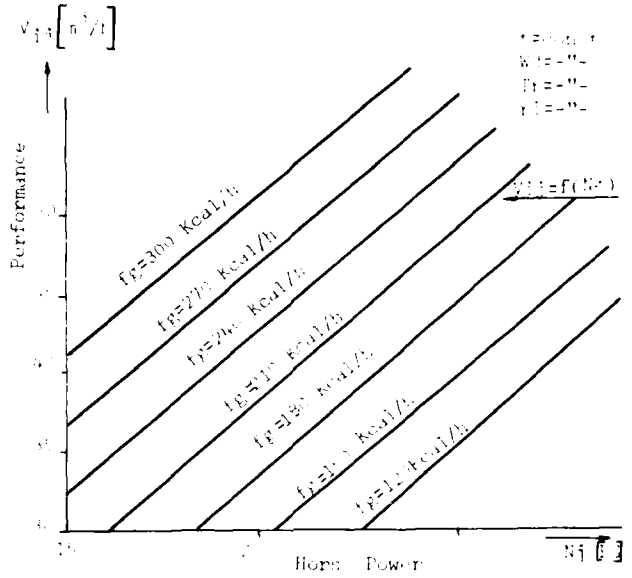

Fig.10. Performance as a function of power

TABLE 5

Average mean performance per hour per year and significance test.

	Year				$\bar{x}$	Difference $\bar{w}$
	1	2	3	4		
Averange mean performance from the model $\bar{x}_B$	36.6	41.62	39.10	30.02	36.83	11.56
Actual averange mean performance $\bar{x}_A$	38.45	40.90	32.23	30.65	35.56	10.25

$$\lambda = \frac{\bar{x}_B - \bar{x}_A}{\bar{w}_A + \bar{w}_B} = \frac{36.83-35.56}{10.25+11.59} = 0.06$$

Since $\lambda=0.06<\lambda=0.618$ for $\alpha=0.01$

we conclude that there is no large difference for 1% level of significance.

APPLICATION

The model can be applied in every case of the MMSE system because the main affect of the parameters ought to the soil parameters with intensive stochastic element. That is to say the stochastic model found is valid for any soil, any construction equipment, any environment.

The only limitation in the MMSE system is the operation of the machine and the action of the operator.

If we have any condition of that operation the stochastic model is valid. For these reason we choose random machine and operator in a Soil and Environment and it seems in following application.

a. Giving as input data shown on the table 4 in the model of relationship of equation (8), the output data shown on table 5, show the obtained results of this application.

In this application it is observed the small difference for 1% significance level when there is small difference the real and the calculated performance.

DISCUSSION

From the experimental results (table 3) it can be seen that the largest values of the acceleration on the various members of the operators body except in one case in which the frequency of the vibration (81 HZ at 1600 RPM)came closed with the frequency of the engine 79.99 HZ, appear in the frequency band 1-15 HZ.

The resonant frequencies of the various members of the operator body appeared in the same frequency band.

The largest values of the vibrational acceleration of the abdominal area appeared in the reasonant band of 4-6 HZ.

The largest value of acceleration of the MMSE systems was bv=0.201 g at the frequency of 136 HZ, engine speed 1300 RPM and soil characteristics (clay 16%, silt 46%,sand 38%). This is the resonant frequency of the machine. Comparing the values of the acceleration measured on the various members of the body it can be seen that the smallest values of the acceleration of the abdominal area, legs, seat and the floor of the machine are the largest values of the acceleration of the head and shoulders.

The variation of the largest value of the vibration acceleration is proportional to the increase of the engine speed for frequencies up to 50 HZ. For larger frequencies, the vibrational acceleration remains constant (fig.2 & 6).

To examine how the performance of the MMSE system varies with time when various parameters dependent or independent) are involved under real conditions the efficiency of the MMSE system was based on the final results of the machine (M^3/h).

Based on the results shown on fig.8,9 and 10 it can be seen that:

a) The efficieny of the system in the first operational stages is small while it increases at the later stages, reaches a highest point and as time passes by, it decreases to a lowest value and stays there with time, till the end of the economic life. This occurs in the real situations.

b) When the shearing stress of the soil increases the performance of the system decreases. This occurs in actual practice and the performance depends on the efforts of the operator.

c) As the vibrational acceleration of the operator and the response time increase, the efficiency of the system decreases.

CONCLUSIONS

The derived stochastic model describes the behaviour of the MMSE system without restrictions in the number of variable used and can be solved with respect to any variable.

Use of this model makes the principle of operation of the MMSE system more understandable, which is very important for constructional equipment with respect to the productional operation of the machine during its economic lifetime.

REFERENCES

1. T.C.Bloomquist, " An experimental model of closed head injury", paper pres at 1978 SESA spring meeting in Wichita Kansas.
2. K.M. Captain, D.W. Wormley, " Representation of the tire-road interface for Vehicle Vibration testing. Paper pres in Spring Meeting of SESA in Chicago.
3. P.A. Drakatos, " The vibration in construction equipment", 46th shock and vibration bulletin, Washington.
4. P.A Drakatos, etc. A.S. Massinas 'Computerised method of constructions equipment cost estimating, AACE Transactions,1978.
5. J.C. Huston, " Analysis of the dynamics of

head-neck injury ",Paper pres at spring meeting 1978,of SESA in Wichita

6.A.S. Massinas, P.A. Drakatos, "Human factors in construction equipment", VII International Congress of Biomechanics,Warsaw.

7.G. Murphy, "Similitude in Engineering", New York, Ronald Press.

8.K.C. Parsons, M.J. Greiffin, "The effect of rotational vibration in roll and pitch axes on the discomfort of seated subjects, Ergonomics" 1978,vol.21,No.8

9.H.M. Parsons, "Man - machine system experiments" John Hopkins pres,London.

10.D.W. Repperger, K.A. Smiles, "A feature selction approach in evaluation of parameter changes on the Human operator under thermal stress",Ergonomics 1978,vo.21.No1.

AN OPTIMUM SEAT-SUSPENSION FOR OFF-ROAD VEHICLES

S. Rakheja and S. Sankar
Department of Mechanical Engineering
Concordia University
Montreal, Quebec, Canada

Low frequency terrain induced vibration transmitted to off-road vehicle operator are quite severe and exceed I.S.O. specified "Fatigue-decreased-proficiency limits". Design of an optimum seat-suspension to protect the drivers from incoming injurious vibrations in bounce, longitudinal, lateral, roll, and pitch modes, is presented. In this paper, the existing bounce seat-suspension is modeled as 2-DOF, non-linear system. Configuration of a horizontal isolator attachable to the existing bounce isolator to attenuate longitudinal and lateral vibration is proposed and modeled including non-linearities. The non-linear models in the three translational modes are linearized, and design parameters are selected through parametric optimization. Optimization problem is formulated to maintain the acceleration PSD's within the ISO specified limits, corresponding to 4 hours exposure while constraining the relative displacements to a minimum possible. Isolation of roll and pitch vibrations is sought through a gimbal arrangement mounted to the bounce isolator. Parametric optimization of the linear rotational model is carried out to maintain bounce acceleration response within 4 hours exposure limit (ISO), subject to constrained pitch and roll accelerations.

INTRODUCTION

Several studies over the past have established that prolonged exposure to low-frequency, large amplitude terrain-induced vibration on agricultural and other off-road vehicles cause operator bodily discomfort, physiological damage and inefficient performance [1,2,3,4]. Vibrations transmitted to agricultural tractor operators are particularly severe due to unsprung nature of the vehicle. Such ride severities limit the speed of certain farm tasks as function of driver's tolerance to discomfort. During recent years a significant concern has been shown in isolating the operator from injurious vibration, as a result, several vibration tolerance criteria have been proposed. International Standards Organization (I.S.O.) proposed tolerance vibration limits that would apply to farm, and earth-moving vehicles [5,6]. As an attempt to meet proposed tolerance criteria, low natural frequency passive suspension seats have successfully been employed in agricultural tractors, industrial, earth-moving, cross-country vehicles, and heavy trucks to isolate the operator from terrain induced vertical vibrations.

However, various studies indicate that in addition to vertical vibrations, operators are subjected to a significant level of vibration in other translational (longitudinal, and lateral) modes, and in the rotational (roll, and pitch) modes [7,8]. The level of transmitted vibrations in all these modes exceed "Fatigue-decreased proficiency limits" proposed by I.S.O. Hence, there is a need for seat-suspension to protect the driver from translational and rotational vibrations, and to enable the operators to perform efficiently.

This paper investigates an optimum design of an agricultural tractor seat-suspension that provides vibration isolation in translational and rotational modes.

RIDE PROBLEM

Dynamic characteristics of agricultural tractor is mainly a function of radial and lateral stiffness of tyres. Short wheelbase, narrow track, and high center of gravity of the tractor cause not only considerable bounce vibration but a large pitching and rolling motion. Significant horizontal components of vibration are also imposed due to high operator's position. Natural frequencies of the tractor predominantly being approximate 3 Hz. in bounce, 1.5 Hz in roll, and 1-4.5 Hz in pitch. Not only are these frequencies difficult for

isolation, but they happen to be close to those to which human body is most fatigue sensitive. Above all, the tires provide very low damping resulting in large amplitude of vibration at these frequencies.

SEAT-SUSPENSION APPROACH TO RIDE PROBLEM

The simplest option to isolate operators from terrain induced vibrations is to adopt a seat-suspension in the existing tractor configurations. A driver seat has a peculiar importance on off-the-road vehicles, since it is the link between the dirver and the controls. The seat therefore must be a steady platform for the actions of the driver, and it must reduce vibration that the vehicle would transmit to the driver.

The objectives of this work are to design a seat-suspension soft-enough to isolate the driver from transmitted vibration in bounce (Z), lateral (Y), lonitudinal (X), pitching (θ) and rolling (ϕ) modes (Fig. 1). Such that the acceleration levels of the transmitted vibration remain below the I.S.O. "Fatigue decreased proficiency limits" corresponding to 4 hour exposure time [5] and relative motion between driver and the controls stay within a minimum possible.

DEVELOPMENT OF SEAT-SUSPENSION MODELS

Mathematical models of proposed suspension configurations in logtudinal and lateral modes, attached to an existing bounce seat suspension are developed to analyse the performance of each horizontal isolator along with the bounce isolator. The mathematical models developed include non-linearities arising due to coulomb friction, shock absorbers, and elastic travel limiting stops. Seal friction and leakage flows in the shock absorber are neglected , thus leading to velocity squared damping charateristics.

Mathematical model of the rotational configuration incorporating bounce, roll, and pitch modes is developed assuming linear suspension elements.

BOUNCE SEAT-SUSPENSION

Bostrom XL-seat suspension model (Figures 2a & 2b) with constant spring rate is considered for analysing the bounce seat-suspension response. Equations of motion for the model are:

$$M_1 \ddot{Z}_1 + K_1 (Z_1 - Z_2) + C_1(\dot{Z}_1 - \dot{Z}_2) = 0$$

$$M_2 Z_2 + F_d^Z + F_C^Z + K_2 (Z_2 - Z_O) + K_1 (Z_2 - Z_1) + F_S^Z + C_1 (\dot{Z}_2 - \dot{Z}_1) = 0$$

where K_1 and C_1 are cushion stiffness constant and damping coefficient repectively (Fig. 3) [9].

M_1 is operator mass (5/7 of human mass [4])

M_2 is the suspension mass

K_2 is the spring rate due to suspension linkage (Fig. 4)

F_C^Z, F_d^Z, F_S^Z are suspension forces due to coulomb friction, shock absorber, and elastic stops respectively, given by

$$F_C^Z = \begin{cases} \frac{F_Z}{\Delta v} (\dot{Z}_2 - \dot{Z}_O) & \text{for } |\dot{Z}_2 - \dot{Z}_O| \le \Delta v \\ F_Z \operatorname{sgn} (\dot{Z}_2 - \dot{Z}_O) & \text{for } |\dot{Z}_2 - \dot{Z}_O| > \Delta v \end{cases} \quad (3)$$

$$F_d^Z = C_Z |\dot{Z}_2 - \dot{Z}_O|^2 \operatorname{sgn} (\dot{Z}_2 - \dot{Z}_O) \quad (4)$$

$$F_S^Z = K_S^Z \cdot S_Z \cdot [Z_2 - Z_O - \frac{d_Z}{2} \operatorname{sgn} (Z_2 - Z_O)] \quad (5)$$

where, F_Z is magnitude of friction force determined from Fig. 4.

$$\operatorname{Sgn} (Z) = \begin{cases} -1 & \text{for } Z < 0 \\ +1 & \text{for } Z > 0 \end{cases}$$

Δv is a small viscous band assumed in the vicinity of discontinuity in Coulomb friction characteristics.

C_Z is the coefficient of velocity squared damping in the shock absorber.

K_S^Z is stiffness constant due to elastic stops.

d_Z is total stroke of the suspension system

$$S_Z = \begin{cases} 0 & |Z_2 - Z_O| < d_Z/2 \\ 1 & |Z_2 - Z_O| > d_Z/2 \end{cases}$$

LONGITUDINAL MODEL

Geometric configuration of a proposed longitudinal passive seat-suspension model is presented in Fig. 5a. The unit is added on to the existing bounce model, without affecting its performance due to uncoupled nature of the assembly. Neglecting longitudinal stiffness due to cushion, the equation of motion is:

$$M \ddot{X}_1 + F_d^X + F_C^X + K_X(X_1 - X_O) + F_S^X = 0$$

where,

$$M = M_1 + M_2$$

$$F_d^X = C_X |\dot{X}_1 - \dot{X}|^2 \operatorname{sgn} (\dot{X}_1 - \dot{X})$$

$$F_c^x = \begin{cases} F_x \text{ Sgn } (\dot{X}_1 - \dot{X}_o) & \text{for } |\dot{X}_1 - \dot{X}_o| > \Delta v \\ \frac{F_x}{\Delta v} (\dot{X}_1 - \dot{X}_o) & \text{for } |\dot{X}_1 - \dot{X}_o| \leq \Delta v \end{cases}$$

$$F_s^x = K_s^x \cdot S_x \cdot [X_1 - X_o - \frac{d_x}{2} \text{ sgn } (X_1 - X_o)]$$

and

$$S_x = \begin{cases} 0 & |X_1 - X_o| \leq d_{x/2} \\ 1 & |X_1 - X_o| > d_{x/2} \end{cases}$$

LATERAL MODEL

Lateral isolator has the same configuration as that of the longitudinal isolator (Fig. 5b), and is uncoupled to the bounce mode. Equation of motion:

$$M\ddot{Y}_1 + K_y (Y_1 - Y_o) + F_c^y + F_s^y + F_d^y = 0 \qquad (7)$$

where,

$$M = M_1 + M_2$$

$$F_c^y = \begin{cases} F_y \text{ sgn } (\dot{Y}_1 - \dot{Y}_o) & \text{for } |\dot{Y}_1 - \dot{Y}_o| > \Delta v \\ F_y (\dot{Y}_1 - \dot{Y}_o) / \Delta v & \text{for } |\dot{Y}_1 - \dot{Y}_o| \leq \Delta v \end{cases}$$

$$F_d^y = C_y |\dot{Y}_1 - \dot{Y}_o|^2 \text{sgn } (\dot{Y}_1 - \dot{Y}_o)$$

$$F_s^y = K_s^y \cdot S_y \cdot [Y_1 - Y_o - \frac{d_y}{2} \text{ sgn } (Y_1 - Y_o)]$$

and

$$S_y = \begin{cases} 0 & |Y_1 - Y_o| < d_{y/2} \\ 1 & |Y_1 - Y_o| > d_{y/2} \end{cases}$$

ROTATIONAL MODEL

Geometric configuration of a proposed gimbal supported arrangement to incorporate rotational modes is shown in Fig. 6. Arrangment consists of two gimbal supported frames, separated by a torsional spring and a torsional damper. Gimbal arrangment may be attached to the base via rigid or flexible supports. The configuration dictates that the operator and suspension mass move rigidly with frames under pitching rotation, whereas, operator mass along with the suspension mass moves rigidly with the inner frame alone when subject to rolling motion. A model of bounce isolator mounted on the gimbal arrangment is illustrated in Fig. 7.

By arranging the support springs equidistant, a completely decoupled rolling mode is obtained. Due to complexity of the model, suspension components are assumed to be linear with no limit stops.

Equations of motion

$$[M][\ddot{Z}] + [C][\dot{Z}] + [K][Z] = [D][Z_o] + [E][\dot{Z}_o] \qquad (8)$$

where

[M] is [6 x 6] mass matrix.

[C] is damping coefficient matrix [6 x 6]

[K] is stiffness coefficient matrix [6 x 6].

[D] and [E] are the matrices representing coefficients of the excitation displacement and velocity vectors.

[Z] is the vector representing the generalized coordinates. The transpose of [Z] is

$$[Z]^T = [Z_1, Z_2, Z_3, \theta_1, \phi_1, \phi_2]$$

$[\dot{Z}]$ represents the vector containing time derivatives of generalized coordinates.

$[\ddot{Z}]$ acceleration vector of the model.

$[Z_o]$ is the vector representing the excitation coordinates.

System matrices are presented in Appendix I.

INPUT DATA FOR COMPUTER MODELS

Vibration levels at the agricultural tractors cab floor have been measured at the National Institute of Agricultural Engineers [NIAE] Silsoe, England. The measurements have been made on the simulated track as well as on the field [10, 11]. The acceleration power spectral densities (PSD) generated via Fast Fourier transform (FFT) and their comparison with I.S.O. "fatigue decreased proficiency" limits are presented in Fig. 8. Acceleration PSD in the bounce mode exhibits a large peak exceeding 1 hour I.S.O. exposure limit at 2.6 Hz. In the longitudinal mode, the acceleration PSD exhibits large amplitude in the frequency range 2.5-4 Hz. In the lateral mode, acceleration PSD peaks to a very large amplitude at 1.2 Hz, and beyond 1.7 Hz the PSD acceleration appears quite satisfactory with 4-hour exposure limit.

Pitch acceleration PSD at the cab-floor indicates large peaks in the frequency range 2.5-4 Hz, similar to the PSD obtained in longitudinal mode. Roll acceleration PSD shows two distinct peaks occuring at frequencies 1 Hz and

3.6 Hz. Roll and pitch acceleration PSD's measured at the cab floor are not compared to any vibration tolerance limits, since there are no standards available for tolerance limits under exposure to rotational vibration.

SIMULATION OF SUSPENSION MODELS

Simulation of suspension models is carried out in frequency domain in order to compare its performance with I.S.O. proposed limits, which are specified in RMS acceleration over third-octave frequency bands. Since frequency domain solution requires linear equations, it is necessary to linearize the non-linear equations characterizing the suspension model.

LINEARIZATION

Linearization is a complex process for systems possessing discontinuous characteristics or strong non-linearities (e.g. coulomb friction) [13]. Therefore, a piecewise linear viscous damping coefficeint equivalent to the damping offered by velocity squared damping, and coulomb friction is determined using energy dissipation approach [12]. Piecewise linear viscous damping coefficient obtained is a function of excitation frequency and the relative-motion across the dissipative element. Linear equivalent is obtained by equating the energy dissipated by the non-linear dissipative element as a function of excitation frequency and relative displacement to that of a linear viscous damper under same conditions. Viscous damping coefficient thus obtained remains constant for a given frequency and relative motion. In the case of a velocity squared damping [12]:

$$C_{eq}(\omega,u) = 8\, C_v\, \omega u/(3\pi) \qquad (9)$$

Coulomb friction;

$$C_{eq}(\omega,u) = 4\, F_c/\pi\, \omega\, u \qquad (10)$$

where,

C_{eq} is the equivalent linear viscous coefficient

ω is the excitation frequency in rad/s.

u is the relative motion across the damping element.

C_v is coefficient of velocity squared damping.

A flow-graph of linearization approach is presented in Fig. 9.

RESPONSE PSD EVALUATION

Input excitations due to random terrain can be characterized by their PSD's and CSD's. Acceleration PSD's recorded at cab-floor [10] are used as excitations to computer models. Acceleration PSD response for the piecewise linearized models is evaluated as follows.

Reponse PSD's for suspension models with multiple inputs and outputs is evaluated as [15]

$$S_p = \mathrm{Re}\left[\sum_{i=1}^{n}\sum_{k=1}^{n} H_{pi}(j\omega)\, H_{pk}^{*}(j\omega)\, CSD_{ik}\right] \qquad (11)$$

where

S_p = PSD of p_{th} response variable.

CSD_{ik} = Spectral density of i^{th} and k^{th} input random variable.

= S_i for $i = k$,

= CSD_{ik} for $i \neq k$.

$H_{pi}(j\omega)$ = Complex frequency response function of the linearized system between i^{th} input and p^{th} output, is determined by

$$\bar{Z}(j\omega) = H(j\omega)\, \bar{Z}_0(j\omega) \qquad (12)$$

$\bar{Z}(j\omega)$, $\bar{Z}_0(j\omega)$ are Fourier transform of the output and input random variabels respectively.

n = total number of input variables

p = number of output variables

$H_{pk}^{*}(j\omega)$ = complex conjugate of $H_{pk}(j\omega)$

Influence of suspension parameters is observed by parametric study of each suspension model. However, the results obtained are not presented here, instead the results obtained for optimized suspension models are presented in the following sections.

OPTIMIZATION

Optimization problem is formulated such that the response acceleration PSD at the driver's location must remain within ISO specified fatigue limits, while maintaining the relative motion between the driver and controls to a minimum possible. The objective function may be formulated as

$$U = \text{minimize} \sum_{f} [S_{\ddot{z}}(f) - S_d(f)]^2 \qquad (13)$$

subject to $[S_u(f)] \leq (S_u)$ maximum limit

where

$S_{\ddot{z}}(f)$ is response acceleration PSD at frequency f

$S_d(f)$ is desired acceleration PSD at frequency f, (from I.S.O. limits)

(S_u) maximum limit, is chosen value of maximum permissible relative displacement PSD, $S_u(f)$.

In addition to the above constraint on relative displacement PSD, some parametric constraints are also incorporated in the optimization problem. Table 1 lists the design variables and additional constraints for each suspension model.

TABLE 1
Design Variables and Parametric Constraints of the Suspension Models

Suspension Model	Design Variables	Constraints
Bounce	K_1, K_2, C_z, F_z, M_2	$K_1 > 0$; $K_2 > 0$; $C_z \geq 0$; $M_2 < 10$ kg.; $0 \leq F_z \leq 100N$
Longitudinal	K_x, C_x, F_x	$K_x > 0.$; $C_x \geq 0.$ $0 \leq F_x \leq 100N.$
Lateral	K_y, C_y, F_y	$\sqrt{K_y/M} > 2.5$ rad/s; $C_y \geq 0.$ $0 \leq F_y \leq 100N$
Rotational	$K_1, K_2, K_3, K_4, K_T,$ C_2, C_3, C_T	$K_1, K_2, K_3, K_4 > 0$ $C_2 > 0$, $C_3 > 0$ $(K_T/I_R)^{\frac{1}{2}} > \omega_{min}$ Peak Roll Acceleration PSD ≤ 1.25 $(\frac{rad}{s^2})^2$/Hz Peak Pitch Acceleration PSD ≤ 1.0 $(\frac{rad}{s^2})^2$/Hz

OPTIMIZATION ALGORITHM

Objective function in equation (13) is formulated as a non-linear programmimg problem. Solution of such problems may be sought through one of the several algorithms available. In most of these algorithms, a constrained optimization problem is modified to an unconstrained one, obtained by combining the constraint equations and the original constrained objective function. The unconstrained optimization problem then can be solved by direct search routines [16]. In this paper a modified unconstrained optimization problem is formulated using penalty function approach. Consider an objective function

$$U(\hat{X}) = U(x_1, x_2, \ldots, x_n) \qquad (14)$$

subject to constraints, $g_k(\hat{X}) = (x_1, x_2, \ldots x_n) \geq 0$. ... $k = 1, \ldots, p$. where $(x_1, x_2, \ldots x_n)$ are design variables. The constrained problem is reduced to an unconstrained optimization problem [18]:

$$U_m(\hat{X}) = U(\hat{X}) + 10^{20} \sum_{k=1}^{p} g_k(\hat{X}), \qquad (15)$$

The unconstrained optimization problem is solved by Hooke and Jeeves pattern search routine. The routine minimizes unconstrained objective function using direct search, by varying augment $(\hat{X})$ until the minimum $U_m(\hat{X})$ is obtained.

RESULTS AND DISCUSSION

Absolute transmissibility, relative transmissibility, acceleration PSD's and the relative motion PSD's are evaluated for the optimum passive models. Results for each suspension model are presented along with the comparison with the I.S.O. proposed PSD limits.

BOUNCE MODEL: To test the validity of the linearized model, the results are obtained for the non-linear equations, via numerical integration. A comparison of the absolute transmissibility obtained for the linearized model to that obtained via numerical integration of non-linear equations is presented in Fig. 10. The piecewise linearization technique is found to be extremely accurate.

The acceleration PSD response of the optimum bounce isolator (Fig. 11a) appears satisfactory for I.S.O. 2.5 hours exposure criteria. The response exhibits a large peak at 1.4 Hz. The peak may be reduced by increasing amount of damping or by increasing the limit on relative displacement, increased damping tends to degrade isolation in the frequency range 2-3 Hz (Fig. 11b), but suppresses the resonant peak significantly. The relative displacement PSD response shows a peak at around 1.25 Hz in both cases, however, increased damping lowers peak relative displacement PSD significantly.

LONGITUDINAL ISOLATOR: Acceleration and relative motion PSD (Fig. 12a) response shows a peak at 1.6 Hz and exceeds I.S.O. 2.5 hour

exposure limit at that frequency. However, the response stays within 4-hour exposure limits beyond 1.75 Hz. Increased damping reduces the resonant peak but the PSD response in the isolation region is deteriorated (Fig. 12b). The relative displacement PSD response is quite low in both cases.

LATERAL MODEL: Lateral mode tends to be the most severe and most difficult for the design of isolator, since the excitation exhibits a large peak at 1.2 Hz. An ideal isolator for such excitation shall possess extremely low natural frequency, and hence resulting in large static and dynamic relative displacements. Optimization problem formulated for such an isolator tends to converge to the lowest natural frequency possible. To overcome this difficulty, a lower limit (ω_n = 0.4 Hz) was placed on the isolator stiffness. The PSD response (Fig. 13a) shows large acceleration PSD peak around 1 Hz. However, reduction in damping results in a better acceleration PSD response but poor relative motion response (Fig. 13b). For better isolation, an isolator with natural frequency far less than 0.4 Hz is needed, hence isolation of lateral excitations via passive means appears to be almost unattainable.

ROTATIONAL MODEL: Rotational model as a combination of linear passive elements is optimized and response PSD plots for bounce, pitch, and roll modes are presented in Figures 14, 15 and 16. Since there are no tolerance limits available for rotational vibration exposure, the model is optimized for best bounce acceleration PSD responses [17]. Bounce acceleration PSD response (Fig. 14) can be made to satisfy ISO - 4. hours exposure criteria, a significant improvement over the bounce isolator's response (Fig. 11b). The relative displacement response is also improved significantly. However, an improved bounce response is obtained only at the expense of pitch response.

Pitch acceleration PSD response exhibit peaks at frequencies around 1 Hz. and 3 Hz (Fig. 15), however the peak value is near $1.(rad/s^2)^2/Hz$. The roll acceleration PSD response (Fig. 16) peaks at 0.6 Hz and stays quite low for the remaining frequency range. The relative rotation PSD response (Fig. 17) is extremely good in both cases.

CONCLUSIONS

From this investigation, it may be concluded that a passive seat-suspension system can be designed to protect the driver from terrain-induced injurious vibration. Bounce, longitudinal, pitch, and roll vibration can be attenuated significantly to meet I.S.O. specified 4.0 hours exposure time fatigue decreased proficiency limits while maintaining the relative displacements relatively small. However, the amplitude of transmitted lateral vibration remains quite high due to the severity occuring at 1.2 Hz. This will require an extremely low natural frequency isolator, which is quite difficult via passive means. The addition of flexibly supported gimbal arrangement provides excellent isolation not only in roll and pitch modes, but also improves suspension performance significantly, in bounce mode.

REFERENCES

1. Rosegger; Rosegger: "Health Effects of Tractor Driving", J. Agr. Engr. Res., Vol. 5, #3, 1960.

2. Henning, G.; E. Goldman: "Effects of Shock and Vibration on Man", Shock and Vibration Handbook, Second edition, McGraw-Hill Book Company, 1976.

3. Dupuis, H; W. Christ: "Study of Risk of Spinal Damage to Tractor Drivers", Rep. Max. Planck Institute Lanard Lantech, Bad Kreuznack, 1966.

4. Fishbien, W.; L.C. Salter: "The Relationship Between Truck and Tractor Driving and Disorders of the Spine and Supporting Structure", Ind. Med. Suvr., Vol. 19, 1950, pg. 444.

5. I.S.O.: Exposure toVibration", International Standards Organization, I.S.O. #2631, 1974.

6. Stikeleather, L.F.: "Review of Ride Vibration Standards and Tolerance Criteria", SAE paper #760413, 1976.

7. Young, R.E.; Suggs ,C.W.: "Active Seat-Suspension for Isolation of Roll and Pitch in Off-Road Vehicles", ASAE paper 73-156, University of Kentucky, June 1973.

8. Matthews, J.:"Ride Comfort for Tractor Operators-II: Analysis of Ride Vibration Pneumatic Tyre Tractors", J. of Agr. Engr. Res., Vol. 9 #2, pp. 147-158, 1964.

9. Lowe, F.J.: "Practical Aspects of Suspension Seat Design", Bostrom (U.K.) report, 1974.

10. Mathews, John: "The Measurement of Tractor Ride Comfort", S.A.E. paper #730795, 1973.

11. Roley, D.G.: "Tractor Cab Suspension", Ph.D. Thesis, University of California, 1975.

12. Bandstra, J.P.: "Comparison Equivalent Viscous Damping in Discrete and Continuous Vibration Systems", ASME paper #81-DET-89, 1981.

13. Roberts, J.B.: "Response of Non-Linear Mechanical System to Random Excitation - Part 2: Equivalent Linearization and Other Methods", Shock and Vibration Digest, Vol. 13, #5, May 1981.

14. Damon, Albert; Howard W. Stoudt; and Ross A. McFarland: "The Human Body in Equipment Design", Hrvard University Press, 1966.

15. Bendat, J.S.: "Measurement and Analysis of Random Data", J.W. Inc., N.Y., 1966.

16. Osman, M.O.M.; S. Sankar and R.V. Dukkipati: "Design Synthesis of a Gyrogrinder Using Direct Search Optimization", Mechanism and Machine Theory, Vol. 17, No. 1, pp.33-45, 1982.

17. Leatherwood, Jack D.; Thomas K.; Dempsey, and Sherman A.Clevenson : "A Design Tool for Estimating Passenger Ride Discomfort within Complex Ride Environments", Human Factors, Vol. 22 (B), pp. 291-312, 1980.

18. Sidall, J.N.: "Analytical Decision Making in Engineering Design", Prentice-Hall, Eaglewood Cliffs, New Jersey, 1972.

APPENDIX 1

$$[M] = \begin{bmatrix} M_1 & 0 & 0 & 0 & 0 & 0 \\ 0 & M_2 & 0 & 0 & 0 & 0 \\ 0 & 0 & M_3 & 0 & 0 & 0 \\ 0 & 0 & 0 & I_p & 0 & 0 \\ 0 & 0 & 0 & 0 & I_o & 0 \\ 0 & 0 & 0 & 0 & 0 & I_R \end{bmatrix}$$

where

$$I_p = I_p^{Op} + M_1 f_1^{\,2} + M_2 f_2^{\,2} + I_p^g$$

$$I_o = I_R^o$$

$$I_R = I_R^{op} + I_R^i + M_1 f_1^{\,2} + M_2 f_2^{\,2}$$

where

I_p^{op} , I_R^{op} = pitch & roll mass moment of inertia of the operator.

I_p^g = pitch mass moment of inertia of gimbal frames.

I_R^i , I_R^o = roll mass moment of inertia of inner & outer frames.

$$[D]\{\dot{Z}_0\} = \begin{bmatrix} 0 \\ 0 \\ C_3\dot{Z}_0 - a_1 C_3\dot{\theta}_0 \\ -a_1 C_3\dot{Z}_0 - a_1^2 C_3\dot{\theta}_0 \\ 0 \\ 0 \end{bmatrix}$$

$$[E]\{Z_0\} = \begin{bmatrix} 0 \\ 0 \\ (K_3 + K_4) Z_0 - (a_1 K_3 - K_4 a_2)\theta_0 \\ -(a_1 K_3 - K_4 a_2) Z_0 + (K_3 a_1^2 + K_4 a_2^2)\theta_0 \\ 0 \\ K_4 b^2 \phi_0 \end{bmatrix}$$

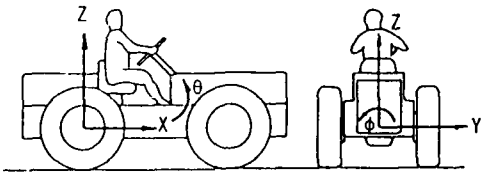

Fig. 1. Orientation of Tractor Co-ordinates

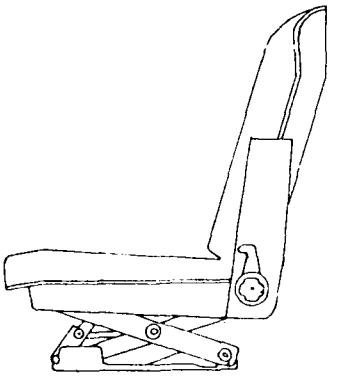

Fig. 2a. Schematic of a Bostrom Seat Suspension.

$$[C] = \begin{bmatrix} C_1 & -C_1 & 0 & 0 & 0 & 0 \\ -C_1 & C_1+C_2 & -C_2 & -a_2C_2 & 0 & 0 \\ 0 & -C_2 & C_2+C_3 & a_2C_2-a_1C_3 & 0 & 0 \\ 0 & -a_2C_2 & a_2C_2-a_1C_3 & a_2^2C_2+a_1^2C_3 & 0 & 0 \\ 0 & 0 & 0 & 0 & C_T & -C_T \\ 0 & 0 & 0 & 0 & -C_T & C_T \end{bmatrix}$$

$$[K] = \begin{bmatrix} K_1 & -K_1 & 0 & 0 & 0 & 0 \\ -K_1 & K_1+K_2 & -K_2 & -a_2K_2 & 0 & 0 \\ 0 & -K_2 & K_2+K_3+K_4 & a_2K_2-a_1K_3+a_2K_4 & 0 & 0 \\ 0 & -a_2K_2 & -a_1K_3+a_2K_4 \\ & & +a_2K_2 & a_1^2K_3+K_4a_2^2 \\ & & & +a_2^2K_2 & 0 & 0 \\ 0 & 0 & 0 & 0 & K_T & -K_T \\ 0 & 0 & 0 & 0 & -K_T & K_4b^2+K_T \end{bmatrix}$$

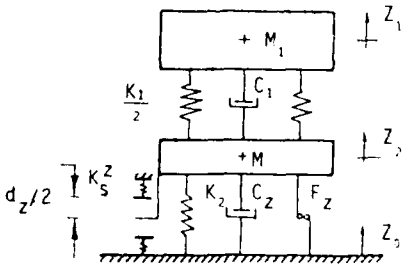

Fig. 2b. Schematic model of a Bostrom Suspension.

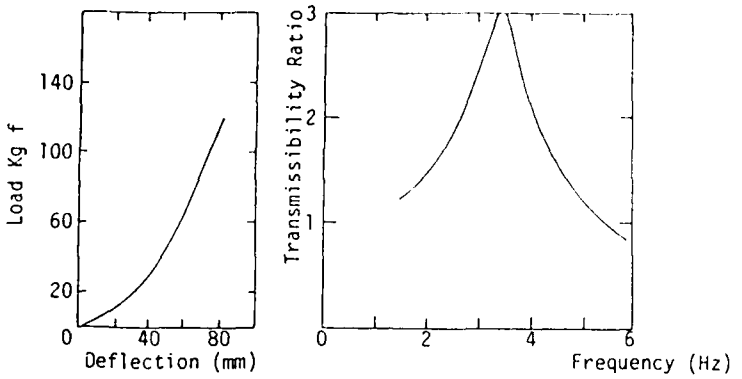

Fig. 3. Cushion Characteristics

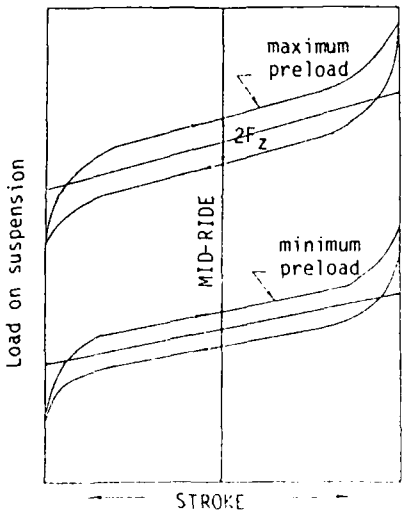

Fig. 4. Suspension linkage characteristic

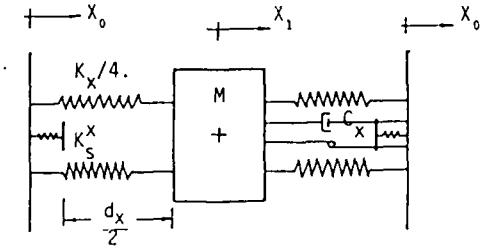

Fig. 5a. Longtudinal Isolator model.

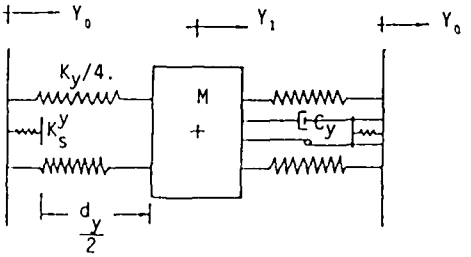

Fig. 5b. Lateral seat-isolator model

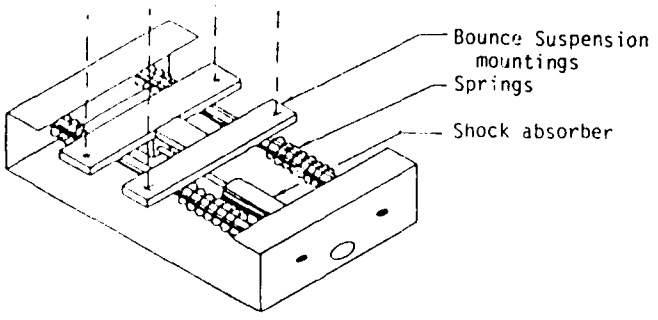

Geometric Configuration

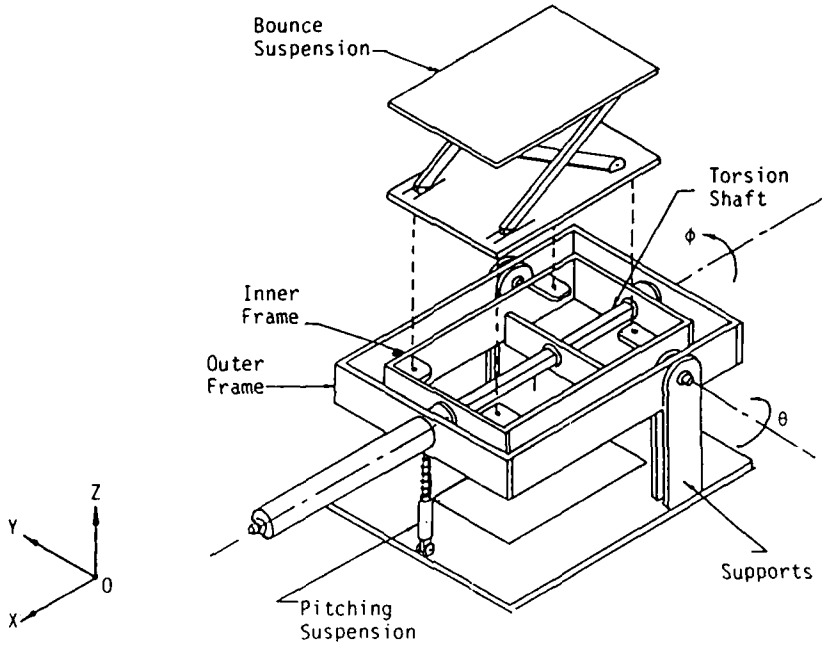

Fig. 6. Geometric Configuration of a gimbal supported rotational isolator

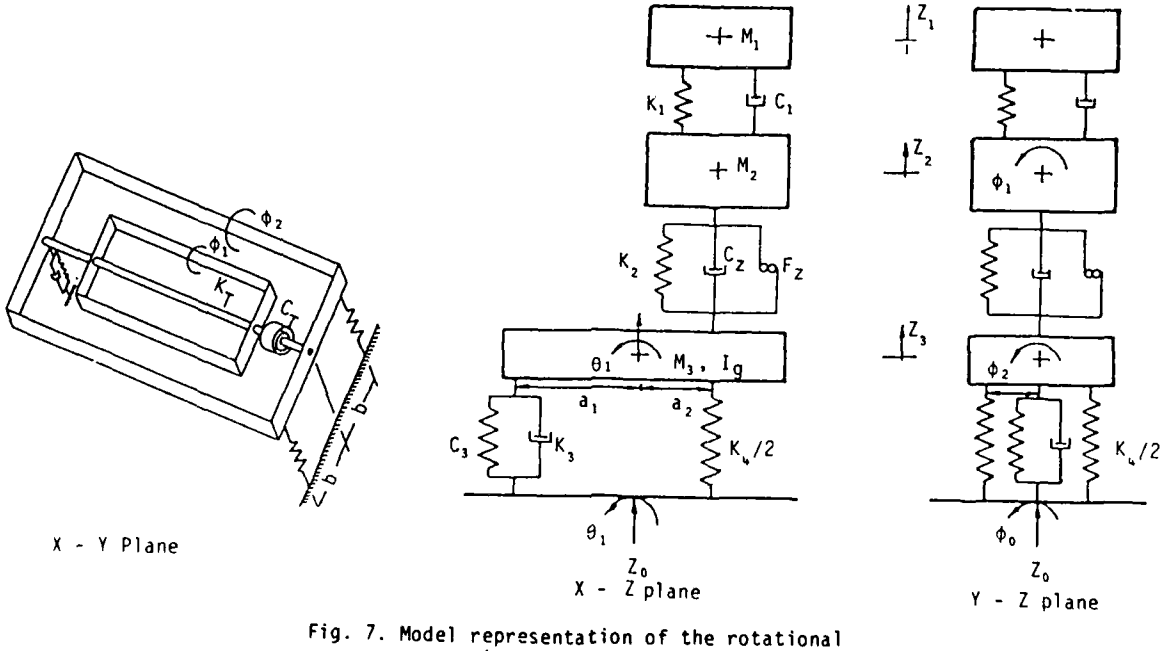

Fig. 7. Model representation of the rotational suspension

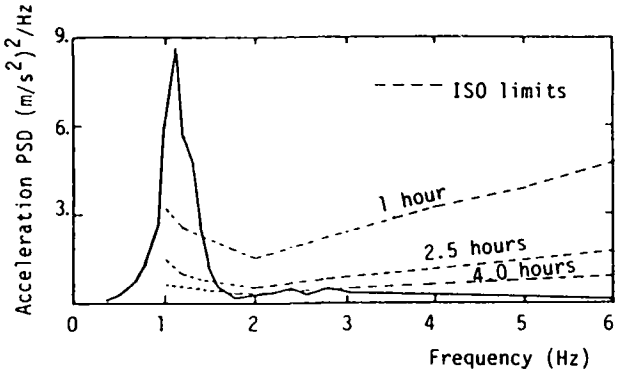

Fig. 8c. Acceleration PSD of lateral vibration measured at cab floor [10,11]

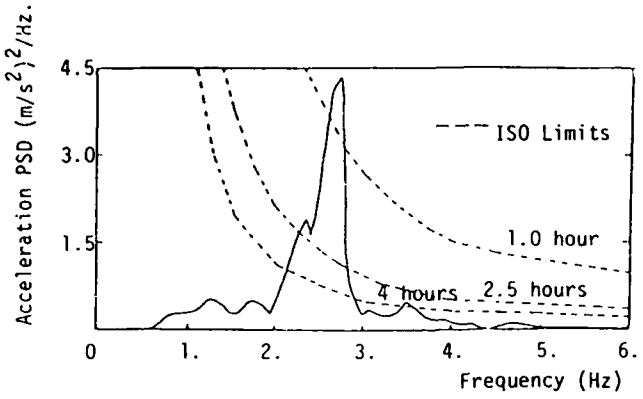

Fig. 8a. PSD of bounce acceleration measured at cab floor [10,11].

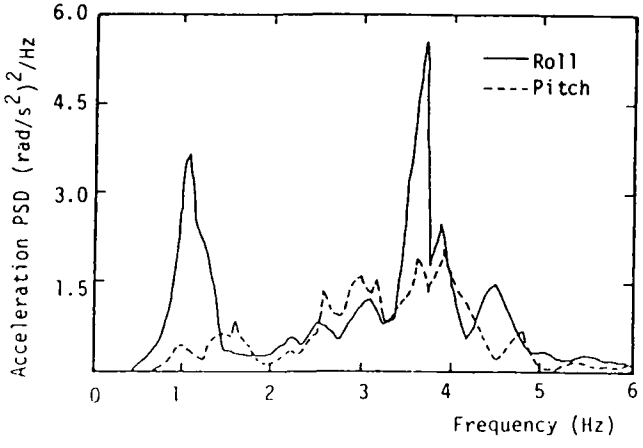

Fig. 8d. Roll and pitch acceleration PSD

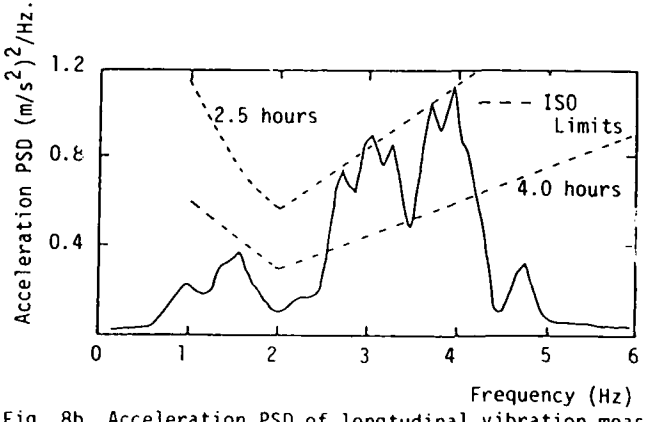

Fig. 8b. Acceleration PSD of longtudinal vibration measured at cab floor [10,11].

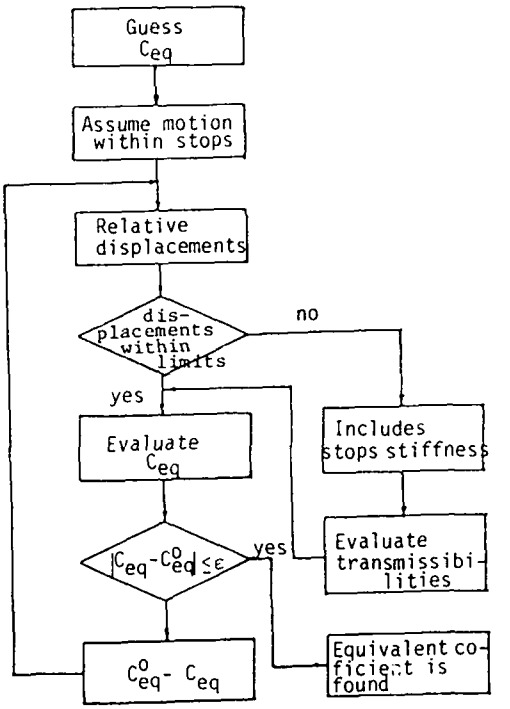

Fig. 9. Flow chart presentation of the piecewise linearization technique.

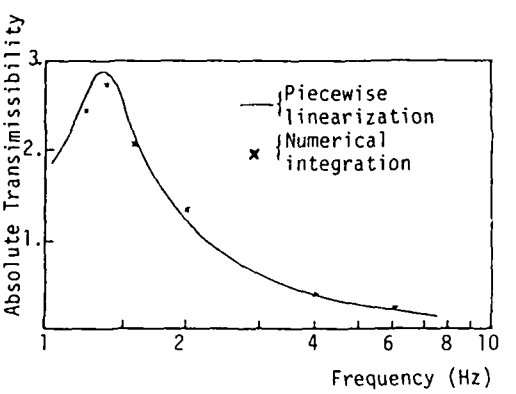

Fig. 10. A comparison of absolute transmissibilities obtained via piecewise linearization and from numerical integration.

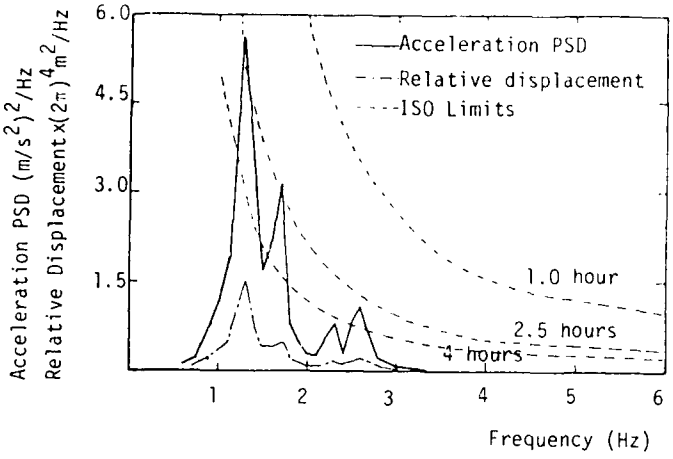

Fig. 11a. PSD response of an optimum bounce isolator.
(K_1=18123 N/m, K_2=7652 N/m, C_z=22 NS^2/m^2, F_z=20N, M_2=10 Kg.)

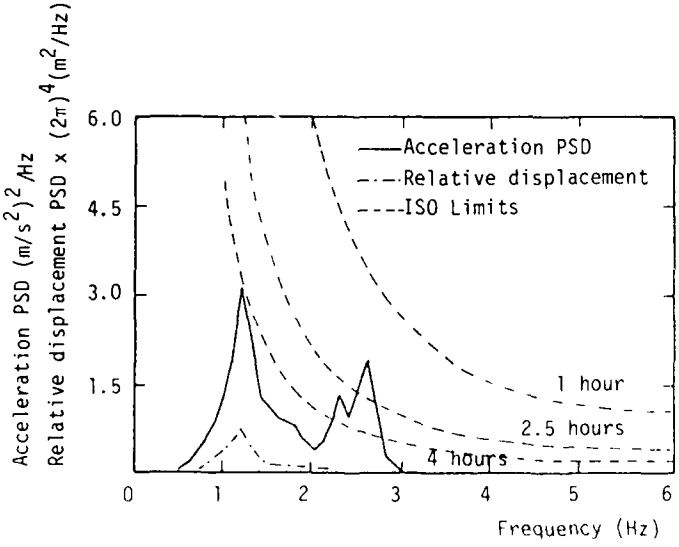

Fig. 11b. PSD response of an optimum bounce seat-suspension.
(K_1=18123, K_2=7652, C_z=40 NS^2/m^2, F_z= 60N)

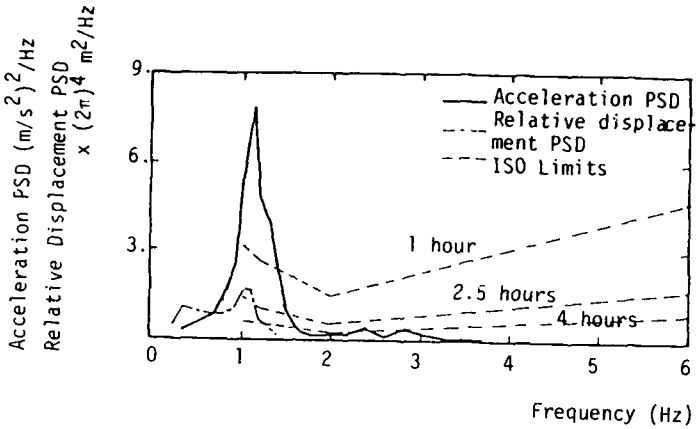

Fig. 13a. Response of an optimum lateral isolator (K_y=1088 N/m, F_y=55N, C_y=278 NS^2/m^2)

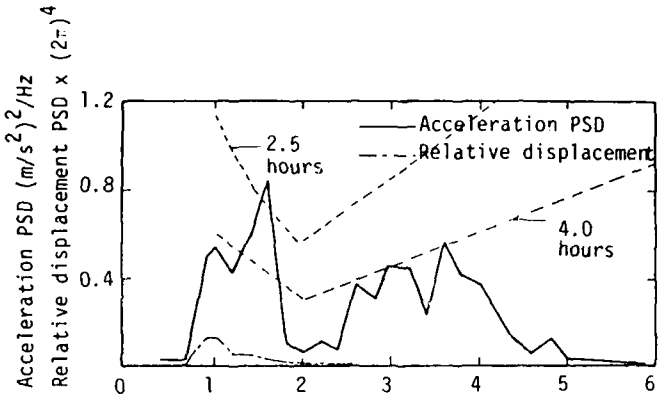

Fig. 12a. Response of an optimum longtudinal isolator (K_x=5032 N/m, C_x=78.53 NS^2/m^2, F_x=0)

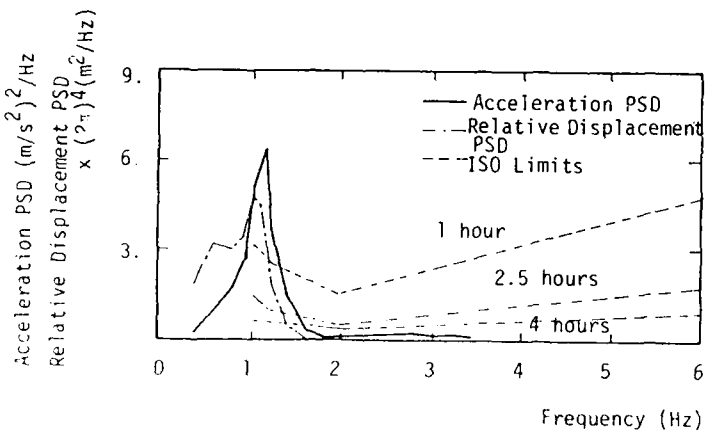

Fig. 13b. PSD response of an optimum lateral isolator (K_y=1088 N/m, C_y=81. NS^2/m^2, F_y=69N).

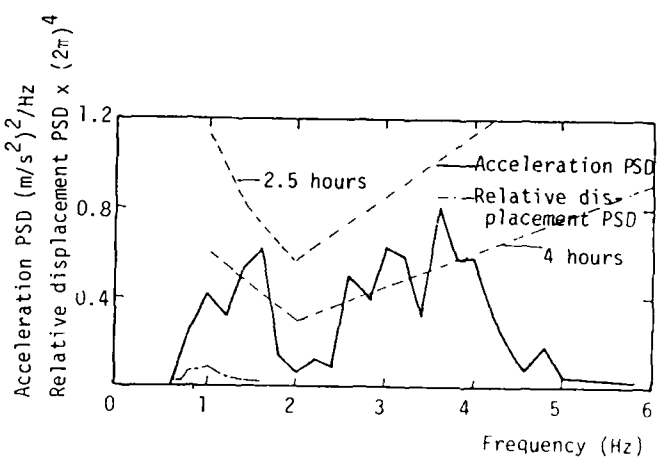

Fig. 12b. PSD response of an optimum longtudinal isolator.
(K_x=5032 N/m, C_x=150 NS^2/m^2, F_x=50N)

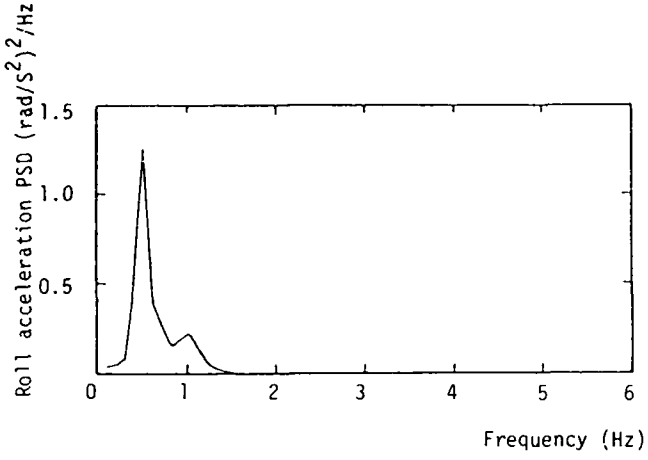

Fig. 16. Roll acceleration PSD response of rotational isolator

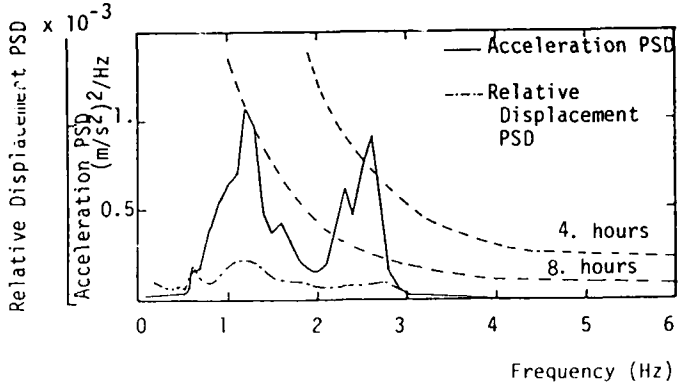

Fig. 14. Bounce PSD response of the rotational isolator. (K_1=31472 N/m, K_2=6225 N/m, K_3=3600 N/m, K_4=4354 N/m, C_3=400 NS/m, C_2=1570 NS/m, K_T=4975 N.m/rad., C_T=532 N.m.s/rad).

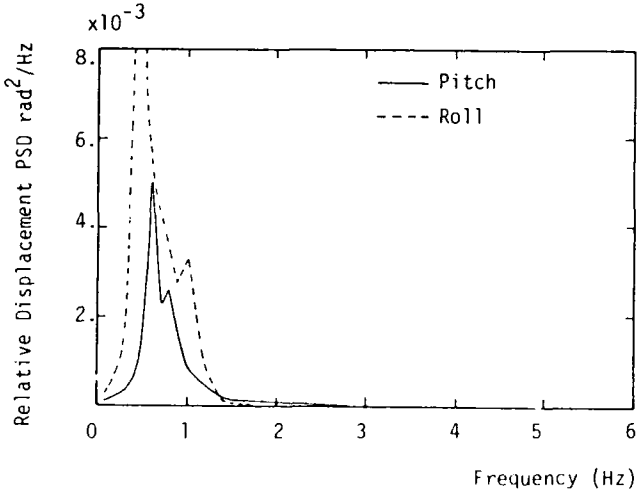

Fig. 17. Relative displacement PSD response of rotational isolator in roll and pitch modes.

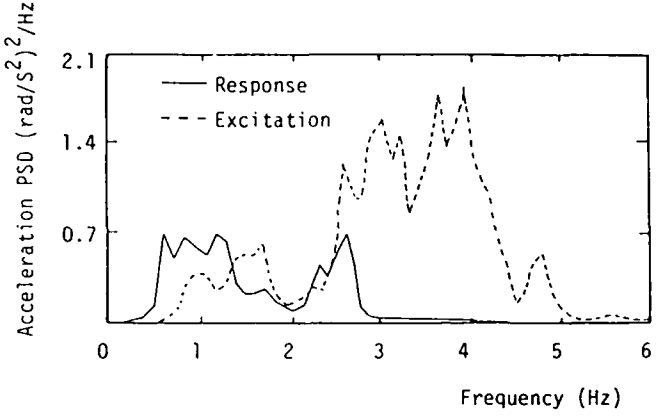

Fig. 15. Pitch acceleration PSD response of rotational isolator. (K_1=31472 N/m, K_2=6225 N/m, C_2=1570 NS/m, K_3=3600 N/m, K_4=4354 N/m, C_3=400 NS/m, K_T=4975 N.m/rad, C_T=532 N.m.s./rad).

DISCUSSION

Mr. Lee (U.S. Army Tank Automotive Command): It would seem to me that an optimum seat is a function of the input to that seat, which is also a function of the terrain and the speed of the vehicle. Therefore, any passive seat would be optimized for a particular speed and terrain; it would not be optimized for the vehicle over all different terrains and speeds.

Mr. Rakheja: That is true. The vehicle speed was taken as 12 kilometers per hour for this particular case, which is sort of an average for the medium size tractors. If the speed varies, the natural frequencies of the tractor will vary slightly. In that case we will probably have to go through a procedure to vary the natural frequencies of the seats the same way. But on the other hand, if the speed doesn't vary very much, it is not going to affect the performance as much.

Mr. Lee: The ISO limits are sinusoidal tolerance curves. Arbitary selections of bandwidths associated with those have more influence on the tolerance limits than the original curves. How did you handle the bandwidth for the ISO curves?

Mr. Rakheja: I also specified the 1/3 octave bandwidth in this particular case.

Mr. Lee: I guess that is one of my objections to the ISO standards; they arbitrarily specify bandwidths associated with sinusoidal tolerance curves that have more influence on the tolerance level than the original curve.

Mr. Rakheja: We took the 1/3 octave bandwidths suggested by them as a test for this particlar case, and we took them on a linear scale rather than on a log scale.

FREQUENCY AND TIME DOMAIN ANALYSES OF OFF-ROAD MOTORCYCLE SUSPENSION

M. van Vliet, S. Sankar and C.N. Bapat
Department of Mechanical Engineering
Concordia University, Montreal, Canada

It is the objective of this investigation to establish a systematic analytical procedure supported by suitable laboratory experiments to provide guidelines in the performance evaluation of motorcycle suspensions. The subject matter is developed by considering the front suspension as a non-linear single degree of freedom system. The non-linearities are introduced to obtain a physically accurate model. They include the effects of seal friction, entrapped gas, turbulent flow, and asymmetric damping. A digital simulation is then performed in both the frequency and time domains. Laboratory testing techniques are then introduced. A conventional front fork is tested and the results presented in both frequency and time domains. A good correlation exists between the analytical results and the experimental results. Having verified the computer model, a parameter variation is performed which illustrates the effects of various suspension components on the performance of the motorcycle suspension.

INTRODUCTION

In the off-road motorcycle suspension, the interrelationship between transmitted force and allowable travel is a paramount design consideration. If the allowable travel is indefinite, any low level of transmitted force can be achieved. Likewise if the transmitted force is unspecified the suspension travel can be reduced to any value. However, the effects of high transmitted force on rider fatique and adverse handling traits of long travel suspensions necessitate a compromise solution.

The front suspension typically consists of an oil-filled telescopic fork in which the frame mounted stanchion tubes and wheel mounted sliders (alloy tubes which slide over the stanchion tubes) effect the springing and damping by means of an internal spring and valving mechanism as shown in Fig. 1. The springing is achieved by a helical spring and pressurized air column. The valving mechanism may be viewed in Fig. 2 consisting of a damping piston and orifice in parallel. The ring housed in the piston body provides an added restriction during fork extension. When the motorcycle encounters a bump, the slider moves up the stanchion tube compressing the spring. At the same time, the oil trapped in the slider lifts the piston valve off its seat and passes through the piston. In addition to the flow past the piston, oil flows through the damper rod orifice due to the volume of stanchion tube entering the slider. On the return or extension stroke the oil that is trapped above the piston causes the valve to drop onto its seat, providing an added restriction.

At present in most motorcycle industries shock dynometers [1,2,3] are used to identify suspension damping characteristics. The dynometer arrangement usually consists of a scotch-yoke mechanical linkage or hydraulic cylinder driving one end of the suspension component with a sinusoidal signal while the other end is mounted to a load cell fixed to an inertial frame. The displacement (or velocity) is plotted against the force resulting in a Lissajous diagram as shown in Fig. 3. This method of testing is limited to verification of damping characteristics only, yielding little insight into the performance of the suspension system.

It is the objective of this investigation to establish a systematic analytical procedure supported by suitable laboratory experiments to provide guide lines in the performance evaluation of motorcycle suspension systems. Previous work [4] yielded an accurate model of the damping elements in the motorcycle suspension. The analysis is extended to include springing, seal friction (stiction), and inertia to obtain a physically accurate model of the suspension

system.

MATHEMATICAL MODEL

In previous work [4] a model for the force exerted by the damper was shown to be (see appendix)

$$F_d = \left(\frac{MR\hat{T}}{V_o - A_c z} - p_a\right) A + T_p \dot{z}^2 \qquad (1)$$

The first term on the right hand side is the non-linear spring force due to the pressurized air column. The second term is the non-linear damping force due to turbulent flow past the piston. T_p is the turbulent flow coefficient shown to be given by

$$T_p = \frac{A_p^3 \rho}{2C_d^2 (A_r^* + A_s^*)^2} \qquad \dot{z} > 0$$

$$T_p = \frac{-A_p^3 \rho}{2C_d^2 A_r^{*2}} \qquad \dot{z} < 0$$

In the previous investigation a shock absorber of 35mm diameter, manufactured by Betor, was modelled. At present the 38mm Marzocchi fork is in more widespread use and is the sample fork in the current investigation. Apart from geometric differences, the forks differ in the number of damper rod orifices and the addition of a hydraulic stop (Fig. 1).

The Marzocchi unit uses a single damper rod orifice which acts as a damper in parallel with the piston-damper. This parallel damper arrangement exists because the flow through the damper rod orifice is independant of the flow through the piston, depending only on the volume of stanchion tube entering the slider. A second effect of the stanchion tube entering the slider is an additional non-linear spring term. Implementing these changes in the analysis of [4], the damper force becomes

$$F_d = \left(\frac{MR\hat{T}}{V_o - A_c z} - p_a\right)(A_p + A_{tube}) + (T_p + T_{or})\dot{z}^2 \qquad (2)$$

where $T_{or} = \dfrac{A_{tube}^3 \rho}{2C_d^2 A_{or}^2} \qquad \dot{z} > 0$

$$T_{or} = \frac{-A_{tube}^3 \rho}{2C_d^2 A_{or}^2} \qquad \dot{z} < 0$$

When the relative displacement z exceeds a value z_1 a hydraulic stop is encountered which is intended to keep the fork from bottoming at the end of the stroke. In the Marzocchi fork the stop is simply an enlargement of the damper rod diameter near the bottom of the fork (Fig.1) The hydraulic stop acts as an additional parallel damper. Following a similar analysis as before the expression for damper force becomes

$$F_d = \left(\frac{MR\hat{T}}{V_o - A_c z} - p_a\right)(A_p + A_{tube}) + (T_p + T_{or} + T_{hyd})\dot{z}^2 \qquad (3)$$

where $T_{hyd} = \dfrac{A_{tube}^3 \rho}{2C_d^2 A_{hyd}^2} \qquad z > z_1,\ \dot{z} > 0$

$$T_{hyd} = \frac{-A_{tube}^3 \rho}{2C_d^2 A_{hyd}^2} \qquad z > z_1,\ \dot{z} < 0$$

$$T_{hyd} = 0 \qquad z < z_1$$

In addition to the damping elements the fork contains seals which exert a stiction force. This stiction can be modelled as a slip-stick mechanism in the model [5]. Consider the front suspension as a single degree of freedom system with mass m, spring k, damper force F_d, and seal stiction F_{seal} as in Fig. 4. For base excitation, $\ddot{y}$ less than F_{seal}/m the system is in the sticking mode. The governing equations in this mode are

$$\ddot{x} = \ddot{y}$$
$$\dot{x} = \dot{y} \qquad (4)$$
$$x = y$$

For base excitation greater than F_{seal}/m, the system is in the sliding mode. The seal stiction can be modelled as coulomb friction depending on the sign of $(\dot{x} - \dot{y})$. Since numerical difficulties arise when $(\dot{x} - \dot{y})$ is zero the stiction is modelled as viscous for small $(\dot{x} - \dot{y})$ [6].

$$F_{seal_1} = F_{coul}\ \text{sign}\ (\dot{x} - \dot{y}) \qquad \text{for } (\dot{x} - \dot{y}) > \varepsilon$$

$$F_{seal_1} = F_{coul}\ \frac{(\dot{x} - \dot{y})}{\varepsilon} \qquad \text{for } (\dot{x} - \dot{y}) \le \varepsilon$$

The governing equation is then

$$m\ddot{x} + \left(\frac{MR\hat{T}}{V_o - A_c(x - y)} - p_a\right)(A_p + A_{tube}) + (T_p + T_{or} + T_{hyd})(\dot{x} - \dot{y})^2 + F_{seal_1} + k(x - y) = 0 \qquad (5)$$

SIMULATION

Frequency Domain:

One method of simulating the dynamic equations characterising the suspension system in the

frequency domain is to use an equivalent linearization technique [7]. The equivalent viscous damper is only an approximation which contains large error when used in velocity squared and coulomb damped systems [8]. Since the fork contains sizable amounts of velocity squared and coulomb damping in addition to being highly discontinuous, an alternative approach was used in this investigation.

The system equations were solved as an initial value problem under harmonic excitation. When steady-state is reached the desired amplitude ratio is stored and the initial value routine restarted at an increased excitation frequency. In this manner, a frequency sweep is performed and the quantities of interest obtained.

The system equations were programed in FORTRAN on a VAX-11/780 digital computer. A predictor-corrector initial value solving routine was used. The results were plotted on a CALCOMP plotter. The quantities of interest are absolute acceleration transmissibility ratio, TR and excitation amplitude Y with frequency f.

The transmissibility characteristics of the motorcycle suspension at various excitation amplitudes are shown in Fig. 5. The flat portion of the curve in the low frequency range is due to seal friction. The curve breaks at a frequency

$$f = \left| F_{seal_1} / 4\pi^2 m Y \right|^{1/2} \qquad (6)$$

Above this frequency, the suspension behaves as a lightly damped system. Since the break frequency can be located on either side of the natural frequency f_N, the input amplitude Y is an influential factor in the performance of the system.

An index which reflects the performance characteristics of the suspension has been proposed [9] as

$$I_f = D(TR_p) + \log_{10}(TR_h)$$

where TR_p = resonant transmissibility

TR_h = transmissibility in higher range ($8\omega_n$ in this case)

D = weighting factor

Considering the transmissibility throughout the frequency range, a weighting value of 2 was used. The value of I_f for 3 excitation amplitudes is shown in Table 1. The minimum I_f indicating better performance.

The performance index can be used to predict changes in the systems' frequency domain behaviour under parameter variation. It is convenient in this application because the system equations need only to be solved twice to obtain an indication of the performance in the frequency domain.

Time Domain:

As in the case of frequency domain simulation, the system equations were solved using an initial value routine. A step displacement or velocity was used for the initial condition. The response to positive and negative displacement steps are shown in Fig. 6. The displacement step response is used only for experimental correlation. However, if it is the only method avalaible for testing, it can be used to classify the performance of the suspension. Performance indices such as percentage overshoot, rise time, peak time and settling time [7] should be used. The percentage overshoot for the various steps (Fig. 6) are shown in Table 2. The difference in the compression and extension values is due to the asymmetric nature of the fork. In actual operating conditions, the velocity step is a more realistic input. The off-road motorcycle repeatedly lands from jumps of up to 2 meters without loss of rider control. If both wheels contact the ground simultaneously, velocity steps of up to 6.3 m/s are realized. The velocity step response is shown in Fig. 7. The two design quantities of interest during the response are transmitted force and relative displacement. When these quatities are plotted for a specific velocity step, the Lissajous diagrams in Fig. 8 are obtained. These force-displacement diagrams can be interpreted physically as follows. Referring to Fig. 8(a) and Fig. 7 the force transmitted along path 0-1-2 occurs during the first quarter period (compression). Path 0-1 is due to the systems' initial veocity and seal stiction. For higher velocity steps, the path 1-2 suddenly increases when the hydraulic stop is encountered (Fig. 8 (c)). Paths 2-3 and 4-5 are due to seal stiction and path 3-4 is the system response during rebound (extension).

The area beneath path 0-1-2 is the energy stored and dissipated during the first quarter period. This energy is determined by the initial condition. Hence for a velocity step v_i

$$\tfrac{1}{2} m v_i^2 = \int_1^2 F \, dz \qquad (8)$$

An optimal performance requirement is that for a specified suspension travel z_{max}, the transmitted force is a constant F_{spec}. Equation (8) then becomes

$$\tfrac{1}{2} m v_i^2 = F_{spec} \, z_{max} \qquad (9)$$

In suspension design allowable travel z_{max} and peak force, F_p are paramount design quantities. For specified input and travel, Equation (9) gives a lower bound (optimum) on the peak force during initial compression

$$F_{opt} = \frac{mv_i^2}{2\, z_{max}} \qquad (10)$$

This optimal value of peak force is compared to the peak force along path 1-2 in Fig. 8. z_{max} is z at point 2 and v_i is the initial velocity. Hence a suitable performance index during compression is

$$I_t = \frac{F_{opt}}{F_p} \times 100\% \qquad (11)$$

When I_t is 100%, the suspension performance is ideal (for a particular v_i). The performance decreases with decreasing I_t. For very lightly damped systems which can be considered as mass-spring systems

$$F_{opt} = \tfrac{1}{2}\, k\, z_{max} \qquad \text{or}$$

$$I_t = 50\%$$

For heavily damped systems F_p may reach any high value at t = 0 as determined by the initial conditions, hence I_t may be very small. It is for this reason that light damping is employed in the suspension during compression.

The compression damping can be specified independent of the rebound damping, however, the final conditions during compression serve as the initial conditions during rebound. Hence the following procedure is suggested for evaluating the motorcycle suspension in the time domain:

1. Select a velocity step v_i.
2. Obtain a force displacement contour and determine I_t. The performance during initial compression is not known.
3. To determine the performance during extension use an appropriate performance index along path 2-4. One such index is the ratio R, of the first 2 successive amplitudes (Fig. 7).

Steps 2 and 3 can be performed simultaneously by simulation or experiment (if impulse testing facilities with digital storage are avalaible). The effects of compression and rebound damping are dominant in steps 2 and 3 respectively. The performance characteristics of the fork used in this investigation are shown in Table 3.

In practice the suspension must respond to a range of inputs. In this range the performance index I_t is more sensitive to the initial velocity than the amplitude ratio R. The input range results in a family of response curves shown in Fig. 9. The variation of I_t over the input range is a characteristic of the suspension. A plot of I_t vs. v_i for the test fork is shown in Fig. 10.

EXPERIMENTAL RESULTS

A single degree of freedom hardware model was used to verify the results obtained from computer simulation. The test rig consisted of a 38 mm Marzocchi fork leg mounted between a mass and an electro-hydraulic shaker. The amount of mass used was determined by measuring the static deflection of an off-road motorcycle with an average size rider on board. The shaker was an ISI unit suitable for low frequency work. The instrumentation consisted of accelermeters mounted on the base and mass. The signals were displayed on a C.R.O. and recorded by polaroid camera. A pictorial view of the test configuration is shown in Fig. 11. To provide guidance for the mass a set of linear bearings with dust seals was used. Unfortunately, the seals introduced stiction of the same magnitude as the fork seals. The additional stiction mechanism differs from the fork stiction because the sign now depends on the sign of absolute velocity $\dot{x}$ instead of the relative velocity $\dot{z}$ $(= \dot{x} - \dot{y})$. Designating the fork seal force and guidance bearing seal force as F_{seal_1} and F_{seal_2}, respectively, Equation (5) becomes

$$m\ddot{x} + \left(\frac{MR\hat{T}}{V_o - A_c(x - y)} - {}_i a\right)(A_p + A_{tube}) + (T_p + T_{or} + T_{hyd})(\dot{x} - \dot{y})^2 + F_{seal_1} + F_{seal_2} + k(x - y) = 0 \qquad (12)$$

where $F_{seal_2} = F_{coul}\ \text{sign}\ (\dot{z}),\ \dot{z} > \varepsilon$

$$F_{seal_2} = F_{coul}\left(\frac{\dot{z}}{\varepsilon}\right), \quad \dot{z} < \varepsilon$$

A frequency sweep at various excitation amplitudes was performed. The results are plotted with the simulation results in Fig. 12. The non-linear nature is evidenced by the strong dependency on excitation amplitude, however there is good agreement between experiment and simulation.

In the time domain a displacement step was used instead of a velocity step because physically the shaker cannot produce a range of velocity steps. Since the forks damping characteristics are asymmetric a set of negative (extension) steps was used to produce larger transients (see Fig. 6). The experimental results are plotted with the corresponding simulation results in Fig. 13. Again there is good agreement between experiment and simulation.

To summarize, the computer simulation was verified by experiment in both frequency and time domains. The mathematical model was modified to include guidance stiction present in the test set up. The effect of this stiction provided very desirable 'skyhook damping' [10], hence the frequency domain characteristics of the off-road motorcycle suspension are more

accurately represented by the results of the previous section (before guidance stiction was introduced in the model).

PARAMETER STUDY

The governing equation contains five terms:

$$m\ddot{x} + \left(\frac{\hat{MRT}}{V_o - A_c(x - y)} - P_a\right)(A_p + A_{tube}) + (T_p + T_{or} + T_{hyd})(\dot{x} - \dot{y})^2 + F_{seal_i} + k(x - y) = 0 \qquad (5)$$

Each term has an associated parameter (mass, damping coefficient, spring rate, etc.) In practice the values of these parameters are determined by the designer and to a lesser extent by the individual rider. Often the effect of a parameter variation is not known until a prototype has been built and tested.

In this section each parameter is varied over a range attainable in pracitce. The effects are observed using the time domain performance index (11).

The effect of damping variation is shown in Fig. 14. Referring to Figs. 9 and 10, it is clear that the decrease in performance for $v_i > 2.8$ m/s is due to the hydraulic stop coefficient T_{hyd}, and vice versa. Fig. 14(b) indicates a compromise for increased damping coefficient T. The performance is improved for small v_i, however the converse is not true for high v_i after the hydraulic stop is encountered ($\hat{v}_i \geq 3$). Fig. 14(c) shows that for increased coulomb damping, (seal stiction) the performance is improved throughout the input range.

Stiffness and inertia are varied in Fig. 15. Fig. 15 (a) seems to indicate an improved peak performance with increased spring stiffness k, whereas Fig. 15 (b) indicates the opposite with increased air spring stiffness $\hat{MRT}$. However, the stiffness variation only alters the point at which the hydraulic stop is met. Hence in the presence of a hydraulic stop, the effects of stiffness variation are unexplicit. The effect of mass variation is shown in Fig. 15 (c). The performance is greatly improved for decreased mass until the hydraulic stop is reached ($v_i = 4.8$ m/s). The effect of decreased mass can be considered as increasing the sensitivity to the remaining parameters in the system (since the initial energy is also decreased). The converse holds true until non-linearities diminish the system performance for high v_i.

In concluding this section one note of caution is in order regarding the parameter study. It should be recalled that only one parameter is varied at a time and the performance noted. In doing so design specifications such as peak force or allowable travel could be exceeded. Hence in practice several parameters must be varied sumultaneously to increase performance and still remain within design specifications.

CONCLUSION

In this paper a frequency and time domain analysis of an off-road motorcycle suspension was carried out. The subject matter was developed by considering the front suspension as a non-linear single degree of freedom system. The non-linearities include the effects of seal friction, entrapped gas, turbulent flow, hydraulic stop, and asymmetric damping. A digital simulation was performed in both the frequency and time domain and a set of performance criteria established. Laboratory testing techniques were introduced. A conventional fork was tested and the results presented in both frequency and time domains. The experimental results correlated well with the analytical results. A parameter variation was performed illustrating the effects of various suspension components on the performance of the motorcycle suspension.

REFERENCES

[1] Jennings, G., "A Study of Motorcycle Suspension Damping Characteristics", SAE Paper No. 740628, 1974.

[2] Wooten, R., "Passenger Car and Light Truck Shock Absorber Inspection Equipment", National Highway Traffic Safety Administration, April 1975.

[3] Simanaitis, D., "Shock Absorbers", Automotive Engineering, November 1976, pp. 34-39.

[4] van Vliet, M. and Sankar, S., "Computer-Aided Analysis and Experimental Verification of a Motorcycle Suspension", ASME Paper No. 81-DET-84, Presented at the 8th ASME Design Engineering Conference, Hartford, Conn., Sept. 20-23, 1981 and accepted for Publication in the Journal of Mechanical Design.

[5] Mansour, W. and Teixeira Filho, D., "Impact Dampers with Coulomb Friction", Journal of Sound and Vibration (1974), 33 (3), pp. 247-265..

[6] Young, R., "A Comparative Study of Shock Isolation Systems Having Linear and Non-Linear Damping", Masters Thesis, Concordia University, 1979.

[8] Bandstra, J., "Comparison of Equivalent Viscous Damping in Discrete and Continuous Vibrating Systems", ASME Paper No.

81-DET-89, Presented at the 8th Design Engineering Conference, Hartford, Conn., Sept. 20-23, 1981, and accepted for Publication in the Journal of Mechanical Design.

[9] Zeidler, D. and Frohrib, D., "Optimization of a Combined Ruzicka and Snowdon Vibration Isolation System", The Shock and Vibration Bulletin, No. 42, Part 4, January 1972, pp.77-83.

[10] Gunter, R. and Sankar, S., "Fail-Safe Vibration Control Using Force Generators", ASME Paper No. 81-DET-85, Presented at the 8th ASME Design Engineering Conference, Hartford, Conn., Sept. 20-23, 1981, and accepted for Publication in the Journal of Mechanical Design.

APPENDIX

Derivation of damper force model, summarized from [4]. The flow characteristic equation through an orifice is

$$Q = C_d A^* [2(\Delta p)/\rho]^{\frac{1}{2}} \qquad (A1)$$

The pressure drop p can be expressed in terms of the force F acting on the piston cross sectional area A_p

$$\Delta p = \frac{F}{A_p} \qquad (A2)$$

For incompressible fluid flow the flow rate Q can be expressed in terms of the relative velocity, $\dot{z}$ as

$$Q = \dot{z} A_p \qquad (A3)$$

Rearranging equations (A1), (A2), and (A3) yields

$$F = T_p \dot{z}^2 \qquad (A4)$$

where $T_p = \frac{A_p^3 \rho}{2 C_d^2 A^{*2}}$ $\quad A^* = A_r^* + A_s^*$ for $\dot{z} > 0$

$A^* = A_r^*$ for $\dot{z} < 0$

In addition to the damping term, there is an entrapped air column in the damper. Considering isothermal, low pressure conditions

$$pV = \hat{MRT} \qquad (A5)$$

The air column decreases with displacement as

$$V = V_o - A_c z \qquad (A6)$$

Combining equations (A2), (A5), (A6) with (A4) yields the expression for the damper force

$$F_c = \left(\frac{\hat{MRT}}{V_o - A_c z} - p_a\right) A_p + T_p \dot{z}^2 \qquad (A7)$$

NOMENCLATURE

A_c	air column area ($A_p + A_{tube}$), m^2
A_{hyd}	hydraulic stop area, m^2
A_{or}	orifice area, m^2
A_p	piston area, m^2
A_{tube}	stanchion tube area, m^2
A_r^*	orifice flow area at ring, m^2
A_s^*	orifice flow area at stanchion tube, m^2
C_d	orifice discharge coefficient, dimensionless
D	weighting factor, dimensionless
F	force, N
F_d	damper force, N
F_{opt}	optimal force, N
F_p	peak force, N
F_{seal_1}	fork seal friction force, N
F_{seal_2}	guidance seal friction force, N
f	frequency, Hz
I	performance index, dimensionless
k	spring constant, N/m
m	equivalent rider and bike mass per fork leg, kg
$\hat{MRT}$	gas constant, N - m
p	pressure, Pa
Pa	atmospheric pressure, Pa
Q	flow rate, m^3/s
T_{hyd}	hydraulic stop coefficient, kg/m
T_{or}	orifice flow coefficient, kg/m
T_p	piston flow coefficient, kg/m
TR	transmissibility ratio, dimensionless
t	time, s
V	volume, m^3
v	velocity, m/s
x	absolute displacement, m
Y	excitation amplitude, m
y	base displacement, m
z	relative displacement, m

z_1 location at hydraulic stop

ε incremental velocity, m/s

ρ mass density, kg/m^3

$\cdot$ differentiation with respect to time

TABLE 1

Frequency Domain Performance

Exitation Amplitude cm (p - p)	TR_p	TR_h	Performance Index, I_f
1.5	1.00	0.053	0.72
2.5	2.18	0.053	3.08
3.5	3.89	0.053	6.50

TABLE 2

Time Domain Performance, Displacement Input

Initial Displacement, m	Percentage Overshoot, %
0.10 (Compression)	48
0.20 (Compression)	40
-0.10 (Extension)	69
-0.20 (Extension)	67

Table 3

Time Domain Performance, Velocity Input

Initial Velocity, m/s	Amplitude Ratio, R	Performance Index, I_t%
1.0	2.25	64
2.0	2.92	70
4.0	3.93	47

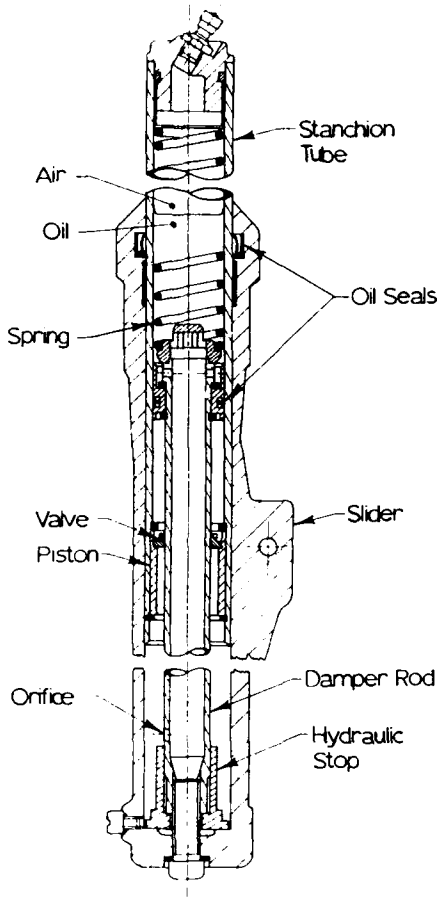

Figure 1: Marzocchi 38 mm Fork Leg

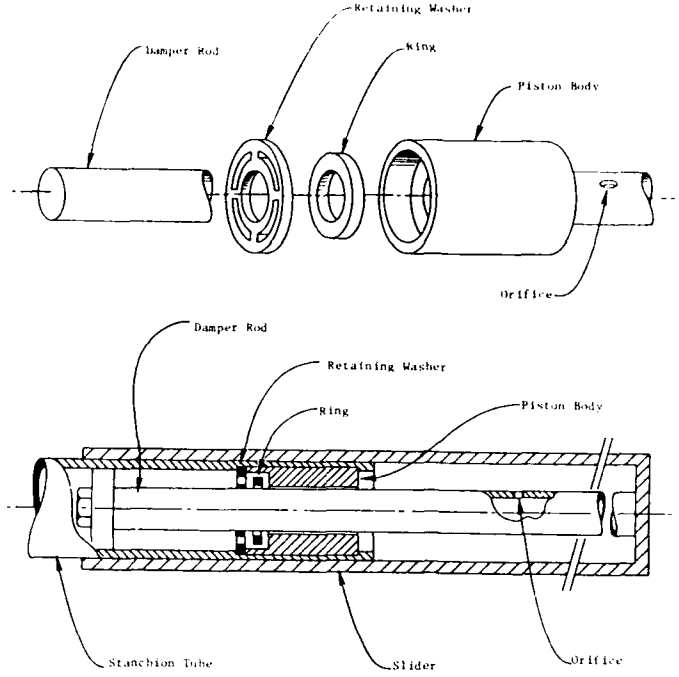

Figure 2: Front Fork Valving Mechanism

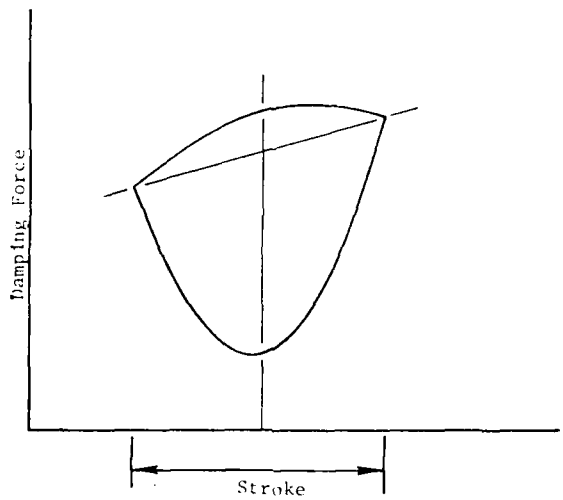

Figure 3: Fork Displacement Diagram

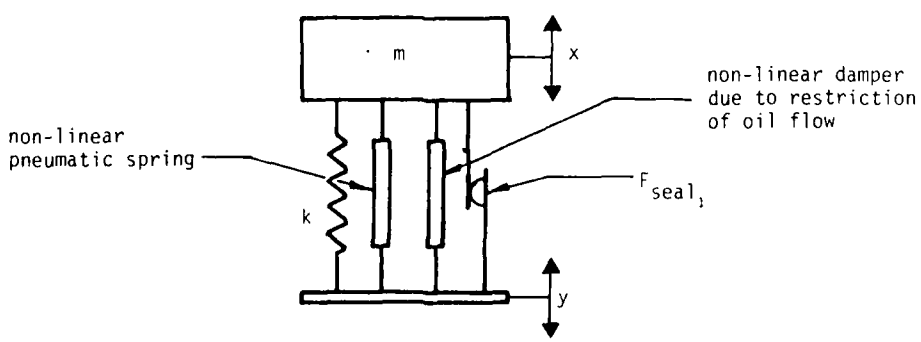

Figure 4: Suspension Model

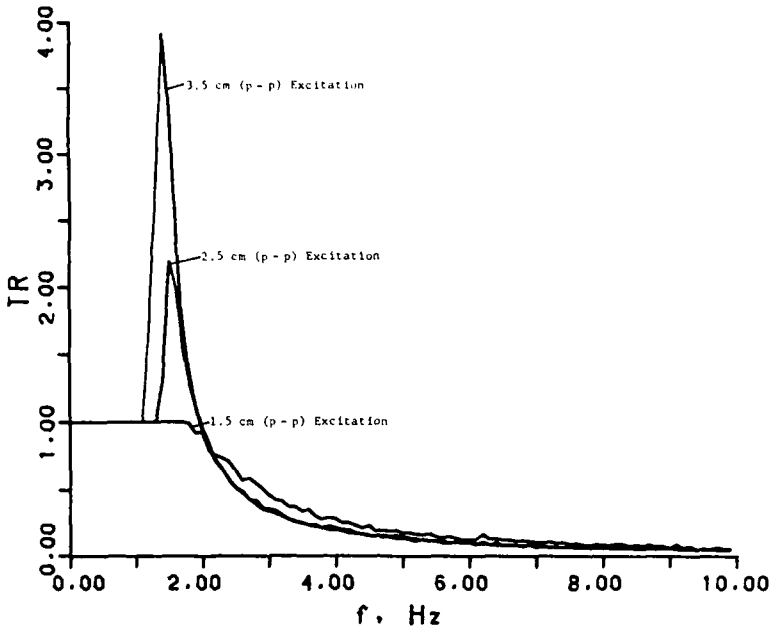

Figure 5: Simulated Transmissibility Characteristics

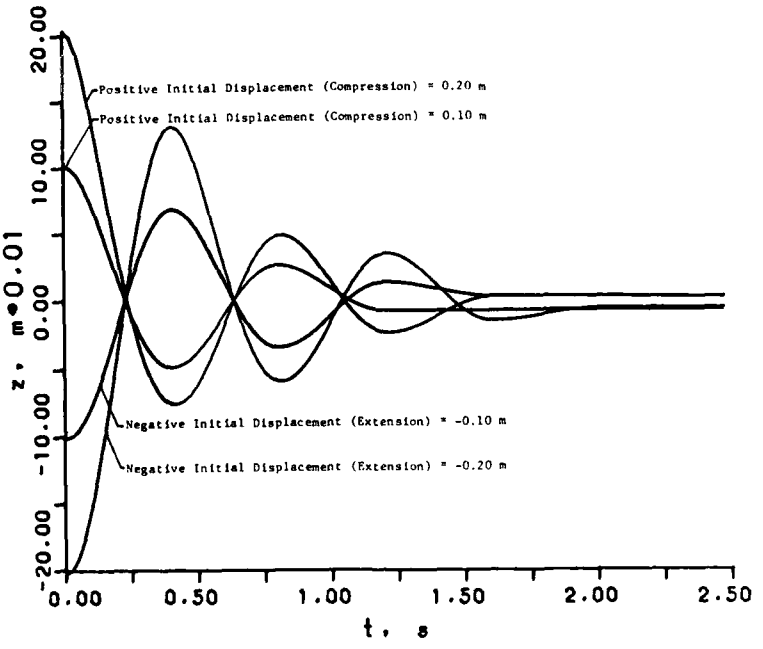

Figure 6: Simulated Displacement Step Response

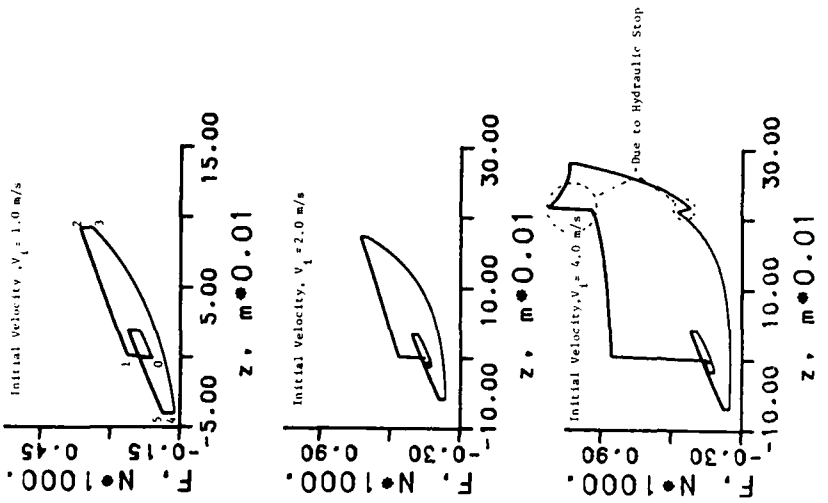

Figure 8: Simulated Lissajous Diagrams

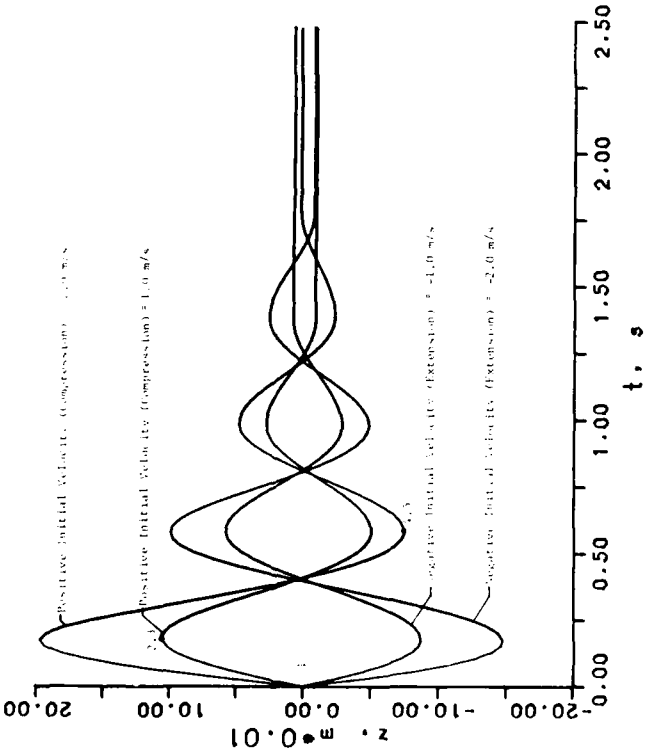

Figure 7: Simulated Velocity Step Response

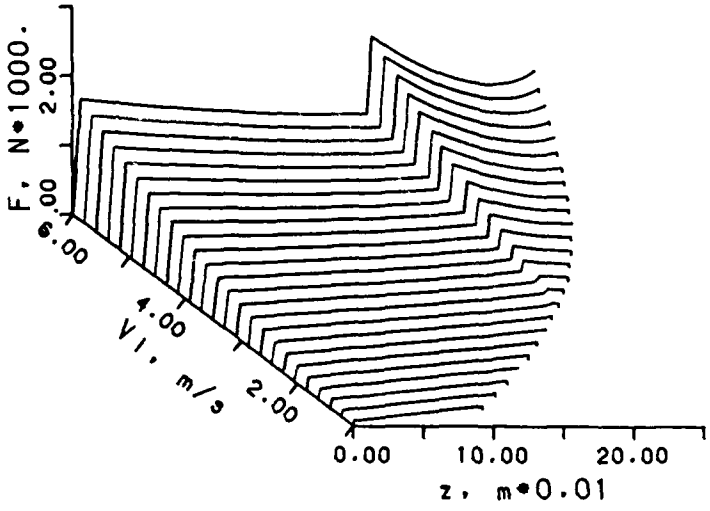

Figure 9: Family of Velocity Step Response Curves

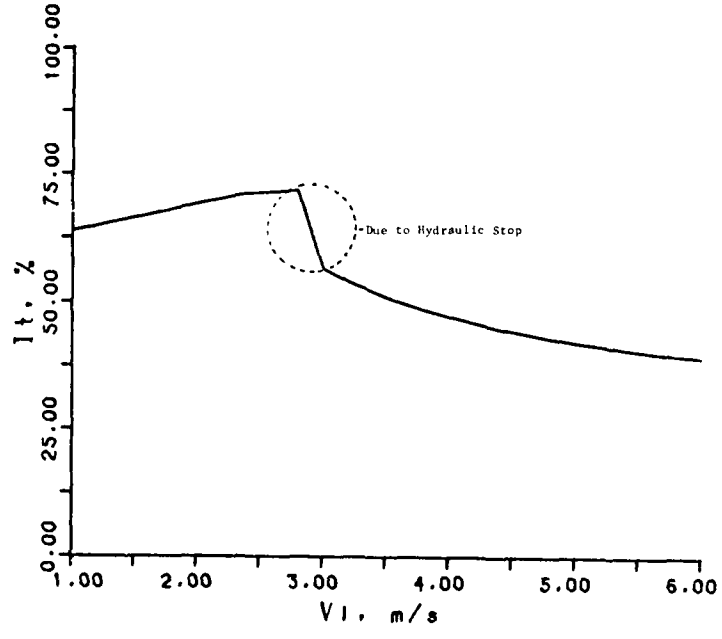

Figure 10: Performance Characteristics

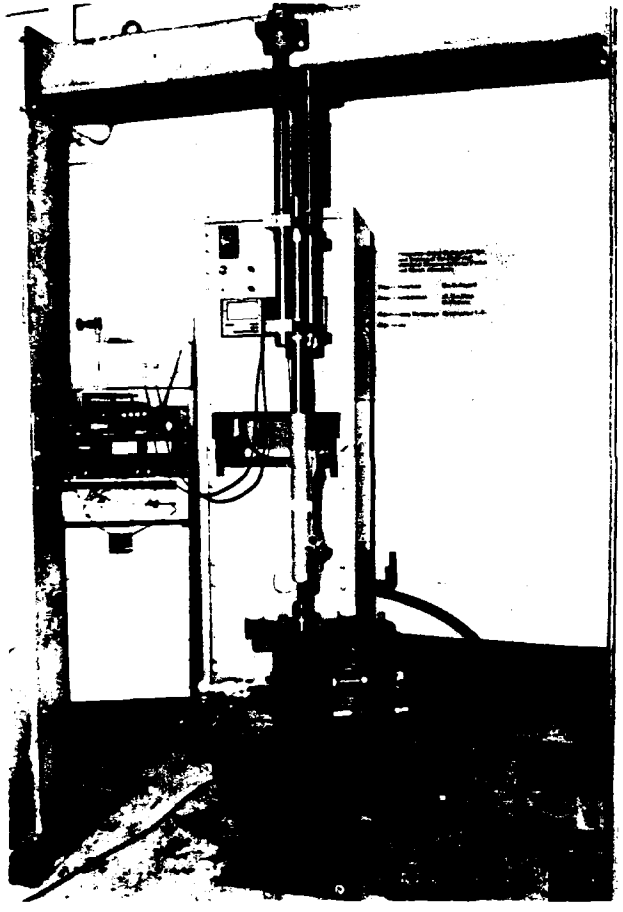

Figure 11: Pictorial View of Experimental Set-Up

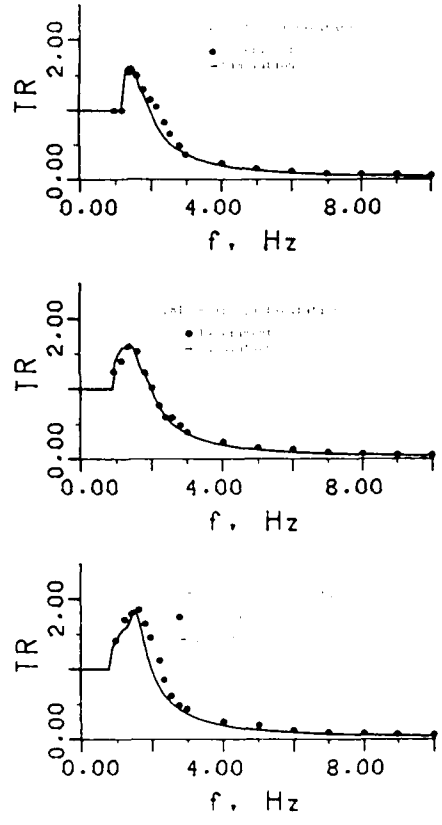

Figure 12: Frequency Domain Result

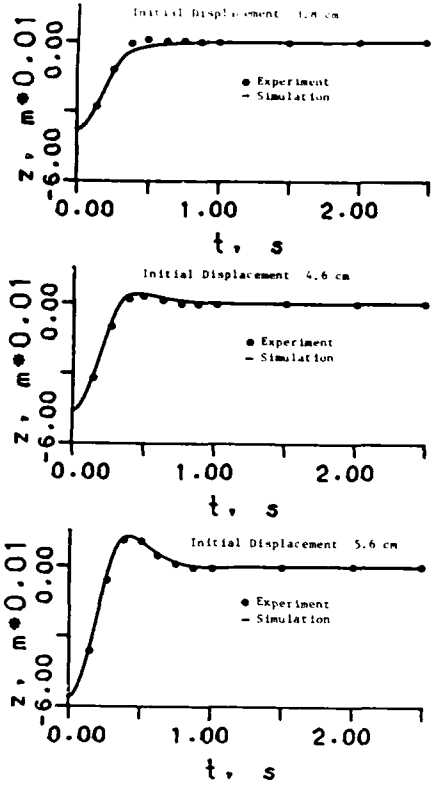

Figure 13: Time Domain Results

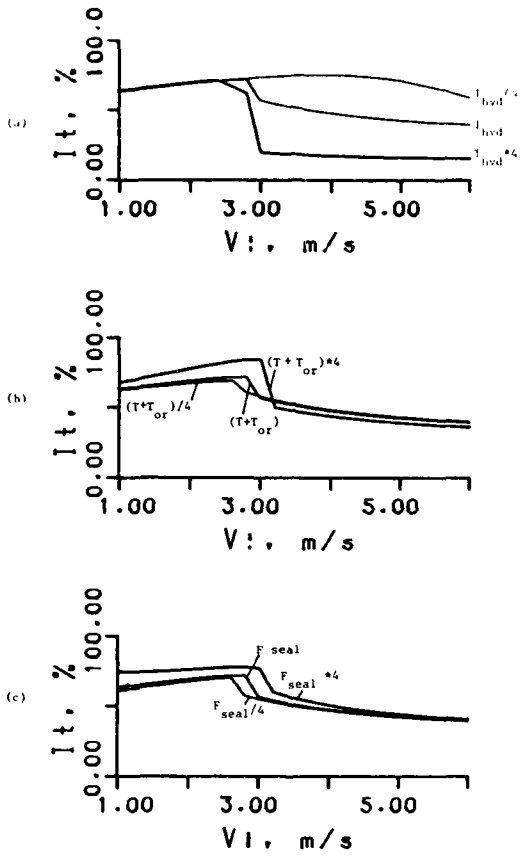

Figure 14: Parameter Variation,

(a) Hydraulic Stop Flow Coefficient
(b) Other Flow Coefficients
(c) Seal Stiction

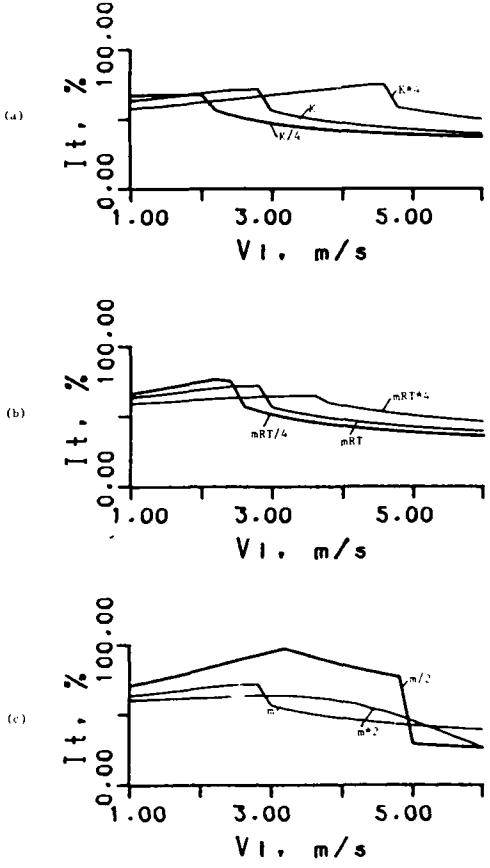

Figure 15: Parameter Variation,

(a) Spring Stiffness
(b) Air Column Stffness
(c) Mass

DISCUSSION

Mr. Lee (U.S. Army Tank Automotive Command): Did you correlate your performance index with actual subjective response at any time? In other words, do people agree with your performance index?

Mr. van Vliet: Yes. We have had a number of discussions with the people that produce this motorcycle; when we pointed out the effect of the hydraulic stop to them, we saw a spike and the performance decreased quite rapidly. They knew that both the hydraulic stop and the compression damping were bad. We mentioned that the compression damping was actually quite high, and we can get better performance by decreasing it. They said, "Yes, in our more advanced prototypes that is what we are doing." So, I think we get a very good correlation. between industry and our suggested performance index. We don't have a table, but various points have correlated well.

BRAKING-TURNING-MANEUVERING STABILITY

OF

HEAVY TRANSPORTERS

Phineas Woods
Martin Marietta Corporation
Denver, Colorado

Stable equilibrium is examined for heavy transporters executing manuevers prescribed by several steering modes. Hydraulic suspension is modeled independently from the structural elements as a finite element fluid model. The fluid system is coupled to the structural system by Rayleigh-Ritz assumed modes which satisfy boundary conditions. Modes of the combined system are determined relative to fixed tire contact points and coupled to rigid body equations of the vehicle in a moving axis system. Equilibrium of forces and moments is defined for several maneuvers. Using equilibrium as a necessary condition for dynamic stability, the variational problem of small increments in velocities and accelerations is cast in the form of an eigenvalue problem to determine stable or unstable equilibrium. Application is made to two simplified models. A limited amount of full scale test data is compared with results.

NOTATION (SI UNITS)

C_f = Fluid compliance matrix, m/N

D = 6 x 6 matrix of coefficients of reference axis velocities

E = 6 x 1 column matrix of applied brake force coefficients

F = 6 x 6 matrix of coefficients of reference axis accelerations

g = Gravitational constant, m/sec^2

G = 6 x 6 matrix of coefficients of variational velocities of ref. axes

I = Unity matrix

$\tilde{I}$ = Relative coordinate transformation matrix

I_f = Fluid inertance matrix, sec^2/N

k = Structural stiffness matrix, N/m

m = Structural mass matrix, $N\text{-}sec^2/m$

$\overline{M}$ = Coupled structural/fluid mass matrix

$\overline{K}$ = Coupled structural/fluid stiffness matrix

$\overline{p}$ = Static pressure head on fluid system, m

also: $\overline{p}$ = Angular rotational roll rate of ref. axis system, rad./sec.

$\overline{q}$ = Angular rotational pitch rate of ref. axis system, rad./sec.

$\overline{r}$ = Angular rotational yaw rate of ref. axis system, rad./sec.

R = Radius of turn in Normal turn or Transverse turn, m

T_F = Transformation matrix from flow units, N, to Discrete coordinates, X in m units

$\overline{u}$ = Component of ref. axis velocity in X-direction, m/sec.

$\overline{v}$ = Component of ref. axis velocity in Y-direction, m/sec.

$\overline{w}$ = Component of ref. axis velocity in Z-direction, m/sec.

$\{\overline{v}\} = \begin{Bmatrix} \overline{u} \\ \overline{v} \\ \overline{w} \end{Bmatrix}$, vector translational velocity, m/sec

$\{\overline{\omega}\} = \begin{Bmatrix} \overline{p} \\ \overline{q} \\ \overline{r} \end{Bmatrix}$, vector rotational velocity, Rad./sec.

$[\omega] = \begin{bmatrix} o & r & -q \\ -r & o & p \\ q & -p & o \end{bmatrix}$ = Components of rotational velocity vector of a node which yield cross product multiplication

$\left[\left[\omega\right]\right]$ = Matrix of all the components of rotational velocity of each d.o.f. arranged in a diagonal

$[\Omega^2]$ = Eigenvalues, (frequencies), of grounded system, (rad./sec.)^2

$\bar{W}$ = Absolute flow of fluid system, N

$\tilde{W}$ = Flow of fluid system relative to structure, N

$\{X\}$ = Structural degrees of freedom

$\{X_G\}$ = Translational displacements of tire contact points

$\{X_O\}$ = "Other" degrees of freedom, meaning, other than X_G

$\{F_I\}$ = Forces at tire contact points

$[MCT]$ = Modal coupling transformation. As used here it invariably means the static reduction of all coordinates to ground

$[RBT]$ = Rigid body transformation. As used here it invariably means the rigid body transformation of grounded coordinates to origin of the moving reference axis system

tp = Force applied tangentially to tire, and in the ground plane, during braking

$\begin{Bmatrix} tx \\ ty \\ tz \end{Bmatrix}$ = Components of tire force projected on body axis coordinates

α = Steering angle; i.e. the angle formed by the plane of the tire with respect to x-axis

$\begin{Bmatrix} tp \\ tm \\ tz \end{Bmatrix}$ = Components of tire force tangent to tire and in ground plane, normal to plane of tire in ground plane and normal to ground plane, respectively

$[A]$ = Coefficients of eigenvalue matrix with motion constrained by ground plane

INTRODUCTION

Heavy transporters are designed to move and to distribute uniformly the weight of massive payloads to an irregular road surface through hydraulic suspension. Originally designed to operate at very low speeds of a few miles per hour, the heavy transporter has evolved towards higher speeds on smoother road surfaces such as an Interstate Highway. Vehicles have been built in the form of a tractor/semitrailer or a self-propelled unit. Both configurations contain a number of interconnected hydraulic suspension units (bogies) for distributing the load. The bogies are steerable and enable the vehicle to make tight turns which would be geometrically impossible to execute with a conventional non-steerable semitrailer of the same length. Additionally, the self-propelled configuration has the capability for moving laterally in crab-like translation, for moving in a transverse arc or for turning in a circular arc within its own length. Such steering characteristics, together with relatively higher speeds and high gravity centers of the payload, introduce a need for understanding the practical limits of braking, turning and maneuvering. This paper addresses these limits.

METHOD OF APPROACH

For either configuration, tricycle stability is assumed in forward motion. Hydraulic suspension is formed for each group of interconnected bogies and combined with a three dimensional model of the vehicle structure. At zero forward speed, the dynamical system behaves as any grounded linear structural system. Tire contact points are then related to a moving axis system. By restricting elastic accelerations and velocities of each element to zero, the quasi-steady elastic displacements of the system are expressed in terms of accelerations and velocities of the moving axis system. Equations expressing equilibrium of forces and moments about the moving axis system are formed for several steering maneuvers and brake force levels. Brake forces are expressed as decelerations of the moving reference axis. Stable equilibrium is then examined on the basis of a variation in the accelerations and velocities of the reference axis caused by some arbitrary disturbance. Stability boundaries are calculated relating speed, radius of turn and vehicle braking. A limited amount of data from a tractor/semitrailer test on a serpentine course are compared with the analytical results.

ANALYSIS

A tractor/semitrailer configuration is shown in Fig. 1; self-propelled configuration in Fig. 2. In Fig. 3 and Fig. 4, tricycle stability is depicted for the two configurations. Thus, in the self-propelled vehicle, the resultant reactions of the three interconnected hydraulic systems forms a vertical force system equivalent

to that of a tricycle. Similarly, the semi-trailer has tricycle stability formed by the king-pin reaction and the resultant forces from the interconnected bogies on each side of the semitrailer.

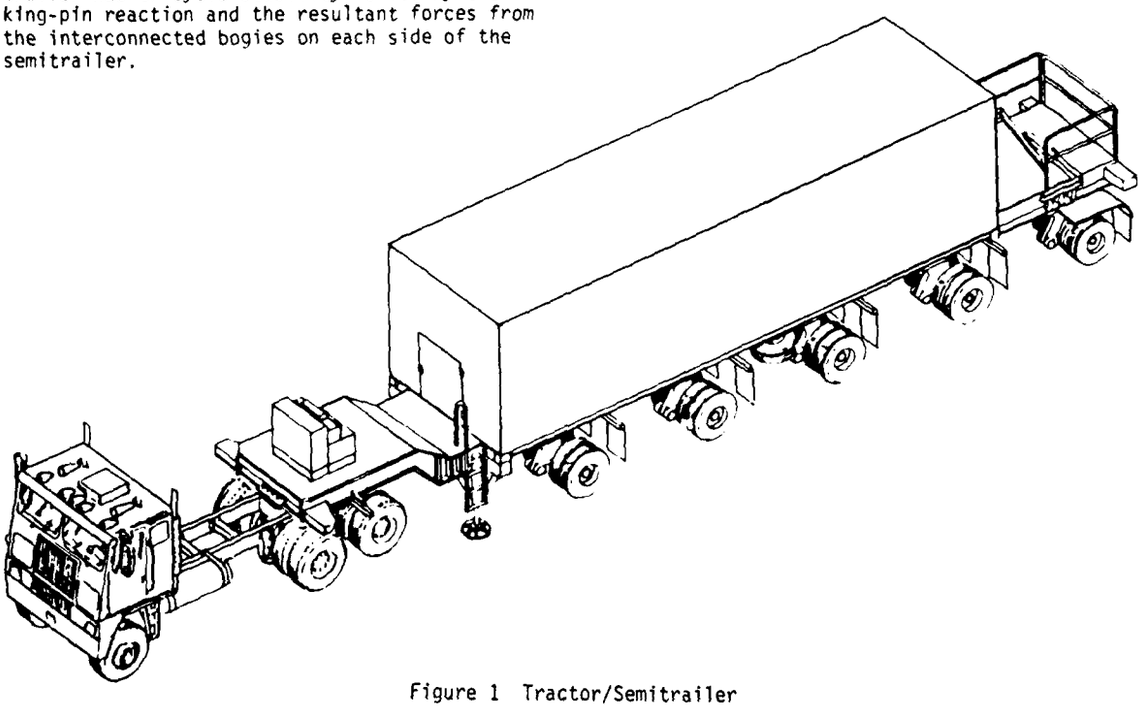

Figure 1 Tractor/Semitrailer

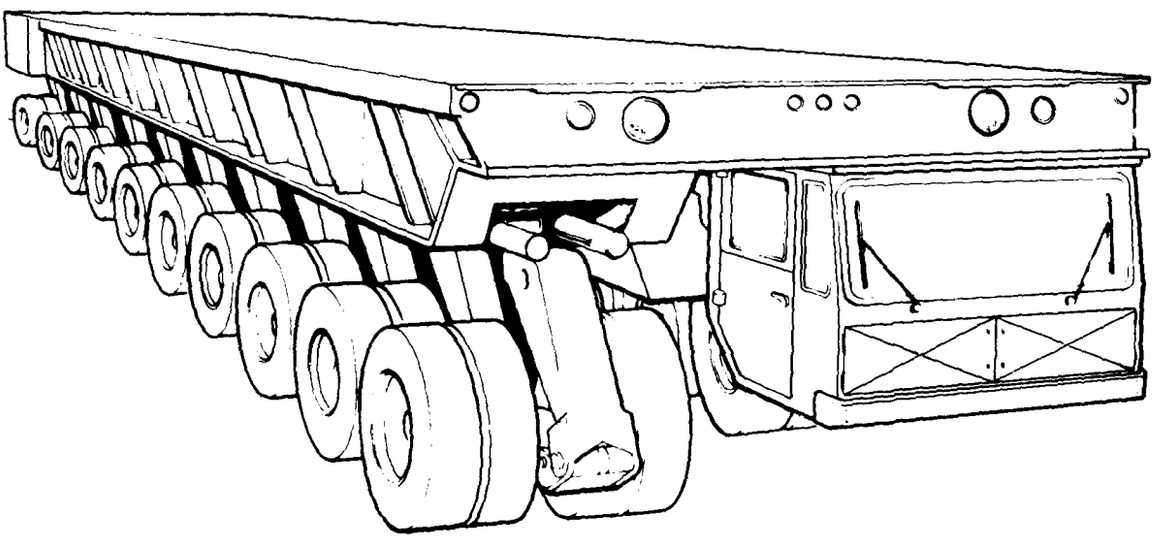

Figure 2 Self-Propelled Transporter

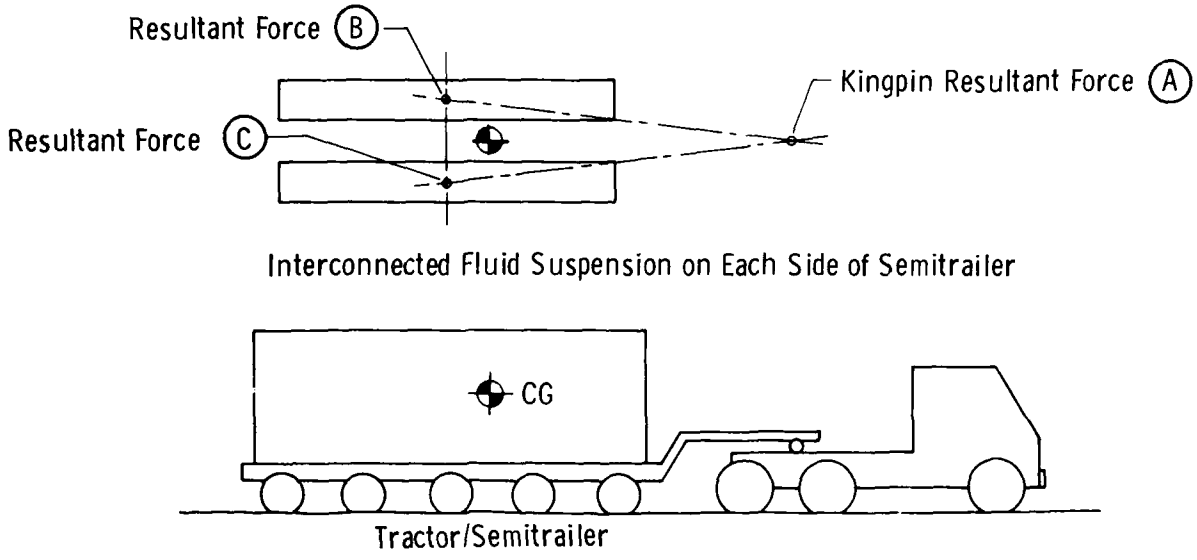

Figure 3 Resultant Forces Forming Tricycle Stability

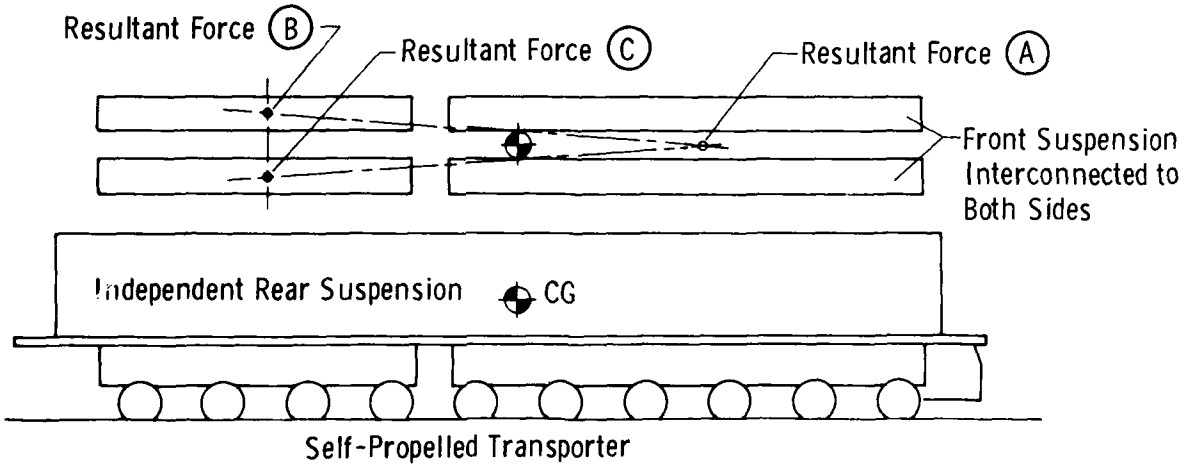

Figure 4 Resultant Forces Forming Tricycle Stability

The first objective in analyzing the vehicles is to construct a linear dynamical system combining the structure and its hydraulic suspension resulting in mass and stiffness matrices of the form.

$$[m]\{\ddot{X}\} + [k]\{X\} = \{-mg\} \qquad (1)$$

Similarly, a finite element model of the fluid elements is constructed in isolation from the structure resulting in inertance and compliance matrices of the form.

$$[I_f]\{\ddot{\bar{W}}\} + [C_f]\{\bar{W}\} = \{\bar{p}\} \qquad (2)$$

Eq. (2) may be constructed using the finite element methods described in References (1) and (2). Using the Rayleigh-Ritz transformation, described in Reference (2); also, shown in Fig. 5.

$$\begin{Bmatrix} X \\ \bar{W} \end{Bmatrix} = \left[\begin{array}{c|c} I & 0 \\ \hline T_F & I \end{array}\right] \begin{Bmatrix} X \\ \tilde{W} \end{Bmatrix} \qquad (3)$$

The two systems in isolation are combined to form

$$[\bar{M}]\begin{Bmatrix} \ddot{X} \\ \ddot{\tilde{W}} \end{Bmatrix} + [\bar{K}]\begin{Bmatrix} X \\ \tilde{W} \end{Bmatrix} = \begin{Bmatrix} -mg + T_F{}^T p \\ \tilde{I}p \end{Bmatrix} = \{0\} \qquad (4)$$

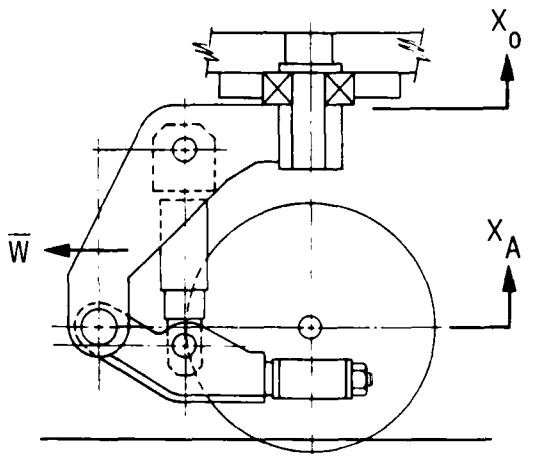

Flow Due to Structural Motion

$$\begin{Bmatrix} \bar{W} \\ \text{Absolute Flow} \end{Bmatrix} = T_f \begin{Bmatrix} X \\ \text{Structure} \end{Bmatrix} + \begin{Bmatrix} \tilde{W} \\ \text{Flow Relative to Structure} \end{Bmatrix}$$

$$\begin{Bmatrix} X \\ \bar{W} \end{Bmatrix} = \left[\begin{array}{c|c} I & 0 \\ \hline T_f & \tilde{I} \end{array}\right] \begin{Bmatrix} X \\ \tilde{W} \end{Bmatrix}$$

Figure 5 Fluid/Structure Coupling

where:

$$[\bar{M}] = \left[\begin{array}{c|c} m + T_F{}^T I_f T_F & T_F I_f I \\ \hline I^T I_f T_F & I^T I_f I \end{array}\right] \tag{5}$$

$$[\bar{K}] = \left[\begin{array}{c|c} k + T_F{}^T C_f T_F & 0 \\ \hline 0 & I^T C_f I \end{array}\right] \tag{6}$$

In Reference (1) it is shown that static coupling between structural displacement, X, and fluid displacement, $\tilde{W}$, cannot exist. This accounts for the zeroes in Eq (6).

It is convenient at this point to distinguish between tire contact coordinates and all other coordinates including fluid coordinates, $\tilde{W}$.

Let: X_G = tire contact coordinates in three dimensions

X_o = all other coordinates

So that Eq (4) may be written

$$[\bar{M}] \begin{Bmatrix} \ddot{X}_G \\ \ddot{X}_0 \end{Bmatrix} + [\bar{K}] \begin{Bmatrix} X_G \\ X_0 \end{Bmatrix} = \begin{Bmatrix} F_I \\ 0 \end{Bmatrix} \tag{7}$$

$$\text{or} \left[\begin{array}{c|c} M_{11} & M_{12} \\ \hline M_{21} & M_{22} \end{array}\right] \begin{Bmatrix} \ddot{X}_G \\ \ddot{X}_0 \end{Bmatrix} + \left[\begin{array}{c|c} K_{11} & K_{12} \\ \hline K_{21} & K_{22} \end{array}\right] \begin{Bmatrix} X_G \\ X_0 \end{Bmatrix} = \begin{Bmatrix} F_I \\ 0 \end{Bmatrix}$$

where: F_I = forces exerted at tire contact points

With tire contact points grounded, the modes of the system in a nonmoving axis system are:

$$\{X_0\} = [\Phi] \{\lambda\} \tag{8}$$

The total displacement is:

$$\begin{Bmatrix} X_G \\ X_0 \end{Bmatrix} = \left[\begin{array}{c|c} [MCT] & 0 \\ \hline [\Phi] & \end{array}\right] \begin{Bmatrix} X_G \\ \lambda \end{Bmatrix} \tag{9}$$

where: MCT = modal coupling transformation; i.e., static reduction of all degrees of freedom, X_G, and X_o, to ground, X_G.

Also, let: $\{X_G\} = [RBT] \begin{Bmatrix} x \\ y \\ z \\ \theta_x \\ \theta_y \\ \theta_z \end{Bmatrix}$ coordinates of origin of reference axis (10)

where: RBT = rigid body transformation of grounded coordinates to origin of reference axis. The X_G coordinates do not contain rotation; only translation.

Returning to Eq (7)

$$\left[\begin{array}{c|c} M_{11} & M_{12} \\ \hline M_{21} & M_{22} \end{array}\right] \begin{Bmatrix} \ddot{X}_G \\ \ddot{X}_0 \end{Bmatrix} + \left[\begin{array}{c|c} K_{11} & K_{12} \\ \hline K_{21} & K_{22} \end{array}\right] \begin{Bmatrix} X_G \\ X_0 \end{Bmatrix} = \begin{Bmatrix} F_I \\ 0 \end{Bmatrix} \quad (7)$$

Substituting Eq (9)

$$\left[\begin{array}{c|c} M_{11} & M_{12} \\ \hline M_{21} & M_{22} \end{array}\right] \left[\begin{array}{c|c} [MCT] & \begin{matrix} 0 \\ [\Phi] \end{matrix} \end{array}\right] \begin{Bmatrix} \ddot{X}_G \\ \ddot{\lambda} \end{Bmatrix} +$$

$$\left[\begin{array}{c|c} K_{11} & K_{12} \\ \hline K_{21} & K_{22} \end{array}\right] \left[\begin{array}{c|c} [MCT] & \begin{matrix} 0 \\ [\Phi] \end{matrix} \end{array}\right] \begin{Bmatrix} X_G \\ \lambda \end{Bmatrix} = \begin{Bmatrix} F_I \\ 0 \end{Bmatrix} \quad (11)$$

Introducing the vector notation for the reference axes

$$\begin{Bmatrix} \dot{\bar{v}} \\ \dot{\bar{\omega}} \end{Bmatrix} = \begin{Bmatrix} \ddot{x} \\ \ddot{y} \\ \ddot{z} \\ \ddot{\theta}_x \\ \ddot{\theta}_y \\ \ddot{\theta}_z \end{Bmatrix} = \begin{Bmatrix} \dot{\bar{u}} \\ \dot{\bar{v}} \\ \dot{\bar{w}} \\ \dot{\bar{p}} \\ \dot{\bar{q}} \\ \dot{\bar{r}} \end{Bmatrix} \quad \& \quad \begin{Bmatrix} \dot{\bar{v}} \\ \dot{\bar{\omega}} \end{Bmatrix} = \begin{Bmatrix} \bar{u} \\ \bar{v} \\ \bar{w} \\ \bar{p} \\ \bar{q} \\ \bar{r} \end{Bmatrix} \quad (12)$$

If now the reference axes shown in Fig. 6 move with acceleration, $\begin{Bmatrix} \dot{\bar{v}} \\ \dot{\bar{\omega}} \end{Bmatrix}$, and velocity, $\begin{Bmatrix} \bar{v} \\ \bar{\omega} \end{Bmatrix}$, we must add $\bar{\omega} \times$ momentum terms. In addition, for a quasi-steady solution, $\ddot{\lambda} = \dot{\lambda} = 0$. Imposing virtual work from the transformation

$$\begin{Bmatrix} X_G \\ X_0 \end{Bmatrix} = \left[\begin{array}{c|c} [MCT] & [RBT] \end{array}\right] \left[\begin{array}{c|c} & 0 \\ \hline & [\Phi] \end{array}\right] \begin{Bmatrix} X \\ \theta \\ \lambda \end{Bmatrix} \quad (13)$$

leads to a general expression for equilibrium

$$\left[\begin{array}{c|c} [RBT]^T & [MCT]^T \\ \hline 0 & \Phi^T \end{array}\right] \left[\left[\begin{array}{c|c} M_{11} & M_{12} \\ \hline M_{21} & M_{22} \end{array}\right] [MCT] \quad [RBT] \quad \begin{Bmatrix} \dot{\bar{v}} \\ \dot{\bar{\omega}} \end{Bmatrix}\right.$$

$$- \left[[\omega] \left[\begin{array}{c|c} M_{11} & M_{12} \\ \hline M_{21} & M_{22} \end{array}\right] [MCT] \quad [RBT] \quad \begin{Bmatrix} \bar{v} \\ \bar{\omega} \end{Bmatrix} \right.$$

$$\left. + \left[\begin{array}{c} K_{12} \\ \hline K_{22} \end{array}\right] [\Phi] \{\lambda\} \right] = \left[\begin{array}{c|c} [RBT]^T & [MCT]^T \\ \hline 0 & \Phi^T \end{array}\right] \begin{Bmatrix} F_I \\ 0 \end{Bmatrix} \quad (14)$$

The generalized elastic coordinate, λ, can be expressed in terms of reference axis accelerations and velocities. From the bottom set of equations in (14)

$$\{\lambda\} = -\left[\Phi^T K_{22} Q\right]^{-1} \left[[\Phi]^T \left[\begin{array}{c|c} M_{21} & M_{22} \end{array}\right] [MCT] \quad [RBT] \begin{Bmatrix} \dot{\bar{v}} \\ \dot{\bar{\omega}} \end{Bmatrix} \right.$$

$$\left. - [\Phi]^T \left[0 \left| \begin{array}{c} [\omega_{22}] \end{array}\right. \right] [\bar{M}] \quad [MCT] \quad [RBT] \begin{Bmatrix} \bar{v} \\ \bar{\omega} \end{Bmatrix} \right] \quad (15)$$

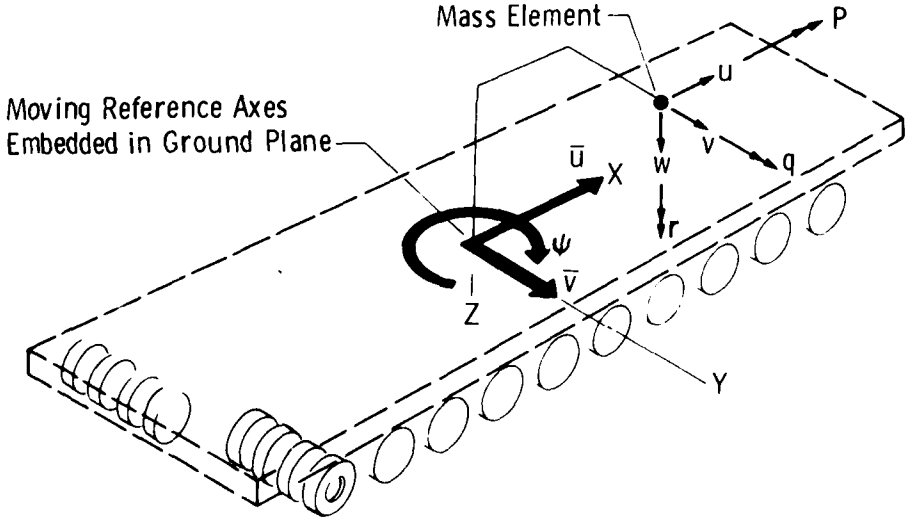

Figure 6 Stability Model

Where the quantity

$$\left[\Phi^T K_{22} \Phi\right] = \left[\Omega^2\right]$$

These are the frequencies of the grounded system corresponding to the modes of Eq (8).

Substituting Eq (15) in the top set in Eq (14) yields the desired expression for equilibrium of forces and moments about the moving reference system in the form

$$[F]\begin{Bmatrix}\dot{\bar{v}}\\ \dot{\bar{\omega}}\end{Bmatrix} - \left[\begin{bmatrix}\bar{\omega}\end{bmatrix}\right][F]\begin{Bmatrix}\bar{v}\\ \bar{\omega}\end{Bmatrix} = \begin{Bmatrix}\Sigma \text{ Forces}\\ \Sigma \text{ Moments}\end{Bmatrix} \quad (16)$$

For reference axes constrained to move in the ground plane

$$[F]\begin{Bmatrix}\dot{\bar{u}}\\ \dot{\bar{v}}\\ \dot{\bar{w}}\\ \dot{\bar{p}}\\ \dot{\bar{q}}\\ \dot{\bar{r}}\end{Bmatrix}\begin{matrix}0\\0\\0\end{matrix} - [D]\begin{Bmatrix}\bar{u}\\ \bar{v}\\ \bar{w}\\ \bar{p}\\ \bar{q}\\ \bar{r}\end{Bmatrix}\begin{matrix}0\\0\\0\end{matrix} \cdot \bar{r} = \begin{Bmatrix}\Sigma Fx\\ \Sigma Fy\\ \Sigma Fz\\ \Sigma Mx\\ \Sigma My\\ \Sigma Mz\end{Bmatrix} \quad (16)$$

That is, the original six degrees of freedom for a moving reference axis system are reduced to three by constraining $\bar{w}$, $\bar{p}$, $\bar{q}$ velocities and their derivatives to zero.

[F] & [D] are calculated as 6 x 6 matrices of constant coefficients defined by

$$[F] = [RBT]^T [MCT]^T \left[[\bar{M}] - \begin{bmatrix}K_{12}\\ K_{22}\end{bmatrix}[\Phi]\left[\Omega^2\right]^{-1}[Q]^T \left[\begin{array}{c|c} M_{21} & M_{22}\end{array}\right][MCT][RBT]\right] \quad (16a)$$

$$[D] = [RBT]^T [MCT]^T \left[\left[\begin{array}{c|c} \omega_{11} & 0\\ \hline 0 & \omega_{22}\end{array}\right][\bar{M}] - \begin{bmatrix}K_{12}\\ K_{22}\end{bmatrix}[\Phi]\left[\Omega^2\right]^{-1}[\Phi]^T \left[\begin{array}{c|c} \omega_{22} & \end{array}\right]\left[\begin{array}{c|c} M_{21} & M_{22}\end{array}\right][MCT][RBT]\right] \quad (16b)$$

where: $\left[\begin{array}{c|c} \omega_{11} & 0\\ \hline 0 & \omega_{22}\end{array}\right] = \left[\begin{array}{ccc|c} \begin{bmatrix}0&1&0\\-1&0&0\\0&0&0\end{bmatrix} & & & 0\\ & \begin{bmatrix}0&1&0\\-1&0&0\\0&0&0\end{bmatrix} & & \\ & & & \\ \hline 0 & & & \end{array}\right]$

The [F] & [D] coefficients become 6 x 3 matrices when the motion of the reference axes are constrained to move in the ground plane. Thus, Eq (16) takes the form

$$\begin{bmatrix}F_1\\ F_2\end{bmatrix}\begin{pmatrix}u\\ v\\ r\end{pmatrix} - \begin{bmatrix}D_1\\ D_2\end{bmatrix}\begin{pmatrix}u\\ v\\ r\end{pmatrix} \dot{r} = \frac{\{E_1\}}{\{E_2\}}\, tp \quad (17)$$

The right hand side of Eq (17) represents the applied forces and moments produced by braking force, tp.

APPLIED BRAKING FORCES

It is assumed that the tires do not slide. Braking torques are applied uniformly at each braked axle and in the plane of the undistorted tire. The braking torques are balanced by tangential forces, tp, at the tire contact point. Thus, the tangential braking forces, tp, are treated as the only externally applied forces. Lateral forces normal to the tire plane and vertical forces normal to the ground plane are not included as applied forces since they are reactions only to the accelerations of the dynamical model as in any grounded spring-mass system. Resolving the applied brake forces into body-axis components, the forces and moments of Eq (17) can be written as

$$\begin{pmatrix}\{E_1\}\\ \{E_2\}\end{pmatrix} tp = \begin{Bmatrix}\Sigma Fx\\ \Sigma Fy\\ \Sigma Fz\\ \Sigma Mx\\ \Sigma My\\ \Sigma Mz\end{Bmatrix} = [RBT]^T [MCT]^T \left\{\begin{Bmatrix}tx\\ ty\\ tz\end{Bmatrix}\text{(A)}, \begin{Bmatrix}tx\\ ty\\ tz\end{Bmatrix}\text{(B)}, \begin{Bmatrix}tx\\ ty\\ tz\end{Bmatrix}\text{(C)}, \{0\}\right\} \quad (18)$$

where:

$$\begin{Bmatrix}tx\\ ty\\ tz\end{Bmatrix} = \begin{bmatrix}c\alpha & s\alpha & 0\\ -s\alpha & c\alpha & 0\\ 0 & 0 & 1\end{bmatrix}\begin{matrix}\text{Applied Brake Force}\\ \begin{Bmatrix}tp\\ tm\\ tz\end{Bmatrix}\begin{matrix}\leftarrow \text{Reaction}\\ \leftarrow \text{Reaction}\end{matrix}\end{matrix}$$

The steering angle, α, has a different value for each bogie, depending on the steering mode. Four steering modes are shown in Fig. (7). Eqs (17) and (18) represent six quasi-steady equations of equilibrium of forces and moments. A seventh equation is provided by the steering mode. Thus, all accelerations, velocities and brake forces can be related. Marginal equilibrium occurs when vertical axle displacement becomes negative; i.e., the tires become unloaded for one interconnected set of bogies. Referring to the tire footprints in Figs. (3) and (4), this condition implies ineffective braking forces on, for example, set © for a right hand turn. Thus,

$$\begin{Bmatrix}tx\\ ty\\ tz\end{Bmatrix}_{\text{©}} = \begin{Bmatrix}0\\ 0\\ 0\end{Bmatrix} \text{ in Eq (18)}$$

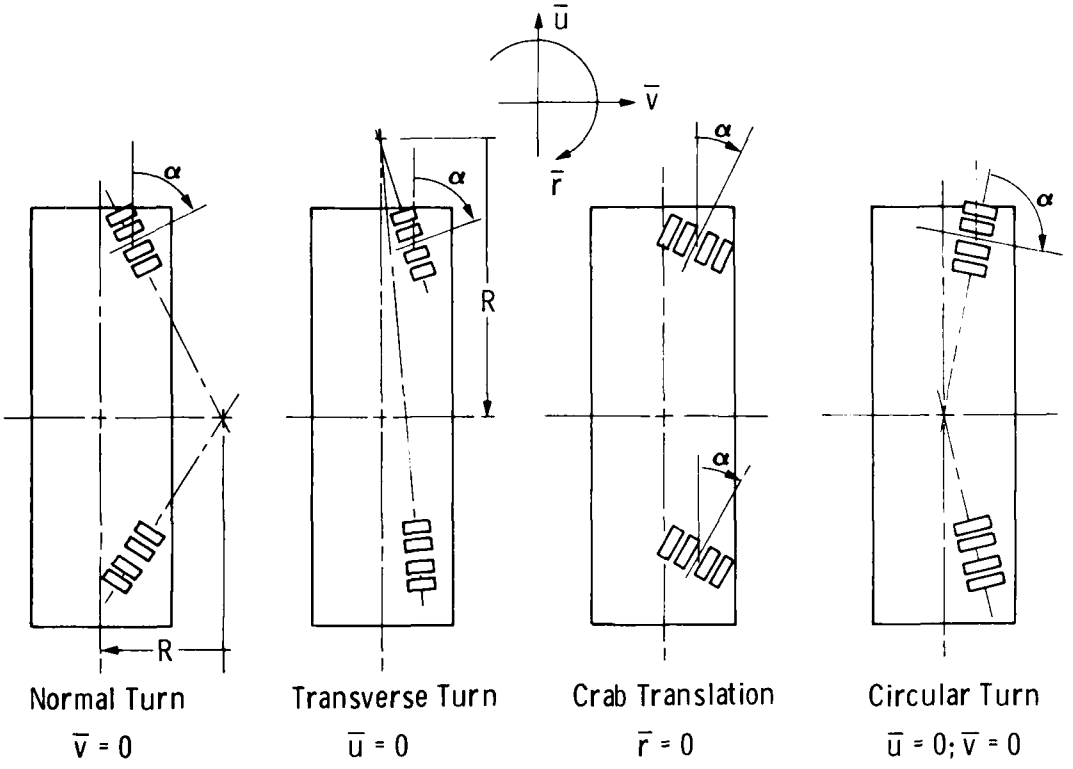

Figure 7 Four Steering Modes of Self-Propelled Transporter

because the tires cannot sustain tension in the vertical direction. In practical applications, the transfer of vertical load from set ⓒ to set ⓑ would be restricted to allowable tire overloads.

STABLE EQUILIBRIUM

Although Eqs (17) and (18) provide the necessary conditions for equilibrium, they are not sufficient to ensure stable equilibrium. If, for example an arbitrary disturbance should cause small increments in velocity and acceleration, it must be shown that such incremental changes will not increase with time.

The conditions for stable equilibrium can be established by variational methods described in Ref (3) and (4). For example, let each acceleration and each velocity in Eq (17) take on an incremental value δu, δv, δw, etc. It is assumed that the applied brake forces are fixed. Expanding the indicated multiplication, neglecting second order products and subtracting the original equations from the result yields the eigenvalue equations

$$[F] \begin{Bmatrix} \delta\dot{\bar{u}} \\ \delta\dot{\bar{v}} \\ \delta\dot{\bar{w}} \\ \delta\dot{\bar{p}} \\ \delta\dot{\bar{q}} \\ \delta\dot{\bar{r}} \end{Bmatrix} = [G] \begin{Bmatrix} \delta\bar{u} \\ \delta\bar{v} \\ \delta\bar{w} \\ \delta\bar{p} \\ \delta\bar{q} \\ \delta\bar{r} \end{Bmatrix} \tag{19}$$

the full 6 x 6 matrices F and D are retained as calculated in Eq (16a) and (16b). After forming the matrix product

$$[F]^{-1} [G] = [A]$$

we may constrain the moving reference axis system to move in the ground plane with the result

$$\begin{Bmatrix} \delta\dot{\bar{u}} \\ \delta\dot{\bar{v}} \\ \delta\dot{\bar{r}} \end{Bmatrix} = [A] \begin{Bmatrix} \delta\bar{u} \\ \delta\bar{v} \\ \delta\bar{r} \end{Bmatrix} \tag{20}$$

where: [A] = is reduced to a 3 x 3 by eliminating the appropriate rows and columns corresponding to $\delta\bar{w}$, $\delta\bar{p}$, $\delta\bar{q}$, and their derivatives = 0.

The characteristic equation of (20) is given by expanding the determinant

$$\begin{vmatrix} (A_{11} - \lambda), A_{12}, A_{13} \\ A21, (A_{22} - \lambda), A_{23} \\ A_{31}, A_{32}, (A_{33} - \lambda) \end{vmatrix} \qquad (21)$$

The coefficients, A_{ij}, are determined by the steering mode. For stable equilibrium, the real part of the roots of the characteristic equation must be negative.

APPLICATIONS TO TWO TRANSPORTERS

The stability of two types of transporters recently delivered to the Air Force has been examined using the method described. Simplified models are shown in Figs. (8) and (9). The hydraulic suspension was modelled in full detail with all lines, line junctions and accumulators. Structural detail was omitted by replacing the entire vehicle bed and payload with a single mass point having six degrees of freedom and equivalent mass and inertia properties. Tires were modelled as three dimensional linear springs.

The first model shown is the tractor/semitrailer type. The tractor suspension was modelled with springs, i.e., leaf springs on front axle, airride on rear axles. Accumulator precharge was assumed at 300 psi with a three liter volume; one accumulator per bogie. Decelerations up to $\dot{\bar{u}} = 0.5g$ were carried out to show the stabilizing effects of braking. For a fully loaded vehicle it would not be possible to develop brake forces which produce this level of deceleration. It is estimated that actual brake forces can produce no more than 0.1g deceleration.

Results are summarized in Fig. (10) where speed versus turning radius are plotted from a marginal equilibrium condition corresponding to Eqs (17) and (18). The steering mode is a normal turn. Stable equilibrium for this vehicle requires the radius of turn to exceed about six feet. The minimum turn capability is 14 ft radius. Consequently, the vehicle has quasi-steady stability at all limit speeds within its turning capability. Two data points are shown taken from actual tests of the vehicle moving along a sine-wave course.

NORMAL AND TRANSVERSE TURNS OF SELF-PROPELLED VEHICLE

Marginal equilibrium is shown in Fig. (11) for normal and transverse turns. Stable equilibrium is determined by the coefficients of the cubic in Eq (21) which yield a minimum turning radius for a transverse turn. For the simplified model shown in Fig. (9) the values are:

$R \geq 1.5$ ft for normal turn

$R \leq 1579$ ft for transverse turn

A similar procedure may be followed to determine the limits of crab and circular steering maneuvers.

SUMMARY AND CONCLUSIONS

The method outlined here produces quasi-steady solutions to braking-turning maneuvers in heavy transporters. By restricting elastic accelerations and elastic velocities to zero, the results become mathematically analogous to structural wing divergence in aircraft. The procedure is reasonably verified by a limited amount of test data.

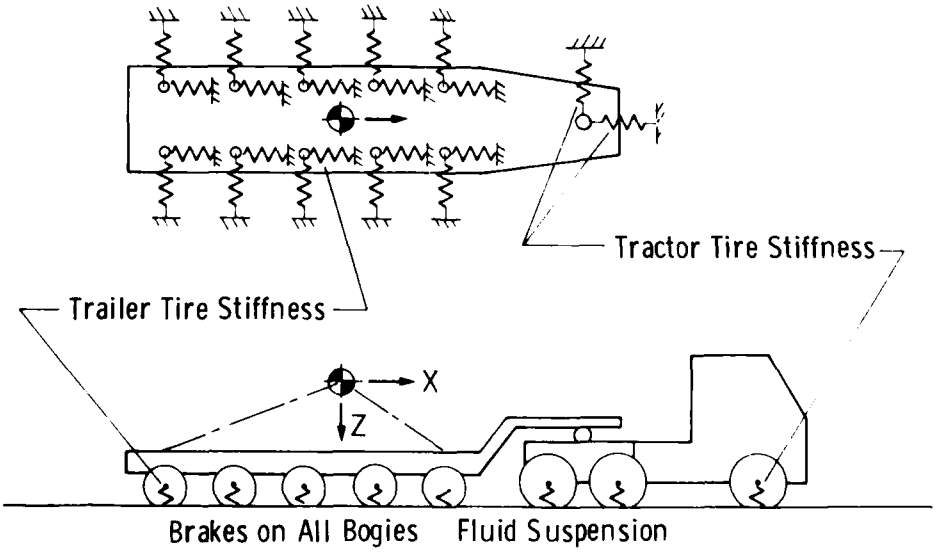

Figure 8 Simplified Model of Tractor/Semitrailer

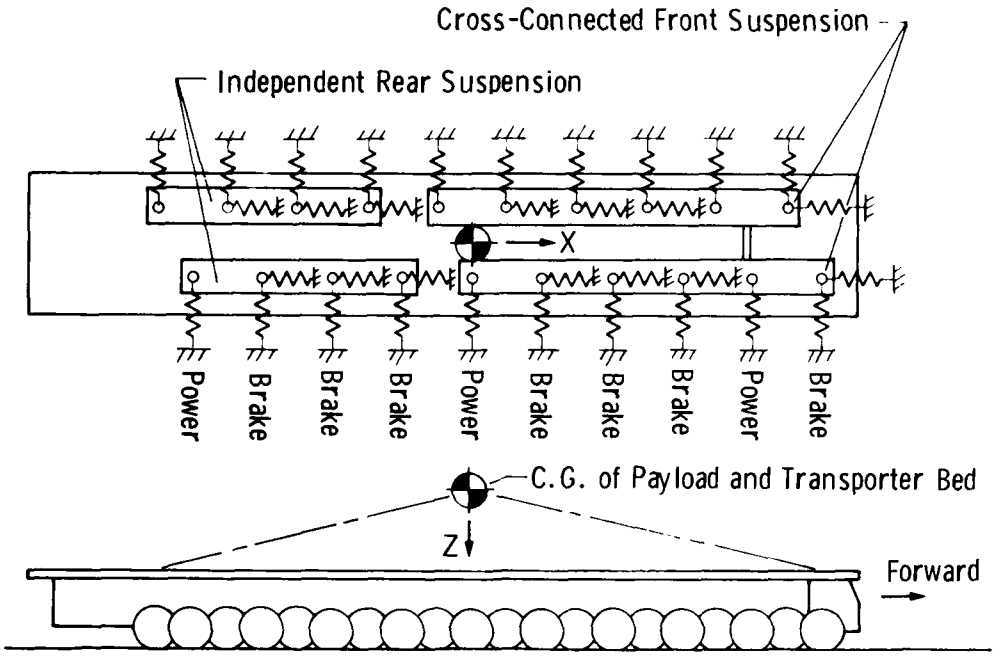

Figure 9 Simplified Model of Self-Propelled Transporter

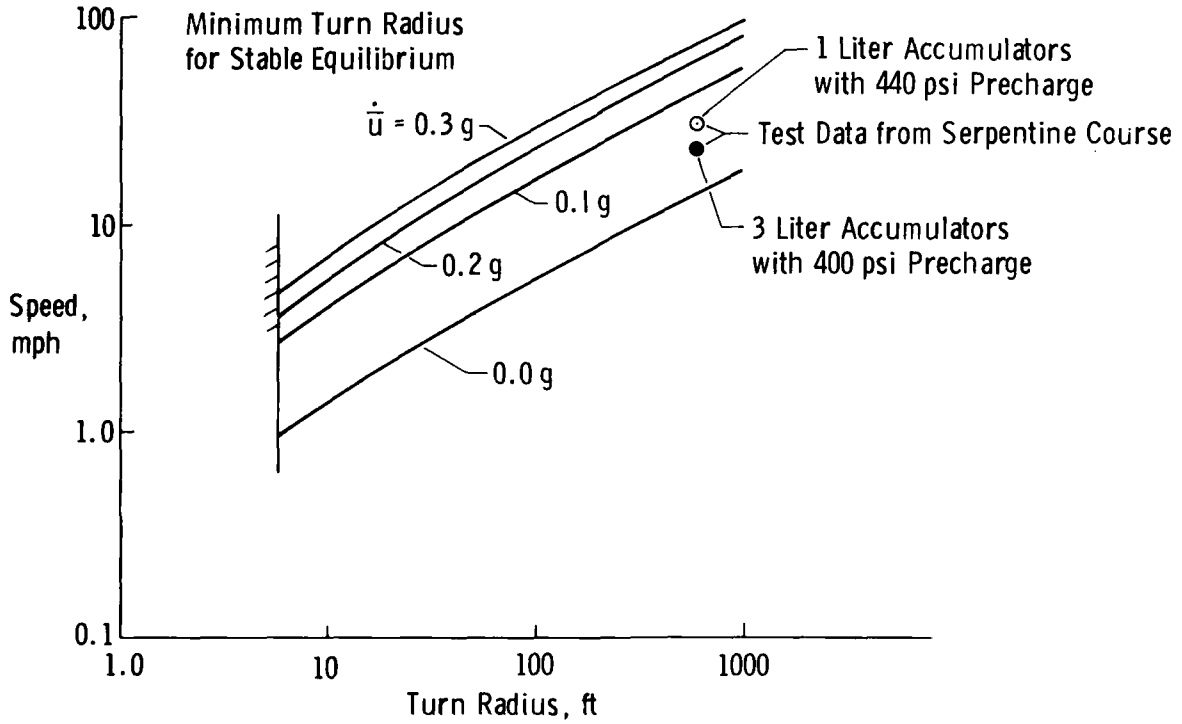

Figure 10 Speed Limit for Stable Equilibrium of Tractor/Semitrailer in Normal Turn

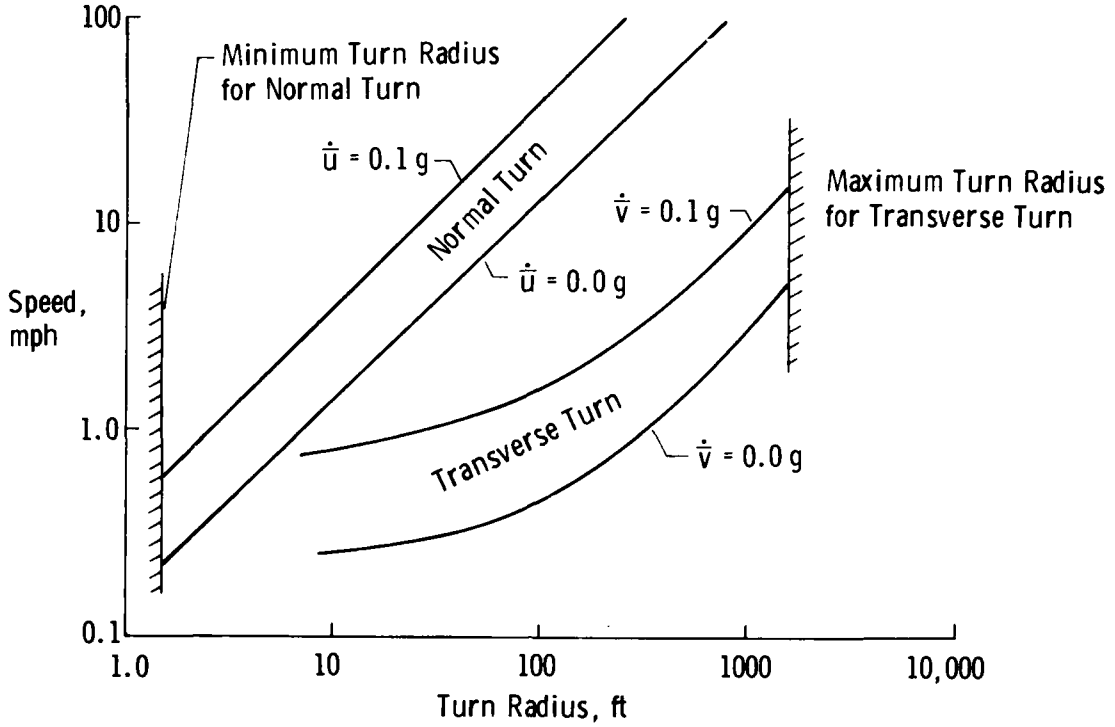

Figure 11
Speed Limit for Stable Equilibrium of Self-Propelled Transporter in Normal Turn and Transverse Turn

REFERENCES

(1) White, C. W. and Berry, R. L., "The Dynamic Interaction of Combined Fluid/Structural Systems" Report No. R-75-48628-002, Task No. D-28-R, Denver Division of Martin Marietta Aerospace, October 1975.

(2) Woods, Phineas, "Performance Analysis of High-Speed Hydraulic Suspension Systems in Multiple Wheeled Land Transporters" Shock and Vibration Bulletin No. 52, Part 4, May 1982.

(3) Thomson, W., "Theory of Vibrations with Applications", pp. 372-374, Prentice-Hall, 2nd Ed., 1981.

(4) Lancos, C., "The Variational Principles of Mechanics", Mathematical Expositions No. 4, Univ. of Toronto Press.

DISCUSSION

Mr. Lee (U.S. Army Tank Automotive Command): Is any attempt made to hold the load level with stabilizer bars because you have a vehicle that can turn very sharply?

Mr. Woods: Yes. On the self-propelled McDonnell Douglas transporter they have a device for doing that. I don't think it has been used very much, and I don't think we know too much about that yet because it is a separate control system.

ACOUSTIC ENVIRONMENTS FOR JPL SHUTTLE PAYLOADS BASED ON EARLY FLIGHT DATA

Michael R. O'Connell and Dennis L. Kern
Jet Propulsion Laboratory
California Institute of Technology
Pasadena, California

Shuttle payload acoustic environmental predictions for the Jet Propulsion Laboratory's Galileo and Wide Field/Planetary Camera projects have been developed from STS-2 and STS-3 flight data. This evaluation of actual STS flight data resulted in reduced predicted environments for the JPL shuttle payloads. Shuttle payload mean acoustic levels were enveloped. Uncertainity factors were added to the mean envelope to provide confidence in the predicted environment.

Introduction

A substantial amount of payload bay acoustic data has been obtained from the second and third shuttle flights. Data was acquired as a part of the shuttle flight test program and the NASA DATE (Dynamic, Acoustic and Thermal Environments) activity. Raw flight data is disseminated to the user community by Goddard Space Flight Center (GSFC) in post flight reports.

Acoustic predictions for the Jet Propulsion Laboratory (JPL) Galileo and Wide Field Planetary Camera payloads were developed in three steps. First, small payload mean levels were determined from STS 2 and 3 flight acoustic data. Then values of uncertainties in the acoustic environment were determined. Finally, payload peculiar effects in the environment were derived. These environment uncertainties and payload effects were added to the small payload mean levels to arrive at maximum expected acoustic levels for these two payloads.

Acoustic Instrumentation

Shuttle payload bay dynamic instrumentation consists of the Development Flight Instrumentation (DFI) system and the Dynamic, Acoustic and Thermal Environments (DATE) system. DFI instrumentation was installed on flights 1 through 5 by Johnson Space Center (JSC). DATE instrumentation, the responsibility of GSFC, was installed on STS-2 through STS-4. DFI microphones were of the vibration compensated type. DATE microphones were isolation mounted. All microphones had omnidirectional sensing.

The four DFI payload bay microphones were mounted to the forward bulkhead, aft bulkhead, the cargo bay sidewall and the DFI pallet for flights 2 and 3. DATE microphones were attached to the pallets and their experiments. For flight 2 eight DATE microphones were installed on the DFI pallet and five were on the OSTA-1 pallet. The OSS-1 experiment was instrumented with five DATE microphones on flight 3. The DFI pallet had two DATE microphones for flight 3. A picture of a typical DATE microphone installation is shown on the OSTA-1 pallet (figure 1). A listing of the microphone locations may be found in references 2 and 3.

All DATE channels were recorded on the Orbiter Experiment (OEX) wide band FM recorder. DFI acoustic channels were recorded on the Ascent Recorder and the Mission Recorder.

Figure 1. OSTA-1 Microphone Locations and Configuration

Data Reduction

Data used in this analysis were reduced and made available by GSFC through the DATE reports (references 1, 2, and 3). The DATE reports display time histories for all acoustic channels in standard 1/3 octave bands. An averaging time constant of 0.5 seconds was used for the time histories. The maximum 1/3 octave band spectrum levels were tabulated by the authors for the four most significant events of flights 2 and 3 which were "main engines at 20% rough burn", "maximum lift off reflection", "transonic" and "supersonic". The spatial mean and standard deviation were calculated for payloads by 1/3 octave bands. Spectral and payload bay acoustic contour plots were made for analysis.

Data Evaluation

Flight to Flight Variation

Shuttle payload bay acoustic data from microphones common to STS 1, 2, and 3 indicates a flight to flight variation of ±1.5 dB for the most significant flight events. Four microphones were common to flights 1, 2, and 3 while six microphones were duplicated on flights 2 and 3. Figure 2 shows variations in the levels at microphone 9219. The small variations on figure 2 are typical for the other microphones that were present for all three flights. Also, the mean level of all payload microphones for STS 2 were within ±1.5 dB of the STS-3 mean level in each 1/3 octave band. One third octave band standard deviations were generally 2dB or less for flights 2 and 3 combined. The flight ensemble standard deviation (flight to flight variation) was not calculated because there have only been three flights. Flight to flight variations in payload bay acoustic level may occur on future shuttle flights due to variables that are discussed later.

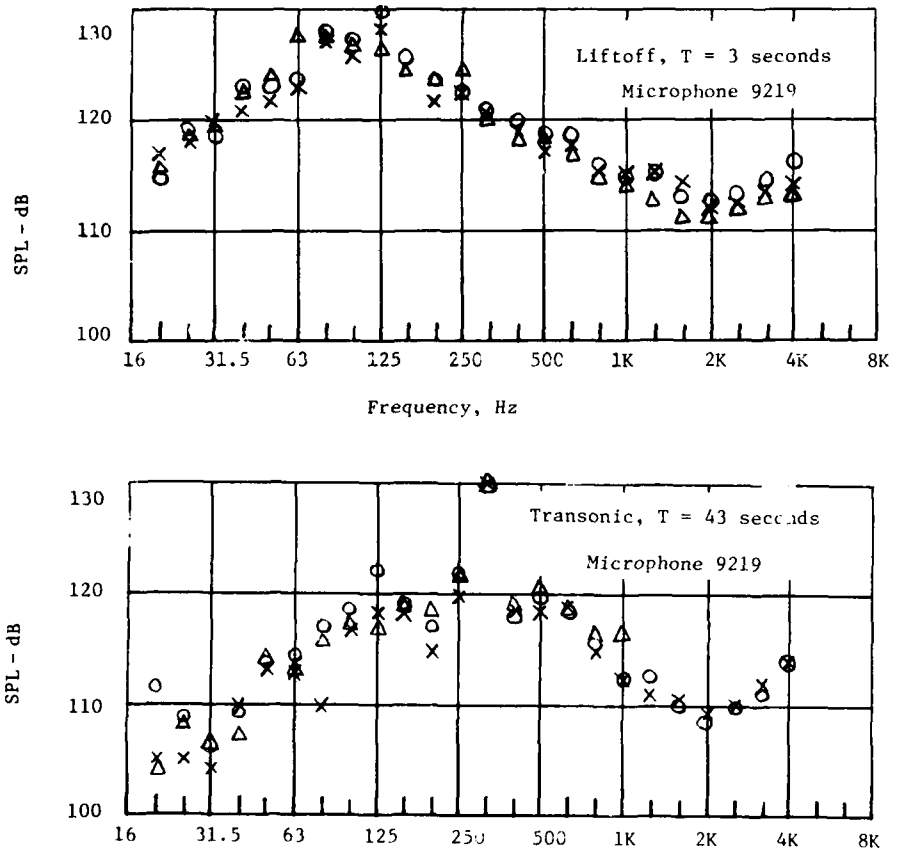

Figure 2. Acoustic Levels, STS 1, 2 and 3 for Microhpone 9219

Payload Bay Acoustic Zones

Shuttle flight data shows that noise levels at payloads did not vary much with microphone location. Figure 3 shows two cross section views of the payload bay with typical acoustic contour plots. Contours from the 250 Hz and 500 Hz bands are shown. Microphone 9230 of STS-3 was omitted from the contours because it was inside an experiment. Contour plots revealed a uniformity of payload acoustic levels extending near to the allowable payload envelope for all flight conditions (see contour for 500 Hz). There were only two exceptions to this uniformity. Levels were 3-5 dB higher than the payload mean near the payload bay doors from 50 Hz to 400 Hz during liftoff (see contour for 250 Hz). Also, discrete tones appeared in the 315 Hz band during transonic and supersonic flight (figure 2). These discrete tones were a localized effect and appear strongest near the pressure equalization vents. The mean level of the discrete is 12 dB lower at the payload than for the sidewall microphone (figure 2), which is near a vent. No local payload effects were noticed in any of the data.

Levels at the sidewall and bulkheads were consistently higher than those measured at payloads. The scatter in the perimeter data was also much greater. Thus, the acoustic environment of the bay perimeter seemed to be characteristically different from that of the payloads. This effect is evident for all flight events, but is most pronounced at liftoff. Liftoff pallet acoustic levels were 5-6 dB below sidewall/bulkhead levels below 80 Hz. During transonic and supersonic flight sidewall/bulkhead acoustic levels were 3-5 dB higher than pallet levels between 80 Hz and 315 Hz. The perimeter zone is defined on figure 3.

For subsequent analysis the bay was zoned into a small payload region and a perimeter region. The small payload and perimeter regions are shown by the contours of figure 3. Small payload mean levels were calculated from 20 payload microphone channels for the four most significant flight conditions. These flight conditions were "main shuttle engines at 20% rough burn", "liftoff maximum reflection", "transonic" and "supersonic".

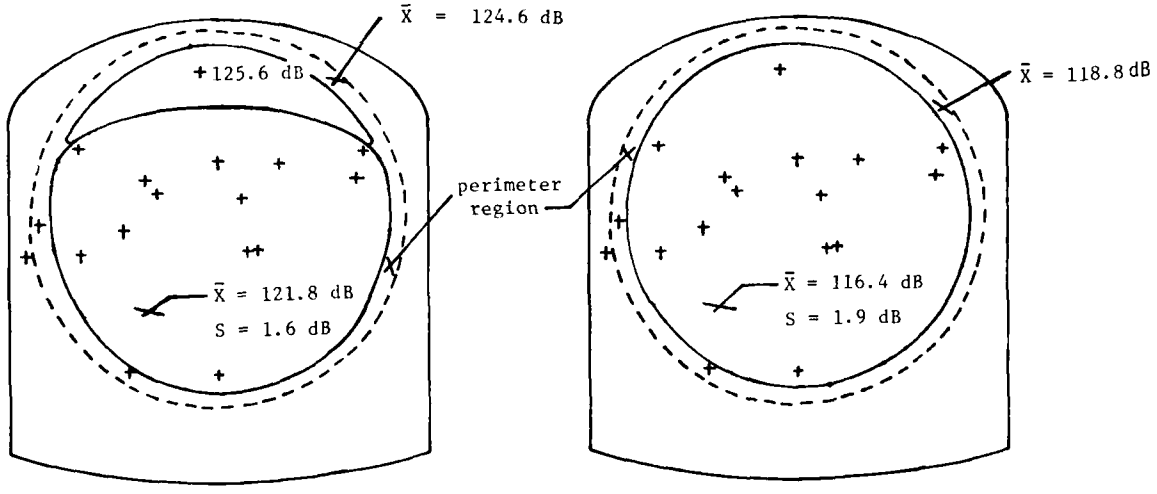

Contour at 250 Hz

Liftoff

Contour shape typical for liftoff from 50 Hz to 400 Hz

Contour at 500 Hz, Liftoff

Contour shape typical for all flight conditions except liftoff from 50 Hz to 400 Hz

Figure 3. Shuttle Payload Bay Acoustic Contours

The acoustically significant shuttle events are shown in a time history plot of the data from microphone 9219, figure 4. Shuttle main engine rough burn is shown as event A. This event occurs during thrust build up when the main engines are momentarily held at 20% thrust. Event B, solid rocket booster (SRB) ignition, levels were diminished 10 dB for flights 2 and 3 by post flight 1 pad modifications. Liftoff maximum reflection is shown as event C. Maximum acoustic reflection from the launch pad occurs about three seconds after liftoff (SRB ignition) when the shuttle is about 40 feet above the pad. Transonic flight is event D and supersonic flight is shown as event E. These events generate acoustic levels in the payload bay from aerodynamic noise on the shuttle exterior.

Spectra for the four most significant events are summarized on figure 5. Liftoff had the most severe mean payload levels at 132.1 dB overall while main engines at rough burn levels reached 125.5 dB. Transonic and supersonic flight levels were lower but of substantially longer durations. Transonic mean levels were 124.6 dB while mean supersonic payload bay noise was 123.3 dB. The mean levels for the four most significant events were enveloped by choosing the mean value giving the largest mean plus two sigma value in each 1/3 octave band. This mean envelope, P_m, is listed in table 1. Environmental uncertainties and payload effects were added to P_m, the mean envelope, to derive maximum predicted payload environments. This process is described in the "Environmental Uncertainties" section.

Four microphones (9231, 9253, 9276, 9278) exhibited a rise in level beginning at 800 Hz. These represent only 4 time histories of the 27 available. The microphones in question were not closest to the payload bay perimeter or the pressure equalization vents. These four microphones were mounted in the same manner as surrounding microphones. Therefore, no physical cause for this sudden rise in noise level at 800 Hz could be ascertained. There were anomolies in the data at 800 Hz for microphone 9231. These four microphones also had low signal to noise ratios above 1000 Hz. For these reasons, data above 800 Hz was discarded for these four microphones.

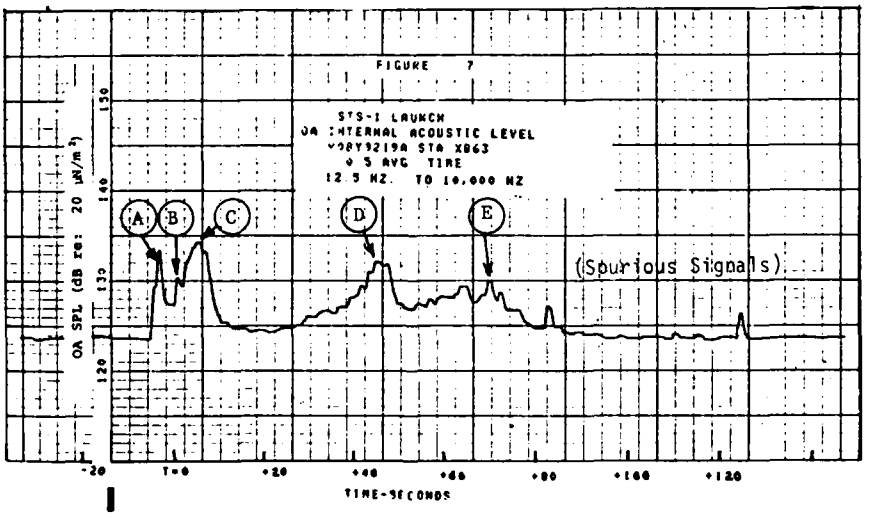

A shuttle main engine start (20% thrust rough burn)

B SRB ignition

C max liftoff reflection

D transonic

E supersonic, Max Q

Reference 1, DATE Report 002

Figure 4. Typical Time History, Microhpone 9219, overall flight STS-1

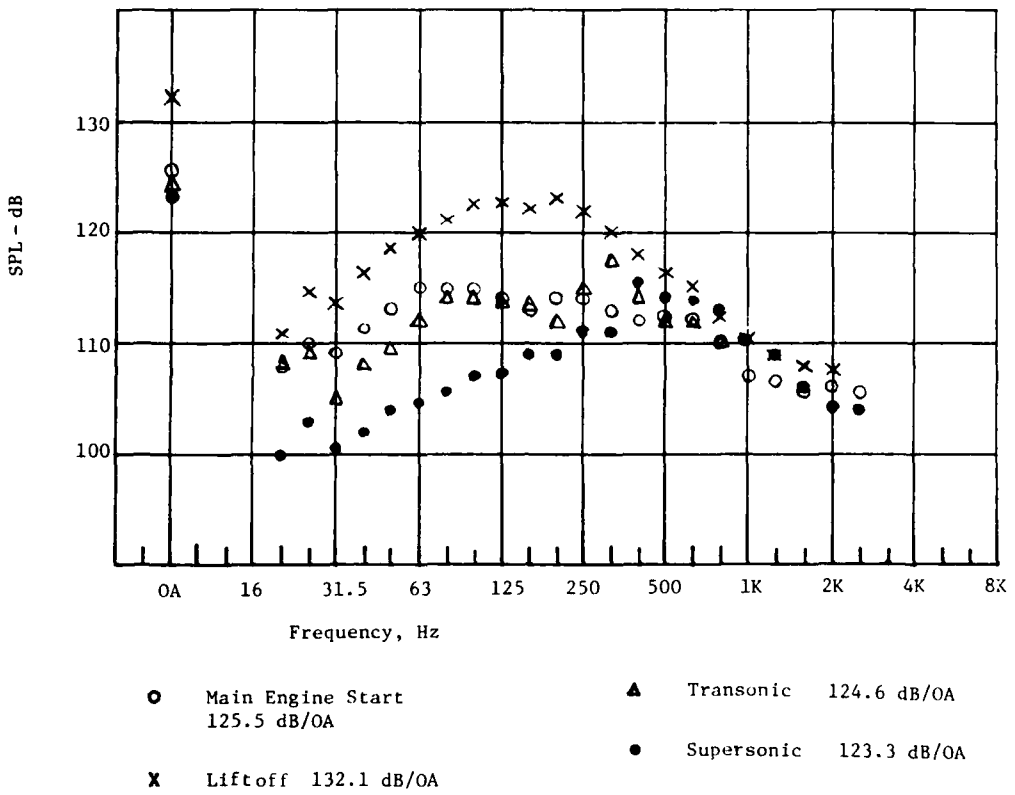

Figure 5. Summary of Payload Mean Levels for Significant Flight Conditions

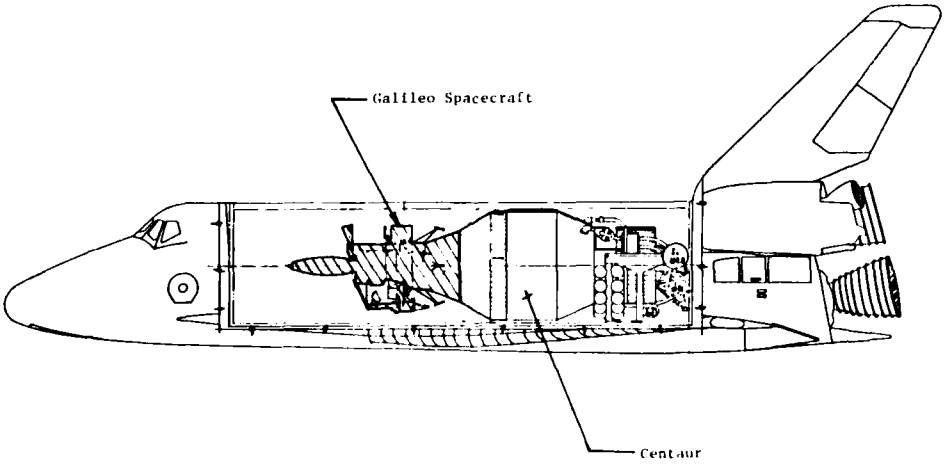

Figure 6. Galileo and Wide Body Centaur in Space Shuttle

Environmental Uncertainties

Several uncertainties were taken into account in developing environmental predictions. These uncertainties fall into two categories. Bias errors in the environment, due to data reduction and payload effects, is the first category. These values are added directly to the mean envelope. The second category is statistically independent random variables. Spatial variations and flight to flight variations are statistically independent random variables. The root sum of the squares of these variations is added to the mean envelope. The following formula is used to arrive at the maximum acoustic environment for a payload by accounting for these uncertainties.

$$P_{max} = P_m + P_e + P_b + P_p + [P_s^2 + P_f^2]^{1/2}$$

where

P_{max} = Maximum expected acoustic environment.

P_m = Mean envelope acoustic environment for small payloads from STS 2 and 3 flight data.

P_e = Data reduction bias errors; 0 dB.

P_b = Spatial bias errors arising from non-representative postioning or small number of microhpones on STS-2; 0dB.

P_p = Payload diameter effect; PACES plus perimeter data.

P_s = Spatial variation uncertainty with-in the payload bay; 2 sigma of 20 payload microphones.

P_f = Flight to flight uncertainty; 3 dB.

P_m is the mean envelope of the payload acoustic environment that was discussed in the "Data Evaluation" section.

Data reduction bias errors, P_e, are believed to be small. Test times will be longer than the actual acoustic environment. P_e is neglected because of this and other conservatisms in this analysis.

Spatial bias errors, P_b, arise from non-representative positioning or small numbers of microphones. Bias error predictions were made for STS-1 through STS-3 by Bolt, Beranek, and Newman (BB&N), reference 4. They conclude that STS-2 had enough microphones to give a true mean for the payload bay. They recommend small corrections to STS-3 data. In our case, P_m, has been found using both flight 2 and 3 data. Our data base is larger than is available from a single flight, and only small payload region microphones have been used. Thus, the effect of the non-diffuse perimeter region acoustic environment has been eliminated from our P_m. The small standard deviation for P_m also indicates that the data set is uniform and relatively free from localized non-representative acoustical effects. For these reasons P_b is also neglected.

Large payloads can have a significant effect, P_p, on local acoustic levels. A large payload is a high volume payload whose boundary extends into the near perimeter acoustic effects. Studies by BB&N, reference 5, show that payloads with a diameter greater than 60% of the payload envelope can be described as a large payload. The optional thermal radiator may also influence the bay acoustic environment by changing the transmission loss and absorptivity in the door region.

PACES, a program by BB&N, reference 5, was one tool used to predict the payload influence from Galileo and WF/PC. PACES is a way of accounting for the non-diffuse character of the acoustic field near the cargo bay doors and sidewalls. Acoustic levels are calculated by the program on a mode by mode basis for the spatial volumes surrounding a payload.

PACES prediction values are actually deltas from the mean small payload acoustic level. PACES sometimes predicts 1/3 octave band levels lower than the ambient sidewall or small payload value. In these cases, the ambient local level from STS data was used instead of the PACES values. For small payloads $P_p = 0$.

Spatial variation, P_s, is calculated directly from the STS 2 and 3 data set (20 payload microphone time histories). The standard deviation from the spatial mean was small for the payload region (generally only 1-2 dB). Two times the standard deviation (2 sigma) was used for P_s. For 2 sigma, 97.5% of the positions in the bay will be enveloped. The values of sigma for the STS-2 and 3 data set are found in table 1.

Flight to flight variation, P_f, is affected by launch drift and vehicle/ pad configuration changes. Drift away from the pad exhaust ports increases pad noise reflection. The shuttle has a thrust to weight ratio of approximately 1.4:1. Since the STS weighs approximately 4.5 million pounds, the inclusion of a heavy payload will not appreciably change the vehicle thrust to weight ratio or launch rise time. Drift increases due to increased launch weight/rise time will probably be negligible. Later shuttles will also have main engines uprated to 109% thrust. Current STS data shows that the solid rockets dominate the

launch acoustic environment. This occurs at about T + 3 seconds (4 SRB nozzle diameters high) when acoustic reflection from the pad is maximum for the solid rockets. At main engine ignition the shuttle main engines are already elevated 1.5 SSME nozzle diameters from the pad. They achieve 4 diameters height at about 1.5 seconds after liftoff. Yet the maximum SSME noise occurring at 20% thrust/rough burn, is 6dB lower than for liftoff at liftoff T + 3. Variations from flights 1 to 3 were within ± 2 dB for each one-third octave band. Therefore, a 3 dB value was assumed for P_f to conservatively envelope flight to flight variations for future shuttle flights.

A small payload prediction, $P_p = 0$, with all environmental uncertainties accounted for is compared to the mean envelope P_m on figure 7. A small payload is generally one which has a diameter that is less than 60% of the diameter of the payload bay.

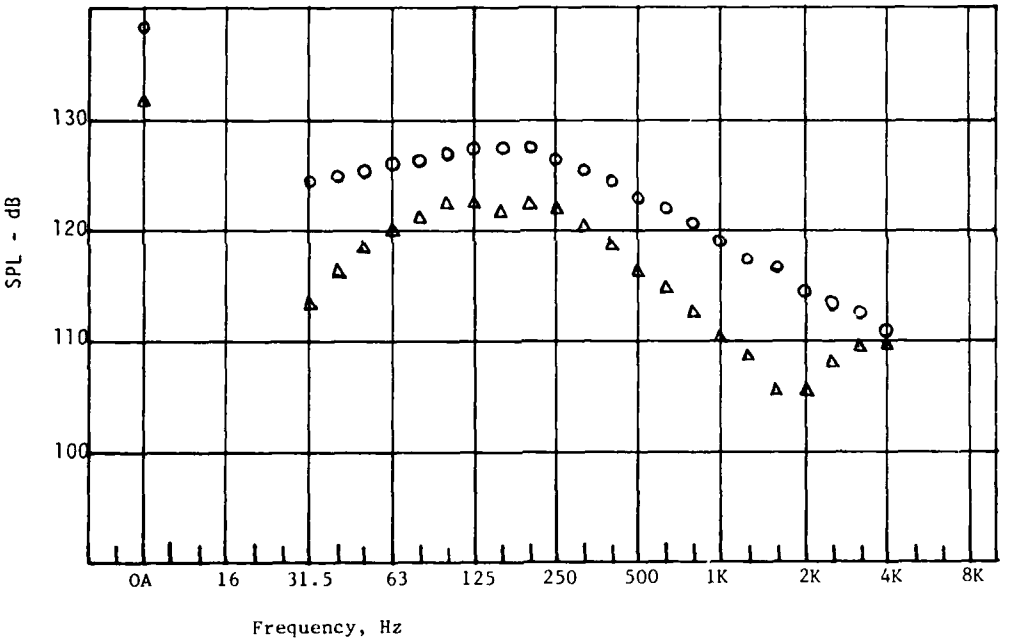

Figure 7. Predicted Small Payload Level and Mean Level Envelope, P_m

Spacecraft Predictions

For large payloads, payload effects are determined on an individual basis. Payload effects and maximum expected environments will be determined for two large payloads.

Galileo Prediction

Galileo is a free flying spacecraft which uses a Wide Body Centaur upper stage. The spacecraft consists of a Jupiter orbiter and an atmospheric probe. An illustration of Galileo in the shuttle bay is seen on figure 6. Galileo itself is less than 60% of the shuttle bay diameter and is a "small" payload. Payload effects in the Galileo acoustic environment are caused chiefly by the Wide Body Centaur. A prediction of Galileo/ Centaur payload effects was performed with the PACES program. The predicted Galileo level was lower than for the empty bay condition even with the Centaur present. This result is based on excitation of individual acoustic modes around the payload. Such reductions from the ambient acoustic energy levels were neglected about Galileo, so that $P_p = 0$ for every 1/3 octave band. Therefore, the Galileo prediction is the same as the small payload/empty bay prediction. The Galileo prediction can be seen in table 1. This prediction is compared with JSC Volume 14 requirement levels on figure 8 (reference 6). The revised Galileo prediction is 7 dB below the current Volume 14 levels. A proposed revision to Volume 14 levels, which would apply to all payloads, is also seen on figure 8. This proposed curve was developed using all the payload bay data, including the perimeter microphones. The revised Galileo level (the small payload/empty bay level) is 1 dB less than this proposed generic payload curve.

Wide Field/Planetary Camera Prediction

Wide Field/Planetary Camera (WFPC) is housed in the science instrument section of the Space Telescope (ST) and its radiator is part of the external surface of the ST. ST is a large earth orbiting telescope. At 43 feet long and 14 feet in diameter ST almost fills the entire payload bay and is in the large payload category (figure 9).

A PACES prediction of the ST influence on local WFPC radiator acoustic levels was performed. The predicted levels are for acoustic modes in the space between the ST and the payload bay perimeter. Deltas from the mean payload level for WF/PC are given by PACES in 1/3 octave bands. These deltas were added to the small payload mean level according to the maximum environment formula. PACES predicted that WFPC levels from 125 Hz to 315 Hz and 800 Hz to 1250 Hz would fall below ambient sidewall levels. In these cases, an envelope of the side wall/door environment was made (excluding the forward and aft bulkheads). Three dB was added to this envelope to account for flight to flight variation. An envelope was then made of the "small payload plus PACES level" and the "sidewall/door level envelope". The details of this operation are represented in table 2. The predicted WFPC radiator level can been seen in table 2 and on figure 10. The revised WFPC level is 2.5 dB below the current Volume 14 level.

Acknowledgements

The study program described in this paper was carried out at the Jet Propulsion Laboratory California Institute of Technology, under NASA Contract NAS 7-100. The evaluation of shuttle flight acoustic data was sponsored by the NASA Headquarters Office of the Chief Engineer. Evaluation of the shuttle payload bay flight acoustic environment would not have been possible without the efforts of the DATE Working Group participants, and in particular its chairman, Bill Bangs of GSFC, in acquiring flight data.

REFERENCES

1) DATE REPORT 002, Dynamics, Acoustic, Thermal Environments; Payload Bay Acoustic and Vibration Data from STS-1 Flight, June '81, NASA.

2) DATE REPORT 003, Dynamics, Acoustic, Thermal Environments; Payload Bay Acoustic and Vibration Data from STS-2 Flight, January '82, NASA.

3) DATE REPORT 004, Dynamics, Acoustic, Thermal Environments; Payload Bay Acoustic and Vibration Data from STS-3 Flight, June '82, NASA.

4) BIAS ERROR CORRECTIONS FOR ACOUSTIC DATA FROM SPACE SHUTTLE FRF AND STS-1 THROUGH STS-3; Piersol; Bolt, Beranek and Newman Inc., December '81.

5) SPACE SHUTTLE PAYLOAD BAY ACOUSTICS PREDICTIONS STUDY, Volumes 1 through 5; Piersol, Rentz, Wilby; Bolt, Beranek and Newman Inc.. March '80.

6) SPACE SHUTTLE PROGRAM, Level II Program Definition and Requirements, Space Shuttle System Payload Accommodations; September 26, '80, JSC07700, Volume XIV, Revision G.

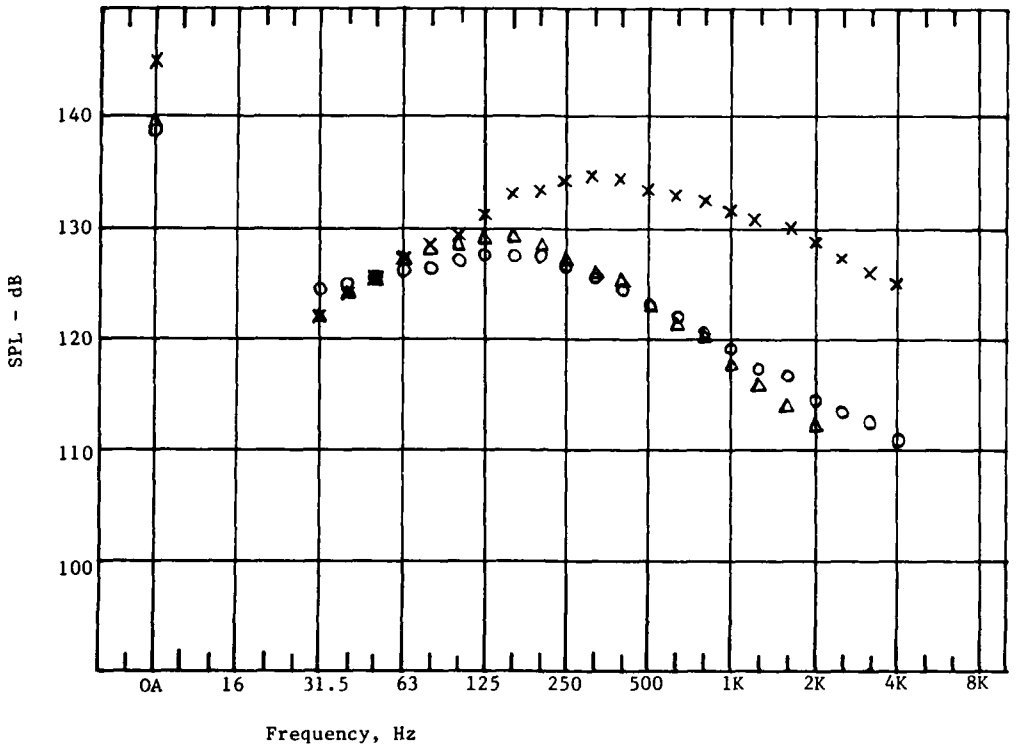

o Predicted Galileo, 138 dB

x JSC Volume 14, reference 6, 145 dB

Δ Proposed JSC Volume 14 Revision, 139 dB

Figure 8. Predicted Galileo Level vs JSC Volume 14

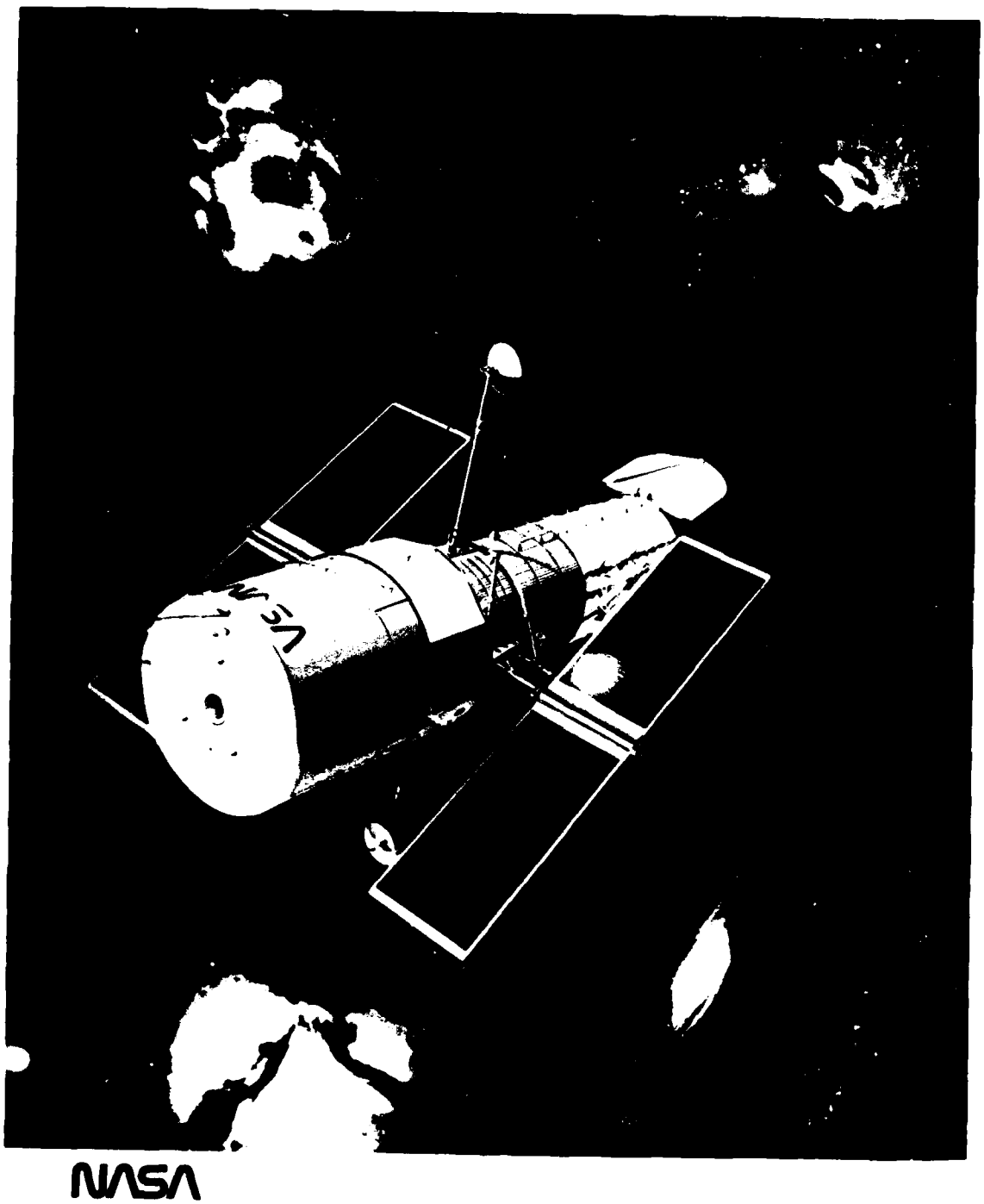

Figure 9. Space Telescope

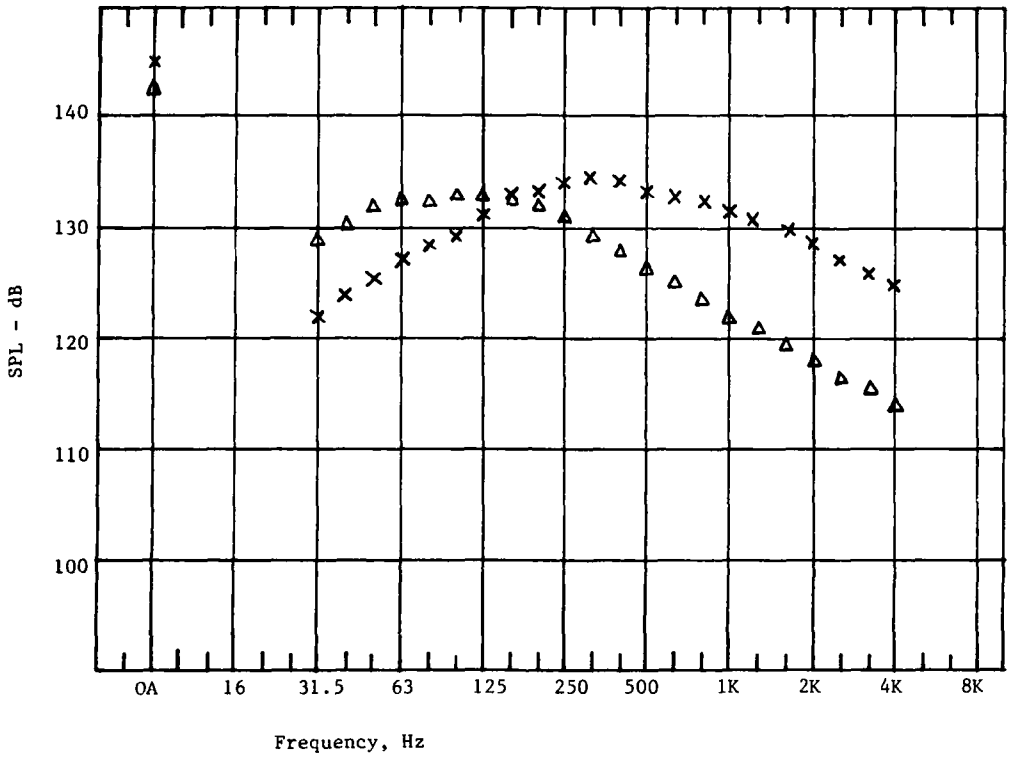

Figure 10. Predicted Wide Field/Planetary Camera vs JSC Volume 14

Table 1

Predicted Galileo Acoustic Environment

Center Frequency Hz	flt Condition	P_m, Envelope dB	$P_S/2$, Sigma dB	$P_m + ((2\ P_S)^2 + 3^2)^{1/2}$ dB	Spectra Smoothed dB
31.5	ME start	113.5	2.3	118.9	124.5
40	Lo	116.5	2.6	122.5	125.0
50	"	118.5	2.4	124.2	125.5
63	"	120.0	2.5	125.8	126.0
80	"	121.3	1.77	125.9	126.5
100	"	122.7	1.64	127.1	127.0
125	"	122.7	1.9	127.5	127.5
160	"	122.0	1.95	126.9	127.5
200	"	122.7	1.79	127.4	127.5
250	"	121.9	1.53	126.3	126.5
315	"	120.2	1.41	124.3	125.5
400	"	118.8	2.46	124.5	124.5
500	"	116.4	1.84	121.1	123.0
630	"	115.0	2.01	120.0	122.0
800	"	112.4	1.35	116.4	120.5
1K	"	110.6	1.78	115.3	119.0
1.25	"	108.9	1.57	113.2	117.5
1.6	ME start	105.4	3.85	113.7	116.5
2K	"	105.8	4.1	114.5	114.5
2.5K	Lo	108.6	1.38	112.7	113.5
3.15K	"	110.6	1.9	115.4	112.5
4K	"	109.7	2	114.7	111.0
			OA	137.0 dB	138.0 dB

Table 2

Wide Field/Planetary Camera Acoustic Prediction

Center Frequency Hz	PACES Delta Radiator dB	Galileo Level + PACES Delta dB (1)	Sidewall Envelope +3 dB (2)	P_{max} Radiator Envelope (1) & (2)	Spectra Smoothed dB
31.5	10	128.9	123.4	128.9	129.0
40	4.4	126.9	126.0	126.9	130.5
50	5.7	129.9	131.7	131.7	132.0
63	7.0	132.8	130.0	132.8	132.5
80	0	125.9	131.4	131.4	132.5
100	2.8	129.9	130.0	130.0	133.0
125	0	127.5	133.3	133.3	133.0
160	0	126.9	131.5	131.5	132.5
200	0	127.4	133.0	133.0	132.0
250	0	126.3	130.5	130.5	131.0
315	1.1	125.4	128.0	128.0	129.5
400	1.8	126.3	126.4	126.4	128.0
500	2.2	123.3	124.8	124.8	126.5
630	2.2	122.2	122.3	122.3	125.0
800	1.5	117.9	120.6	120.6	123.5
1K	.9	116.2	119.0	119.0	122.0
1.25	1.0	114.2	118.0	118.0	121.0
1.6	2.1	115.8	116.0	116.0	119.5
2K	2.3	116.8	115.0	116.8	118.0
2.5	2.2	114.9	116.0	116.0	116.5
3.15	2.2	117.6	117.0	117.6	115.5
4K	2.1	116.8	119.0	119.0	114.0
				OA	142.5

DISCUSSION

Mr. Sepcenko (Planning Research Corporation): How did you process the data? Your time history shows quite a non-stationary effect during lift-off.

Mr. O'Connell: The data were processed at the Goddard Space Flight Center and I am not entirely sure about all of the details of how they analyzed it.

Mr. On (Goddard Space Flight Center): The way we analyze data is, we first investigate the effect of averaging time; we analog the 1/3 octave band filter time histories, and we do that with something like 0.1 second, 0.2 and 0.5 second averaging times. We concluded that the 0.5 second averaging time didn't deviate too much from the 0.2 second averaging time. So we used that 1/3 octave band filtered time history, and we picked up the different flight events such as lift-off, as defined for T minus 60 to T plus 12 seconds. We plotted the maximum 1/3 octave band levels, and we createed a 1/3 octave band spectrum.

Mr. Sepcenko. Is your total time half a second?

Mr. On: Yes, that is the averaging time in the analysis. But we feed the data through, time history-wise, in 1/3 octave band filters, so we actually have a 1/3 octave band filter versus time history profile with an averaging time of 0.5 second. The only reason why the 0.1 second averaging time shows a higher level is, during the Space Shuttle Main Engine rough burn the peak is very narrow.

Mr. Sepcenko: I was concerned during the hold-down before the lift-off. Why is it that you never went below 30 Hz? Don't you have any resonances in the payload?

Mr. On: There were other considerations. First, acoustic reverberant chambers normally can't go that low. Also, there was some question regarding the high frequency distortion on the low frequency end of the transducer. The high frequency content passing through the charge amplifiers on the transducer can cause sub-harmonic distortion, so we tried to cut everything off at 25 Hz. Even though we had data down to 12 Hz, I think it was questionable whether the 25 Hz data were good.

Voice: If you intend to procure equipment to withstand these environments, what exposure time would you recommend?

Mr. O'Connell: We are testing to three minutes, with one minute for acceptance testing and three minutes for qualification testing.

Voice: I realize these payloads are usually one-way trips. Have you ever considered the kind of levels you would experience on a re-entry?

Mr. O'Connell: They would be similar to the aerodynamic levels that you saw in the transonic and supersonic regimes. They are not as high as the lift-off levels, so any test to the lift-off levels would also be adequate to cover that environment.

COMPUTER AIDED SYNTHESIS OF A SATELLITE ANTENNA STRUCTURE WITH PROBABILISTIC CONSTRAINTS

V.K. Jha

SPAR Aerospace Limited
Ste-Anne-de-Bellevue, Quebec, Canada

and

T.S. Sankar and R.B. Bhat

Department of Mechanical Engineering
Concordia University
Montreal, Quebec, Canada

The satellite antenna structures have to be designed to withstand the severe environmental conditions encountered by the satellite without failure, and hence they have to be designed with very strict reliability requirements. At the same time these structures should be as light as possible, in weight, to minimize the cost of launching the satellites into space. The design of satellite antenna structures thus poses the challenging requirement of meeting two seemingly conflicting but essential requirements namely high structural reliability and the lowest possible weight. A computer aided design procedure capable of meeting these design requirements is presented in this paper.

The computer aided procedure presented here involves synthesis of a finite element analysis program capable of analyzing complex structures and a state of the art optimization algorithm into one unified design system. This system is used for designing antenna structures subjected to random excitations and having design requirements specified in a probabilistic manner. An approach has been presented to handle probabilistic design requirements. The design of a typical satellite antenna structure realized using the proposed design procedure is presented here. Starting from the best guessed design, a saving of 43% in weight is demonstrated. The proposed system is very versatile and the possibilities of extending it for designing other complex structures are also discussed.

INTRODUCTION

The concept of designing minimum weight structures for a given strength is gaining wide acceptance in industry. One particular industry where this criterion is of significant benefit and of vital necessity is the aerospace industry. Design and manufacture of communications satellite forms a significant portion of the work performed in the aerospace industry. The antenna of a communication satellite serves the important function of transmitting and receiving the signal to and from earth. The satellite antenna structures must be designed to withstand any of the different environmental conditions encountered by the satellite without failure and hence these structures have to be designed under very strict reliability requirements. At the same time these structures should be as light in weight as possible to minimize the cost of launching the satellite into space. The designer of the satellite structures is thus faced with two seemingly conflicting but essential requirements, namely high structural reliability and the lowest possible weight.

The problem is further complicated by the fact that the satellite structures are subjected to randomly varying excitations and hence the response quantities can be expressed only in a probabilistic sense. As a result, in any structural optimization, the constraints on these parameters have to be formulated in a probabilistic manner.

The present paper describes a computer aided design procedure for satellite antenna strucutres with design requirements specified in a probabilistic manner. The procedure involves synthesis of a finite element program SPAR [1] and an optimization procedure based on Zoutendijk's [2] method of feasible direction into one unified system, for designing minimum weight satellite antenna structures subjected to random excitations.

Here, a circular dish with the surface of a paraboloid has been taken as a representative shape for the spacecraft antenna structure considered. Actual industrial specifications on the constraints are placed upon the required natural frequency, the peak displacement, and the peak stress. A vibrational environment typical of what an actual spacecraft antenna structure experiences has been used. Using the procedure developed, the complete design of the structure is carried out. The final design information results in the thickness of the face sheet of the antenna as well as the rib sizes of the supporting structure on the back of the antenna dish. Starting from the best guessed design, a saving of 43% in weight is demonstrated.

The minimum weight design of the spacecraft antenna structure requires simultaneous application of structural analysis and optimization techniques. Most of the work done previously in this area have been aimed at optimizing structures subjected to deterministic loads, that is, either static loads or steady state harmonic loads. Dobbs[3] presented a method for automated design of structures subjected to static loads with constraints placed upon nodal displacements of the structure. This method is based upon Kuhn-Tucker [4] necessary conditions for achieving a local optimum. An iterative procedure is used to resize the structure until the Kuhn-Tucker conditions are satisfied. Each iteration requires solution of a set of linear algebraic equations equal in number to the constraints. Rizzi [5] modified this method by including only the active constraints in the solution of the linear algebraic equations at each iteration, thereby making the method more efficient.

A good marriage and integration between the advances in the state of the art of optimization and that of the analysis capabilities did not take place until recently. The first significant work in this area was published by Sobieski and Bhat [6], who demonstrated the feasibility of the integration between an efficient optimization method and a state of the art structural analysis problem. Sobieski and Bhat proposed a system which could be employed for the solution of static structures, as wellas vibrating structures with frequency constraints. Since most of the problems relating to the spacecraft strucutures deal with dynamic loading conditions, the structural optimization attempted must consider all the constraints on the dynamic structural response to such loads. Such an optimization system is capable of dealing with dynamic loads and its application to satellite antenna design is presented in this paper.

DESCRIPTION OF AN ANTENNA SYSTEM AND DESIGN CONSIDERATIONS

A satellite antenna system is generally a circular dish, the curved profile of this circular dish following the contours of the generated surface of a paraboloid. The antenna serves the primary function of receiving and transmitting the communication signals reaching and leaving the spacecraft. The antenna is an integral part of the communications subsystem of any satellite. The structural survival of an antenna is of utmost importance for the successful operation of any satellite.

The antenna structure is located on the top deck of the spacecraft structure. The vibrations to the spacecraft structure are transmitted from the launch vehicle at the base of the structure and since the antenna structure is located at the top of the satellite, it experiences the most severe vibrations in comparison to the rest of the spacecraft structure. Antenna structures are positioned just under the nose cone of the launch vehicle and often there exists very limited clearance between the nose cone and the antenna structure. Therefore, the maximum displacement of the antenna structure under the transmitted vibrational load becomes very critical in design. This maximum displacement should be strictly controlled in a manner that it does not exceed the clearance between the antenna structure and the nose cone of the launch vehicle. The random excitations experienced by the antenna structures have their power spectral densities varying in a arbitrary manner in the frequency domain.

The solution requirements for the satellite antenna design can be divided into four major areas. Satellite antenna structures are designed with very low margins of safety in order to minimize the weight of the structure and hence a highly reliable estimate of their structural response is crucial. The first requirement, therefore, is to reliably analyze and compute the complete dynamic response of these strutures to random excitations of varying power spectral densities. Since the response of the structure has to be numerically computed, a finite element analysis is normally required for this purpose. Thus the second requirement is to develop an overall finite element software capable of carrying out the random response analysis. Third, a well formulated optimization algorithm is required to minimize the weight of the structure subject to the required strength and frequency constraints. Finally, in order to implement the analysis technique, the finite element program and the optimization for the satellite antenna design, these three procedures have to be synthesized into a unified system in a

logical sequence. Such a unified system is presented here.

METHODOLOGY OF SYNTHESIS

Structural Analysis

A new analysis technique developed for proper determination of the response of these structures for excitations with arbitrarily varying power spectral densities has been presented by Sankar, Jha and Bhat [7]. A mathematical model is developed by enveloping the profile of the spectral function by linear segments of varying slopes with the power spectral densities being plotted in a logarithmic scale. The net excitation is then the sum of the different excitations contributed by these individually arranged segments. Since it is possible to calculate the response of the system for these individual segments, the net response of the system can be obtained by summing up the individual responses for the linear cases. Analytical expressions are derived for a general profile and experimental verification for the validity of the model is also reported in [7].

The analyzer package used in here is based on a finite element program called SPAR, developed by NASA [1]. The SPAR program in its existing form was not found suitable for application in this particular investigation. Additional software was generated to compute the dynamic displacement and the stress response of the system, when it is subjected to random excitations. The details are presented in [7].

Optimization Algorithm

The algoritm used for the optimization procedure here in this investigation has the above mentioned desired features and is based upon the method of feasible directions [8]. Zoutendijk [2] first put forward a generalized method of feasible directions to minimize a constrained function. Vanderplatts and Moses [9] later modified this algorithm to improve its stability and efficiency, and this modified algorithm is employed here.

The algorithm starts from an initial design vector X, and the value of the objective function, the constraints, the gradients of the objective function and that of the violated constraints are computed. A step is taken in the direction of the gradient which is derived using the gradient information of both the objective function and the constraints. The size of the step is determined using a one dimensional search in the direction of the move. The procedure is repeated until the optimum solution is found.

SYNTHESIS OF ANALYSIS AND OPTIMIZATION

For achieving a minimum weight design it is essential to synthesize the structural analysis and the optimization algoritm into one unified system. The logic used in synthesizing such a system for this investigation is shown in figure 1. Principal components of the synthesized system are described below.

The Analyzer

Function of the analyzer is to compute the values of the behavioral response variables, such as frequencies, displacements, stresses, etc., of the structure. The analyzer used here is based upon the Finite Element Program SPAR [1] and is described in detail in reference [7].

Its input comprises of structural cross-sectional dimensions, material properties, element connectivity data, nodal point coordinates, and the loads. The output results generated by the analyzer are the different response parameters. Since the analyzer has to be executed many times in the loop as shown in the flowchart described in Fig. 1, it has been conveniently split into non-repeatable and repeatable parts.

The Optimizer

Function of the optimizer is to calculate the new vector of the design variables on the basis of the initial set of values of the design variables as well as on the basis of the constructed objective function and specified constraints. The optimizer automatically changes the values of the design variables until an optimum design is achieved that would satisfy all the constraints placed on the problem. The algoritm used for optimization has been described earlier.

The Front Processor

The optimizer communicates with the analyzer through a front processor. The front processor is a user-written and problem dependent program. The function of the front processor is to convert the variables of the optimization process to a set of input parameters, written in a format required by the analyzer. In the case of the structural optimization, these parameters are generally the structural member geometry.

The End Processor

Function of the end processor is to compute the value of the objective function and the constraints and also to output them in a format required by the optimization program. The end processor reads the user supplied constants defining the limits imposed upon behavioral variables. It also reads the probabilities associated with each constraint that is required to be satisfied. Output data sets defining the stresses and the displacements are

then retrieved from the SPAR data library using the data handling subroutine DAL. The values of the stresses and the displacements are then compared with the bounds imposed on them by the design requirements on the application in question. Based upon this comparison, values of the constraint functions are computed. The value of the objective function is computed by retrieving the mass information from the SPAR data sets. The values of the objective function and the constraints are then output in a format meaningful for the optimization subroutine.

The Terminator

Function of the terminator program is to issue a termination command when the termination criterion is satisfied. The termination criterion is actually checked in the optimization subroutine and a flag is raised when the criterion is satisfied. Using this flagged information, instructions are issued to the NOS-JCL to stop further executions.

The Connecting Network

Connecting network is essentially the brain of the whole system. It gets various elements and components of the system to do their individual tasks whenever required. This coordination is accomplished with the help of several procedure files. The connecting network controls execution of the various elements/programs in a predetermined sequence of computations, perform logical functions such as branching on an if-test, looking or skipping to a labelled statement; stores permanently or temporarily, the data generated by the various programs.

OPTIMIZATION WITH PROBABILISTIC CONSTRAINTS

A typical problem in structural optimization subjected to probabilistic constraints can be stated as following:

Minimize W(X)

Subject to

$$P(G_j(X) \leq G_j \text{ spec}) \geq P_j, \quad j = 1, \text{NCON} \tag{1}$$

where W(X) is the weight of the structure and P denotes the probability distribution.

The constraints specified in the inequality (1) imply that the probability that $G_j(X)$, which represents a parameter like stress or displacement, is less than or equal to a specified value G_j is greater than or equal to a probability P_j. Here NCON is the number of such constraints in the problem. Constraint (1) could also be expressed in an integral form as

$$\int_{-\infty}^{G_{jspec}} f_j[G_j(X)]\, df_j \geq P_j \tag{2}$$

where $f_j[G_j(X)]$ is the probability density function of the parameter $G_j(X)$.

The integral (2) defining the probabilistic constraints cannot be used as such in the optimization routine and hence must be expressed in a different format.

Since the excitations on the structure have been assumed to be Gaussian and the structure is taken to be a linear system, the response parameters defining the constraints $G_j(X)$ are also by definition Gaussian. Using this important property, it is possible to express the integral representation in equation (2) in a different form as explained below.

Let $\bar{G}_j(X)$ be the first moment or the mean value of the parameter $\{G_j(X)\}$. Further, let σ_{G_j} be the second moment or the standard deviation of the parameter $G_j(X)$. For the required limiting probability P_j, and the specified constraint value G_{jspec} on G_j, tables for the unit normal variate give a value of

$$\frac{G_{jspec} - \bar{G}_j(X)}{\sigma_{G_j}}$$

corresponding to the probability level P_j. Let this value be denoted by η_j. The condition stated through the probabilistic constraint of equation (2) can then also be satisfied by the adjoint deterministic constraint stated by the inequality expression

$$\frac{G_{jspec} - \bar{G}_j(X)}{\sigma_{G_j}} \geq \eta_j \tag{3}$$

Since the excitation is taken as a centered random process with zero mean, the mean value of $\bar{G}_j(X)$ is always zero, and σ_{G_j} will become equal to the root mean square value of the parameter $\{G_j(X)\}$. Hence equation (3.0) may be rewritten in the following manner:

$$\frac{G_{jspec}}{G_{j\,rms}} \geq \eta_j \tag{4}$$

which is in a very simple form and can easily be applied to structural optimization problems where constraints are expressed probabilistically. G_{jrms} for any parameter like stress or

displacement can be determined from the knowledge of all the charateristics of the excitation process and the transfer functions of the structure at hand.

The value of η_j will vary depending upon the acceptable probability level P_j specified on the constraint. The value of η_j is equal to 1 if P_j is equal to 0.65, 2 if P_j is equal to 0.95 and 3 if P_j is equal to 0.9927.

The selection of the probability level P_j will be different for different situations and applications. Its value depends upon the risks involved if the structure fails, i.e. the risks involving cost, human life, health hazard, etc. With the variation in the specified probability level, the optimum solution for a structure will change. In general, a high reliability imposition in the probability will result in a heavier structure. A value of η_j equal to 2 has been chosen in designing the satellite antenna structure.

DESIGN REQUIREMENTS FOR THE ANTENNA STRUCTURE

Design requirements for the spacecraft antenna structures include requirements on frequency, displacement, structural integrity, size and shape and manufacturability of the antenna.

The requirements on the natural frequencies of the antenna structure are placed so that the natural frequencies of the antenna structure will be above the natural frequencies of the satellite, thus avoiding the possibility of coupling between the satellite and the antenna structure. The loads experienced by the antenna structure would increase significantly if such coupling did take place. Hence, a requirement on the first natural frequency of the antenna structure is to be imposed.

The requirements on the maximum displacement of the structure are imposed in order to ensure that there would be no interference between the edges of the antenna structure and the inside walls of the nose cone of the launch vehicle during the launch of the satellite into space.

The structural integrity requirements are imposed to ensure that the stresses generated in the antenna structure by the launch vibrations will not cause any structural failure. The random vibrations produce rapidly fluctuating displacements and stresses which can only be estimated in a statistical sense due to the inherent nature of the applied random vibrations. Thus the structural integrity requirements can only be specified with a specified reliability factor or a corresponding probability. Hence, the structure must be designed to meet these structural reliability requirements.

The basic geometry, size and shape requirements are placed on the antenna structure to ensure that the antenna structure will fit within the inside envelope of the launch vehicle. Hence, during the optimum design process, suitable size limiting constraints have to be included in order to keep the design within the specified envelope.

The manufacturability of the design is an essential implicit requirement in all such applications. The optimum design may yield thickness of the cross sections which may be too thin to manufacture. In addition, there may be a few other manufacturability requirements placed on the cross-sectional dimensions of the structure depending on the shape. These manufacturability requirements can be met by imposing appropriate side constraints on the design variables governing these thickness parameters.

The specified requirements on the design are stated as follows:

i) The first natural frequency of the antenna structure should be greater than 15 Hz.

ii) The maximum displacement of any point on the antenna structure should not exceed 2.54×10^{-2}m, when subjected to the random vibrations as shown in Fig. 2. The confidence level associated with this requirement should be at least 95%.

iii) The maximum stress in any element of the antenna structure should not exceed 1.38×10^{8}Nm^{-2}, when the structure is subjected to the random vibrational loading specified in Fig. 2.

iv) Minimum thickness of any section must be 5.0×10^{-4}m. This requirement is based upon the manufacturability requirements.

The above requirements reflect the typical magnitude and the general nature of the requirements imposed on the antenna design in the aerospace industry, at present.

DESCRIPTION OF THE FINITE ELEMENT MODEL

The finite element mathematical model of the antenna structure is presented in Fig. 3. The model consists of 33 nodes connected with 24 plate elements and 24 beam elements. Out of the 33 nodes, 32 nodes have six degrees of freedom, and the central node is fixed representing the boundary conditions for the structure. The total number of degrees of freedom of the system used in the present analysis is 192. The size of the elements near the base has been kept smaller in comparison to the elements on the outer edges of the structure. The finer division near the base has been done because the most critical stresses are expected near the base since the smaller element size would ensure greater accuracy in the estimate of

stresses in the plate elements. The coordinate system used for the analysis is shown in Fig. 3. The excitation axis of the structure has been taken as the z axis. This is the direction in which the most damaging excitations are experienced by the antenna structure.

FORMULATION OF THE DESIGN PROBLEM FOR OPTIMIZATION

The purpose of the optimization is to design an antenna with minimum possible weight and yet capable of meeting all the imposed design requirements. Hence, for the optimization, the particulars are:

The Objective Function is the weight of the structure and is specified in the form $f(\bar{x})$, where $\bar{x}$ is the vector of design parameters.

The four parameters, describing the antenna design selected for optimization and shown in Fig. 4 are stated below:

a) the thickness of the dish;

b) the height of the ribs at the back of the dish;

c) the width of the ribs; and

d) the thickness of the ribs.

The thickness of the dish and the height of the ribs are assumed to be linearly decreasing from the central support of the dish to the outer edge, and the slope parameter defining the thickness and the heights at various locations are to be optimized.

The variables for optimization, thus, are:

x_1, the slope defining thickness of plate;

x_2, the slope defining the height of the ribs;

x_3, the width of the ribs; and

x_4, the thickness of the rib section.

The constraints on the optimization, which reflect all the design requirements are as follows:

The Deterministic Constraints

1. Natural frequency $\geq$ 15 Hz
2. 0.002 radians $\leq x_1 \leq$ 0.05 radians
3. 0.02 radians $\leq x_2 \leq$ 0.50 radians
4. 7.6×10^{-3}m $\leq x_3 \leq$ 2.54 m
5. 5.0×10^{-4}m $\leq x_4 \leq$ 0.254 m

The Probabilistic Constraints

1. P[Maximum displacement $\leq 2.54 \times 10^{-2}$m $\geq$ 95%
2. P[Maximum stress in ribs $\leq 1.38 \times 10^{8}$ $Nm^{-2} \geq$ 95%
3. P[Maximum stress in dish surface $\leq 1.38 \times 10^{8}$ $Nm^{-2} \geq$ 95%

Thus the problem is now fully defined for carrying out an optimal design using the procedure established earlier.

Optimum Design of the Antenna

The analysis system described in [7] was used for the response analysis.

The initial values of the design variables were chosen by using the standard beam fromulae to satisfy the stress and displacement constraints. This was done to choose realistic and meaningful starting values. The weight saving thus obtained then becomes quite meaningful.

The Initial Design Parameters

The parameters describing the initial design of the antenna are given by the following:

x_1 = .004 radians

x_2 = .05 radians

$x_3 = 1.27 \times 10^{-2}$m

$x_4 = 1.30 \times 10^{-3}$m

Weight of the structure = 8.9 kg

First natural frequency = 8.4 Hz

Maximum RMS displacement = 1.2×10^{-2}m

Maximum RMS stress = 8.11×10^{7} Nm^{-2}

Initial analysis also indicates that the starting design does not satisfy the frequency and stress constraints.

The Final Design of the Antenna

After the completion of the automated optimum design performed by employing the proposed Computer-Aided Design Procedure a feasible design realizing a weight less than the initial in-feasible design is obtained. The design history of the optimization cycle is shown in Fig. 5.

The final optimum design is obtained as follows:

x_1 = .002 radians

x_2 = .08 radians

$x_3 = 1.72 \times 10^{-2}$m

$x_4 = 7.6 \times 10^{-4}$m

Objective function = 5.08 kg

First natural frequency = 15.06 Hz

Maximum RMS displacement = 4×10^{-4}m

Maximum RMS stress = 5.69×10^7 Nm^{-2}

DISCUSSION OF THE RESULTS

It can be seen that the proposed analysis -optimization system can automatically yield an optimum design of an antenna structural system. In the problem solved here, the initial starting design values did not meet all the design requirements, that is, the initial solution was actually infeasible since it did not satisfy the stress and the frequency constraints; yet the analysis optimization system successfully produced a design which met all the requirements imposed on the design. The results show that starting with an antenna design with a weight of 8.9 kg a final optimum design weighing only 5.08 kg could be realized, thus resulting in a net saving of 43% in weight.

The history of the design cycle is shown in Fig. 5. Most of the reduction in the weight takes place in the first four iterations. The optimization calculations could have been stopped at this stage by choosing a larger value as the convergence criterion. The parameter governing the thickness of the plate sections of the antenna dish is denoted by x_1. x_1 shows a rapid decrease during the first iteration and then stays at that value for subsequent iterations. This fixed value of x_1 is the minimum constraint value of x_1. The manufacturability of the dish dictates that certain minimum thickness be kept. The parameter governing the height of the rib, x_2, shows an oscillating pattern. Its final value is higher than its starting value, which suggests that an increase in the height of the rib provides a more effective structure. The width of the ribs, x_3, also shows an oscillating pattern in the beginning. The thickness of the rib section is given by x_4 and this parameter shows a continuous decrease in its value as the iterations continue indicating the direct relationship of the thickness to the weight of the structure. Thus Fig. 5 gives good insight into the total optimization process.

The size of the finite element chosen for this antenna design is not large enough to include sufficient nodes on the skin of the dish. This precludes the possibility of getting local plate vibration modes. The size of the model was kept small to limit the computation time. In actual practice it is possible to have a larger size finite element model for more accurate results.

EXTENSION OF THE PROPOSED METHOD FOR DESIGNING OTHER STRUCTURES

The method presented here for designing satellite antenna structures can be extended to perform dynamic analysis and the optimum design for other complex structures. For example, the random loads experienced by building structures, automoblie structures, off-shore drilling platform structures, etc., can all be described in a manner similar to the random loads experienced by satellite antenna structures. Hence the approach developed for designing satellite antenna structure can be extended for designing these complex structures.

The analysis-optimization system developed here is modular in nature. That is, one module of the system can be replaced by another user written module. The software for the system is basically problem independent, that is, for a new problem, the system can be used mostly as is. The areas requiring modification are where the details of the finite element model are specified and where the constraints on the design are defined.

Various steps which should be taken to adopt this system for any other application are shown in Fig. 6.

CONCLUSIONS

The satellite antenna design has been accomplished using the computer-aided synthesis of analysis and optimization. The optimum design for the antenna yields a weight of only 5.08 kg, which is 43% lower in weight in comparison to the best guessed initial design which had a weight of 8.9 kg. This optimum antenna design meets all the functional requirements in terms of the frequency, stress and displacement constraints imposed upon the design. Normally, the duration of the design process in industry for typical satellite antenna structures is approximately two to three months and this duration can be considerably reduced to practically a few days by employing the proposed analysis-optimization computational system. Many other similar complex structures subjected to certain forms of random excitations of varying power spectral densities can also be designed for optimum considerations using the proposed approach. The stochastic constraints on design can be handled in a manner proposed in this paper. The system synthesized for designing the satellite antenna structures is very adaptable and can be easily extended for designing other complex structures.

REFERENCES

1. Wheatstone, W.D., "Spar Structural Analysis Reference Manual", NASA CR - 158979 - 1, 1978.
2. Zoutendijk, G., "Methods of Feasible Directions", Elsevier, Amsterdam, 1960
3. Dobbs, M.W. and Nelson, R.B., "Application of Optimality Criterion to Automated Structural Design", AIAA Journal, Vol. 14, 1976, pp. 1436-1443.
4. Kowalik, J. and Osborne, M.S., "Methods of Unconstrained Optimization Problems", Elsevier, New York, 1968.

5. Rizzi, P., "Optimization of Multiconstrained Structures Based on Optimality Criterion", Proceedings AIAA/ASME/SAE, Materials Conference, 1976.

6. Sobieski, J. and Bhat, R., "Adaptable Structural Synthesis Using Advanced Analysis and Optimization Coupled by a Computer Operational System", AIAA/ASME/ASCE, 20th Structural Dynamics and Material Conference, St. Louis, April, 1979.

7. Jha, V.K., Sankar, T.S. and Bhat, R., "Determination of Response of Satellite Antenna Structures Subjected to Random Excitations with Arbitrarily Varying Power Spectral Densities", Presented at 53rd Shock and Vibrations Conference, Danvers, Mass., To be published in the bulletin.

8. Vanderplatt, G., "CONMIN - A Fortran Program for Constrained Function Minimization", NASA TMX-62, April 1972.

9. Vanderplatts, G.N. and Moses, F., "Structural Optimization by Methods of Feasible Directions", Journal of Computers and Structures, Vol. 3, 1973, pp. 739-755.

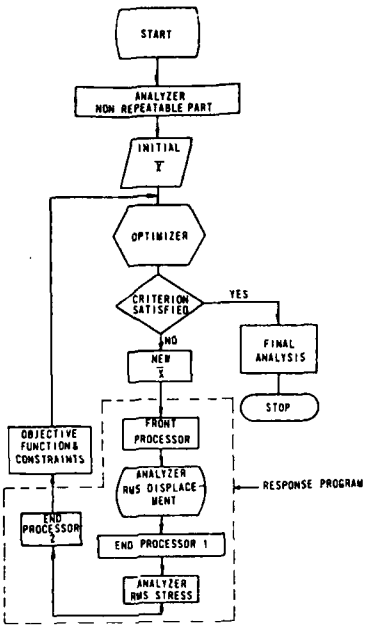

Figure 1: Basic Flow Chart of Analyzer - Optimizer System

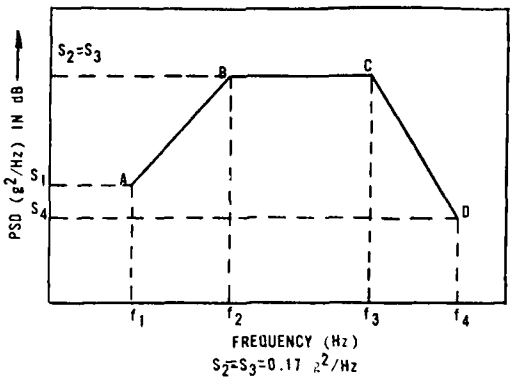

$S_2=S_3=0.17\ g^2/Hz$

$f_1=2Hz$

$f_2=20Hz$

$f_3=500Hz$

$f_4=2000\ Hz$

Figure 2: The Input Power Spectral Density Profile for Antenna Reflector Design

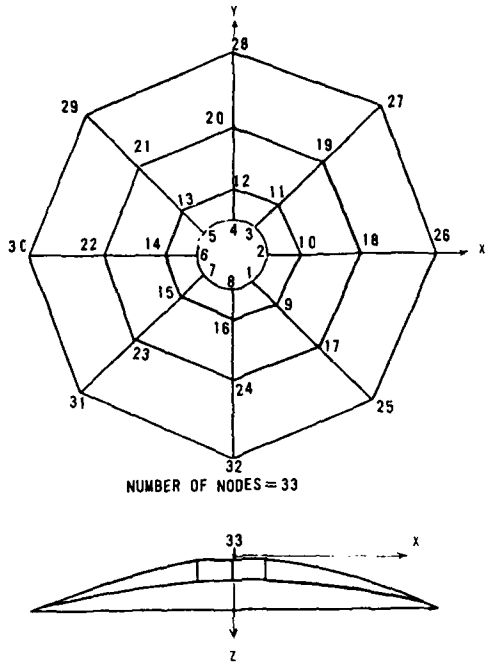

Figure 3: Node Locations-Finite Element Model of Antenna Reflector

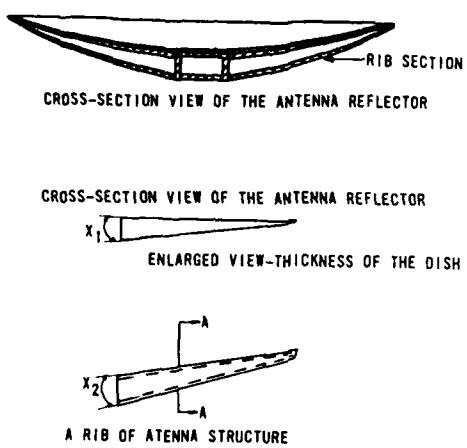

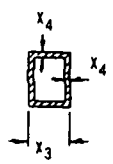

X_1- SLOPE GOVERNING PLATE THICKNESS
X_2- SLOPE GOVERNING RIB HEIGHT
X_3- WIDTH OF THE RIBS
X_4- THICKNESS OF THE RIB SECTION

Figure 4: Design Variables to be Optimized for the Antenna Reflector

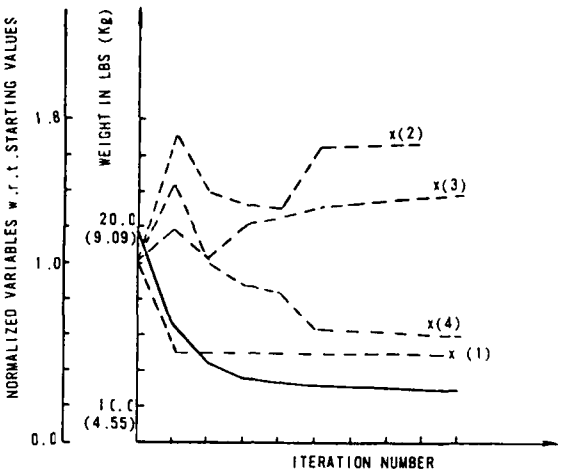

Figure 5: Design History for Antenna Reflector Structure

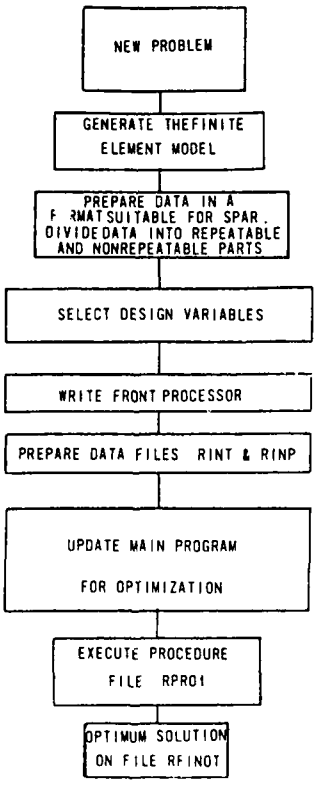

Figure 6: Sequence of Operations to Adapt the System to General Structural Design

DISCUSSION

Mr. Calapodas (U.S. Army Applied Technology Laboratory): What considerations went into selecting the finite element program that you used? If I recall correctly, you used "SPAR."

Mr. Jha: Yes. SPAR is a new program, and it is probably one of the most flexible finite element programs available now. It has a very modular nature because you can execute mass matrices and stiffness matrices in any order you want. It can also interface with the user in a FORTRAN program. In this case, SPAR did not have the capability to compute random response, and I needed that. I also needed to input the right number of response calculations the way I wanted them. All of this can be done separately in a FORTRAN program, and all of the data which are computed within SPAR can be taken out in a FORTRAN program. Then you can compute your response and feed that back into this program, as a data package which can be used further within the program. So, I would say its flexibility is the best feature. That is why it was chosen.

Mr. Lee: Using your optimization procedure, how do you ensure that you don't end up with a local minimum and not the absolute?

Mr. Jha: I guess the only way to do that is to take three or four arbitrary starting points, and if you zero in on the same point, then you are sure that you are converging to the right place. If you start from four different points and get three optimum points, then you have local conditions.

DYNAMIC BEHAVIOUR OF A SATELLITE ANTENNA STRUCTURE IN RANDOM VIBRATION ENVIRONMENT

V.K. Jha
SPAR Aerospace Limited
Ste-Anne-de-Bellevue, Quebec, Canada

and

T.S. Sankar and R.B. Bhat
Department of Mechanical Engineering
Concordia University
Montreal, Quebec, Canada

Satellite antenna structures are often subjected to random excitations with power spectral densities varying in an arbitrary manner in the frequency domain. A mathematical model for effectively describing such excitations is proposed in order to compute the dynamic response of the antenna structure. The mathematical model of the excitation is developed analytically by enveloping the profile of the power spectral densities by linear segments of varying slopes. The validity of the proposed mathematical model is experimentally verified. The dynamic response of the satellite antenna structure is obtained using the proposed mathematical model for the excitation. The finite element program SPAR has been used as the main frame for this dynamic response analysis. The eigenvalues and mode shapes along with displacements and stresses for the antenna structure subjected to random excitations encountered during normal operation are presented, employing the proposed mathematical model for the excitations.

INTRODUCTION

Satellite antenna structures are often subjected to random excitations which have their powerspectral density varying in an arbitrary manner in the frequency domain. In order to analyse and design these structures against such loading, it is essential to describe the power spectral densities of excitations analytically in a functional form and compute the resulting response. Although a mathematically exact description of the actual power spectral density variation to which antenna structures are subjected is not normally feasible, there are means to describe them approximately which are sufficiently reliable in most practical situations. For example, when the power spectral density is almost flat over a very large frequency range of interest, it is meaningful to model it as a pure white noise [1], or if its flatness is limited to a certain discrete range of frequencies it can be approximated as a band limited white noise [2]. Profiles of many typical power spectral density variations which are analytically describable for setting up system response equations are reported in [3]. However, when the power spectral density of the excitation varies arbitrarily and shows discontinuities in the frequency domain, an exact analytical modelling becomes often impossible, for carrying out analytical computation of the response.

A mathematical model for effectively describing excitations having arbitrarily varying power spectral densities in the frequency domain is proposed in this paper to enable structural response computation. The mathematical model is developed by enveloping the profile of the spectral function in a dB vs. logarithmic frequency plot with lines of varying slopes. The net excitation is then the sum of the different excitations contributed by these individual linear segments. Since it is possible to calculate the response of the system for these individual segments, the net response of the system can be obtained by summing up the individual responses. Analytical expressions are derived for a general profile and experimental verification for the validity of the model is also reported in this paper.

The above analytical model for the excitation, has been used to carry out a complete dynamic response analysis of a communication satellite antenna structure. The analysis includes determination of eigenvalues, stress responses and the displacement responses for

the structure when it is subjected to random excitations encountered in its normal operation. The structural analysis program used in here is based on a finite element program called SPAR, developed by NASA [4]. The SPAR program in its existing form did not have the capability for performing random response analysis. Hence, additional software was generated to compute the dynamic displacement and the stress response of the system, when it is subjected to random excitations.

RANDOM VIBRATION ENVIRONMENT FOR THE SATELLITE ANTENNA STRUCTURE

Various sources which give rise to the structural loads experienced by the antenna structure are as follows:

a) The acoustic noise generated by the rocket engines of the launch vehicle;
b) The shock loads at the time of separation of the satellite from the final stage of the launch vehicle;
c) The random vibrations generated by the pulsations of the rocket engine fuel burning process.

The predominant load on the structure comes from the random vibrations generated by the above sources. To the designer, the loads are specified in the form of a power spectral density profile over the frequency range. The structure must then be designed to withstand these random vibrational loads, assuming that the structure is excited at its mounting points by these excitation processes. A typical profile of random vibration to which antenna structures are subjected is given in Fig. 1.

The Mathematical Model for the Random Vibration Environment of the Antenna

The basic concept behind the proposed analytical model is that any given profile of the power spectral density variation in the frequency domain can be enveloped by a series of appropriately chosen linear segments when the power spectral densities are plotted in a logarithmic scale. These linear segments may then have negative, positive or zero slopes. Figure 1 shows how a general profile can be enveloped by an arrangement of such linear segments. Since these set of linear segments can be defined analytically, a proper optimal combination of these linear segments provides an analytical description for the entire spectral profile.

As mentioned earlier, this envelope model essentially involves three types of segments. They are segments with positive slopes, segments with zero slopes, and segments with negative slopes. In Fig. 2 these segments are represented by sample line segments, AB, BC, and CD respectively. The relationship between the slope specified in dB/octave, the power spectral density value and the frequency is given by

$$S_x(f) = S_x(f_\ell)\ (f/f_\ell)^{N/3} \qquad (1)$$

where

N = slope of the segment in dB/octave

f = frequency at any point within the segment in Hz or cycles/second

$S_x(f)$ = power spectral density value at frequency f

f_ℓ = frequency at the beginning of the envelope process (e.g., f_1 in Fig. 2 for region AB)

$S_x(f_\ell)$ = power spectral density value at f_ℓ

Determination of the Structural Response

Assuming linear characterization of the total structure, the net response of the structure is the sum of the response due to various linear segments and can be computed as follows.

The response power spectral density for a single degree linear structural system subjected to random excitations is given by the standard relation

$$S_y(f) = |H(f)|^2 .\ S_x(f) \qquad (2)$$

where

$S_x(f)$ = power spectral density of the input

$S_y(f)$ = power spectral density of the output

$H(f)$ = the complex frequency response of the system relating the input and the output.

The mean square value of the response can then be obtained from equation (2) as

$$\sigma^2 = \int_{f_1}^{f_2} S_x(f)|H(f)|^2\, df \qquad (3)$$

In general, it is possible to consider any slope, N, of the excitation power spectral density profile to obtain the mean square response using equation (3). However, the integral in equation (3) can be evaluated analytically only if the numerical value of the term (N/3) in equation (1) is an integer. If this is not the case, one can obtain only the mean square value of the response by appropriate numerical evaluation of the integral in equation (3).

In the present analysis the value of (N/3) is considered to be an integer to enable closed form evaluation of the integral in equation (3) analytically. As an example, a profile is represented completely by three different types of segments in Fig. 1. The expressions after carrying out the necessary integration for these three different types of linear segments shown in Fig. 2 are given in the following sections.

The general expression for the mean square response in the three regions shown in Fig. 2 is:

$$\sigma^2 = \frac{S_x(f_\ell)}{f_\ell^{N/3}} \int_{f_\ell}^{f_u} f^{N/3} |H(f)|^2 df \qquad (4)$$

where

f_ℓ = lower limit of the frequency for the segment

f_u = upper limit of the frequency for the segment

$S_x(f_\ell)$ = the excitation power spectral density value at the lower frequency limit f_ℓ of the segment

N = slope of the particular linear segmet in dB/octaves

H(f) = the complex frequency response of the system

The mean square response parameter of the antenna structure calculated through equation (4) can be either displacement, velocity or the acceleration, depending upon the type of frequency response function H(f) used in evaluating equation (4). In antenna design the design specifications require use of the acceleration and the displacement response for the structure, hence expressions for the acceleration and the displacement response are derived in the following sections.

The Acceleration Response

The frequency response relating the base acceleration excitation and the acceleration response for a single degree of freedom system is given by

$$H(f) = \frac{f_n^2 + 2i\zeta f f_n}{f_n^2 - f^2 + 2i\zeta f f_n} \qquad (5)$$

where f_n is the natural frequency of the system and ζ the damping ratio. Substituting equation (5) into equation (4) and expressing frequencies as nondimensional ratios in the form $\Omega = f/f_n$, the mean square acceleration response is computed as

$$\sigma^2 = \frac{S_x(f_\ell) \cdot f_n^{(1+N/3)}}{f_\ell^{N/3}} \int_{\Omega_\ell}^{\Omega_u} \frac{\Omega^{N/3}(1 + 4\zeta^2\Omega^2)d\Omega}{(1 - \Omega^2)^2 + 4\zeta^2\Omega^2} \qquad (6)$$

For any positive or negative value of the integer (N/3), the expression within the integral in equation (6) can be broken down into partial fractions and integrated in closed form. The most common slope is used for specifying a given random loading environment in spacecraft structures is 6 dB/octave, and hence the expression in equation (6) is integrated for N = ±6 for the segments AB and CD and N = 0 for the segment BC, as shown in Fig. 2. The response for each of these segments is calculated as follows:

a) Acceleration Response Under Linear Segment AB

Substituting N = 6 in equation (6) and noting that $f_\ell = f_1$, $f_u = f_2$ and $S_x(f_\ell) = S_1$ from Fig. 2 the mean square response acceleration is

$$\sigma^2_{AB} = \frac{S_1 \cdot f_n^3}{f_1^2} \int \frac{\Omega^4(1 + 4\zeta^2\Omega^2)d\Omega}{(1 - \Omega^2)^2 + 4\zeta^2\Omega^2} \qquad (7)$$

Breaking the integrand into partial fractions

$$\frac{\Omega^2(1 + 4\zeta^2\Omega^2)}{(1 - \Omega^2)^2 + 4\zeta^2\Omega^2} = 4\zeta^2 + \left(\frac{1 + 8\zeta^2 - 16\zeta^4}{4i\zeta}\right)\left\{\frac{\Omega}{1 - \Omega^2 - 2i\zeta\Omega} - \frac{\Omega}{1 - \Omega^2 + 2i\zeta\Omega}\right\} - 2\zeta^2\left\{\frac{1}{1 - \Omega^2 - 2i\zeta\Omega} + \frac{1}{1 - \Omega^2 + 2i\zeta\Omega}\right\} \qquad (8)$$

Using solutions for standard integration of the type

$$\frac{\Omega d\Omega}{1 \pm \Omega^2 \pm 2i\zeta\Omega}$$

and integrating

$$\sigma^2_{AB} = \frac{S_1 \cdot f_n^3}{f_1^2}\left[I_{AB}(\Omega_2,\zeta) - I_{AB}(\Omega_1,\zeta)\right] \qquad (9)$$

where

$$I_{AB}(\Omega,\zeta) = 4\zeta^2\Omega + \frac{(1 + 8\zeta^2 - 16\zeta^4)}{4\zeta}\tan^{-1}\left(\frac{2\zeta\Omega}{1 - \Omega^2}\right) - \frac{1 + 16\zeta^2 - 16\zeta^4}{8(1 - \zeta^2)^{\frac{1}{2}}}\ln\left[\frac{\Omega^2 + 2\Omega(1 - \zeta^2)^{\frac{1}{2}} + 1}{\Omega^2 - 2\Omega(1 - \zeta^2)^{\frac{1}{2}} + 1}\right] \qquad (10)$$

b) Acceleration Response Under Linear Segment CD

Substituting N = -6 in equation (6) and noting that $f_\ell = f_3$, $f_u = f_4$ and $S_x(f_\ell) = S_3$ from Fig. 2, the man square response acceleration is

$$\sigma^2_{CD} = \frac{S_x(f_3) \cdot f_3^2}{f_n} \int_{\Omega_3}^{\Omega_4} \frac{(1 + 4\zeta^2\Omega^2)d\Omega}{\Omega^2(1 - \Omega^2)^2 + 4\zeta^2\Omega^2} \qquad (11)$$

Breaking the integral again into partial fractions

$$\frac{1 + 4\zeta^2\Omega^2}{\Omega^2[(1 - \Omega^2)^2 + 4\zeta^2\Omega^2]} = \frac{1}{\Omega^2} + \frac{1}{4i\zeta}\left[\frac{1}{1 - \Omega^2 + 2i\zeta\Omega} - \frac{\Omega}{1 - \Omega^2 + 2i\zeta\Omega}\right] + \frac{1}{1 - \Omega^2 + 2i\zeta\Omega} + \frac{1}{1 - \Omega^2 - 2i\zeta\Omega} \qquad (12)$$

Using the standard integrals

$$\sigma^2_{CD} = \frac{S_3 \cdot f_3^2}{f_n} [I_{CD}(\Omega_4,\zeta) - I_{CD}(\Omega_3,\zeta)] \quad (13)$$

where

$$I_{CD}(\Omega,\zeta) = -\frac{1}{\Omega} + \frac{1}{4\zeta} \tan^{-1}\left(\frac{2\zeta\Omega}{1-\zeta^2}\right) +$$

$$\frac{3}{8(1-\zeta^2)^{\frac{1}{2}}} \ln \left[\frac{\Omega^2 + 2\Omega(1-\zeta^2)^{\frac{1}{2}} + 1}{\Omega^2 - 2\Omega(1-\zeta^2)^{\frac{1}{2}} + 1}\right] \quad (14)$$

c) Acceleration Response Under Linear Segment BC

Substituting N = 0 in equation (6) and noting that $f_\ell = f_2$, $f_u = f_3$ and $S_x(f_\ell) = S_2$ from Fig. 2, the mean square response acceleration is calculated as:

$$\sigma^2_{BC} = S_2 f_n [I_{BC}(\Omega_3,\zeta) - I_{BC}(\Omega_2,\zeta)] \quad (15)$$

where

$$I_{BC}(\Omega,\zeta) = \frac{(1+4\zeta^2)}{4\zeta} \tan^{-1}\left(\frac{2\zeta\Omega}{1-\Omega^2}\right)$$

$$+ \frac{(1-4\zeta^2)}{8(1-\zeta^2)^{\frac{1}{2}}} \ln \left[\frac{\Omega^2 + 2\Omega(1-\zeta^2)^{\frac{1}{2}} + 1}{\Omega^2 - 2\Omega(1-\zeta^2)^{\frac{1}{2}} + 1}\right] \quad (16)$$

The Displacement Response

The frequency response relating the base acceleration excitation and the displacement response for a single degree of freedom structural system is given by

$$H(f) = \frac{1}{f_n^2 - f^2 + 2i\zeta f f_n} \quad (17)$$

where f_n is the natural frequency of the system and ζ is the damping of the system. Substituting equation (17) in equation (4) and expressing the frequencies in the form of nondimensional ratio $\Omega = f/f_n$, the mean square displacement response may be determined through the expression

$$\sigma^2 = \frac{S_x(f_\ell) \cdot f_n^{\left(\frac{N}{3}-1\right)}}{f_\ell^{N/3}} \int_{\Omega_\ell}^{\Omega_u} \frac{\Omega^{N/3}\, d\Omega}{(1-\Omega^2) + 4\zeta^2\Omega^2} \quad (18)$$

Equation (18) can now be integrated to yield the displacement response for any of the linear segments AB, BC or CD, shown in Fig. 2.

a) Displacement Response Under Linear Segment AB

Substituting N = 6 in equation (18) and noting that $f_\ell = f_1$, $f_u = f_2$, and $S_x(f_\ell) = S_1$, the mean square displacement response is

$$\sigma^2_{AB} = \frac{S_1}{f_1^2 \cdot f_n} [I_{AB}(\Omega_2,\zeta) - I_{AB}(\Omega_1,\zeta)] \quad (19)$$

where

$$I_{AB}(\Omega,\zeta) = \frac{1}{4\zeta} \tan^{-1}\left\{\frac{2\zeta\Omega}{1-\Omega^2}\right\}$$

$$- \frac{1}{8(1-\zeta^2)^{\frac{1}{2}}} \ln \left[\frac{\Omega^2 + 2\Omega(1-\zeta^2)^{\frac{1}{2}}}{\Omega^2 - 2\Omega(1-\zeta^2)^{\frac{1}{2}}}\right] \quad (20)$$

b) Displacement Response Under Linear Segment CD

Substituting N = -6, in equation (18) and noting that $f_\ell = f_3$, $f_u = f_4$ and $S_x(f_\ell) = S_3$, the mean square displacement response is

$$\sigma^2_{CD} = \frac{S_3 f_3^2}{f_n^5} [I_{CD}(\Omega_4,\zeta) - I_{CD}(\Omega_3,\zeta)] \quad (21)$$

where

$$I_{CD}(\Omega,\zeta) = \frac{1-4\zeta^2}{4\zeta} \tan^{-1}\left(\frac{2\zeta\Omega}{1-\Omega^2}\right) - \frac{1}{\Omega}$$

$$+ \left(\frac{3-4\zeta^2}{8(1-\zeta^2)^{\frac{1}{2}}}\right) \ln \left\{\frac{\Omega^2 + 2\Omega(1-\zeta^2)^{\frac{1}{2}} + 1}{\Omega^2 - 2\Omega(1-\zeta^2)^{\frac{1}{2}} + 1}\right\} \quad (22)$$

c) Displacement Response Under Linear Segment BC

Substituting N = 0 in equation (18)

$$\sigma^2_{BC} = \frac{S_2}{f_n^2} [I_{BC}(\Omega_3,\zeta) - I_{BC}(\Omega_2,\zeta)] \quad (23)$$

where

$$I_{BC}(\Omega,\zeta) = \frac{1}{4\zeta} \tan^{-1}\left(\frac{2\zeta\Omega}{1-\Omega^2}\right)$$

$$+ \frac{1}{8(1-\zeta^2)^{\frac{1}{2}}} \ln \left[\frac{1 + 2\Omega(1-\zeta^2)^{\frac{1}{2}} + \Omega^2}{1 + 2\Omega(1-\zeta^2)^{\frac{1}{2}} + \Omega^2}\right] \quad (24)$$

Thus, if any general excitation were to be approximated by n linear segments of positive, negative or zero slopes, then the total response of the structure may be obtained by the superposition principle stated by

$$\sigma^2_{total} = \Sigma\, \sigma_i^2 \quad \text{where } i = 1,n.... \quad (25)$$

where n is the number of segments

σ_i is the RMS response of the i^{th} segment

Experimental Verification of the Excitation Model

The object of this experiment procedure is to verify the validity of the analytical results stated previously by comparing the experimen-

tally obtained response with the analytically computed response. Since any profile can be represented by a combination of positive, negative and zero slope segments, a profile consisting of these three types of segments was chosen as the input excitation. The profile used for the experiment is reproduced in Fig. 2.

The test set up, described schematically in Fig. 3 consists of a simple cantilever mounted on a rigid support. The structure was mounted on a vibration table and was subjected to base accelerations. The structure tested was an aluminum cantilever beam of length 30 cm and a cross section of 2.5 x 1.25 cm. The structure was initially subjected to pure harmonic excitation at varying frequencies in order to obtain the natural frequencies of the system. The frequency response of the system is given in Fig. 4 which shows that the first two natural frequencies occur at 102 and 645 Hz. The damping ratios of the system associated with the first two natural frequencies were calculated from Fig. 4 and are found to be 0.004 and 0.00625. Subsequently, the structure was subjected to a random acceleration input at the support and the response was measured at the tip of the beam. An excitation signal having a power spectral density profile same as the one shown in Fig. 2 was recreated in the tests. The positive and negative slopes were 5 dB/octave and the limiting frequencies were f_1 = 20 Hz, f_2 = 200 Hz, f_3 = 400 Hz and f_4 = 700 Hz corresponding to Fig. 2. The power spectral density of the excitation from f_2 to f_3 was taken as 0.1 g/Hz. The excitation signal was chosen in such a manner that the two regions with the non-zero slopes contained the first and second natural frequencies of the structure. The root mean square acceleration measured at the tip of the structure was 62 g RMS.

The computed value of root mean square acceleration using the analytical expressions derived previously in this paper was 61.3 g RMS, showing a good agreement with the rest results. Thus, it can be seen that the analytically obtained response is within 2% of the measured response. It was also demonstrated earlier that by choosing sufficiently large number of segments a mathematical model of a general profile can be reliably generated to compute the response of the structure. This experiment verifies the validity of this type of modelling technique for describing any arbitrary power spectral density of excitation for analytically evaluating the responses of a linear dynamic system.

DETERMINATION OF RESPONSES FOR A SATELLITE ANTENNA STRUCTURE

General Description of an Antenna System

A satellite antenna system is generally a circular dish, the curved profile of this circular dish following the contours of the generated surface of a paraboloid. The antenna serves the primary function of receiving and transmitting the communication signals reaching and leaving the spacecraft. The antenna is an integral part of the communications subsystem of any satellite. The structural survival of an antenna is of utmost importance for the successful operation of any satellite. Antenna structures are positioned just under the nose cone of the launch vehicle and often there exists very limited clearance between the nose cone and the antenna structure. Therefore, the maximum displacement of the antenna structure under the transmitted vibrational load becomes very critical in design. Hence it is of utmost importance to compute the dynamic response of the antenna structure as reliably as possible.

Description of the Finite Element Model

The geometry details for the satellite antenna under investigation are given in Fig. 5. The finite element mathematical model of the antenna structure is presented in Fig. 6 to 8. The model consists of 33 nodes connected with 24 plate elements and 24 beam elements. Out of the 33 nodes, 32 nodes have six degrees of freedom and the central node is fixed representing the support boundary condition for the structure. The total number of degrees of freedom of the system used in the present analysis is 192. The size of the elements near the base has been kept smaller in comparison to the elements on the outer edges of the structure. The finer divisions near the base has been done because the most critical stresses are expected near the base since the smaller element size would ensure greater accuracy in the estimate of stresses in the plate elements. The coordinate system used for the analysis is shown in Fig. 6. The excitation axis of the structure has been taken as the z axis. This is the direction in which the most damaging excitations are experienced by the antenna structure.

General Description of the Response Analysis Software

The main frame of the response analysis program used here is SPAR [4]. The finite element program SPAR is a versatile general purpose finite element program of structural analysis. The program consists of a number of modules or processors which perform the basic task of finite element analysis. These processors communicate with each other through the data base. The data base consists of one or more direct access libraries, which contain the data set output from the different processors. These data sets have a specific identifying name with which any particular processor can access them whenever they are required as inputs for that particular computation. Figure 9 shows the schematic of the general structure of the overall finite element program. Each processor of SPAR performs a specific function e.g. processor TAB, creates data sets containing tables of joint locations, section properties, material constants, etc.,

processor K assembles the stiffness matrix of the structure, processor M assembles the mass matrix of the structure, etc. Further, the processor AUS performs various matrix manipulations such as multiplication, addition, transpose, etc. This processor provides a great deal of flexibility to the user in adopting SPAR program to suit any computational needs. Other program and analysis details about the SPAR processors are contained in Reference [4].

Determination of RMS Displacement Responses

SPAR has the capability of calculating all the displacements and stresses of complex structures when subjected to static loading conditions. It also has the additional capability of performing eigenvalue analysis, and various matrix manipulations needed for a basic dynamic response calculations. However, additional software had to be designed and written, which in conjunction with the available capabilities of SPAR, can be used for determining the required responses of a structure under random vibrational environments. A brief account of the different response calculation procedures is provided in the following pages.

The spacecraft antenna structures are normally required to be designed for a specified level of base excitation. Let y_i, $(i = 1,2,\ldots n)$ denote the absolute displacements of the antenna structure and x denote the base displacement. The displacements relative to the base are then given by $(y_i - x)$, $(i = 1,\ldots n)$. Considering viscous damping c, the equations of motion are

$$[m]\{\ddot{y}\} + [c]\{\dot{y} - \dot{x}\} + [k]\{y - x\} = 0 \qquad (26)$$

Where [m], [k] and [c] are the mass, stiffness, and damping matrices respectively of the antenna structure.

Defining $z_i = y_i - x$, the equations of motion are

$$[m]\{\ddot{z}\} + [c]\{\dot{z}\} + [k]\{z\} = -[m]\{\ddot{x}\} \qquad (27)$$

where $\{\ddot{x}\}$ is a column matrix in which all elements are equal.

The relative displacement {z} can be expressed in terms of normal modes, ϕ, and the normal coordinates, η, related by the expression

$$\{z\} = [\phi]\{\eta\} \qquad (28)$$

Substituting (28) in (27), the equations of motion are

$$[m][\phi]\{\ddot{\eta}\} + [c][\phi]\{\dot{\eta}\} + [k][\phi]\{\eta\} = -[m]\{\ddot{x}\} \qquad (29)$$

Premultiplying by $[\phi]^T$

$$[\phi]^T[m][\phi]\{\ddot{\eta}\} + [\phi]^T[c][\phi]\{\dot{\eta}\} + [\phi]^T[k][\phi]\{\eta\} = -[\phi]^T[m]\{\ddot{x}\} \qquad (3)$$

Since

$$[\phi]^T[m][\phi] = [M] \text{ (generalized mass matrix)}$$

$$[\phi]^T[c][\phi] = 2[\zeta][k][\omega]^{-1}$$

and $$[\phi]^T[k][\phi] = [K] \text{ (generalized stiffness matrix)}$$

or

$$[M]\{\ddot{\eta}\} + 2[\zeta][K][\omega]^{-1}\{\dot{\eta}\} + [K]\{\eta\} = -[\phi]^T[m]\{\ddot{x}\} \qquad (31)$$

The r^{th} equation of motion then is

$$\ddot{\eta}_r + 2\zeta\omega_r\dot{\eta}_r + \omega_r^2\eta_r = \frac{T_r}{M_r}\ddot{x} \qquad (32)$$

where

$$T_r\ddot{x} = -\{\phi_r\}^T[m].\{\ddot{x}\} \qquad (33)$$

The solution of equation (33) is given by

$$\eta_r(t) = \frac{T_r}{\omega_r^2 M_r} \cdot H_r(\Omega) \cdot \ddot{x}(t) \qquad (34)$$

where $H_r(\Omega)$ is the system transfer function relating the input to the output of the system and Ω is the nondimensional frequency ratio, ω/ω_r.

The response $z_i(t)$ of i^{th} degree of freedom at time can be expressed in terms of normal modes

$$z_i(t) = \sum_{r=1}^{n} \phi_{ir}\,\eta_r(t) \qquad (35)$$

The mean square of the dispalcement response is then given by the averaging process

$$\overline{z_i^2(t)} = \lim_{T\to\infty} \frac{1}{2T} \int_{-T}^{T} z_i^2(t)dt \qquad (36)$$

Substituting $\eta_r(t)$ from (34) in (35) and (36)

$$\overline{z_i^2(t)} = \lim_{T\to\infty} \frac{1}{2T} \sum_{r=1}^{n}\sum_{s=1}^{n} \frac{T_r \cdot T_s \phi_{ir}\phi_{is}}{\omega_r^2\,\omega_s^2\,M_r \cdot M_s} \int_{-T}^{T} |H_r(\Omega)|\,|H_s(\Omega)|\,\ddot{x}^2(t)dt \qquad (37)$$

For a lightly damped system, the magnification factors $H_r(\Omega)$ have pronounced peaks in the neighborhood of the corresponding natural frequencies ω_r. The products $|H_r(\Omega)|\,|H_s(\Omega)|$ for $r \neq s$ are small in comparison to the products when $r = s$, thus for lightly damped system, it is reasonable to disregard the cross product terms of the transfer functions. With this assumption, transformation of equation (37) from time domain to frequency domain, yields the solution for frequency response as

$$\overline{z_i^2(t)} = \sum_{r=1}^{n} \frac{\phi_{ir}^2 T_r^2}{M_r^2 \cdot \omega_r^2} \cdot \frac{1}{2\pi} \int_0^{\infty} |H_r(\Omega)|^2 . S_x(\Omega)d\Omega \qquad (38)$$

$H_r(\Omega)$ will depend upon the type of output function desired. The input to the satellite system is the base acceleration process given in terms of the power spectral density. The output required could be the response acceleration power spectral density or the displacement power spectral density depending on design criteria employed. The technique for modelling arbitrary input process can be used to handle either the acceleration or the displacement response or both. In equation (38), if the desired response is the displacement response, then for a constant power spectral density, indicating a wide band input, equation (38) reduces to

$$z_{i_{rms}} = \left[\sum_{r=1}^{n} \frac{S_r(\Omega) T_r^2 \phi_{ir}^2}{8 \zeta_r \omega_r^3 M_r^2} \right]^{\frac{1}{2}} \qquad (39)$$

In the analysis for the antenna structure, first the SPAR structural analysis program is executed to generate the structure geometry data, the mass matrix, and the stiffness matrix of the structure. SPAR is then used to compute all the eigenvalues and the different vibration mode shapes for the given satellite strucutre. This data is then used for generating the generalized masses for each mode of vibration. This computation is performed within the SPAR program using its matrix manipulation capabilities. The root mean square (RMS) displacement response of the structure is calculated in a separate program developed for this investigation.

Determination of RMS Stress Responses

In order to arrive at a design of a structure satisfying both the displacement and the stress constraints, it is necessary to know completely the displacement and the stress responses of the antenna structure. Once the RMS displacement response is determined using the method described in the previous section, the RMS stress response can next be calculated on the basis of the response values obtained. The displacements are all treated as the enforced joint displacement loads on the structure. The forces and the stresses in the structure resulting from these displacements are then the desired stress responses for design purposes. The static analysis capability of SPAR was employed for this purpose. A block diagram showing the basic operations for these stress computations is shown in Fig. 11.

NUMERICAL RESULTS

Using the finite element model described in the previous section togehter with the proposed mathematical modelling technique, and the finite element program a response analysis for the structure was carried out. A summary of the analysis results produced by the proposed analysis system are given below:

First natural frequency = 15.06 Hz
Maximum RMS displacement = 4.0×10^{-4}m
Displacement = $(\Delta x^2 + \Delta y^2 + \Delta z^2)^{\frac{1}{2}}$
Maximum RMS stress = 5.69×10^{7} Nm^{-2}

The analysis system produces stresses for all the finite elements in the model as well as displacements corresponding to the nodes of the finite element model. Table 1 gives the first eight eigenvalues and the associated natural frequencies. RMS displacement response for the antenna is given in Table 2. Table 3 depicts RMS stresses in the ribs of the antenna structure.

CONCLUSIONS

Dynamic response characterisitcs for a satellite antenna structure subjected to random excitations with power spectral density varying arbitrarily in the frequency domain have been computed. A mathematical model is proposed for describing random excitations of arbitrarily varying power spectral densities and for computing the dynamic response of structures to such excitations.

The model essentially envelopes the power spectral density with linear segments of rising and falling slopes as well as flat portions in decibel versus octave frequency scale. Mean square acceleration response of a typical dynamic system is evaluated using a sample power spectral density of excitation having one segment of rising slope, one flat segment and one segment of falling slope. Experiments were conducted on the same dynamic system under a similar power spectral density input which is synthesized in the same segmental fashion as described in the analytical study. The agreement between the experimentally measured mean square acceleration and that evaluated analytically using the proposed model is quite good.

The response analysis program together with the finite element analysis program SPAR [4] can also be used for computing the dynamic response of other complex structures.

The dynamic response parameters computed for the satellite antenna structure include natural frequencies, mode shapes, displacements and stresses. The parameters are essential for designing the antenna strucutre.

REFERENCES

1. Eringen, A.C., "Response of Beams and Plates to Random Loads", Journal of Applied Mechanics, Vol. 24, 1957, pp. 46.

2. Roberts, J.B., "The Response of a Simple Oscillator to Band Limited White Noise", J. Sound and Vibrations, March 1966, pp. 115-126.

3. Bhat, R.B., Rao, B.V., and Wagner, H., "Structural Respone to Random Acoustic Excitation", Earthquake Engineering and Structural Dynamics, Vol. 2, 1973, pp. 117-132.

4. Wheatstone, W.D., "SPAR Structural Analysis Reference Manual", NASA CR-158970-1, 1978.

5. Giles, G.L. and Haftka, R.T., "SPAR Data Handling Utilities", NASA TM-78701, September 1978.

Table 1

NATURAL FREQUENCIES FOR THE SATELLITE ANTENNA

S.N.	FREQUENCY(Hz)
1	15.063575
2	15.234206
3	15.234261
4	15.420096
5	21.618775
6	22.050751
7	22.837375
8	24.651631

Table 2

RMS DISPLACEMENTS (METER x .0254) AT VARIOUS NODES OF SATELLITE ANTENNA STRUCTURE

NODE	ΔX	ΔY	ΔZ	$\Delta\theta_x$	$\Delta\theta_y$	$\Delta\theta_z$
1	.8451E-08	.1716E-06	.2987E-06	.8512E-08	.2396E-07	.5691E-07
2	.1608E-06	.1570E-06	.3212E-06	.1277E-07	.2478E-07	.7523E-07
3	.7095E-07	.8213E-08	.2756E-06	.1882E-07	.7148E-08	.2338E-07
4	.5700E-07	.5868E-07	.3030E-06	.2377E-07	.1455E-07	.2726E-07
5	.8063E-08	.1044E-06	.2717E-06	.6778E-08	.2025E-07	.3494E-07
6	.1014E-06	.9771E-07	.2969E-06	.1136E-07	.2255E-07	.4689E-07
7	.1931E-06	.7928E-08	.2706E-06	.1765E-07	.9712E-08	.6389E-07
8	.7342E-07	.7543E-07	.3006E-06	.2282E-07	.1191E-07	.3487E-07
9	.1060E-05	.3823E-03	.1454E-04	.4234E-04	.4278E-05	.1402E-03
10	.3558E-03	.3548E-03	.1471E-04	.3408E-04	.3556E-04	.1863E-03
11	.1569E-03	.7719E-06	.8651E-05	.2803E-05	.3674E-05	.5741E-04
12	.1284E-03	.1289E-03	.1865E-04	.2751E-04	.2584E-04	.6763E-04
13	.1056E-05	.2356E-03	.1259E-04	.3466E-04	.4683E-05	.8741E-04
14	.2218E-03	.2207E-03	.1418E-04	.2941E-04	.3125E-04	.1155E-03
15	.4295E-03	.6100E-06	.7583E-05	.3000E-05	.4817E-04	.1569E-03
16	.1640E-03	.1647E-03	.1481E-04	.3060E-04	.2857E-04	.8557E-04
17	.1325E-04	.3222E-02	.9716E-04	.7716E-04	.8888E-05	.3778E-03
18	.3083E-02	.3072E-02	.8467E-04	.7532E-04	.8222E-04	.5066E-03
19	.1318E-02	.1167E-04	.7953E-04	.1191E-04	.4594E-04	.1519E-03
20	.1110E-02	.1116E-02	.1598E-03	.5821E-04	.3568E-04	.1839E-03
21	.1705E-04	.2000E-02	.1176E-03	.3626E-04	.1516E-04	.2409E-03
22	.1918E-02	.1901E-02	.1048E-03	.5667E-04	.7157E-04	.3096E-03
23	.3615E-02	.8601E-05	.6035E-04	.8793E-05	.1141E-03	.4177E-03
24	.1411E-02	.1424E-02	.1214E-03	.6674E-04	.4852E-04	.2286E-03
25	.1887E-03	.1177E-01	.7396E-03	.1151E-03	.3681E-04	.6184E-03
26	.1129E-01	.1113E-01	.6182E-03	.1251E-03	.1572E-03	.8178E-03
27	.4845E-02	.7748E-04	.3173E-03	.2400E-04	.7294E-04	.2579E-03
28	.4001E-02	.4101E-02	.1034E-02	.6898E-04	.8576E-04	.2947E-03
29	.1848E-03	.7243E-02	.7300E-03	.1322E-03	.4488E-04	.3645E-03
30	.7100E-02	.6891E-02	.7458E-03	.4705E-04	.9700E-04	.5179E-03
31	.1238E-01	.8258E-04	.3294E-03	.1950E-04	.1346E-03	.6974E-03
32	.5133E-02	.5274E-02	.6502E-03	.5915E-04	.5933E-04	.3896E-03
33	0.	0.	0.	0.	0.	0.

Table 3

RMS STRESSES x 6.295 x $10^3 Nm^{-2}$ IN THE RIBS OF THE SATELLITE ANTENNA

INDEX	CONNECTED JOINTS		MAX COMBINED P/A + BENDING TENSION	COMP	P/A
1	1	9	133.33	-124.89	4.22
2	2	10	1372.29	0.00	1011.16
3	3	11	183.09	-177.56	2.77
4	4	12	388.69	-381.86	3.41
5	5	13	287.75	-288.25	-.25
6	6	14	0.00	-881.74	-626.09
7	7	15	131.58	-131.79	-.11
8	8	16	279.92	-277.58	1.17
9	9	17	217.72	-169.64	24.04
10	10	18	4614.69	0.00	3739.17
11	11	19	439.56	-397.46	21.05
12	12	20	710.14	-662.12	24.01
13	13	21	669.08	-669.54	-.23
14	14	22	0.00	-2900.09	-2300.03
15	15	23	165.47	-165.62	-.07
16	16	24	350.16	-337.22	6.47
17	17	25	459.26	-23.80	217.73
18	18	26	8252.28	0.00	7226.20
19	19	27	635.35	-473.07	81.14
20	20	28	907.74	-528.61	189.56
21	21	29	877.61	-878.05	-.22
22	22	30	0.00	-5106.76	-4353.49
23	23	31	165.05	-165.58	-.26
24	24	32	280.20	-213.14	33.53

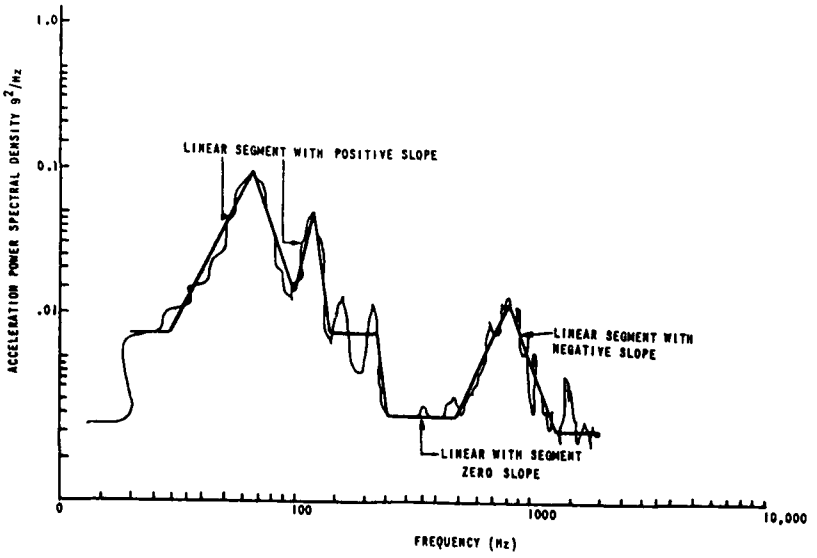

Figure 1: Linear Segments Envelope of the Power Spectral Density Profile

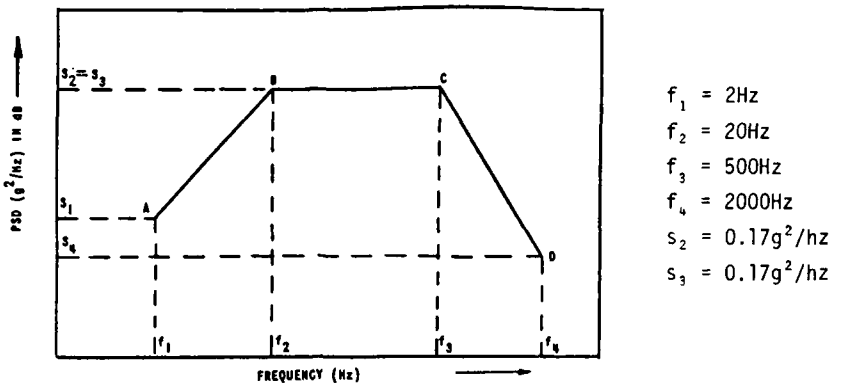

Figure 2: The Input Power Spectral Density Profile for the Antenna

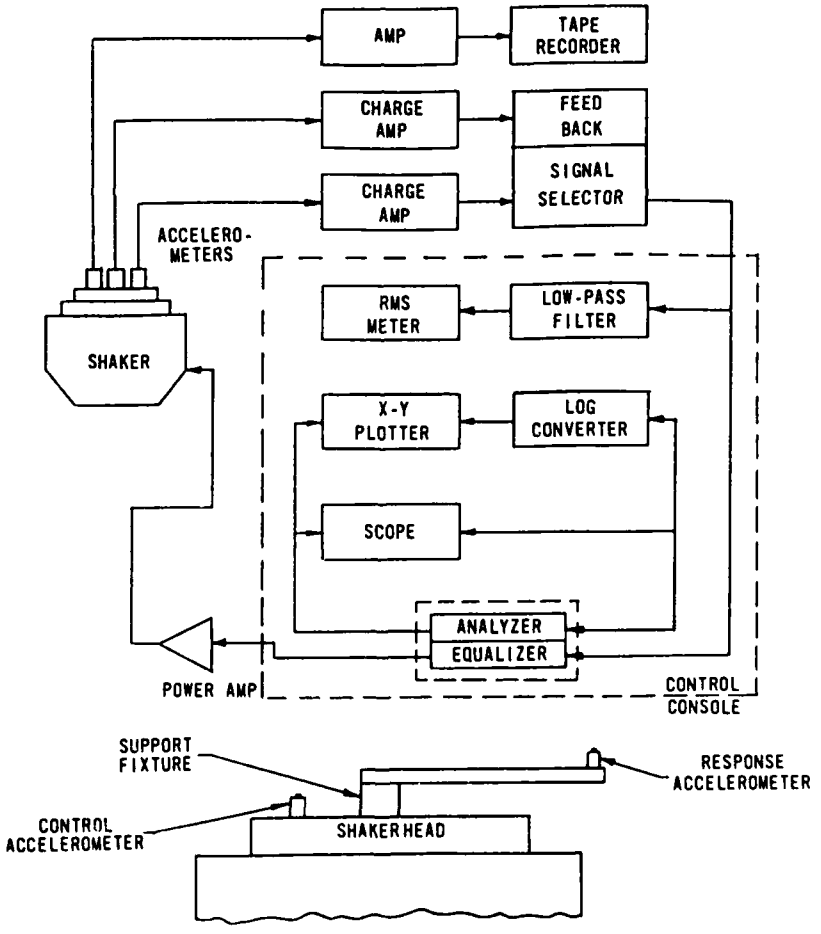

Figure 3: The Experimental Set-Up

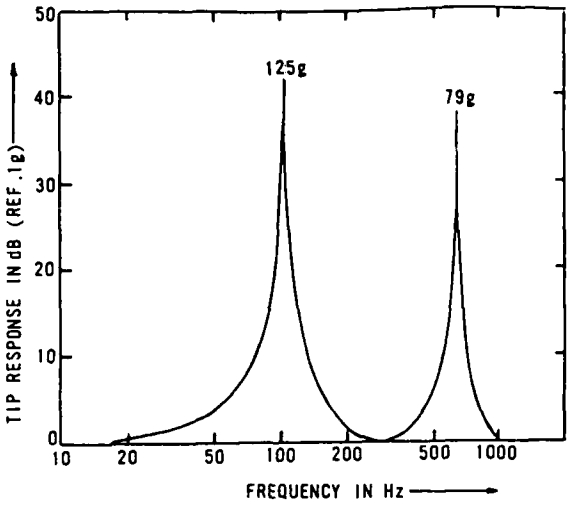

Figure 4: The Frequency Response Plot of the Cantilever Structure

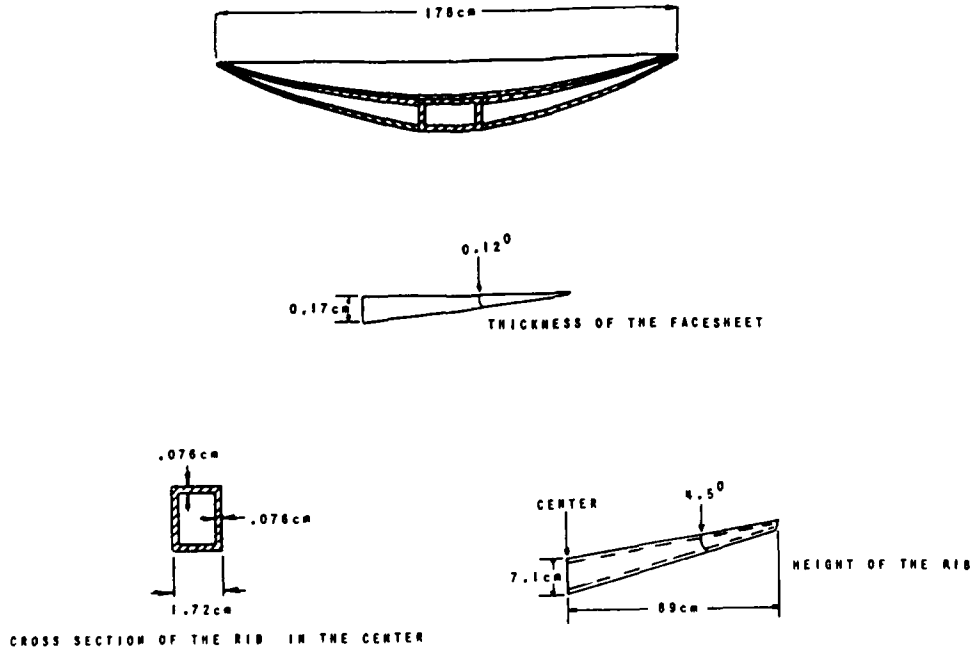

Figure 5: Geometry Details of the Antenna Structure

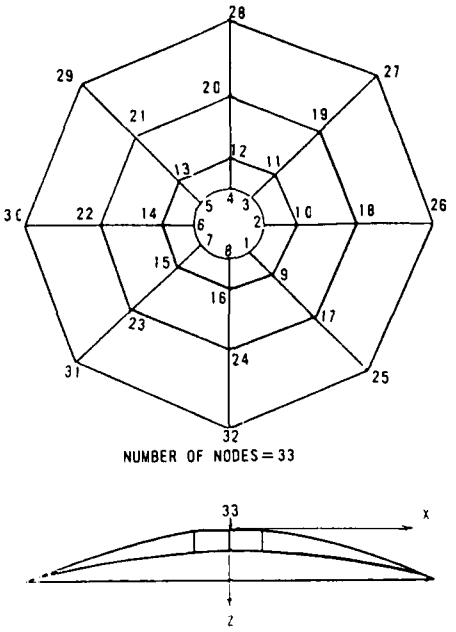

Figure 6: Node Locations - Finite Element Model of the Antenna Reflector

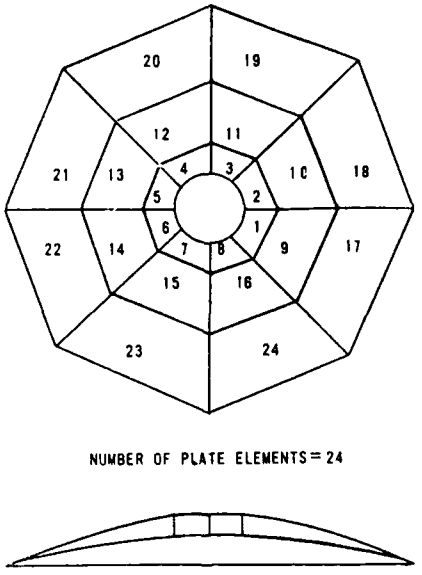

Figure 7: Plate Elements in Finite Element Model of the Reflector

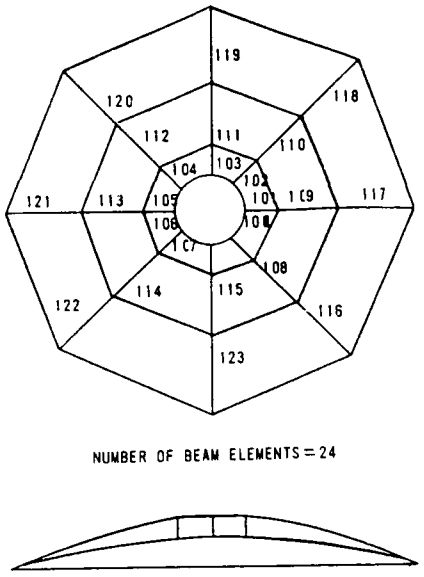

Figure 8: Beam Elements - Finite Element Model of the Antenna Reflector

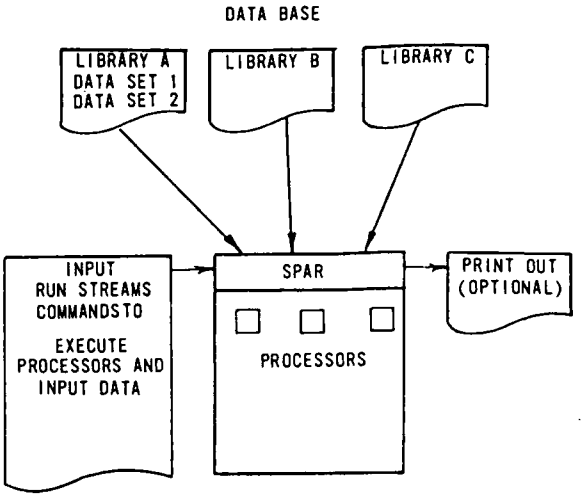

Figure 9: SPAR Program Block Diagram

DISCUSSION

Mr. Lee (U.S. Army Tank Automotive Command): How do you take the PSD of a non-stationary wave point?

Mr. Jha: We assume the power spectral density profile we get is stationary.

INVESTIGATION OF THE ACOUSTIC CHARACTERISTICS OF AIRCRAFT/ENGINES OPERATING IN A DRY-COOLED JET ENGINE MAINTENANCE TEST FACILITY

V. R. Miller, G. A. Plzak, J. M. Chinn
AF Wright Aeronautical Laboratories
Flight Dynamics Laboratory
Wright-Patterson AFB, OH

and

R. J. Reilly
Independent Consultant
St. Paul, MN

A measurement program was undertaken to measure the acoustic environment in an Air Force hush house facility, during the operation of aircraft and uninstalled jet engines to ensure that structural sonic fatigue design limits were not exceeded. Data from external runway operations and other engine test facilities were also compared. The correspondence between noise levels at the hush house deflector ramp and the far-field was examined. The effect of axial distance between jet exhaust nozzle and the hush hush exhaust muffler on acoustic levels inside the hanger was also investigated.

INTRODUCTION AND BACKGROUND

The U.S. Air Force has a continuing concern for reducing the noise created by aircraft engines, both on the ground and in the air. Operational military aircraft are extremely noisy by nature, particularly during take-off and landing. Another major source of airfield noise is from the running of aircraft engines on the ground for maintenance purposes. Since the advent of the jet engine, the Air Force has used attenuators or detuners to reduce this ground-running noise as much as possible.

Since conventional attenuators or mufflers reduced engine exhaust noise by only 20 dB, noise levels around the aircraft were still very high. To avoid creating a nuisance to local inhabitants, ground test facilities were situated as remotely as possible from occupied areas, usually on the opposite side of the airfield runway opposite the maintenance area. Even so, it was often impossible with conventional attenuators to avoid creating a noise nuisance when ground testing aircraft, particularly in adverse wind conditions. Because of the community noise problem, there was a need to prohibit or severly restrict engine testing at night and/or weekends. Protracted engine testing and the prohibition of this work at night and on weekends affected the time to restore an unserviceable aircraft to flight-ready status. Such restrictions are a great hindrance on operational airfields which work a 24-hour day, and on airfields where night-flying necessitates that aircraft be recovered the following day.

The original designs for these noise suppressors were water-cooled and were only usable with the aircraft for which they were designed. This resulted in precision aircraft maneuvering and elaborate measures to maintain aircraft position during engine power changes and burn-off of fuel. Other disadvantages were also encountered. Noise surveys indicated that the close-coupled suppressor did not reduce the noise radiated from unenclosed portions of the fuselage. With wet-cooling, the suppressor exhaust includes not only water vapor, but raw fuel, free carbon, and sulpheric acid vapor as well, creating an unsightly vapor cloud which not only deposited pollutants on other vehicles and buildings, but also adversely affected air quality. This exhaust adversely effected some types of acoustical treatment and supporting structure.

In the mid 1960's a Swedish firm, Nyby, designed a complete aircraft acoustical enclosure, or hush house, for a SAAB Draken aircraft. The enclosure employed an acoustically-treated muffler (augmenter tube) which was sized so that the high velocity of the jet exhaust in the muffler produced an ejector effect which pumped outside air through the enclosure to cool the exhaust gases and eliminated the need for water spray. This same

firm has provided similar hush houses for the SAAB Viggen and F-4K Phantom aircraft.

Study of the Nyby design pointed to a number of operational advantages for the dry, air-cooled complete enclosure concept over the water-cooled attenuators/noise suppressors:

1. Easy installation of the aircraft with few alignment difficulties (since the augmenter must have a large diameter to pump the required cooling flow, close alignment of the aircraft and augmenter is not necessary).

2. Aircraft and operators protected from the weather.

3. Environmentally acceptable (no water spray inquired, so it produces no vapor plume or associated pullution).

4. Noise suppression potential sufficient to permit location of hush house near maintenance areas to allow 24 hour-a-day operation.

5. Low maintenance, since no equipment or support structures are located in the direct jet blast or the hot mixed core flow.

The USAF recognized these advantages and adopted the hush house concept, as adapted by Aero System Engineering, Inc., as the approach for controlling ground run-up noise.

Since aircraft engines can be operated in the hush house at maximum power settings, increased acoustic levels and acoustically-induced stress levels may result. This could cause sonic fatigue damage to aircraft/engine structure or create excessive aircraft equipment vibration and malfunction. Problems of this kind plagued existing water-cooled test facilities for years, particularly in the case of uninstalled engines. Some engines needed vibration bands or an acoustic blanket to prevent structural damage. The potential for premature sonic fatigue damage and/or failures existed since original aircraft structural design criteria did not take into account aircraft operation in hush houses. This potential problem was evaluated by instrumenting critical structure on three different aircraft (F-4E, F-15 and F-16) and one engine (F100-PW-100) with microphones and recording the acoustic levels. Comparisons of measured and allowable structural acoustic stress levels were made to highlight any problem areas which

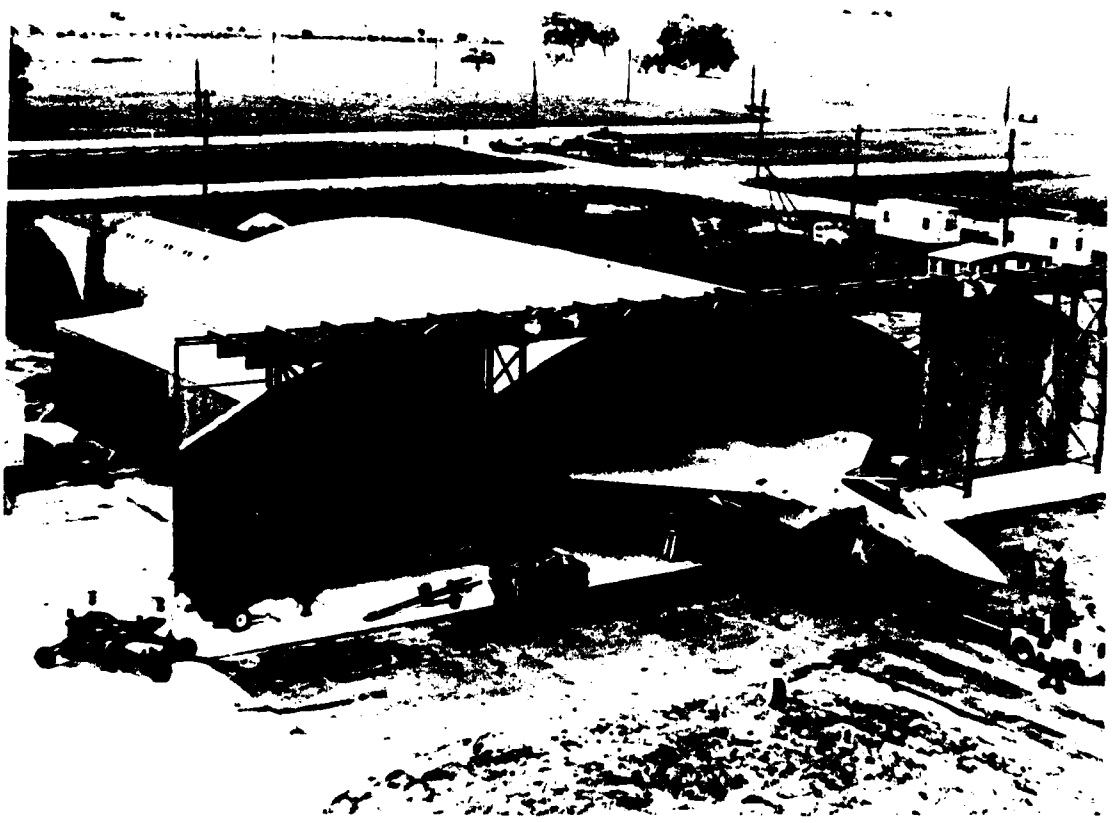

FIG.1 PHOTO OF HUSH HOUSE SHOWING AIRCRAFT INSTALLATION

might exist. Data from external runway operations and engine test facilities were also compared. The correspondence between noise levels at the hush house deflector ramp and the far-field was examined. The effect of axial distance between the jet nozzle and the hush house exhaust muffler on acoustic levels inside the hangar was also investigated.

HUSH HOUSE DESCRIPTION

The hush house used during this program is shown in Figure 1. The major components are shown in Figure 2. This sketch is similar to one found in Reference 8, which has basically the same major components but which are arranged differently. This structure consists of a sound-absorbent hangar with dimensions of approximately 84 by 65 feet (25.6 by 19.8 meter). The inside surfaces of the hangar are covered with approximately 10,500 square feet (975.5m^2) of sound absorbing panels that are 4 inches (10.2 cm) thick with a 20 gauge (0.093 cm) perforated face sheet (304 stainless steel, 16% open area), and filled with a 4.8 lb/ft^3 (76.9 kg/m^3) thermal, fibertype fill. The fiberglass is wrapped in a fiberglass cloth. The hangar fully encloses both uninstalled engines and entire aircraft during ground run-up. The hush house is suitable for testing aircraft of any size and configuration which are geometrically compatible. The aircraft are restrained by tail hooks, wheel chocks, and/or conventional steel cable tie-downs during aircraft run-up.

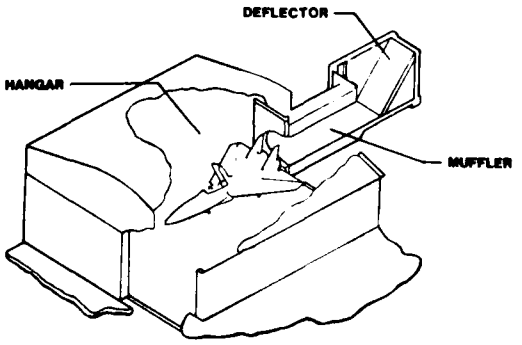

FIG.2 SKETCH ILLUSTRATING HUSH HOUSE COMPONENTS

The inlet areas are located on both sidewalls and allow large air flows and low air velocity past the aircraft or engine under test. The intake system consists of sound-absorbent baffles arranged as a labyrinth, protected by an exterior bird screen. The engine jet exhausts into a muffler or augmenter tube. The air-cooled muffler and the jet engine under test are arranged geometrically to function as a large ejector pump. Large volumes of air are pumped through the intake system, over the aircraft and into the muffler to cool the engine exhaust. The muffler is made in sections, each of which consists of several chambers. Its design allows for thermal expansion by overlapping edges of successive sections. The inner shell is made of perforated and corrugated 321 stainless steel with 4.5 lb/ft^3 (72.1 kg/m^3) Basalt wool fill, 4 inches (10.2 cm) thick placed behind the shell. The exhaust gases leaving the muffler are directed vertically by a deflector.

The hangar area is equipped with roll-down doors for the primary and secondary air inlets on each side and the muffler. This feature is used to shut off outside air in the event of a fire and to maintain a comfortable working environment in the hangar.

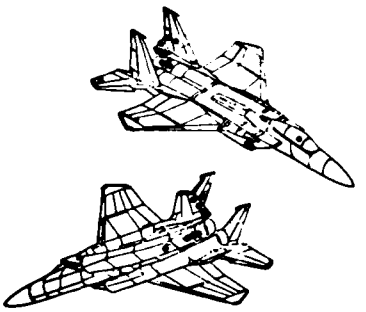

FIG.3 TRANSDUCER LOCATIONS

INSTRUMENTATION

The test instrumentation consisted of microphones which were generally located at the aft end of the aircraft or engine being tested. Surfaces instrumented included nozzles, tails (vertical and horizontal), fuselage, and fairings. Figure 3 shows the general locations which were instrumented on the F-15 aircraft (Ref 1). The microphones were mounted and positioned two inches (5.1 cm) from the surface in question, with their diaphragms pointed toward the surface. The microphones were located as close to rivet lines as possible in order to minimize vibration input. The microphones used were Gulton Industries Model MVA2100 with 5/8 inch (1.6 cm) diameter diaphragms.

Other microphones were located inside the hangar area around the aircraft/engine under test. Another microphone was positioned downstream of the trailing edge of the jet exit deflector ramp outside of the mixing region of the exit flow. Several positions were instrumented by another USAF organization on a 250 foot circle centered at the deflector ramp exit to measure far-field noise levels in the rear quadrant of the hush house.

A mobile data acquisition van contained the signal conditioning electronics and magnetic tape recorders. A landline carried the data signal from each microphone to the van. The signal conditioning equipment was capable of attenuation or amplification in 10dB steps over the range -10dB to +60dB. A time code was produced by a time code generator and recorded on tape. The microphones were calibrated by a B & K Type 4220 pistonphone. The magnetic tape records were played into a frequency analyzer which was interfaced with a computer and plotter.

TEST PROCEDURES

The airplane or engine under test was restrained in a stationary position. For the F-15 and F-4 aircraft, one engine was operated from idle to maximum afterburner power while the second engine was at idle. Engine parameters such as fuel flow, fan turbine inlet temperature, etc., were either recorded or estimated. Surface meteorological conditions during data acquisitions were also recorded. The tests were made with the hangar doors closed. All data were recorded once the engine had stabilized except for the throttle snap runs. A snap is an abrupt movement of the throttle from idle to maximum afterburner.

SONIC FATIGUE LIFE PREDICTION

Tolerable sound pressure levels were established for aft fuselage and empennage external skin panels to verify the ability to withstand the sonic fatigue design load imposed. The analyses which were performed to establish the tolerable levels utilized sonic fatigue design techniques and methods presented by Rudder and Plumblee (Ref 2). These methods are applicable to skin/stringer, honeycomb, composite, box, wedge, and corrugated structures. The aircraft/engine structure was analyzed for sonic fatigue using loads predicted for the composite mission profile, ground operation, and the maximum flight envelope.

The analytical prediction criteria used were based on the following assumptions:

1. The temperature over the surface of a panel was uniform.

2. The substructure is temperature dependent.

3. The most damaging structural response occurs at the fundamental mode frequency of the panel.

4. The excitation force is random amplitude broadband noise.

5. The damping ratio of the structure is 0.016.

6. Panel edge conditions are between simply supported and clamped.

The following steps were followed to predict the allowable noise levels (Ref 3):

1. Determine panel physical properties.

2. Calculate panel fundamental response frequency.

3. Establish stress concentration factors.

4. Obtain mission profile to establish life criteria and cycles to failure.

5. Determine dynamic stress level from appropriate random S-N (dynamic stress - cycles to failure) curve.

6. Apply Miner's Rule to account for multiple loading, if applicable.

7. Calculate allowable sound pressure level.

8. Adjust allowable level for curvature when necessary.

Although these are the basic steps, the actual details of each step can be quite involved. For example, when the resonant frequency and acoustic level must be corrected for curvature effects, various techniques are used to calculate the random rms stress according to the type of structure. Appropriate random S-N curves concentration, temperature, and mean stress effects.

Structural drawings were reviewed to determine panel physical properties. From the drawings, the panel size (length and width), thickness (chem-milled and land), material, method of attachment, curvature, fastener size, fastener spacing, etc., were determined. The chem-milled panel size was used for the frequency calculation. The calculation of the allowable acoustic level was based on the rms stress at the chem-milled radius. The rivet line panel dimensions were used to calculate the panel frequency with the allowable acoustic level based on the rms stress at the rivet line. When skin thickness and material were different from one side to the other, both were evaluated.

Knowing the physical properties of the panels, the panel fundamental frequency could be determined. These frequencies were corrected for curvature effects. The panel frequency was then used in the allowable acoustic spectral computation.

A stress concentration K_t factor was determined for chem-milled radii and for the rivet line as influenced by the condition of the fastener holes. These K_t factors were used to adjust the random fatigue curves for the material to obtain the stress value. Fastener

types were of the rivet, driven or non-driven type. Fasteners on the panels were not always the same. Differences occurred in the size of the fasteners, the spacing between fasteners, and the type of fastener (rivet, etc.). Those which produced the greatest K_t factor and thus the most critical root-mean-square stress were chosen for the computation of the allowable noise level.

Random fatigue curves used to determine rms dynamic stress were based on results using broadband random amplitude excitation. These curves should not be confused with the damage stress S-N curves (i.e., sinusodial) defined in structural handbooks. Random fatigue curves give the dynamic rms stress for chem-milled panels and at the rivet lines for a number of "R" factors (minimum stress divided by the maximum stress). The effect of combined environments (temperature, pressure differential, etc.) is accounted for by super-position of the individual stresses when calculating the "R" factor. This then defines the appropriate S-N curve to be utilized for the cycle loading calculations. If there is no thermal or steady mean stress, i.e., zero mean, then "R" = -1. The allowable acoustic level was adjusted when curvature existed. The allowable levels were determined using the following equation from Reference 2:

$$\tilde{\sigma}_x = 1.62 \times 10^{-4} \left(\frac{E}{\gamma}\right)^{\frac{1}{4}} \frac{a^{1.25}}{h^{1.75}} \frac{\Phi(f)}{\zeta^{.56}} \frac{(b/a)^{1.75}}{(AR)^{.84}} \qquad (1)$$

where $\tilde{\sigma}_x$ - dynamic stress - ksi_{rms}

E - modulus of elasticity - psi

γ - mass density - lb. $sec^2/in.^4$

a - panel short dimension - inch

b - panel long dimension - inch

$\Phi(f)$ - acoustic power spectral density of fundamental frequency - psi^2/Hz

h - skin thickness - inch

ζ - fundamental mode damping ratio - dimensionless

AR - aspect ratio function = $3\ (b/a)^2 + 3\ (a/b)^2 + 2$ - dimensionless

The design nomograph based on equation (1) is presented in Figure 4. The appropriate random fatigue curve must be inserted into this figure to make it complete. It should be noted that the positioning of the appropriate S-N curve in this figure is not a simple matter. The S-N curve can not be placed straight forwardly on the basis of nomograph-derived stress.

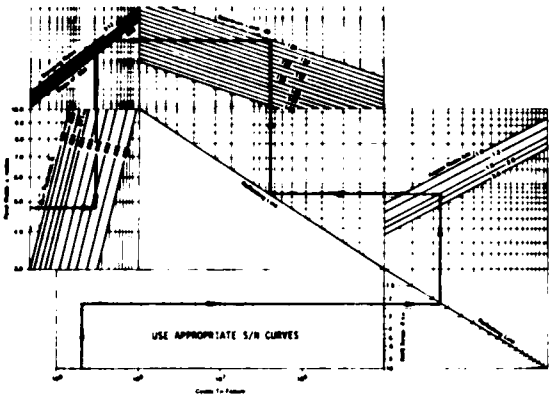

FIG.4 RANDOM DYNAMIC STRESS NOMOGRAPH

TEST RESULTS AND COMPARISONS

Octave band sound pressure levels (SPL) which should not be exceeded for aircraft/engine structure were generated by the methods described above. A typical set of allowables are shown in Table 1 (Ref 4). These limits are specifically for the F-16 aircraft. Each aircraft or engine has its own set of allowables. Levels mush greater than the allowables could cause sonic fatigue of the structure. Measured SPL's with the engine at maximum afterburner power are plotted on Figure 5. Data are included from two measurement locations. Also plotted are the corresponding maximum allowable noise levels from Table 1. The measured data are 6-18dB below the maximum allowable noise levels. This trend was generally true at all measurement locations investigated. Consequently, no aircraft/engine structure sonic fatigue problems are anticipated from operation in the hush house.

An interesting result occurs when comparing the hush house SPL's measured at maximum afterburner, with levels obtained during ground run-up on a concrete pad (Ref 4). Figure 6 shows that for frequencies below 1000 hertz the hush house levels are as much as 10dB below those for ground run-up. This reduction is attributed in part to the hush house muffler. The low frequency portion of the spectrum is generated well downstream of the engine nozzle in the case of freefield operation. It is conjectured that the muffler, which is sound absorbent, also modifies the aerodynamic development of the jet interaction zone and prevents large scale vortex motion with its attendant low frequency pulsation.

The noise field around an aircraft in a hush house is not necessarily less when compared

TABLE 1 SOUND PRESSURE LEVEL LIMITS FOR AIRCRAFT STRUCTURE-dB Re 0.00002 Pa(REF.4)

Structure	Octave Band Center Frequencies (Hz)							
	63	125	250	500	1000	2000	4000	8000
Engine Nozzle	134	141	145	148	150	152	158	155
Upper Fus Skin F.S. 479-494	136	143	143	145	145	146	146	147
Lower Fus Skin Aft of ECS Dump	140	145	149	151	154	155	151	151
Rudder Act Fair Aft Closure	136	140	140	141	143	143	144	144
Upper Outlet Fus Skin F.S. 446-463	136	145	145	145	145	146	146	147
H.T. Act Access Cover	141	146	150	152	152	152	152	152
Engine Access Doors	137	142	146	146	146	147	147	148
Upper Fus Access Cover 16B6505	137	142	146	146	146	147	147	148
Upper Fus Skin F.S. 390-400	136	143	145	145	145	146	146	147
Fiberglass Fairing at Base of V.T.	137	142	146	146	146	147	147	148
Rudder Act Access Panel	136	140	140	141	143	143	144	144

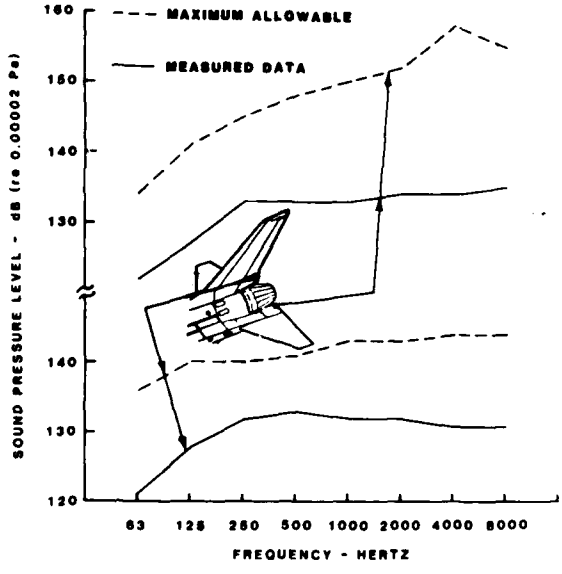

FIG. 5 COMPARISON OF MEASURED HUSH HOUSE DATA WITH MAXIMUM ALLOWABLES

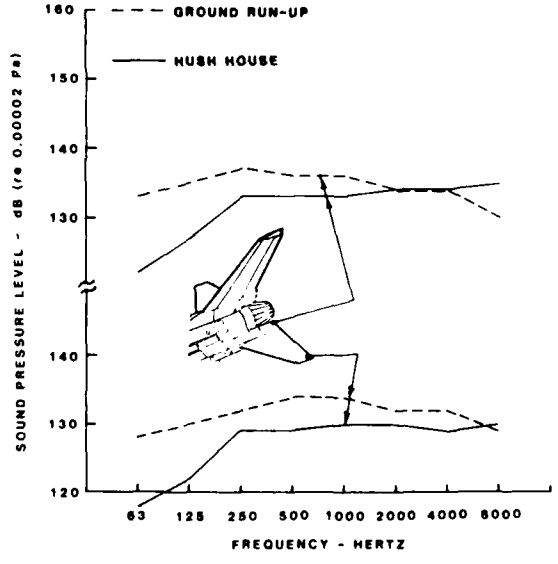

FIG. 6 COMPARISON OF OCTAVE SPL MEASURED IN HUSH HOUSE AND GROUND RUN-UP

to ground run-up data measured for similar conditions and microphone locations. Figure 7 illustrates a case in point. This figure presents data near the F-4E wing tip from Reference 5 which compares ground run-up SPL at maximum afterburner with that measured in a dry-cooled hush house, of a different design, at a naval air station. The ground run-up data are actually less in the range of 63 to 4000 hertz, with a difference of 2dB in the overall level. Other research has shown similar differences with the same hush house (Ref 6). Shown for comparison purposes are measured data for the Air Force hush house (Ref 5). Note that the sound pressure levels for the Air Force hush house below 1000 Hz are within 1dB of the ground run-up data and 2 to 4dB less than the Navy hush house. This could be significant from a structural response standpoint since noise levels much greater than those measured during ground run-up could cause sonic fatigue problems with aircraft structure. It

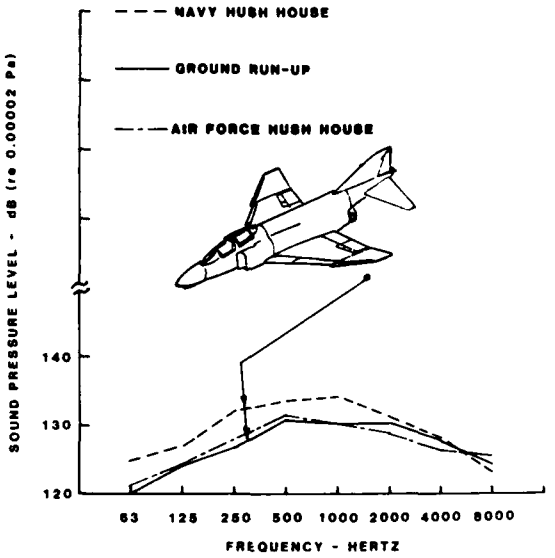

FIG. 7 COMPARISON OF OCTAVE SPL MEASURED IN TWO HUSH HOUSES AND GROUND RUN-UP

is worth noting that the Navy hush house consists of flat plane side walls and roof panels with a forward inlet location. The Air Force hush house has a curved, arched roof with sidewalls containing the inlets (acoustically treated labyrinth) and flat panels only at the end walls.

The same two measurement locations shown in Figure 6 were used to obtain a comparison between hush house data and data for an existing water-cooled noise suppresor (Ref 4).

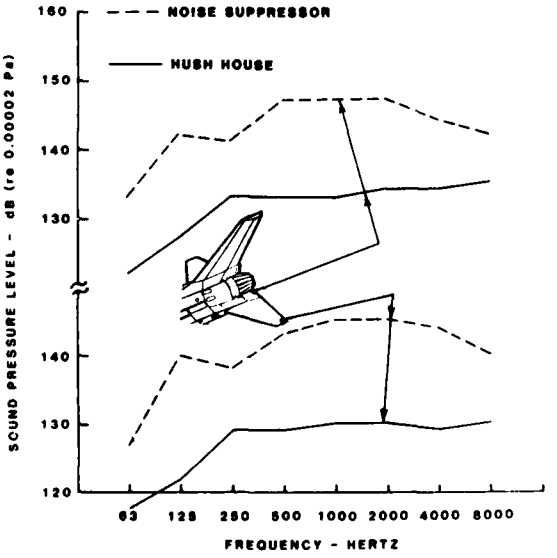

FIG. 8 COMPARISON OF OCTAVE SPL MEASURED IN HUSH HOUSE AND WATER-COOLED NOISE SUPPRESSOR

The noise suppressor SPL in Figure 8 is greater across the entire spectrum by 5 to 15dB. This increase could be important from a sonic fatigue and structural response standpoint. Some of this increase is due to the smaller size of the noise suppressor, where the walls are closer to the microphones than in the hush house.

An increase in the acoustic environment will produce a corresponding dynamic stress increase on the aircraft structure. For example, a 3dB increase in acoustic loading corresponds to 41 percent increase in dynamic stress. Stress increases of this magnitude will decrease the life of a typical aluminum stiffened panel. Increases in sound pressure level can also cause problems with equipment and avionics. Equipment on-board an aircraft may not be qualified to the noise levels reached during hush house operation and may be sensitive to acoustic excitation. Equipment could respond in such a manner that would modify or possibly disrupt its mode of operation or even result in mechanical failure.

Figure 9 shows the correspondence between measured afterburner data at the engine exhaust (Ref 4), at the hush house jet exit deflector ramp (Ref 4), and at a far-field

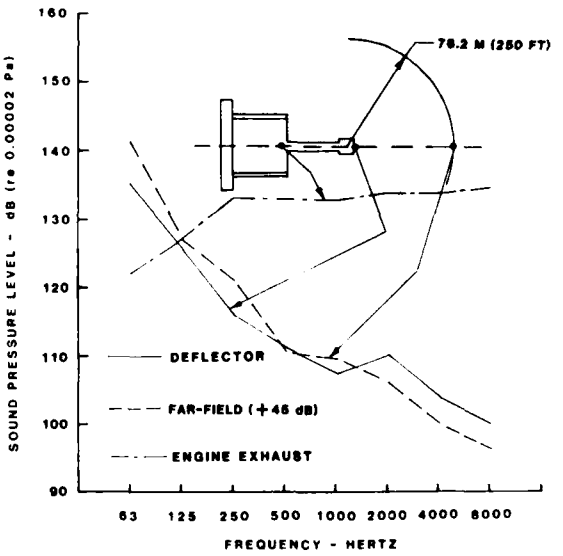

FIG.9 SIMILARITY BETWEEN ENGINE EXHAUST NOISE, DEFLECTOR RAMP NOISE AND FAR-FIELD NOISE

position on an arc 250 feet (76.2 meters) behind the ramp (Ref 7). For this comparison 45dB was added to the sound pressure levels measured at the far-field position to account for the spreading of the acoustic waves. Shifting the far-field sound spectrum in this way shows the similarity with the deflector ramp spectrum. The general character of the noise at the deflector ramp's trailing edge is seen to be similar to the far-field noise over the entire

frequency range.

There are several factors that affect the sound pressure level in the interior of the hush house. The attenuation of the muffler affects the SPL due to the wall impedence of the lining. The amount and type of acoustical materials on the ceiling and walls of the hush house interior provide sound absorption which can influence the acoustic energy. The volume of the enclosure also has an effect. One parameter that influences the SPL directly is the jet nozzle axial position relative to the entrance of the muffler. The distribution of sound between the hush house interior and the muffler varies with the distance between the nozzle exit and the muffler inlet. The low frequency noise which is generated downstream of the nozzle inside the muffler propagates mostly down the muffler and into the atmosphere. The high frequency noise that is generated near the nozzle radiates into the hush house interior. Noise levels in the interior will increase with increasing axial distance (distance between nozzle and muffler inlet) according to the results of a model study (Ref 8). The radial position of the engine exhaust to longitudinal axis of the muffler also has an effect, but, according to Reference 8, is not as important as the axial distance correction. Consequently, this effect will not be considered here. The effect of nozzle axial distance on the noise level near the engine exhaust was examined in the hush house tests.

Measured data from the F-15 and F-16 aircraft, which are powered by the F100 engine, as well as data from an uninstalled F100-PW-100 engine are presented in Figure 10. (The F-15 has two F100-PW-100 engines while the F-16 has one F100-PW-200 engine. The only significant difference between the engines is that the F100-PW-200 has a backup fuel control system while the F100-PW-100 does not.) This figure presents octave band sound spectra measured at the engine exhaust during maximum afterburner operation. The comparison between the F-15 and F-16 (lower curve) shows the changes in the spectrum with changing axial distance (X) of the nozzle from the muffler inlet. Since the F-15 nozzle is located farther from the muffler, the F-15 spectra should be higher than the F-16 according to Reference 8. Inspection of the spectra shows this to be generally true except in the very lowest octave bands.

Special considerations must be made when making comparisons between the F100-PW-100 Placing an engine in an airframe requires that an air inlet duct be attached to the engine. Although the engine air inlet duct is not a performing part of the engine, it affects the engine thrust or power output by causing some inlet air pressure losses or distortions which, in turn, affect the thrust and exit velocity of the engine. Since exit velocity controls the sound power output of the jet, a change in exit velocity caused by placing the engine in an airframe will affect its resultant

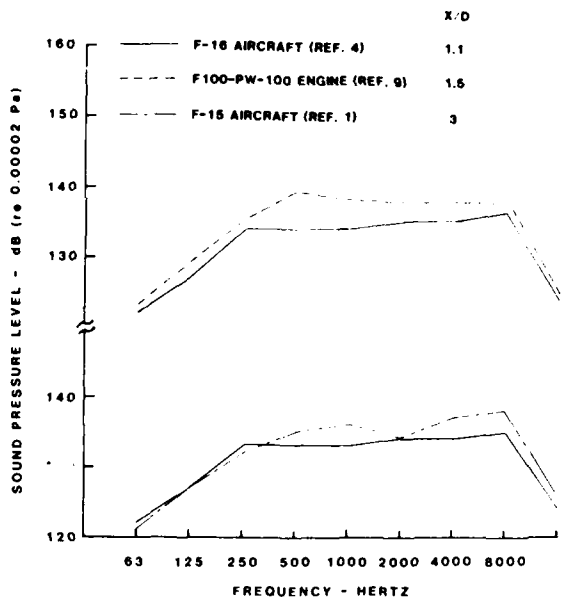

FIG.10 COMPARISON OF OCTAVE SPL MEASURED IN HUSH HOUSE NEAR ENGINE EXHAUST PLANE

SPL. This change in SPL is given by (see Ref 12):

$$\Delta dB = 65 \log (V_i/V_o) \qquad (2)$$

where ΔdB = change in SPL, dB ref 0.00002 Pascal

V_i = exit velocity of F100 engine when placed in an airframe, feet/second

V_o = exit velocity of F100-PW-100 engine when uninstalled, feet/second

The thrust of the F100-PW-100 engine in the installed condition at maximum afterburner is approximately 24,000 lb_f at sea level standard day conditions. The F100 engine under similar conditions but installed in an F-16 airframe yields about 19,400 lb_f of thrust. Using equation (2) and knowing that the exit velocities corresponding to the thrust values given are 3400 and 3100 feet per second for the F100-PW-100 engine and F-16 aircraft, respectively, the predicted ΔdB is -2.5dB. This means that the difference in SPL between the spectra for the F100-PW-100 and F-16 is predicted to be 2.5dB. This assumes that the axial distance is approximately the same for both engine and aircraft, which it is (X/D = 1.1 for the F-16, X/D = 1.5 for the F100-PW-100). A comparison of the upper curves in Figure 10 shows that the differences are 1 to 4dB across the frequency range shown, which is in good agreement with the predicted value.

The prediction of the noise field in the hush house is important since it provides a way to calculate the SPL impinging on structure. Room (geometrical) acoustics should give satisfactory results for the hush house in the mid and high frequencies since the room dimensions are large compared to the characteristic wave length of the noise considered. The formula given to calculate the SPL in the hush house, assuming all the reflection terms comprise a diffuse field, is (Ref 10):

$$SPL = PWL + 10 \log \left(\frac{Q}{2\pi r^2} + \frac{4}{R} \right) + 10$$

(dB ref 0.00002 Pascal) (3)

where PWL = Sound power level - dB ref 10^{-12} watt

Q = Directivity factor of the source - dimensionless

r = Distance from the source to point of interest - ft

R = Room constant = $S\bar{\alpha}$ - ft^2

S = Total area of all surfaces inside hush house - ft^2

$\bar{\alpha}$ = Average sound absorption coefficient of surfaces inside hush house

The directivity factors are from Reference 11 and were measured under free field conditions. Q may increase or decrease from the value in free space because of reflections from nearby surfaces. It is assumed, however, that the directivity is not altered by the hush house. $\frac{Q}{2\pi r^2}$ describes the direct sound field diverging from the source while $\frac{4}{R}$ describes the reverberant sound field associated with reflections from the walls, floor, and ceiling. The reverberant sound field dominates at locations far from the source. Conversely, very close to the source, the direct sound field will dominate and determine the SPL. Some typical values for the sound absorption coefficient vary from 0.6 at 63 HZ and 0.7 at 125 Hz to 0.9 and greater at 250 HZ and above.

Predictions of the SPL at two positions in the hush house are shown in Figure 11. These predictions are based on equation (3) and the corrections for engine location with respect to the muffler inlet X/D given in Reference 8. Sound power level and directivity factor data were obtained from Reference 11. Measured data are also shown, and the predicted values compare favorably with the measured data except in the very lowest and highest frequencies.

The low frequency response of the hush house cannot adequately be predicted by room acoustics as evidenced in Figure 11. A more adequate but more difficult approach is that based on wave acoustics, i.e., the motion of waves in a bounded space. The mathematics of wave acoustics has been applied to problems of room acoustics in simple enclosures and has been used to supplement results predicted by the more conventional equations of geometric acoustics (such as equation (3)). These conventional equations are normally unreliable in the low frequencies.

The hush house interior may be treated as a complex resonator having numerous modes of vibration, each with its own characteristic frequency. When a jet engine is operated in the hush house, a steady-state vibration having the frequency of the source is set up, together with the normal vibration modes in the interior. The characteristic frequencies of vibration in the interior depend on the shape and size of the interior. The effect of the position of the source and/or receiver is also important.

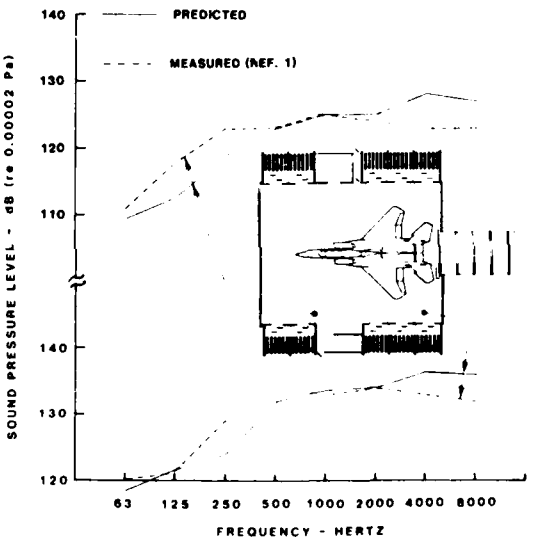

FIG. 11 COMPARISON OF PREDICTED AND MEASURED SPECTRA IN HUSH HOUSE AT MAXIMUM AFTERBURNER

The deviation in the higher frequencies is not entirely understood at this time. Air inlets which are a part of the intake system line the walls on either side of the aircraft under test. This intake system has a series of sound absorbant baffles arranged as a labyrinth. This arrangement creates a series of cavities which appear to make the hush house more sound absorbant than was predicted, therefore resulting in over predictions in the high frequencies. It is also possible that the discrepancies between the measured and predicted values can also be attributed, in part, to errors in the directivity (which was assumed to be the same as free field).

SUMMARY AND RECOMMENDATIONS

No structural damage due to sonic fatigue is anticipated with aircraft structure in the Air Force hush house. Measured hush house sound pressure levels on aircraft structure are less than those measured in water-cooled noise suppressors and open field ground run-up. Hush house noise levels increase as the axial distance between the jet nozzle and the muffler inlet increases. The distribution of energy depends on this axial distance. Aircraft installed equipment qualification levels should be checked against the hush house sound pressure levels to determine if equipment are qualified for this type of environment.

REFERENCES

1. Miller, et al, "Acoustic Measurements of F-15 Aircraft Operating in Hush House, NSN 4920-02-070-2721," AFWAL-TM-81-82-FIBE, AD A109828, September 1981.

2. Rudder and Plumblee, "Sonic Fatigue Design Guide for Military Aircraft," AFFDL-TR-74-112, May 1975.

3. Johnson, "F-4 aft Fuselage and Empennage Allowable Acoustic Noise Levels," MDC Report A6196, October 1979.

4. Miller, et al, "Acoustic Measurements of F-16 Aircraft Operating in Hush House, NSN 4920-02-070-2721," AFWAL-TM-81-83-FIBE/FIBG, AD A109829, September 1981.

5. Miller, et al, "Acoustic Measurements of F-4E Aircraft Operating in Hush House, NSN 4920-02-070-2721," AFWAL-TM-81-84-FIBE/FIBG, AD A 109827, September 1981.

6. Holehouse, "Sonic Fatigue of Aircraft and Submarine Structure," Rohr Industries Report 81-041, April 1981.

7. Lee, "Far-Field Acoustic Data for the Texas ASE, Inc. Hush House," AFAMRL-TR-81-148, April 1982.

8. Grunnet and Ver, "Aerodynamic and Acoustic Tests of a 1/15 Scale Model Dry Cooled Jet Aircraft Run-up Noise Suppression Study," FluiDyne Engineering Corp., October 1975.

9. Miller, et al, "Acoustic Measurements of the F100-PW-100 Engine Operating in Hush House, NSN 4920-02-070-2721," AFWAL-TM-81-133-FIBE, AD A 108814, September 1981.

10. Beranek, Noise and Vibration Control, McGraw-Hill, New York, 1971.

11. Powell, "USAF Bioenvironmental Noise Data Handbook: F-15A Aircraft, Near and Far Field Noise," AMRL-TR-75-70, Vol. 63, November 1975.

12. Hermes and Smith, "Measurement and Analyses of the J57-P21 Noise Field," AFFDL-TR-66-147, November 1966.

CRITERIA FOR ACCELERATED RANDOM VIBRATION TESTS WITH NON-LINEAR DAMPING

Ronald G. Lambert
General Electric Company
Aircraft Equipment Division
Utica, New York 13503

Closed form analytical expressions have been derived which relate the parameters for accelerating Gaussian random vibration tests such that the fatigue damage accumulated is the same for both the accelerated and non-accelerated cases. The same failures, only sooner, is the objective. Non-linear structural damping, the significant parameter considered, was chosen for its practical importance. Numerical examples are included.

INTRODUCTION

It is typically of great interest and practical importance to accelerate a Gaussian random vibration qualification or acceptance test of an electronic black box in the laboratory from the actual service conditions.

The test duration is compressed by a relatively large factor (e.g. 100 or 1,000) with an attendant increase in the applied vibration level. The applied vibration level is expressed both in terms of acceleration power spectral density and acceleration rms value. The resulting cumulative fatigue damage at each input vibration level does not necessarily mean structural facture or failure. It means that useful life is being consumed and indicates the potential, large or small, for failure.

The derived equations calculate the appropriate increase in vibration levels as functions of the desired test duration compression factor, the structural assembly's damping linearity term, and the critical material's ductility. These equations are of power law form.

The damping linearity term proves to be a significant factor as the vibration input level is increased. Its influence is twofold. First, it causes a non-linear increase in the rms stress level of a critical structural element. Secondly, it causes an alteration in the material's fatigue life for a given rms stress level. The first effect is due to the fundamental definition of the damping linearity term. The second effect is due to the skewing of the stress peak envelope probability density function in the important stress peak region of two-to-four times the rms stress level.

This paper shows the criteria for selecting the form of the input vibration level-duration relationship and assigning values to the parameters.

CRITICAL STRUCTURAL ELEMENT

Black box structural elements (e.g. solder joints, wires, device leads, support structures) that are subjected to random vibration will always accumulate some amount of fatigue damage. Each structural element typically will accumulate damage at a rate different from the other elements and will have its own test level acceleration factor. The derived acceleration criteria expressions apply to a single structural element. In general the single acceleration factor chosen for the test of a relatively complex structural assembly is the one corresponding to the critical structural element (i.e. the element that accumulates the most damage). Alternative methods for including the less critical elements are discussed in a later section.

GENERAL FATIGUE CONSIDERATIONS

It will be shown in a later section that curves of equal cumulative fatigue damage have the same slope as the material's fatigue curve. Fatigue curve parameter values are readily available from many published sources (e.g. MIL-HDBK-5C, SAE J1099). Therefore it is useful to work with fatigue curve parameters for determining test acceleration factors whether or not large fatigue damage is accumulated. The sinusoidal stress "S-N" fatigue curve forms the basis of parameter values. The classical random stress fatigue curve treats the linear damping case. The random stress, non-linear damping fatigue curve expression can be used for both linear and non-linear damping cases.

SINUSOIDAL FATIGUE CURVE

A material's sinusoidal (i.e. cyclic) fatigue S-N curve parameter is used in all of the developed expressions and is as follows:

$$S = A\ N_s^{-1/\beta} \quad (1)$$

where S = applied sinusoidal stress cyclic amplitude
A = material constant; true cyclic ultimate stress
$A = 2^{-1/\beta}\sigma'_f$ (stress units) (2)
N_s = applied stress cycles to failure
β = 1/b = slope parameter (3)
σ'_f = fatigue strength coefficient
b = fatigue strength exponent

Values of σ'_f and b are tabulated in reference [1] for various materials. Table 1 lists typical fatigue curve constants. Refer to the symbols section for Metric - Conventional Units conversion. Equation (1) is a reasonable approximation for most structural materials.

TABLE 1. TYPICAL FATIGUE CURVE CONSTANTS

MATERIAL	β	$\bar{A}$		$\bar{C}$	
		(MPa)	(ksi)	(MPa)	(ksi)
Aluminum Alloy 6061-T6	8.92	756	110	343	50
Copper Wire	9.28	565	82	254	37
Aluminum Alloy 7075-T6	9.65	1238	180	551	80
Soft Solder Tin-Lead (63-37)	9.85	105	15	47	7
4340 (BHN 243)	10.5	1124	163	484	70
Magnesium Alloy	22.4	299	43	94	14

CLASSICAL RANDOM FATIGUE CURVE

The classical random stress case involves a narrow-band Gaussian process of zero mean value and standard deviation (i.e. rms) value of σ to represent the instantaeous stress. The positive envelope of this Gausian process is represented by a Rayleigh probability density function. Using Miner's Cumulative Damage Rule it can be shown [2] that the Classic Random Fatigue curve is as follows:

$$\sigma = C\ N_f^{-1/\beta} \text{ (stress units)} \quad (4)$$

where σ = rms stress value
C = material constant
N_f = median number of random stress cycles to failure
β = slope parameter from material's S-N curve

$$C = \left[\frac{A}{\sqrt{2}}\right]\left[\Gamma\left(\frac{\beta}{2}+1\right)\right]^{-1/\beta} \text{ (stress units)} \quad (5)$$

$\Gamma(\alpha)$ = Gamma Function [3]

Typical sinusoidal and random fatigue curves are shown in Figure 1.

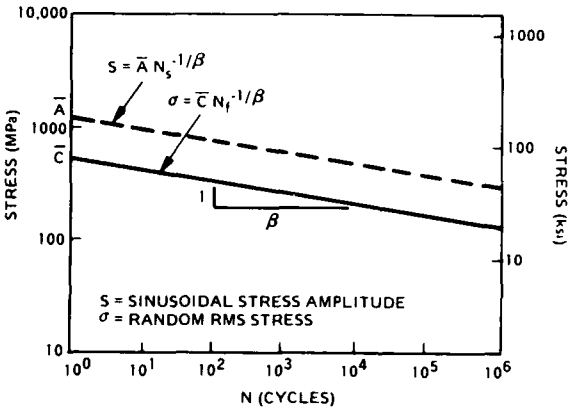

Figure 1. Typical Sinusoidal and Random Fatigue Curves

DAMPING LINEARITY TERM

The fatigue process is directly related to the value of rms stress σ at a structural element inside a black box. It is usually more convenient for test purposes to use the black box input vibration rms aceleration level $\ddot{X}$ or acceleration spectral density W in equations that relate σ to $\ddot{X}$ as follows:

$$\sigma = C_1 \ddot{X}^{\eta} \quad (6)$$

σ = rms stess level (stress units)
C_1 = constant (stress units per g)
$\ddot{X}$ = rms acceleration level (g)
η = damping linearity term

This relationship is linear for $\eta = 1$. It will be shown in Appendix A that $\eta < 1$ for internal stress-strain hysteresis or viscoelastic damping mechanisms and that $\eta > 1$ for coulomb friction damping mechanisms. Damping mechanisms for which $\eta \neq 1$ are considered to be non-linear mechanisms. Experimental values for η are presented in a later section.

The vibration input rms acceleration level $\ddot{X}$ is related to the acceleration spectral density W (also commonly refered to as power spectral density PSD) as follows:

$$\ddot{X}^2 = \int W(f)\, df \quad (g^2) \quad (7)$$

W(f) = acceleration density as a function of vibration frequency f (g^2/Hz)

For simplicity in the analysis, the value of W(f) will be taken to be a constant value W across the structural element resonance stress response bandwidth. Thus, $\ddot{X}$ is proportional to the square root of W:

$$\ddot{X} = C_2 W^{1/2} \quad (g) \quad (8)$$

C_2 = constant (square root of Hz)

$$\sigma = C_3 W^{\eta/2} \quad (9)$$

C_3 = constant

The methods described are not limited to a constant PSD curve as implied by equations (8) and (9).

Figure 2 shows a typical σ - $\ddot{X}$ relationship for several values of η with C_1 = 1.0 ksi/g in equation (6). It can be seen that there is a non-linear increase in the rms stress level of the critical structural element as the vibration input level is increased for η = 1.2.

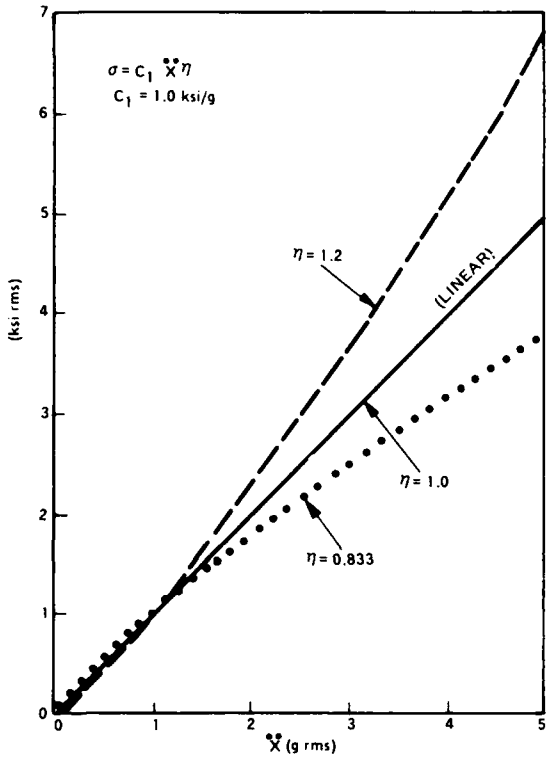

Figure 2. Typical σ - $\ddot{X}$ Relationships

The approach described is not necessarily limited to a single degree-of-freedom system as implied by equations (6), (20), and others in the Appendix. The single degree-of-freedom system is presented for clarity and simplicity in the development of the equations.

NON-LINEAR RANDOM FATIGUE CURVE

It is shown in reference [4] that non-linear damping causes an alteration of the critical material's random stress fatigue life relative to the linear case. This is due to the skewing of the Rayleigh stress peak envelope probability density function in the important stress peak region of two-to-four times the rms stress level. Most fatigue damage occurs in this stress level region [2]. Relative to linear damping the stress peaks will be either accentuated or de-emphasized depending on whether η is greater or less than unity, respectively.

The general linear/non-linear damping random stress fatigue curve equation is as follows:

$$\sigma = C_m N_f^{-1/\eta\beta} \text{ (stress units)} \qquad (10)$$

where σ = rms stress value
C_m = material constant
N_f = median number of random stress cyles to failure
β = slope parameter of material's S-N curve
η = damping linearity term

$$C_m = \left[\frac{A'^{/\eta}}{\sqrt{2}}\right]\left[\Gamma\left(\frac{\eta\beta}{2} + 1\right)\right]^{-1/\eta\beta} \text{(stress units)} \quad (11)$$

$\Gamma(\alpha)$ = Gamma Function [3]

Figure 3 shows fatigue curves for 7075-T6 Aluminum Alloy for several values of damping linearity. It can be seen that the fatigue life, N_f, is altered as a function of η for a fixed value of rms stress σ.

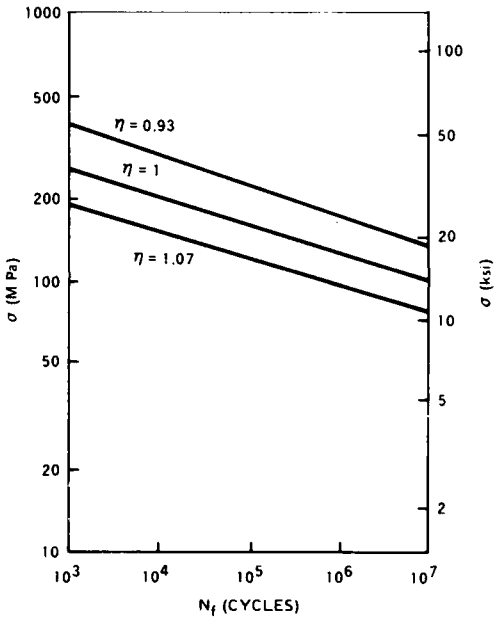

Figure 3. Fatigue Curves for Several Values of η; 7075-T6 Aluminum Alloy

CUMULATIVE FATIGUE DAMAGE

Miner's linear cycle ratio cumulative damage rule has proven to be reasonably accurate for random stress cases and is as follows:

$$D = \frac{N}{N_f} \qquad (12)$$

N_f = median number of random stress cycles to failure

N = average number of applied random stress cycles

D = cumulative damage: $D \geq 0$

Fatigue fracture occurs for $D = 1$. (i.e. $N = N_f$). No fracture occurs for $D < 1$. De-

fine $N_{Service}$ and N_{Test} as the desired life (in terms of applied stress cycles) in the Service and Test stress environments, respectively. Values of $D_{Service}$ or D_{Test} greater than unity imply that fatigue fractures will occur sooner than the desired life.

EQUAL DAMAGE

The equation for lines of equal cumulative damage (i.e. D = constant) is derived as follows:

From equations (4) and (12)

$$N_f = N/D$$

$$\sigma = \bar{C}\, N_f^{-1/\beta} = \bar{C} \left(\frac{N}{D}\right)^{-1/\beta}$$

$$\sigma = \left[(\bar{C})\,(D)^{1/\beta}\right] N^{-1/\beta}$$

$$\sigma = \bar{C}_D\, N^{-1/\beta} \qquad (13)$$

where

$$\bar{C}_D = (\bar{C})\,(D)^{1/\beta} \qquad (14)$$

$$\frac{C_D}{\bar{C}} = D^{1/\beta} \qquad (15)$$

Equation (13) is the equation for constant damage. It is of the same power law form and has the same slope parameter β as the corresponding fatigue curve. However, the y-intercept, C_D, has a different value than C. Figure 4 shows lines of constant damage using equation (13) for very little damage (D = 0.001), large damage (D = 1.0) and very large damage (D = 10) for Copper wire. These curves have the same slope on a log-log plot.

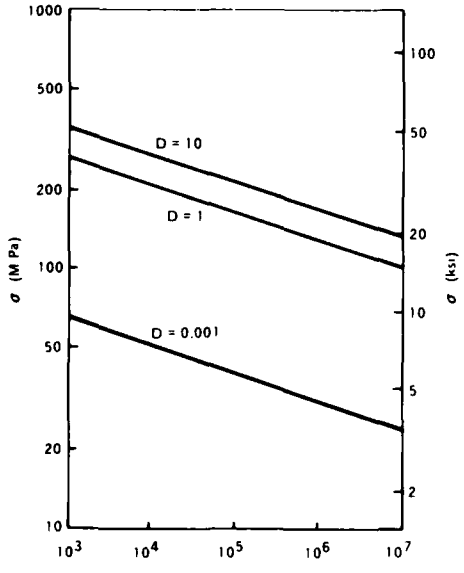

Figure 4. Constant Damage Lines

CYCLES-TEST DURATION RELATIONSHIP

The fatigue process is directly related to the number of applied stress cycles. For a single degree-of-freedom system subjected to wide band Gaussian random vibration, the stress response will be a narrow band random process centered about the resonant frequency f_o. It can be shown [2] that the average number of applied stress cycles is as follows:

$$N = f_o\, T \quad \text{(cycles)} \qquad (16)$$

f_o = resonant frequency (Hz); the center frequency of the stress response spectra

T = test duration (seconds)

For a two degree-of-freedom system [5]:

$$N = f_{eff}\, T \qquad (17)$$

f_{eff} = effective frequency (Hz)

= rate of zero crossings

$$f_{eff} = \sqrt{\frac{\sigma_a^2}{\sigma_T^2} f_a^2 + \frac{\sigma_b^2}{\sigma_T^2} f_b^2} \qquad (18)$$

where

f_a = 1st mode reasonant frequency (Hz)

f_b = 2nd mode reasonant frequency (Hz)

σ_a = 1st mode rms stress level

σ_b = 2nd mode rms stress level

σ_T = total rms stress level

$$f_a < f_{eff} < f_b$$

$$\sigma_T = \sqrt{\sigma_a^2 + \sigma_b^2} \qquad (19)$$

APPROACH SUMMARY

The fatigue process has been shown to be directly related to the rms stress level σ and applied stress cycles N in the critical structural element within the more complex structural assembly. Refer to equations (10) and (16) in particular. The rms stress level σ is related to the black box input vibration acceleration level $\ddot{X}$, the power spectral density W, and the structural damping linearity parameter η as shown in equations (6) and (9). Miner's linear cycle ratio cumulative damage rule as shown in equation (12) is used to calculate damage. The above equations will be used in the following section to derive the acceleration factors $\ddot{X}_2/\ddot{X}_1$ and W_2/W_1 in terms of the time duration compression factor T_1/T_2 such that the damage D is the same at both the service environment (subscript 1) and the test environment (subscript 2). In all cases η = constant.

ACCELERATION FACTOR DERIVATION

For equal damage at both the service and test environments,

$$D = D_1 = D_2$$

$$D = \frac{N_1}{N_{f_1}} = \frac{N_2}{N_{f_2}}$$

$$\frac{N_{f_1}}{N_{f_2}} = \frac{N_1}{N_2} = \frac{T_1}{T_2}$$

$$\sigma = C_1 \ddot{X}^{\eta} = C_m N_f^{-1/\eta\beta}$$

$$\frac{\sigma_2}{\sigma_1} = \left(\frac{N_{f_1}}{N_{f_2}}\right)^{1/\eta\beta} = \left(\frac{T_1}{T_2}\right)^{1/\eta\beta}$$

$$\frac{\sigma_2}{\sigma_1} = \left(\frac{\ddot{X}_2}{\ddot{X}_1}\right)^{\eta}$$

$$\frac{\ddot{X}_2}{\ddot{X}_1} = \left(\frac{T_1}{T_2}\right)^{\frac{1}{\eta^2\beta}} \qquad (20)$$

$$\frac{W_2}{W_1} = \left(\frac{T_1}{T_2}\right)^{\frac{2}{\eta^2\beta}} \qquad (21)$$

Equations (20) and (21) represent the final derived equations that express the acceleration factor criteria. These equations are of power law form. The exponents are related to the material's fatigue curve slope parameter (i.e. ductility) β and to the square of the damping linearity parameter η.

DUCTILITY EFFECT

Equation (20) can be used to show the effect of the material's ductility. Ductility is the ability of the material to be deformed without fracturing. Ductile materials have values of $\beta \cong 20$ Brittle materials have values of $\beta \cong 9$. (See Table 1). Equation (20) can be plotted in a normalized fashion. Figures 5 and 6 show plots of acceleration factor for several β values at $\eta = 1.2$ and 0.84, respectively. Table 2 shows the data points for $T_1/T_2 = 1000$. It can be seen that the acceleration factor is not sensitive to small differences in β (e.g. $\beta = 9.28, 10.5$) but is sensitive to large differences (e.g. $\beta = 9.28, 22.4$). Also, the acceleration factor is less sensitive to β differences for $\eta = 1.2$ than for $\eta = 0.84$.

DAMPING LINEARITY EFFECT

Figure 7 is a plot of equation (20) for several η values with $\beta = 9.28$. Table 3 shows the data points for $T_1/T_2 = 1000$. The acceleration factor is sensitive to η values.

EQUAL DAMAGE

Equal cumulative fatigue damage exists at all points along any one line (i.e. curve) of figures 3, 4, and 5. However, the damage is not equal from curve to curve.

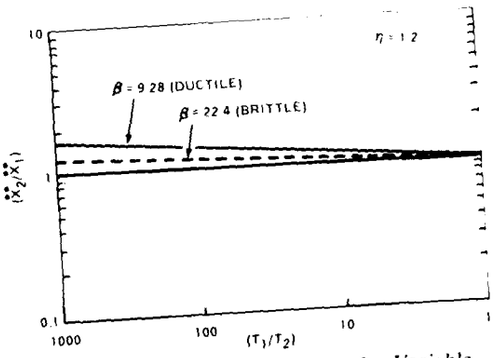

Figure 5. Acceleration Factor for Variable β with $\eta = 1.2$

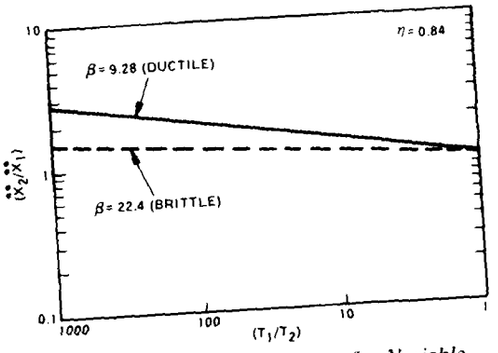

Figure 6. Acceleration Factor for Variable β with $\eta = 0.84$

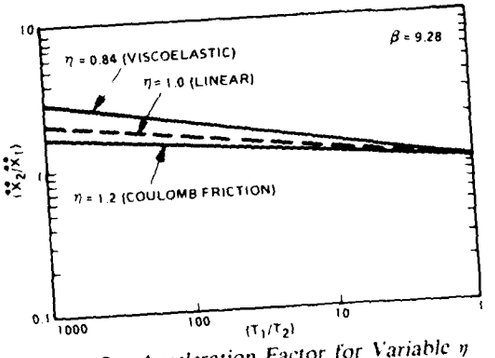

Figure 7. Acceleration Factor for Variable η

TABLE 2. ACCELERATION FACTORS FOR VARIABLE β ($T_1/T_2 = 1000$)

η	β	$\ddot{X}_2/\ddot{X}_1$
0.84	9.28	2.87
0.84	10.5	2.54
0.84	22.4	1.55
1.2	9.28	1.68
1.2	10.5	1.58
1.2	22.4	1.24

TABLE 3. ACCELERATED FACTORS FOR VARIABLE η
($T_1/T_2 = 1000$; $\beta = 9.28$)

η	$\ddot{X}_2/\ddot{X}_1$
0.84	2.87
0.93	2.36
1.00	2.11
1.07	1.92
1.20	1.68

THEORETICAL η VALUES

Appendix A derives η values for several idealized cases which are summarized in Table 4.

Linear damping has a damping parameter value of unity. Coulomb friction damping, which is representative of riveted or bolted structural assemblies, has a parameter value greater than unity. Viscoelastic damping or internal stress-strain hysteresis damping have parameter values less than unity. The latter damping mechanism is typical of dip-brazed or adhesive bonded structural assemblies.

TABLE 4. THEORETICAL η VALUES

Damping Type	η
Linear	1.0
Internal Stress-Strain Hysteresis • Structural materials • Viscoelastic adhesives stressed in shear	 0.833 0.784
Coulomb friction	1.5

EXPERIMENTAL η VALUES

Limited experimental data shows that most real structures, even simple ones, have more than one damping mechanism present. Different damping mechanisms will predominate over different vibration input level ranges. For example, a simple cantilever beam, made up of a viscoelastic adhesive sandwiched between two metal beam elements with the composite beam riveted at the clamped end, had a value of $\eta = 1.2$ at low vibration levels (friction predominating) and progressively reducing to $\eta = 0.84$ at high vibration levels (viscoelastic damping predominating). The high vibration levels were approximately four times higher than the lower levels. An aluminum dip-brazed computer black box with multilayer board assemblies (MLA) epoxy bonded to webs had $\eta = 0.94$. Some MLAs, with the boards epoxy bonded to metal plates which were attached to rigid structures along two edges with wedge clamps, had $\eta = 1.1$. Other MLAs, with the boards bonded to metal plates with a cured elastomer on which the same edge wedge clamps were used, had $\eta = 1.04$. This value remained relatively constant for a change in vibration input level of a factor of four. Figure 3 shows that even these small deviations in damping linearity have a significant effect on fatigue life. The value of η is best determined empirically. It should be noted that the value of η may not necessarily be related to the critical structural element and its value of β.

CONDITIONS OF SIMILITUDE

Certain conditions of similitude must be imposed upon the service and laboratory accelerated test environments if the developed mathematical relationships are to be appropriately and accurately applied. The fundamental hypothesis is that the damage states and damage rates must be the same for both environments. Specifically the states of stress (torsion, bending, axial), the corresponding fatigue strengths, the resonant mode shapes, the internal response stress spectrum shapes, and the type and location of failure mechanisms must be the same for both environments.

Extreme temperature, humidity, or corrosive element differences between the service and test environments may result in similitude violations, if such differences are sufficient to alter the material's fatigue strength parameters. Threshold sensitive or other nonlinear response effects in general tend to violate conditions of similitude.

The condition that the shape of the vibration acceleration input spectra or the overall acceleration rms levels must be the same for both environments has purposely been omitted from the previously listed conditions. This is because the fatigue damage state and rate are only indirectly related to the input acceleration spectrum. They are directly related to the response stress spectrum at the location where damage is accumulating. The response stress spectrum is related to the vibration acceleration power spectral density value in the vicinity of resonances.

NON-CONSTANT η VALUE

Equations (20) and (21) as well as Figures 5 and 6 illustrate the significant effects for those cases where the value of η remains relatively constant over the input levels of W_2 and W_1 (correspondingly $\ddot{X}_2$ and $\ddot{X}_1$). For those cases where the η value is not constant a modified approach must be used as follows:

$$\frac{\sigma_2}{\sigma_1} = \frac{T_1^{1/\eta_1\beta}}{T_2^{1/\eta_2\beta}}$$

η_1 = value of η at input level W_1, $\ddot{X}_1$

η_2 = value of η at input level W_1, $\ddot{X}_2$

$$\frac{\sigma_2}{\sigma_1} = \frac{\ddot{X}_2\eta_2}{\ddot{X}_1\eta_1}$$

$$\ddot{X}_2\eta_2 \quad T_1^{1/\eta_1\beta}$$

$$\ddot{X}_1\eta_1 \quad T_2^{1/\eta_2\beta}$$

$$\ddot{X}_2 = \ddot{X}_1^{\eta_1/\eta_2} \left[\frac{1}{T_1^{\eta_1\eta_2\beta}} \right] \left[\frac{1}{T_2^{\eta_2^2\beta}} \right] \quad (22)$$

$$W_2 = W_1^{\eta_1/\eta_2} \left[\frac{2}{T_1^{\eta_1\eta_2\beta}} \right] \left[\frac{2}{T_2^{\eta_2^2\beta}} \right] \quad (23)$$

It is recommended that equations (20) and (21) be initially used to establish an approximate value for W_2, $\ddot{X}_2$, and the corresponding value of η_2. Then use equations (22) and (23) to calculate the final values of W_2 and $\ddot{X}_2$. Note that absolute values of T_1 and T_2 must be used (i.e. there is no dimensionless ratio T_1/T_2).

MULTIFACTOR CONSIDERATIONS

In general, all the structural elements in a relatively complex electronic black box will not have the same acceleration factor. Yet a single factor value must be chosen for the accelerated test. Such a selection is considered to be subjective. The value chosen will result in a proper test for only one class of structural elements. The other elements will be either under- or over-tested. An average factor would give average results. The most conservative approach would be to select the largest acceleration factor value.

In some cases the one or two critical elements in a black box will have nearly identical β and η values. Then any of the above mentioned approaches would be sufficiently appropriate.

An alternative approach is to run the accelerated test in several steps using the criteria of the most critical element to that of the least critical element in sequential fashion. This involves estimating the damage accumulated by each critical element using equation (12) for each test step and adjusting the duration of each step to ensure that the damage accumulated by each critical element is the value that would be accumulated in a single step test independent of the other critical elements. This requires a fatigue analysis of the critical elements.

CONCLUDING REMARKS

1. The acceleration test criteria is of the power law form. The vibration level acceleration factor is equal to the time duration compression ratio raised to an exponent. The exponent is inversely proportional to the product of the critical material's fatigue slope parameter β and the square of the damping linearity η.
2. The acceleration factor is not sensitive to small differences in β (e.g. β = 9.28, 10.5) but is sensitive to large differences (e.g. β = 9.28, 22.4). It is also sensitive to η values.
3. Vibration input level acceleration factors have typical values of 3 or less for time compression ratios of 1000.
4. The derived values of η agree reasonably well with measured values for real structures when consideration is given to the various predominant damping mechanisms existing in the structures.
5. Actual structures usually contain more than one damping mechanism. It is recommended that η values be determined experimentally.
6. The value of η used to calculate the acceleration factor should be chosen less than the actual measured value if it is desired to add conservatism when specifying an acelerated life test.
7. Acelerated and non-accelerated fatigue life tests should maintain the same input random vibration spectrum shape so that effects of multimode responses and the uncertainty in predicting response reasonances cannot be questioned as factors that may degrade the integrity of the tests.

REFERENCES

1. Technical Report on Fatigue Properties - SAE J1099, Society of Automatic Engineers, Inc., February 1975.
2. R.G. Lambert, "Analysis of Fatigue Under Random Vibration," The Shock and Vibration Bulletin No. 46, Naval Research Laboratory, Washington, D.C., August 1979.
3. R.G. Lambert, "Computation Methods," March 1980, Performed on Navy Contract N00019-78C-0407. (AD-A 103211/9).
4. R.G. Lambert, "Fatigue Life Prediction For Various Random Stress Peak Distributions", The Shock and Vibration Bulletin 52, Naval Research Laboratory, Washington, D.C., May, 1982.
5. R.G. Lambert, "Fatigue Analysis of Multi-degree-of-Freedom Systems under Random Vibration," The Shock and Vibration Bulletin No. 47, Naval Research Laboratory, Washington, D.C., September 1977.
6. M. Gertel, "Specification of Laboratory Tests" pp. 24-9 to 24-10, Volume 2, Shock and Vibration Handbook, edited by Harris and Crede, McGraw-Hill Book Company, 1961.
7. B. Lazan and L. Goodman, "Material and Interface Damping", pp. 36-33 to 36-35, Volume 2, Shock and Vibration Handbook, edited by Harris and Crede, McGraw-Hill Book Company, 1961.

8. C. Crede and J. Ruzicka, "Theory of Vibration Isolation", pp. 30-7 to 30-8, Volume 2, Shock and Vibration Handbook, edited by Harris and Crede, McGraw-Hill Book Company, 1961.

SYMBOLS

A	material fatigue curve constant; true ultimate stress
b	fatigue strength exponent
C_1, C_2, C_3	stress per acceleration constant
C, C_m, C_D	random fatigue curve constant
D	cumulative fatigue damage
f_o, f_a, f_b	resonant frequency
f_{eff}	effective frequency
ksi	thousands of pounds per square inch
N	average number of applied stress cycles
N_s	number of sinusoidal stress cycles to failure
N_f	median number of random stress cycles to failure
PSD	acceleration power spectral density
rms	root mean square
S	applied stress amplitude
T	test duration
$\ddot{X}$	acceleration amplitude
W, W(f)	acceleration power spectral density
α	general variable
β	fatigue curve slope parameter
$\Gamma(\alpha)$	Gamma Function of argument α
η	damping linearity parameter
$\sigma, \sigma_a, \sigma_b, \sigma_t$	random rms stress value
σ'_f	material fatigue strength coefficient
MPa	mega-Pascals
6.895	MPa/ksi

APPENDIX A

DAMPING TERM DERIVATION

The value of the power law damping linearity term η for several damping mechanisms of interest in a simple idealized single-degree-of-freedom (SDF) system is derived as follows. The derivation technique used is the one detailed in reference [6]. Only a brief description of the derivations will be given. Basically the stress σ of the structural element (i.e. the spring element in the idealized SDF system) is related to the input rms acceleration level $\ddot{X}$. This relationship will be of the power law form

$$\sigma = C_1 \ddot{X}^{\eta}$$

The value of η (also C_1) can be obtained from the derived power law equation by inspection of corresponding parameters.

The non-linearities in damping for CASE B and CASE C are assumed to cause little or no shift in the response frequencies so that equations developed for linear systems are approximately correct for the non-linear cases of interest. This is believed to be a valid assumption for the ranges of interest in the parameter η.

CASE A (LINEAR DAMPING)

Refer to Figure 8

Define $z = y-x$

At resonance $\ddot{z}_{rms} \cong \ddot{y}_{rms}$

$m\ddot{y}_{rms} = \sigma a$

σ = rms stress; a = cross-sectional area of stressed element (e.g. spring)

$\frac{\ddot{y}}{\ddot{X}} = \frac{y}{X} = Q$; $\ddot{x}$ = rms input acceleration

$\ddot{y}$ = rms response acceleration

$$m Q \ddot{X}_{rms} = \sigma a \; ; \; C_1 = \frac{mQ}{a}$$

$\therefore \eta = 1$

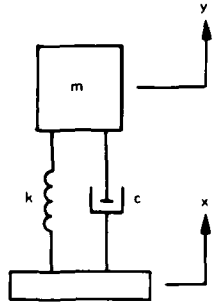

Figure 8. Vibration System with Linear Damping

CASE B (INTERNAL STRESS-STRAIN HYSTERESIS)

Refer to Figure 8 and References [6] and [7]

$z = y - X$; $\ddot{z} = \ddot{y} - \ddot{X}$

$\ddot{y}$ = rms response acceleration

$\ddot{X}$ = rms input acceleration

$m\ddot{y} = \sigma a$; $f_n = \frac{1}{2\pi}\sqrt{k/m}$

$\ddot{X} = C_2 W_o^{1/2}$ $\qquad Q = y/X = \ddot{y}/\ddot{X}$

$\ddot{y} \quad \sqrt{\frac{\pi}{2} f_n W Q}$

$Q = \frac{Kv\pi\sigma^2}{EJ_o\sigma^n}$; n = 2.4 for most structural materials stressed below 0.8 of fatigue strength. n = 8 for higher stresses.

$$\frac{\ddot{y}}{\ddot{X}} = \sqrt{\frac{\pi}{2}\frac{f_n Q}{C_2 0.5}}$$

$$\ddot{X} = \frac{\ddot{y}}{\sqrt{\frac{\pi}{2}\frac{f_n Q}{C_2 0.5}}} = \frac{\sigma a}{m\sqrt{\frac{\pi}{2}\frac{f_n}{C_2 0.5}}}\left[\frac{EJ_o\sigma^n}{kv\pi\sigma^2}\right]^{1/2}$$

$$\ddot{X} = \left\{\frac{a(EJ_o/Kv\pi)^{1/2}}{m\sqrt{\frac{\pi}{2}\left[\frac{f_n}{C_2 0.5}\right]}}\right\}^{1/2} \sigma^{n/2}$$

$$\sigma = \frac{m}{a}\left[\frac{\pi^2 f_n Kv}{2EJ_o C_2 0.5}\right]^{1/n} \ddot{X}^{2/n}$$

$$\therefore \eta = \frac{2}{n}$$

Structural materials	n	η
	2.4	0.833
Viscoelastic adhesives stressed in shear	2.55	0.784

CASE C (COULOMB FRICTION)

Refer to Figure 9 and Reference [8]

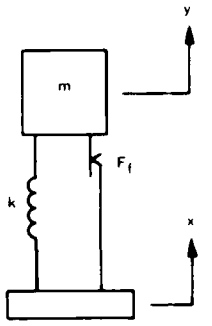

Figure 9. Vibration System with Friction Damping

$$m\ddot{y} = \sigma a$$

$$m\ddot{y} = \sigma a \; ; \; \ddot{X} = C_2 W_o^{1/2}$$

$$\ddot{y}/\ddot{X} = Q \; ; \; \ddot{y} = \sqrt{\frac{\pi}{2} f_n W_o Q}$$

$$y = \sqrt{\frac{\pi}{2}\frac{f_n Q}{C_2 0.5}} \; ; \; \ddot{X} = \frac{\sigma a}{mQ}$$

$$Q = \frac{2K\ddot{X}}{F_f C_2 0.5\, 4\pi^2 f_n^2}$$

$$\therefore \sigma = \left[\frac{m}{a}\sqrt{\frac{K}{F_f C_2 0.5\, 4\pi f_n}}\right] \ddot{X}^{1.5}$$

$$\eta = 1.5$$

VIBRATION TEST ENVIRONMENTS FOR ELECTRONICS MOUNTED IN A REMOTELY PILOTED VEHICLE

Vernon R. Beatty
Harris Corporation
Melbourne, Florida

This paper describes the development of vibration test environments for an Airborne Data Terminal which is mounted in a Remotely Piloted Vehicle. Results of finite element analysis and mechanical model testing showed that vibratory inputs to electronic components would exceed expected fragility levels. Expected in-service vibration levels were measured and used to redefine the vibration test requirements. Component vibratory inputs were then reduced below expected fragility levels. Costly overdesign was eliminated and the actual design is now based on the real-world vibration environment.

INTRODUCTION

Electronics equipment used in aerospace and avionics applications can provide unique packaging problems for the design engineer. These problems usually result from customer-defined thermal and dynamic requirements. The dynamic environment that usually causes the most concern is vibration. For electronics equipment the two basic areas of concern are the chassis and the electronics. The chassis is normally less difficult to analyze and predict failures. The electronics, however, provide the engineer with a more difficult problem since vibratory inputs to these components are necessary for failure prediction, yet hard to predict analytically.

An example of potential vibration-induced electronics failures is an Airborne Data Terminal (ADT). The ADT is an electronic assembly which is mounted in a Remotely Piloted Vehicle (RPV) and provides communications between the ground and the RPV. The ADT (shown in Figure 1) consists of a cast aluminum housing, a bolted-on motherboard and front cover, 20 printed circuit boards, and several electronic components. These "components" are actually vendor-supplied electronic subassemblies. They consist of a synthesizer, an up-down converter assembly, an oscillator, a traveling wave tube amplifier (TWTA), a transmit antenna switch, a TWTA power supply, and two transmit antennae enclosed in radomes. Potential vibration-related failures of these electronics include broken leads, solder joints, or other mechanical parts; loss of operation due to the acceleration-sensitive nature of the component; loss of antenna pointing accuracy due to vibratory motion; chatter of relays or other moving parts; or microphonic disturbance.

Many tradeoffs were made during the design of the ADT due to system-imposed constraints. These design constraints include the power dissipation of the electronics necessitating forced air cooling; the limited volume in the RPV for ADT installation; the limited number of ADT mounting points (four); the need for a sealed interface between the radomes and the RPV skin; the weight budget; and the 5g vibration specification. All of the above constraints affected the ADT design from a vibration standpoint. However, the most significant constraint was the 5g vibration specification.

THE 5G VIBRATION SPECIFICATION

The 5g vibration environment was first recognized as a source of potential electronics problems during early design. This environment is defined in

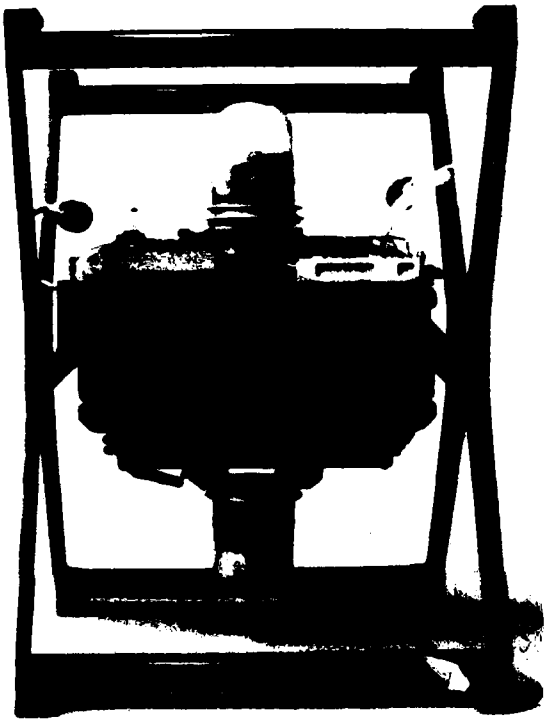

Figure 1-ADT Configuration

MIL-STD-810C[1], Method 514.2, Procedure I, Category C, Curve M of Figure 514.2-3. The environment is shown in Figure 2 and consists basically of 9 hours of logarithmic sinusoidal cycling from 5 to 500 Hz at predominately 5 g's acceleration.

Examination of MIL-STD-810C reveals that this test requirement is for equipment installed in helicoptors. Since no vibration measurements had been taken in the RPV, this test requirement was considered a "best guess" estimate of the RPV vibration environment. Cursory structural analysis of the ADT showed vibratory inputs to the components could easily be 50 to 60 g's. This initial information showed the need for shaping the component vibration requirements to reflect expected inputs. It also pointed out the need for more detailed analysis of the ADT.

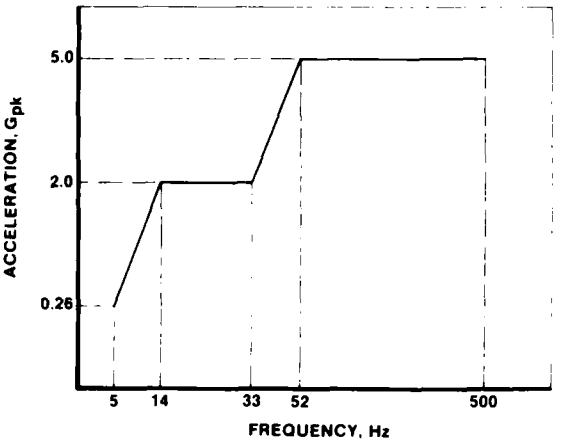

Figure 2-5G Environment

FINITE ELEMENT ANALYSIS

A STARDYNE[2] finite element model was made to determine ADT natural frequencies and mode shapes. The model consisted of the following:

484 nodes
266 beam elements
153 triangular plate elements
263 quadrilateral plate elements
23 cube elements

This model is shown in Figure 3.

Twenty seven modes from 93 Hz to 488 Hz were then extracted and identified using a graphics postprocessor. Forced response analysis was done using the 5g environment as base excitation to the ADT. Response plots provided profiles of maximum expected component vibratory inputs, which were once again estimated to be 50 to 60 g's. These vibratory inputs exceeded the fragility levels determined from analysis of component designs. The need for obtaining measured component vibratory inputs was now evident. This was done during mechanical model testing.

MECHANICAL MODEL TEST RESULTS

To determine ADT natural frequencies, mode shapes, and component vibratory inputs, a mechanical model was fabricated and tested using the 5g environment as input to the ADT. A view of the mechanical model during vibration testing is shown in Figure 4.

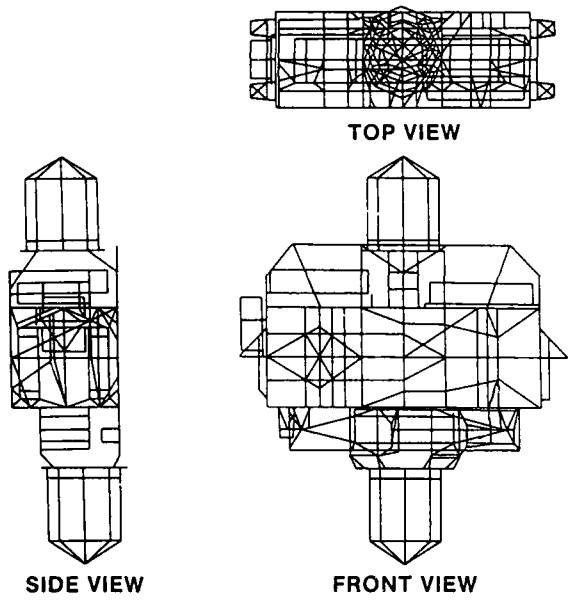

Figure 3-ADT Finite Element Model

Two configurations of the ADT were tested - one hard-mounted (unisolated), and one with 120 Hz isolators. The high frequency (120 Hz) isolator system was developed to determine if isolators could effectively minimize component vibratory inputs. Due to the large (5g) input a higher frequency isolator was needed to decrease resonant displacement and minimize the possibility of isolator stress cracking. A comparison of maximum component inputs and expected fragility levels is shown in Table 1.

The test measurements showed that inputs exceeded expected fragility levels for both the hard-mounted and isolated conditions. The ineffectiveness of the isolators was due to the coupling between the 120 Hz isolator mode and the 130 Hz first resonant mode of the chassis. The urgency of establishing a method of reducing component vibratory inputs was now obvious.

DESIGN CHANGES TO REDUCE COMPONENT INPUTS

Five design changes were proposed to reduce component inputs: (1) isolating the components; (2) isolating the chassis; (3) damping the chassis; (4) isolating and damping the chassis; and (5) changing the vibration specification. These potential design changes were all analyzed and a final solution was then proposed.

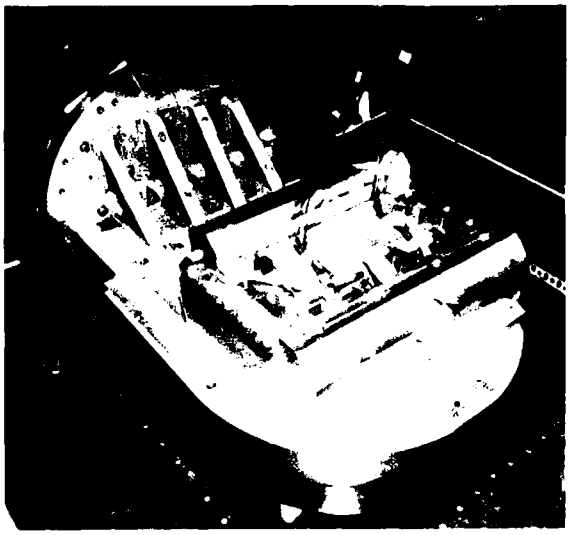

Figure 4-ADT Mechanical Model During *Vibration Testing*

Selectively isolating components was not done because severe volume constraints within the ADT limited sway space, and several components needed "direct" mounting to the ADT to permit heat transfer. Similarly, mechanical model testing had already shown that isolating the chassis would not effectively reduce component inputs. Damping the chassis was not done due to severe volume and weight constraints. Forced response analysis had also shown that constrained layer damping would not effectively reduce component inputs. Since isolating or damping the chassis proved separately to be nonviable solutions, their combination also did not provide promise.

The one solution that provided the largest gain for the least effort was changing the vibration specification. The 5g requirement was clearly a "first-cut" estimate and was not based on measured RPV levels. Initial testing of the RPV now indicated that operating vibratory levels near the ADT

TABLE 1

Comparison of Maximum Component Vibratory Inputs

Component	Maximum Input Acceleration (g's)		
	Hard-Mounted Test	120 Hz Isolator Test	Estimated Fragility Level
Synthesizer	19	25	50
Up-Down Converters	58	26	50
Oscillator	19	25	16
TWTA	96	66	20
Transmit Antenna Switch	21	15	20
TWTA Power Supply	24	30	8
Transmit Antenna	39	48	10

mounting points were probably less than 5 g's. It was now both necessary and possible to measure the vibratory inputs to the ADT during RPV operation.

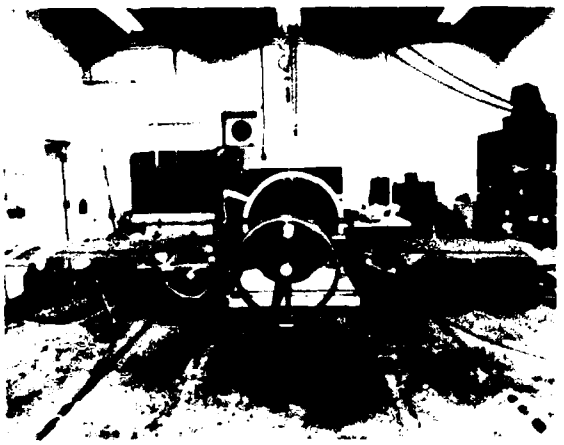

Figure 5-Tethered RPV Test Setup

TETHERED RPV TEST RESULTS

The ADT mechanical model was mounted in a tethered RPV as shown in Figure 5. A wind tunnel fan provided aerodynamic excitation while the RPV was operated at various engine speeds simulating a typical mission. Time histories of ADT vibratory inputs were recorded on magnetic tape to be reduced and analyzed later.

The close proximity of the ADT to the RPV engine implied that the ADT vibration environment would be primarily engine-induced. Since the RPV power plant is a two cylinder reciprocating piston engine, it was also felt that the vibration environment would be periodic and related to engine speed. The measured test data were first reduced by making acceleration versus frequency plots at various engine speeds. A typical acceleration versus frequency plot is shown in Figure 6.

This plot clearly shows the apparent periodic nature of the input and the direct relation of the harmonics to engine speed. To determine the presence of aerodynamic-induced vibrations, power spectral density (PSD) plots were made. A typical PSD plot is shown in Figure 7.

The PSD plot shows the absence of aerodynamic-induced vibrations, indicating that the ADT vibration environment is engine-induced. Aerodynamic-caused vibration levels

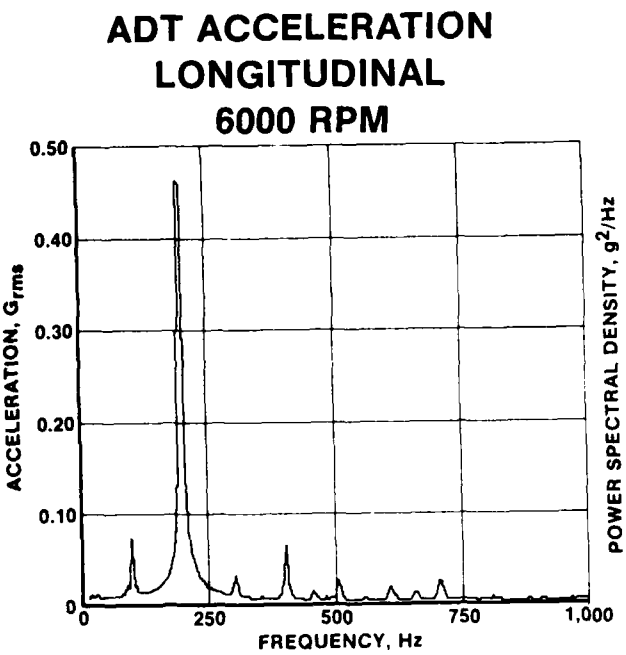

Figure 6-Tethered RPV Acceleration Versus Frequency Plot

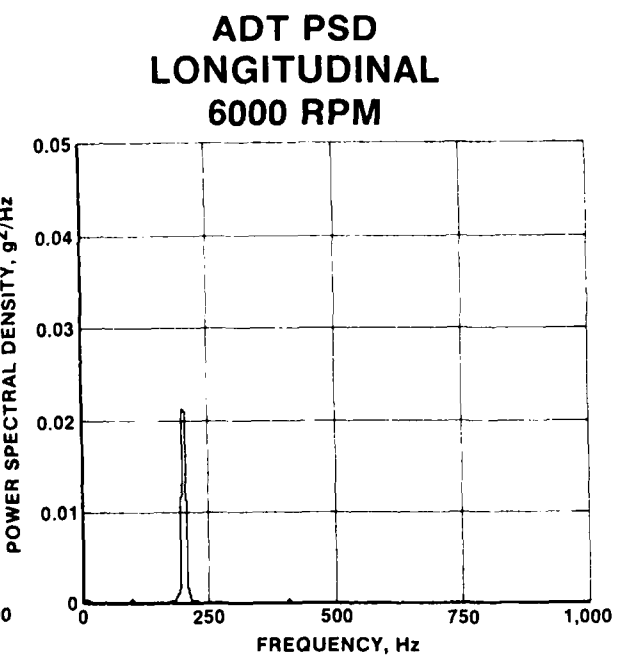

Figure 7-Tethered RPV PSD Plot

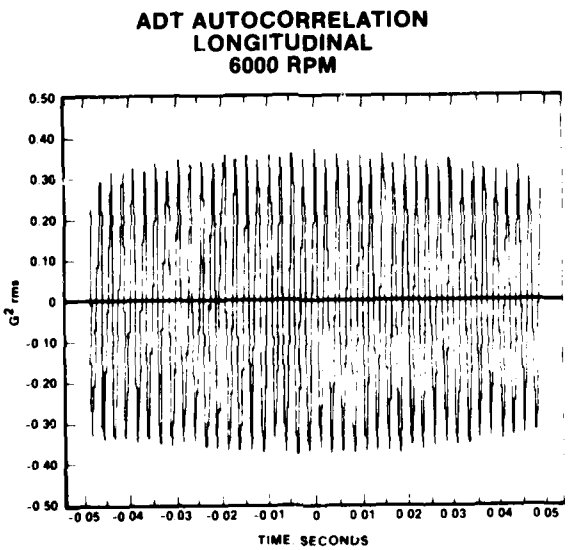

Figure 8-Tethered RPV Autocorrelation Plot

were at least an order of magnitude lower than those caused by the RPV engine. Engine-induced vibration levels ranged from .10 to 1.00 g's.

Finally, to further prove the environment's periodicity, auto-correlation plots were made. A typical autocorrelation plot is shown in Figure 8. The shape of this plot also implies that the ADT vibration environment is indeed periodic.

The data reduction showed the ADT vibration environment to consist of three harmonically-related sinusoids whose frequency varied with RPV engine speed and whose amplitudes were caused by engine-induced effects. The measured levels were considerably less than 5g's, and more importantly they were a better estimate of the ADT environment. The justification for now changing the vibration specification was found in Paragraph 1.2 of MIL-STD-810C:

> "WHEN IT IS KNOWN THAT THE EQUIPMENT WILL ENCOUNTER CONDITIONS MORE SEVERE OR LESS SEVERE THAN THE ENVIRONMENTAL LEVELS STATED HEREIN, THE TEST MAY BE MODIFIED BY THE EQUIPMENT SPECIFICATION."

REDEFINED TEST SPECIFICATIONS

The measured vibration data and the RPV flight profile then formed the basis for several test environments which redefine the ADT vibration specification. The four test environments include Qualification, Reliability, Limited Environmental Test (LET), and Acceptance. All the environments except Acceptance are based on the measured RPV data.

The Qualification environment consists of an Accelerated Life test simulating 1000 RPV missions and an Operational test. The Reliability environment is based on demonstrating an ADT operational life of 2,200 hours. Vibration is required for 550 of the 2,200 operating hours. The LET environments consist of an Operational test and a Structural test. The LET testing will be done on all units designated for flight prior to Qualification testing, if any. Acceptance testing will be done on all production units. The excitation will be 15 minutes of low level random as shown in Figure 9. Excitation will be perpendicular to the circuit boards.

In developing the Qualification, Reliability, and LET environments the

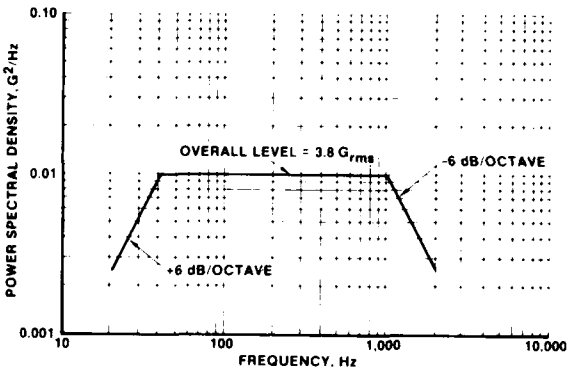

Figure 9-Acceptance Test Environment

measured amplitudes were grouped according to excitation direction and harmonic (1st, 2nd, 3rd, etc.) for each operating engine speed tested. The measured amplitudes were then multiplied by various combinations of the three raw data multipliers[3] shown below:

(1) A=1.25 (Accounts for variations in RPV designs)

(2) B=1.10-1.50 (Accounts for single axis test excitation, as opposed to simultaneous three axis excitation in the RPV)

where:

$$B=\frac{\sqrt{G_x^2 + G_y^2 + G_z^2}}{G_{max}}$$

G_x = acceleration in lateral direction

G_y = acceleration in longitudinal direction

G_z = acceleration in vertical direction

G_{max} = maximum of G_x, G_y, and G_z

(3) C=2.239 (Accounts for an accelerated test simulating 1000 missions and includes a factor of four (4000 missions) which accounts for only one item being tested)

The fatigue curve (S-N curve) of the ADT chassis material, A356-T6 aluminum, was used to determine C as shown below:

$$C^D = E$$

Where:

D = 10.29 (Slope of S-N curve)
E = 4000 missions

An example of this test level derivation procedure is the Qualification Accelerated Life environment. Qualification Accelerated Life is the only accelerated test and, therefore, provides the highest ADT vibratory inputs. The vibration levels for the Accelerated Life test are shown in Figures 10-12. These levels are clearly lower than the 5 g environment which is also shown in Figures 10-12 for comparison. The excitation directions are in reference to the RPV. The test levels of Figures 10-12 and the simplified RPV flight profile of Figure 13 define the Qualification Accelerated Life test environment.

Table 2 shows which raw data multipliers were used in developing the Qualification, Reliability, and LET test environments.

Table 3 provides test times and operational data for the test environments.

The above-described test environments provide a series of tests which will simulate in-service conditions. Since the measured levels were significantly lower than the 5g ADT specification, component survivability has been enhanced. However, it was not evident that component inputs had been reduced below expected fragility levels.

FINAL MEASUREMENT OF COMPONENT VIBRATORY INPUTS

Since measured ADT vibratory inputs were less than 5 g's, the possibility of chassis isolators was encouraging. Forced response analysis had shown that the redefined test specifications decreased component inputs, but levels were still above expected fragility levels. Therefore, changing the vibration specification alone would not solve the component

TABLE 2

Raw Data Multipliers

Test	Raw Data Multiplier		
	Design Variation (A)	Cross Axis (B)	Accelerated Life (C)
Qualification			
Accelerated Life	Yes	Yes	Yes
Operational	Yes	Yes	No
Reliability	Yes	No	No
LET			
Operational	Yes	Yes	No
Structural	Yes	Yes	No

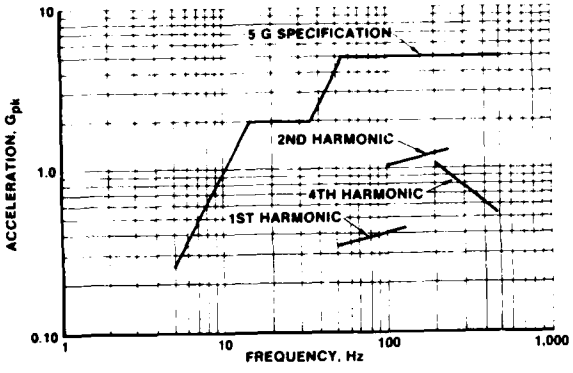

Figure 10-Qualification Accelerated Life Lateral Vibration Levels

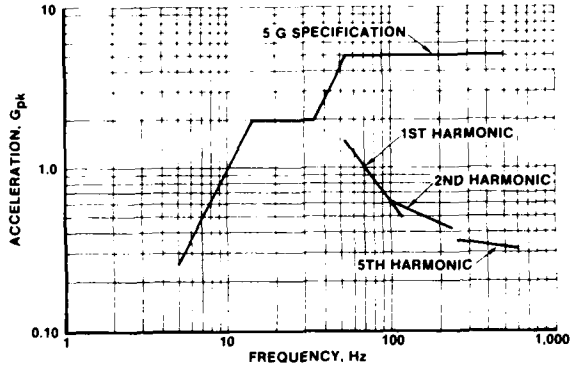

Figure 11-Qualification Accelerated Life Longitudinal Vibration Levels

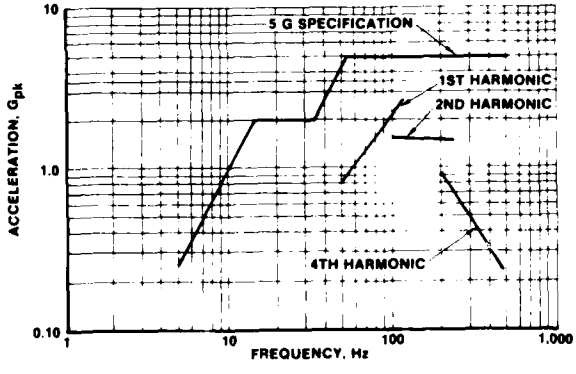

Figure 12-Qualification Accelerated Life Vertical Vibration Levels

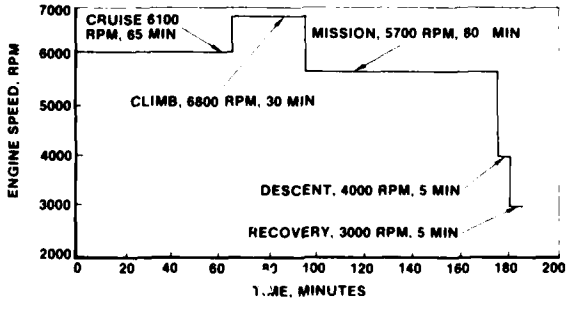

Figure 13-Simplified RPV Flight Profile

TABLE 3

Test Times and Operational Parameters

Test	Number of Axes	Test Times Per Axis (min)	Operational?	Engine Speed (RPM)
Qualification Accelerated Life	3	185	No	3,000-6,800
Operational	3	15	Yes	5,700
Reliability	1	33,000	Yes	3,000-6,800
LET Operational	3	15	Yes	5,700
Structural	3	15	No	3,000-6,800

problem. Analysis showed that an isolator system with a 50 Hz vertical resonance and 70 Hz horizontal (radial) resonances would solve the component problem. These isolators were then designed and fabricated. Software was written to allow duplication of the redefined test environments on the shaker[4].

The ADT mechanical model was equipped with the isolators and maximum component inputs were once again measured. The test environment was Qualification Accelerated Life. These measurements and expected component fragility levels are shown in Table 4.

The data in Table 4 shows that the combination of 50/70 Hz isolators and the redefined test environments reduced component vibratory inputs below expected fragility levels.

TABLE 4

Final Measured Component Vibratory Inputs

Component	Maximum Acceleration (g's)	
	Test	Expected Fragility Level
Synthesizer	8.3	50
Up-Down Converters	4.2	50
Oscillator	8.3	16
TWTA	9.1	20
Transmit Antenna Switch	8.6	20
TWTA Power Supply	7.0	8
Transmit Antenna	8.0	10

CONCLUSIONS

- Cursory structural analysis provided the first indication that component vibratory inputs exceeded expected fragility levels.
- Excellent correlation between ADT natural frequencies and mode shapes predicted by finite element analysis and measured by mechanical model testing was obtained.
- Mechanical model testing verified that component vibratory inputs exceeded expected fragility levels for both a hard-mounted and an isolated ADT when the input was the 5g military vibration specification.
- Of five design changes considered for reducing component vibratory inputs, four were eliminated due to severe design constraints. The one change that provided the most gain for the least effort was redefining the ADT vibration specification.
- The tethered RPV tests revealed that the ADT vibration environment consists of three harmonically-related sinusoids whose frequency varies with engine speed and whose amplitudes are caused by engine-induced effects.
- Redefined ADT vibration test environments include Qualification, Reliability, Limited Environmental Test, and Acceptance and reflect the measured RPV vibration environment.
- Mechanical model testing showed that the redefined vibration environments and 50/70 Hz ADT vibration isolators provided a solution which reduced component vibratory inputs below expected fragility levels.
- This study shows how a joint effort between industry and the Government redefined the ADT vibration environments. A significant cost savings resulted because overdesign of the components was eliminated. The actual ADT design is based on the expected vibration environment.

ACKNOWLEDGEMENTS

The author wishes to thank three individuals for their contributions to this study. Ken Peters of Harris Corporation convinced program management of the need for this project and obtained the funding for this study. Jay Lipeles of International Dynamics Corporation wrote the forced response software and provided guidance during the duration of this work. Sam Crews of the U.S. Army AVRADCOM provided the raw data mutlipliers and various test categories used in developing the test environments.

REFERENCES

1. MIL-STD-810C, Environmental Test Methods, March 10, 1975.
2. STARDYNE, User Information Manual, Systems Development Corp., April 1, 1980.
3. S. T. Crews, "The Structural Dynamic Interface Required for Developing Helicopter Target Acquisition Systems."
4. S. M. Landre, "Vibration Test Software for Electronics Mounted in a Remotely Piloted Vehicle, September 1982," The Shock and Vibration Bulletin, September 1983.

VIBRATION TEST SOFTWARE FOR ELECTRONICS MOUNTED IN A REMOTELY PILOTED VEHICLE

S. M. Landre
Harris Corporation Information Systems Division
Melbourne, Florida

This paper presents a description of vibration test software that was developed for testing electronics mounted in a Remotely Piloted Vehicle (RPV). The vibration test software simulated the actual vibration environment that the Airborne Data Terminal (ADT) experienced when mounted in an RPV. This software was developed because there was no known software that could simulate the required vibration enviroment on a shaker. When the software was implemented it operated successfully and generated a simulated RPV vibration environment.

INTRODUCTION

During the development program the actual vibration environment of the ADT was measured during simulated RPV flight tests. Data analysis showed that the measured vibration nput to the ADT was periodic and related to RPV engine speed. The vibration was primarily composed of three engine-induced harmonics: first, second, and fourth or fifth (depending on direction). Data analysis also revealed that the engine induced vibration dominated over aerodynamic noise.

ADT vibration test requirements (originally specified from MIL-STD-810C [1], Procedure I, Figure 514.2-3, curve M) were changed to reflect the measured vibration environment. When this change occurred the manufacturer of Harris Corporations vibration control system (Gen Rad) was contacted to determine if there was any software available that would reproduce the RPV engine-induced vibration on a shaker. None was found. As a result, it was decided to develop the software at Harris.

SYSTEM PERFORMANCE REQUIREMENTS

The modified ADT vibration test requirements consist of subjecting the ADT to various periodic waveforms, each composed of three harmonics. The primary harmonic of each waveform, the RPV engine speed, ranges from 3000 to 6800 RPM (50 to 113 Hz). The RPV flight profile (see Figure 1) shows the various RPV engine speeds and associated time durations of a typical flight mission. This profile has been defined as a step function to simplify testing, and defines the primary harmonic of each waveform and the duration the ADT will be subjected to the particular waveform.

The acceleration level of each harmonic used to generate a waveform reflects measured values. Figure 2 shows the Qualification acceleration test levels for the ADT in the vertical Z-axis. The curves shown in this figure define the acceleration levels for each harmonic in the appropriate range of test frequencies.

SYSTEM IMPLEMENTATION

The vibration software was written in Time Series Language (TSL) [2] for a General Radio 2503 vibration control system. The software is composed of a main program and 35 subroutines. The purpose of the main program is to interface with the test operator and the main subroutines. The subroutines have been structured so that each one performs one specific task. This programming approach is very flexible and provides an easy means for software additions, modifications, and debugging. Shown in Figure 3 is a very basic flow diagram of the principle software algorithms.

All of the test parameters have been set up as variables so that any type of mission profile can be simulated, with as many as six harmonics

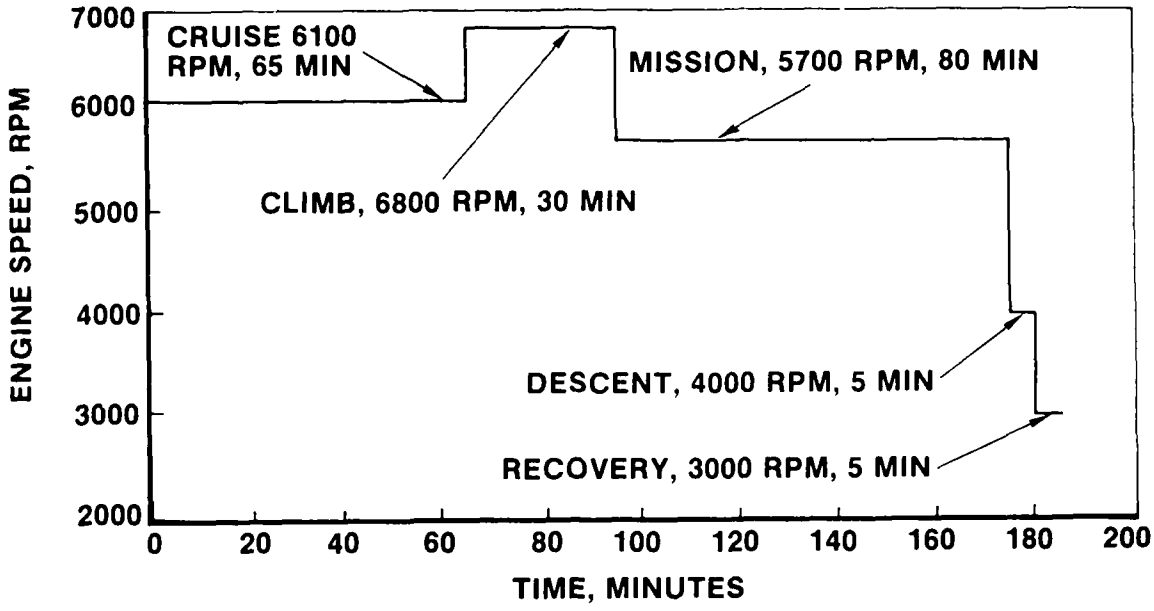

Figure 1. - Simplified Flight Profile of the RPV

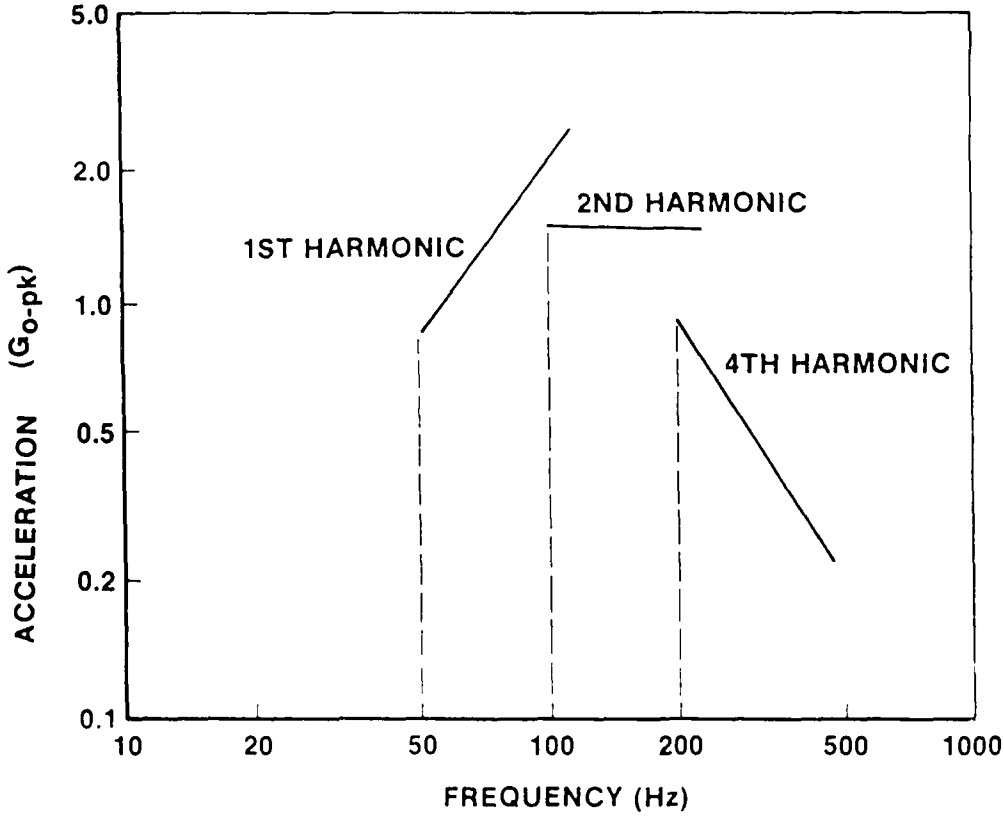

Figure 2. - Vertical, Z-axis, Harmonic Qualification Acceleration Levels

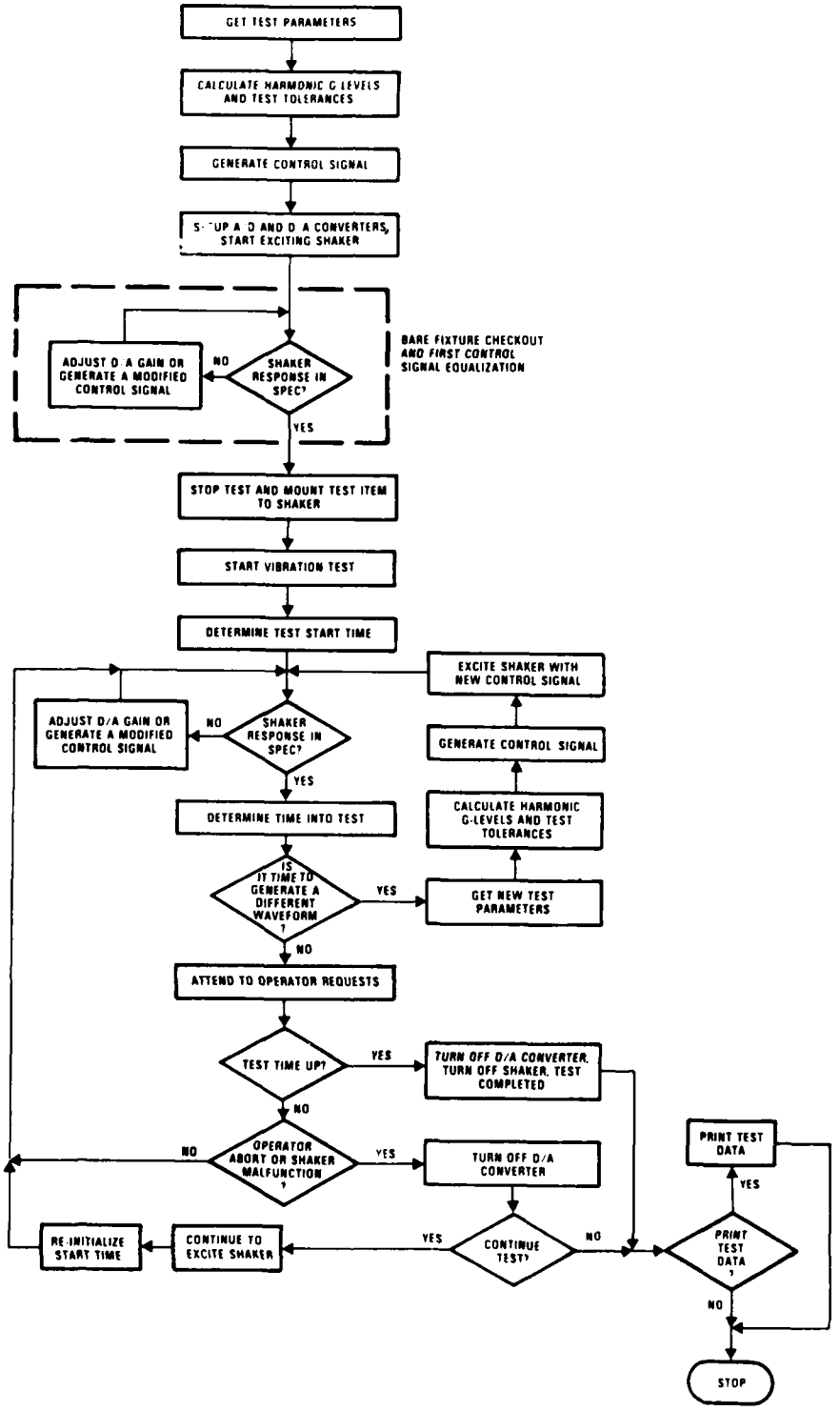

Figure 3. - Flow Diagram of the Principle Software Algorithm

comprising a waveform (only three are needed for the ADT testing). Different harmonic acceleration test data can be entered for each of three test axes. Acceleration data is entered into the computer, for each harmonic, by listing the harmonic number (1 = engine speed, 2 = 2x (engine speed), etc.), along with the first and last g-levels of the curve defining the data. The software is set up to accept straight line data, plotted in log-log format. Minimum and maximum frequencies are determined for each harmonic from the mission profile data. The slope (k) of each curve is calculated using the following relationship:

$$k = \ln (A_L/A_F)/\ln(f_L/f_F)$$

where, A = acceleration level (gs)

f = frequency (Hz)

F = first data end point

L = last data end point

The above relationship is a also used to calculate g-levels between data end points. An example output listing of the test parameters required by the software is shown in Figure 4. This is a listing of the ADT Qualification test parameters.

The test parameters are used to generate an initial control signal. The control signal is generated by placing the g-level for each harmonic in a (1 x N) frequency matrix, where N = number of frequency elements. Figure 5 shows an example of data contained in a frequency matrix. An Inverse Fourier Transform (IFT) is performed on the frequency matrix to produce a time domain signal (control signal) composed of the desired harmonics. Figure 6 shows the result of performing an IFT on the data in Figure 5. Sinusoidal phasing of the harmonics was desired on the shaker, relative to the data frames taken by the computer. To do this a cosine control signal is generated, which, when used to excite the shaker, produces a sine response. This occurs because of a 90° phase shift through the electronics and the electrodynamic shaker. A force/current and velocity/voltage analogy applies here, which accounts for the phase difference [3].

After the control signal is generated, it is used to excite a shaker. The shaker response is sampled and a Fourier transform is performed on the data to obtain g-levels at each exciting frequency. The g-level at each of the exciting frequencies is compared to g-level test tolerances. If the first harmonic

1 PROGRAM NAME IS RPV-ADT

2 MISSION PROFILE DATA:

TIME (MIN.)	ENGINE SPEED (RPM)
0.	6120.
65.	6120.
65.	6780.
95.	6780.
95.	5700.
175.	5700.
175.	4020.
180.	4020.
180.	3000.
185.	3000.

3 X AXIS HARMONIC VIBRATION TEST DATA:

HARMONIC #	FIRST G-LEVEL	LAST G-LEVEL
1	1.5	0.5
2	0.62	0.43
5	0.36	0.32

4 Y AXIS HARMONIC VIBRATION TEST DATA:

HARMONIC #	FIRST G-LEVEL	LAST G-LEVEL
1	0.34	0.43
2	1.05	1.3
4	1.05	0.54

5 Z AXIS HARMONIC VIBRATION TEST DATA:

HARMONIC #	FIRST G-LEVEL	LAST G-LEVEL
1	0.84	2.65
2	1.55	1.5
4	0.92	0.24

6 THE G-LEVEL TOLERANCES ARE: +10.% AND -10.%
7 THE TIME INCREMENT BETWEEN STORING TEST DATA IS 300 SECONDS

Figure 4. - Program Listing of Qualification Test Parameters

response is out of tolerance, then the D/A converter gain is appropriately adjusted until it is in tolerance. If the other two harmonics are found to be out of specification, then a modified control signal is generated to account for the differences and used to excite the shaker. The above procedure is repeated until the shaker response is within the required tolerance limits. This equalization procedure is performed whenever the test frequencies change or if the control signal goes out of specification during a test.

The software keeps track of time with an internal clock. When a test is started, the start time is stored in memory. The current

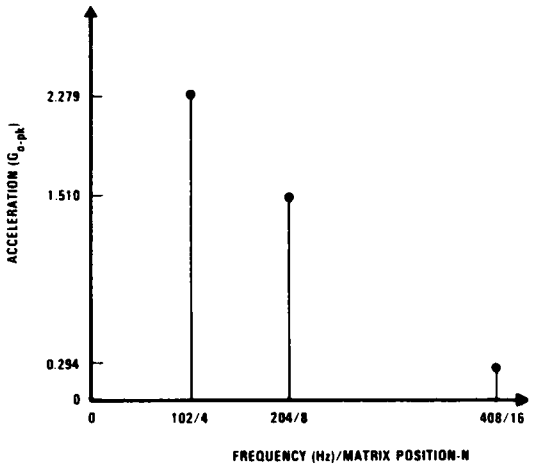

Figure 5. - Example of Data Contained in a Frequency Matrix for an Engine Speed of 6120 rpm (102 Hz)

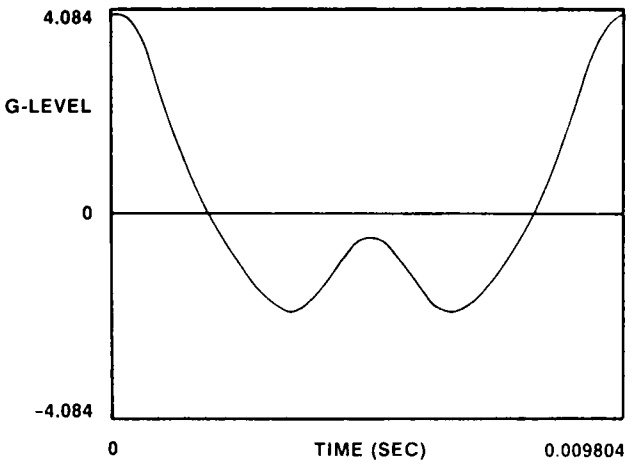

Figure 6. - Generated Control Signal for Engine Speed of 6120 rpm (102 Hz)

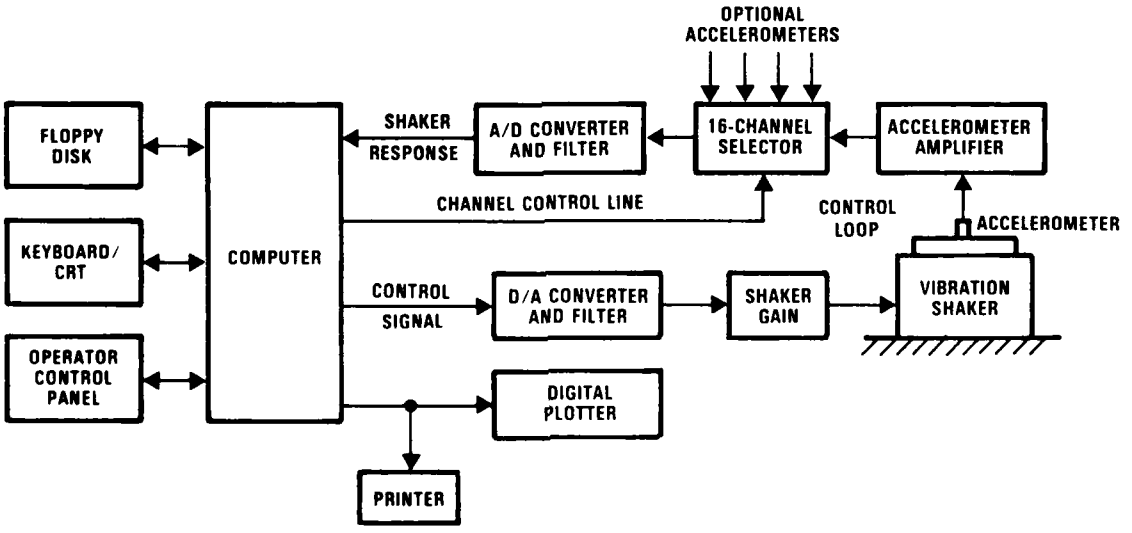

Figure 7. - System Hardware Diagram

time is continuously compared to the starting time to determine when to:

1. store data
2. change control signal
3. end test.

In addition to the software generated for this computer program, two Gen Rad software routines were used, ADDA and RTIME. The ADDA program is used to set up and control the A/D and D/A converters. The RTIME program is used to read the internal clock.

A system hardware diagram, shown in Figure 7, shows the hardware used to implement the software with a vibration shaker. Computer peripherals include a floppy disk, keyboard/CRT, operator control panel, printer, digital plotter, A/D and D/A converters, signal filters, and a 16-channel selector. The floppy disk is used for storing the software and test data. Communication between the operator and computer is through the keyboard/CRT and operator control panel. Hardcopies of test data and test parameters can be generated with the printer and digital plotter. The remaining hardware shown in Figure 7 is used in the vibration control loop.

PROGRAM OPERATION

To use the software described in the preceding paragraphs, the computer must be powered up and initialized, and then the software transferred from disk to memory. When the main program is started, the operator is given a choice of six operations, numbered 0 through 5, (see Figure 8). Operations 0 through 2 must be performed sequentially prior to operations 3 and 4.

The "Set-Up" operation is used to manipulate test parameters, and generate an initial control signal. When this operation is selected, the operator is again given a choice of eight operations, numbered 0 through 7, (see Figure 9). Test parameters can be entered into the computer from either the keyboard, using an interactive dialogue, or from the disk if previously stored. Once the test parameters have been entered, they may be modified, listed on the printer or CRT, stored on disk, and used to generate an initial control signal. The control signal may be displayed on the CRT and plotted on the digital plotter. When finished in the set-up mode, operation 7 is selected to return to the main program.

A bare fixture evaluation is performed to equalize the shaker for the first test engine speed and verify the shaker integrity. When equalized, the computer will continue to excite the shaker without monitoring the shaker's response, until the operator aborts this step or aborts the shaker through its self-protection system. If the later option is selected, the operator must still abort the computer after the shaker has been shut off.

MAIN MENU

0 SET-UP
1 RUN BARE FIXTURE
2 RUN TEST
3 CONTINUE TEST AFTER ABORT
4 POST-TEST
5 STOP

Figure 8. - Main Program Options

INPUT MENU

0 INPUT TEST PARAMETERS FROM DISK
1 INPUT TEST PARAMETERS FROM KEYBOARD
2 MODIFY TEST PARAMETERS
3 LIST TEST PARAMETERS
4 STORE TEST PARAMETERS ON DISK
5 GENERATE CONTROL SIGNAL
6 DISPLAY CONTROL SIGNAL
7 RETURN TO MAIN MENU

Figure 9. - Set-Up Subroutine Options

Upon completing the bare fixture evaluation, the test item can be mounted to the shaker and the vibration test started. In the bare fixture evaluation and test modes, the computer is controlled through an operator control panel with the use of momentary toggle switches. In the test mode, control signal test data is periodically stored on disk at a predefined time interval (see Line 7 in Figure 4). This data (see Figure 10) can be reviewed at the end of the test by choosing the "Post-Test" operation.

TIME INTO TEST		FIRST HARMONIC	INDIVIDUAL HARMONIC PEAK G LEVELS			OVERALL PEAK G
MIN.	SEC.	FREQ (RPM)	1	2	4	LEVEL
0	0	6120	0.58	0.45	0.34	1.39
5	1	6120	0.57	0.42	0.30	1.40
10	1	6120	0.59	0.43	0.32	1.49
15	0	6120	0.56	0.44	0.30	1.43
20	0	6120	0.55	0.43	0.31	1.35
25	1	6120	0.55	0.43	0.32	1.53
30	5	6120	0.56	0.42	0.30	1.22
35	1	6780	0.46	0.42	0.31	1.10
40	0	6780	0.47	0.43	0.32	1.25
45	2	6780	0.53	0.38	0.32	1.35
50	43	5700	0.67	0.43	0.32	1.40
55	13	5700	0.66	0.35	0.33	1.51
60	1	5700	0.63	0.34	0.32	1.35
65	8	5700	0.62	0.35	0.32	1.35
70	7	5700	0.61	0.37	0.30	1.29
75	2	5700	0.60	0.60	0.30	1.59
80	9	5700	0.61	0.51	0.31	1.41
85	2	5700	0.61	0.31	0.31	1.25
90	2	4020	1.01	0.51	0.31	1.91
95	1	3000	1.49	0.61	0.33	2.02
96	1	3000	1.47	0.61	0.34	2.16

Figure 10. - Listing of Control Signal Test Data

While in the test mode, the operator can obtain current information about the control signal and monitor up to 15 other accelerometers. One cycle of the control signal can be displayed on the CRT or plotted on the digital plotter (see Figure 11). The test levels of each exciting frequency and their tolerance limits, and other test data, can be displayed on the CRT (see Figure 12). The software is also set up to monitor the maximum and average g-levels of up to 15 other accelerometers. This option allows the collection of real time data during a test without having to tape the data and analyze it after the test. The computer will notify the operator if the test level drops out of specification by printing an "OUT-OF-SPEC" message on the CRT. It then corrects the condition. In addition, when the test frequencies and levels are being changed, the computer will keep the operator informed via the CRT.

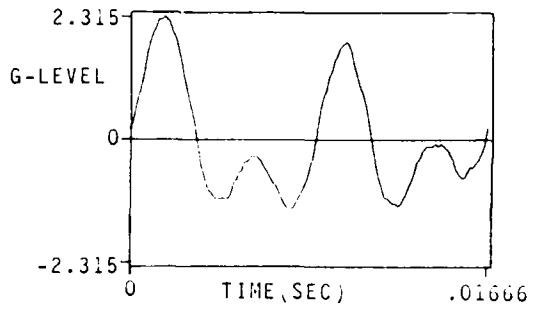

Figure 11. - Plot of Control Signal

TEST AXIS: Z
TEST TIME: 0 MIN. 39 SEC.

HARMONIC #	FREQ (HZ)	LOW TOL LEVEL	TEST LEVEL	UPPER TOL LEVEL
1	102.	2.06	2.27	2.52
2	204.	1.35	1.49	1.65
4	408.	0.25	0.27	0.31

Figure 12. - List of Control Signal Test Data Taken During a Test

ACTUAL TEST RESULTS

After the test software was generated, it was used to test a mechanical model of the ADT. The ADT was tested at Qualification test levels for the full time duration of 3 hours and 5 minutes in each axis. Overall, the test software worked very well. The only problem that occurred was that out-of-tolerance conditions occurred frequently at some of the low test frequencies and low g-levels. As a result, the computer continually generated modified control signals to resolve out-of-tolerance conditions. It was later verified that, for a constant control signal, some of the lower frequency responses would not stay constant due to the addition of 60 cycle noise. The test levels would fluctuate in and out of specification. This problem was later resolved by averaging a few sampled responses before comparing g-levels to tolerances.

Average equalization time, when changing test frequencies and g-levels, is 6-8 seconds. The computer generally goes through 2-3 control signal iterations before equalizing. I consider this time to be very good considering that the software is not written in assembly language. Equalization time, when changing test frequency, could be reduced to less than a second by pre-generating all control signals for each test level and storing them on disk. This could be done when running the bare fixture evaluation. When it is time to change the test level, the computer would have to retrieve the required control signal from the disk, instead of having to generate a new one.

SUMMARY

Vibration test software was developed for testing electronics mounted in an RPV due to non-existence of this type of software. The vibration test software simulates the actual vibration environment that an ADT experienced when mounted in an RPV.

Successful operation of the software has been demonstrated. Equalization time is considered good and could be improved. The shaker even emits noises similar to the actual RPV.

ACKNOWLEDGEMENTS

The author would like to acknowledge Bill Grafton of Gen Rad who supported technical problems encountered with the software/hardware interfaces and supplied the ADDA and RTIME software routines.

REFERENCES

1. MIL-STD-810C, Environmental Test Methods, March 10, 1975.

2. TSL25, Time Series Language for 2500 - Series Systems, GenRad Inc., Santa Clara, California, 1981.

3. Crandall, S. H., "Random Vibration," The Technology Press of the MIT and John Wiley & Sons, Inc., New York, U.S.A., 1958, pp 291-318.

Automated Vibration Schedule Development for Wheeled and Tracked Vehicles at Aberdeen Proving Ground

by W. H. Connon III, Materiel Testing Directorate,
Aberdeen Proving Ground, MD

This paper describes an automated method of developing laboratory vibration schedules from field vibration data. Data are collected from a test vehicle negotiating a variety of test courses utilizing a pulse code modulation (PCM) data acquisition system which allows on-vehicle digitization of approximately 60 channels of data simultaneously. Power spectral densities (PSD's) are then computed for the data using an array processor. In addition to computing the average PSD over a given time frame (usually about 30 seconds), the standard deviation of the PSD (at each spectral line) and the peak value at each spectral line are computed for each channel and all three spectra are saved in a file for further analysis. The schedules are developed from the spectral data using vehicle dependent techniques. Schedules for wheeled vehicles are determined by overlaying (automatically) spectra for various runs to produce a random spectrum of a form that can be utilized by a modern digital vibration control system. Schedules for tracked vehicles are determined by removing the fundamental and four additional harmonic bands from the spectrum while retaining the random floor. Other programs are then used to access these isolated frequencies and the random floors and order them into a form usable by a swept narrow band random on random digital vibration system control program. Since somewhat standard procedures were used, the paper will not discuss the philosophy of vibration schedule development, but will concentrate on the computer programs developed the handle large quantities of data in an efficient manner.

INTRODUCTION

A laboratory vibration schedule is a description of an environment, generally expressed in terms of displacement or acceleration as a function of frequency, which is used to control an electrodynamic shaker. The development of laboratory schedules is the art of taking large quantities of time domain field vibration data and reducing them to a single frequency domain function.

As military equipment becomes increasingly complex and expensive, the use of laboratory vibration schedules developed from test data measured under actual operating conditions (rather than using standard schedules) is becoming commonplace. The complexity of the analysis required to create vibration schedules from field data and the volume of data available require the use of a digital computer to do the processing; thus, a series of computer programs have been written for this purpose. The purpose of this paper is to present a new capability which makes the development of laboratory vibration schedules more efficient. The basic techniques utilized are not new, having been used in a similar fashion at White Sands Missile Range since the late 1970's (Ref 1); consequently, this paper will not discuss the basic philosophy or techniques of vibration schedule development. Rather it will briefly describe the system used to acquire the vibration data and then will concentrate on the computer programs developed to handle large quantities of data in an efficient manner.

DATA ACQUISITION

At the US Army Aberdeen Proving Ground, acceleration data are collected while operating test vehicles over various test courses using a pulse code modulation (PCM) telemetry system (a block diagram is presented in Figure 1). The system has signal conditioning capability for both strain-gauge and piezoelectric type accelerometers. The strain-gauge type signal conditioning package provides bridge excitation, amplification and low-pass filtering, while the piezoelectric type signal conditioning package contains a charge amplifier and low-pass filter for each channel. The filter cutoff requirements for both signal conditioners are established by means of plug-in resistor assemblies and are set for each channel. The output of each channel of each signal conditioning device is connected to a PCM encoder which digitizes each channel in sequence using a 10-bit successive-approximation analog-to-digital converter. The digital data stream is then encoded into a nonreturn to zero-level (NRZ-L) code for transmission via a radio telemetry link. The system is capable of handling up to 128 channels of data; however, a practical

upper limit for vibration tests is approximately 60 channels due to a transmission limitation of 100,000 words per second (total rate) and the requirement for a reasonable frequency response of 400 to 500 Hz from each channel. The encoder, signal conditioning and transmitter just described are mounted in the test vehicle, generally in the right front seat of wheeled vehicles or on the turret or other exterior flat surface of tracked vehicles.

The transmitted digital data stream is received at a remote data handling station. A bit synchronizer is used to recover the serial PCM pulse train from data link noise and perturbations. The "clean" pulse train is then recorded on a PCM tape recorder to preserve the actual transmitted data stream. Voice annotation and IRIG-B time code are simultaneously recorded on the tape. For on-site data verification and reformatting of the data, a PCM decommutator is used to transform the NRZ-L serial data stream to a 16-bit parallel binary output. The data is then passed through a data merger, where time code is added in a digital form, then through a digital computer and onto a disc storage device. A typical data run lasts for approximately 30 seconds during which time 3,000,000 words of data are recorded. Each word represents an acceleration at a particular location at an instant in time. The disc is presently configured to store up to 8 runs. When the disc is full, the data are written to digital magnetic tape and the disc is then overwritten with the next series of runs.

Because of the speed with which the data are acquired, data analysis is not performed during the data acquisition process. After the test data for a particular run are stored on the disc, two forms of "quick look" processing are available to validate the data. The primary form of processing is a time domain amplitude distribution of each channel in the data stream. During this analysis, the rms, + peak, - peak, +99% and -99% (data are less than or greater than these values 99% of the time are calculated for each channel and are printed in tabular form. The secondary form consists of time histories of selected channels in scaled engineering units which are plotted on a graphics terminal.

While conducting a test, it is desireable to look at the waveform of at least some portion of the data in real-time. A PCM word selector is used to convert selected portions of the data from the digital format to an analog signal. The word selector, connected to the output of the decommutator, selects any words in the data stream (up to 32) in any sequence and performs an 8-bit digital to analog conversion. A low-pass filter is used to smooth the resulting analog signal, and the signals are displayed on a panel of oscilloscopes (up to 14) or on an oscillograph (up to 12). An analog tape can also be made at this time.

Prior to each day's testing and whenever a configuration change is made in the instrumentation system, an electrical calibration is performed on each channel. Strain-gauge type accelerometer channels are calibrated by shunting the accelerometer with a calibrated resistor which produces an electrical output equivalent to a calculated acceleration (based on the resistance value and the transducer sensitivity). The calibration is performed in both the positive and negative directions and provides for a three-step calibration (including zero). The piezoelectric portion of the data acquisition system is calibrated by applying a 100 Hertz sine wave through calibrated capacitors and through the remainder of the system. The sine wave is applied at three different voltage levels to provide a three-step calibration equivalent to three different rms acceleration levels (calculated from the capacitor value and the transducer sensitivity).

After the calibration data are recorded, a linear least-squares curve fit is performed to determine the appropriate scale factors (slopes) and offsets (intercepts) for each channel and to determine system linearity. All of the scale factors and offsets are stored in a file and are used to scale the data, which are always stored in integer form.

DATA REDUCTION

With that basic introduction into the data acquisition system, attention can now be focused on the data reduction process.

The time domain data must be changed to the frequency domain so that it can be used in the laboratory and so that the vibration shaker amplitude can be controlled as a function of frequency. The familiar power spectral density (PSD) function (also called the autospectral density function) is used to describe the data in the frequency domain. This function describes the general frequency composition of the data in terms of the spectral density of its mean square value and is described in detail in reference 2.

A computer program called PSDFL computes PSD's from raw data and stores them in a file. The program assumes that the data are in normal PCM digital multiplexed form and are located on the data disc. The program makes use of a control file, $PSDCN, which contains:

a. The name of the calibration file (a file which contains the values required to convert the integer data to engineering units).

b. The name of the amplitude distribution file (a file which contains information on the location of the desired channels in the data stream and a brief location description of the desired channels).

c. The data sample rate.

d. The Fast Fourier Transform (FFT) block size (currently limited to 2048 words but to be updated to 4096 words).

e. The word length (number of bits) of the data (typically 10).

When the program is run, the operator enters the run number, the starting disc track (location of data on the disc) and the number of tracks to be used based on the amount of data analyzed (one track is approximately 1/15 of a second). The program creates a data storage file with a name based on the run number (three digits) and on the root name of the amplitude distribution file. The created file name always begins with $. For example, if the amplitude distribution file was named @MANSV and the run number was 1, the created file would be $MA001. If the file name already exists at the time of attempted creation, the program will be aborted. Each segment of time domain data is windowed with a Hanning window to reduce spectral leakage. The program then computes three PSD's for each channel listed in the amplitude distribution file. The first PSD computed is a linear average of PSD's computed for segments of data of a length defined in the control file. During this analysis period, the standard deviation and the peak value in each spectral line are computed. One standard deviation is then added to the average value to create a PSD which represents the average value plus one standard deviation at each spectral line (limited by the peak value in each spectral line). Both this PSD (average plus one standard deviation) and the peak value PSD are also saved in the file. Each data file corresponds to a test run (specific test course, speed and test condition) and consists of a major title (a line that specifies the amplitude distribution file used) and information on each channel analyzed, organized as follows:

a. An ASCII title line which contains the run number and a brief description of the channel location.

b. An ASCII information line which contains:

(1) The FFT block size.

(2) The data sample rate.

(3) The analysis bandwidth.

(4) The peak value contained within the PSD.

(5) The number of linear averages used.

c. A binary record block which contains formatted integer data (the data are formatted by dividing the entire spectrum by the peak value, then multiplying these values by 10,000 to save file storage space; i.e., integer numbers use 1/2 the storage space of real numbers).

An example of one data channel from one file is presented in Figure 2.

The program PSDFL is run on the data for N runs with data from X channels being analyzed from each run (note that X need not be the same for each run). The program will produce N PSD files (one for each run).

It is not unusual for a vibration test to consist of 50 to 60 channels of data and 40 test runs. Computing PSD's in this quantity can be an extremely time consuming process. For this reason, the computations contained in the program PSDFL are performed using an array processor. The array processor is a high-speed peripheral device particularly well suited for performing the large numbers of reiterative multiplications and additions required in digital signal processing. The parallel structure of the device allows the "overhead" of array indexing, loop counting and data fetching from memory to be performed simultaneously with arithmetic operations on the data, thus allowing much faster execution than on a typical general-purpose computer where these operations occur consecutively. By making use of the array processor, the program PSDFL can analyze 50 channels of data, computing PSD's, standard deviations and peaks over 26 linear averages (block size of 1024) and storing all information in a file (150 separate spectra) in approximately 10 minutes.

At this point, an overlay process is started (for wheeled vehicles; tracked vehicles will be discussed later). A program called SETFL is run to create a master storage file. The operator names the file and enters a title line for the file. The program then creates a blank PSD file (which has the same format as the files created by PSDFL) with all PSD data values initially set to zero.

A program called PKPSD is then used to create the overlayed spectrum. The operator enters the name of the master storage file (created by SETFL), the names of the data files (created by PSDFL, essentially the data runs) and the data elements (channel locations) within those files to be analyzed (those locations for which a common composite spectrum is desired). The program does not

require that the data elements to be analyzed be the same for each file analyzed; however, all data to be compared must have the same analysis bandwidth (a check is made by the program and the data are rejected if this is not the case).

The data used for the overlay process for each particular channel to be included in the process are the average plus one standard deviation PSD data (the middle line of Figure 2). Some of the rationale for the use of these data (rather than the average or the maximum) are as follows:

a. The peak value at each spectral point is a value that occurs rarely (once) and is susceptible to contamination by noise (false data from any source). To create a schedule based on peak data is to assume that the test item is subjected to such an environment for a reasonable length of time, which is false. The result is an overtest.

b. Some conservatism is built in by adding a standard deviation to the average to account for other terrain and vehicles for which no data were obtained, effects of tire pressure, vehicle wear, track tension, etc.

A vehicle master spectrum is created from all data analyzed from one vehicle (all files, all elements) by computing the average, the standard deviation and the peak value for each spectral line. The value saved in the master spectrum (for each spectral line) is the average value of the data analyzed increased by one standard deviation or the peak value of that spectral line, whichever is the lesser.

Thus the vehicle master spectrum produced is an average spectrum of all data analyzed (which are average plus one standard deviation spectra) with some degree of conservatism added but never exceeding the maximum value obtained from the data analyzed in each spectral line.

If it is desired to create a single schedule which is a composite of more than one vehicle, a master spectrum for all vehicles is obtained by overlaying each vehicle's master spectrum and taking the maximum value at each spectral point. Since the vehicle spectrum data have been constrained to be at or less than any peak value measured, the master spectrum will also be at or less than any peak values measured. A typical overlayed spectrum is presented in Figure 3.

It is the responsibility of the operator to determine the data locations and data runs to be overlayed and to insure that the data for each of the runs and locations chosen for the overlay process are valid. The program PKPSD prints the channel description of each channel used in the overlay process so that the operator may verify that the requested data has been analyzed.

A program called CRVIB is next used on the master spectrum to define the break points (frequency and amplitude points which define the spectrum in the digital vibration control system) and to allow the operator to smooth the spectrum for laboratory simulation. The master spectrum is plotted on a graphics terminal, and the cursor is turned on. The operator may position the cursor at any location on the plot and enter the location of the point (frequency and amplitude) by hitting any key (except E). The location of the cursor, in screen coordinates, is converted to engineering units of frequency (Hz) and amplitude (g2/Hz), and these values are stored in a file called $CRPSD. The program utilizes the "rubber band line" technique when the cursor is moved, thus giving the operator a preview of the smoothed spectrum (Figure 4). An example of a breakpoint file is presented in Figure 5.

Laboratory test time can be reduced over actual test time in the field by applying an exaggeration factor to the amplitude of the schedule. The rationale is based on an equivalent damage theory assuming that the failure mechanism is fatigue. The techniques for computing an exaggeration factor are based on a detailed knowledge of the test vehicle real-world scenario. (i.e., the real-world exposure time), the desired test time and the material fatigue characteristics). The procedures are well documented in references 1, 3 and 4 and are not part of these programs.

The break points (and thus the spectrum) may now be exaggerated (for test time compression) using the program CRPSD. It is left to the operator to compute the exaggeration factor based on the desired test time to real time ratio and to check that this exaggeration factor will not, when applied to the test spectrum, cause the spectrum to exceed the peak spectrum by more than 25%. The operator must enter the exaggeration factor (by which the PSD level is exaggerated) and the name of a new storage file into which the exaggerated spectral data will be stored. The program takes the breakpoint data from file $CRPSD, multiplies the amplitudes by the exaggeration factor and stores the values into $CRPSD. The program then takes the new breakpoints (exaggerated) and generates a complete spectrum (with the same analysis bandwidth) by calculating points between breakpoints using a straight line fit in a log-log domain. This created spectrum (the actual laboratory schedule) is stored in the storage file named by the operator when running the program. An example of a completed spectrum is presented in Figure 6.

A program called SHAKR is then run using the just developed laboratory schedule spectrum as data. The program computes the peak acceleration of the schedule at each frequency and compares this value to the shaker peak acceleration as limited by shaker displacement at that frequency. The maximum ratio (schedule/shaker) is determined over the entire spectrum. The entire laboratory schedule is then divided by this ratio to retain the basic shape of the spectrum. The new schedule breakpoints, the ratio, and the ratio of the rms value of the modified schedule to that of the original schedule are retained in a file. It is the responsibility of the operator to extend the test time based on the reduction factor if the original schedule is actually reduced, that is, if the ratio is greater than one.

Because of the occurence of speed-related periodics in the spectrum, tracked vehicle data are handled differently. The average, average plus one standard deviation and peak spectra are computed using PSDFL as before. All desired data in a common axis for a given run (speed) are then overlayed (computing the average plus one standard deviation) as described before in PKPSD. A program called REMPR plots this file (one run (speed) and one axis) on the graphics terminal, and the operator identifies the periodics by means of the cursor. The program computes the center frequency and PSD value of each periodic selected and computes the rms level of the random floor (with the periodics removed). This information is saved in a file. A typical PSD and file are presented in Figures 7 and 8, respectively.

A program called ACCPR accesses the files created by REMPR, reads the center frequencies, etc. and creates another file (essentially a breakpoint file) which lists the center frequencies and associated PSD levels in groups of harmonics (all fundamentals, and 2nd harmonics etc.). The average and standard deviation of all the random rms values are computed, and the average plus one standard deviation random rms value (limited by the maximum value) is presented (Figure 9). This information is used in a swept narrow band random vibration control scheme developed by Sandia Laboratories (reference 5). The variability of vehicle speed is accounted for by sweeping up to five dynamically changing narrow band random spectra at various rates across a broad band random spectrum to simulate field environments. Since the level (amplitude) of each narrow band can have only one value, changing levels are accomplished by completely changing the test schedule.

Several programs called PLPSD, PSDLG, SLPSD and INPSD are available as aids in analysis of PSD data. Program PLPSD plots PSD data (from any of the created files which contain PSD data) in a linear-linear format using operator defined minimum and maximum values. Program PSDLG accomplishes the same task but plots the data in a log-log format, while program SLPSD plots data in a semilog format. Program INPSD integrates the spectrum between operator-specified frequency bands to compute the rms acceleration level within the band. This information can be compared to time domain amplitude data to check the validity of the spectral data.

As an aid to record keeping, the programs PSDFL, PKPSD and CRPSD write the name of the operator-created file, the name of the program, the date of file creation, and a brief description of the content of the file to a master file called VIBFIL. A sample entry is presented in Figure 10.

A summary of the entire procedure is presented in Figure 11.

SUMMARY

The data acquisition and data reduction procedures (programs) presented in this paper are tools to accomplish the task of developing laboratory vibration schedules from vast quantities of field data in a fast, efficient manner. The ability to analyze up to 60 data channels simultaneously has reduced schedule development time from months to weeks. The data acquisition and reduction procedures are general in their application, thus allowing flexibility in schedule development. A discussion of the philosophy of test schedule development (which data locations to overlay, use of exaggeration factors, overlay techniques such as averaging or enveloping, etc.) has been specifically avoided in order to concentrate on the data acquisition and reduction procedures even though the decisions concerning philosophy were the most difficult tasks encountered while developing the programs; however, a few comments on the general subject are in order. It is important to determine the real world environment to which the test item is to be exposed so that the developed schedule will be as realistic as possible. From this information, proper selection of test courses and/or operating conditions can be made. This selection is critical because fatigue is influenced far more by larger amplitudes than by average ones. Because low level amplitudes can become insignificant in the fatigue life, the percent of life durations spent on more severe terrains are more important than those on average terrains and must be considered carefully. Because development of specialized schedules is becoming a common occurrence, and because the development philosophy used will determine the shape and magnitude of the final schedule, we in the testing community must now begin to focus more attention on the

establishment of definitive guidelines for the development of specialized vibration schedules.

References

1. Albert D. Perez, "Development of Dynamic Test Criteria for Roland Missile System" US Army White Sands Missile Range, March 1977.

2. Julius S. Bendat and Allan G. Piersol, "Random Data: Analysis and Measurement Procedures" Wiley-Interscience, 1971.

3. Allen J. Curtis, Nickolas G. Tinling and Henry T. Abstein, Jr., "Selection and Performance of Vibration Tests", Shock and Vibration Information Center, SVM-8, 1971.

4. Cyril M. Harris and Charles E. Grede, "Shock and Vibration Handbook, Second Edition", McGraw-Hill, 1976.

5. F. Thomas Mercer, "Swept Narrow Band Random on Random", Sandia National Laboratories Report SAND80-1534, August 1980.

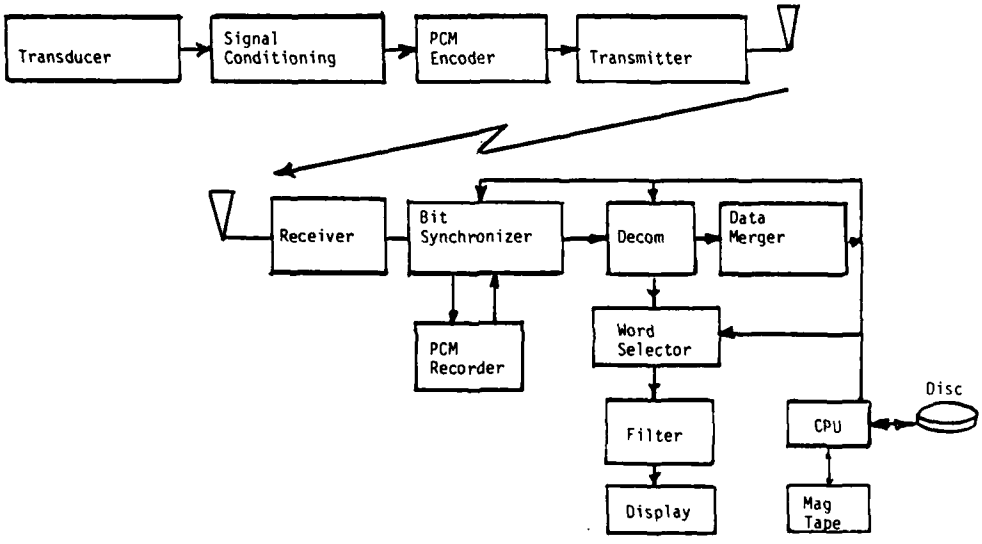

Figure 1. Block Diagram of PCM Data Acquisition System.

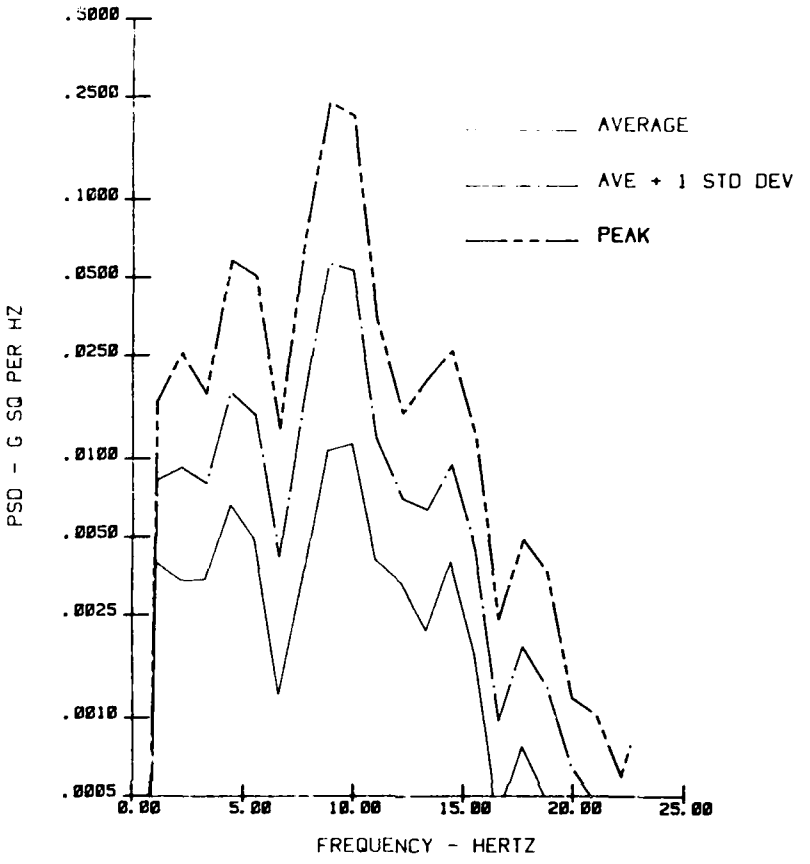

Figure 2. Typical PSD Data File.

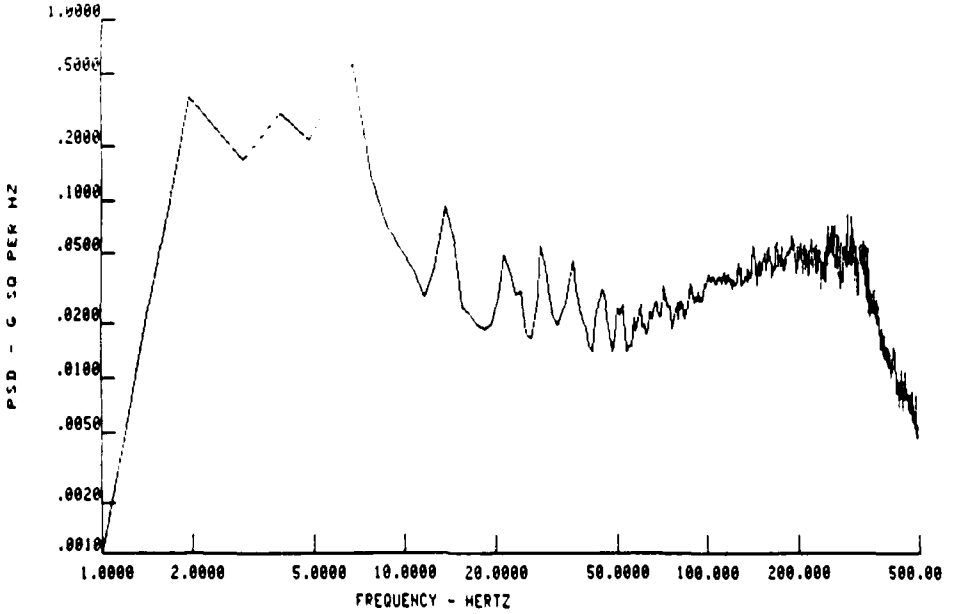

Figure 3. Typical Wheeled Vehicle Composite Spectrum.

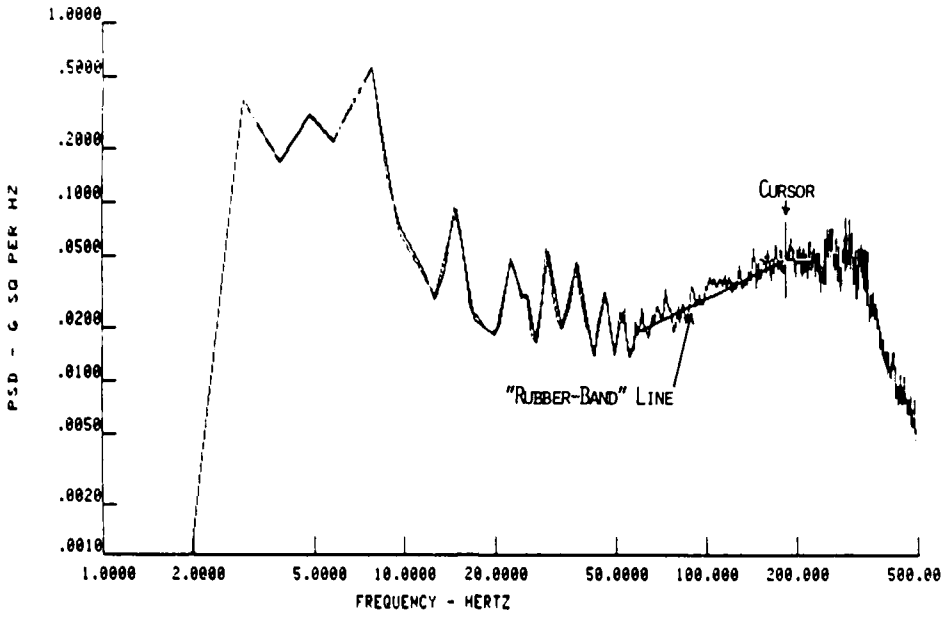

Figure 4. Defining Breakpoints With the Program CRVIB.

```
18     NUMBER OF BREAK POINTS
        3.34        .00002    FREQUENCY AND AMPLITUDE
        4.45        .01533    FREQUENCY AND AMPLITUDE
        8.75        .00018    FREQUENCY AND AMPLITUDE
        9.97        .00133    FREQUENCY AND AMPLITUDE
       11.09        .00171    FREQUENCY AND AMPLITUDE
       12.26        .00024    FREQUENCY AND AMPLITUDE
       15.54        .00033    FREQUENCY AND AMPLITUDE
       23.47        .00002    FREQUENCY AND AMPLITUDE
       24.52        .00002    FREQUENCY AND AMPLITUDE
       26.77        .00004    FREQUENCY AND AMPLITUDE
       29.03        .00002    FREQUENCY AND AMPLITUDE
```

Figure 5. Typical Breakpoint File From Program CRVIB.

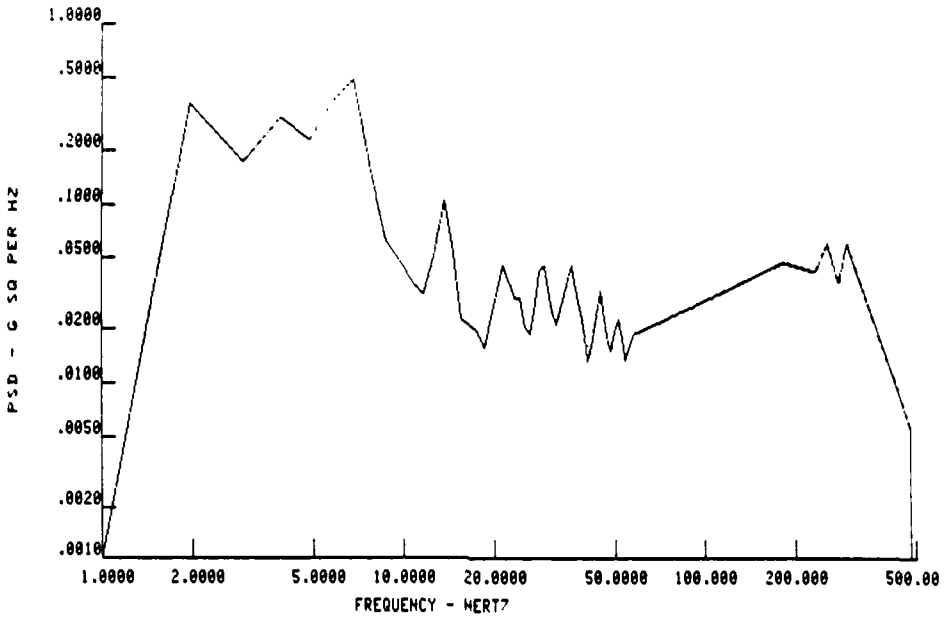

Figure 6. Typical Completed Spectrum.

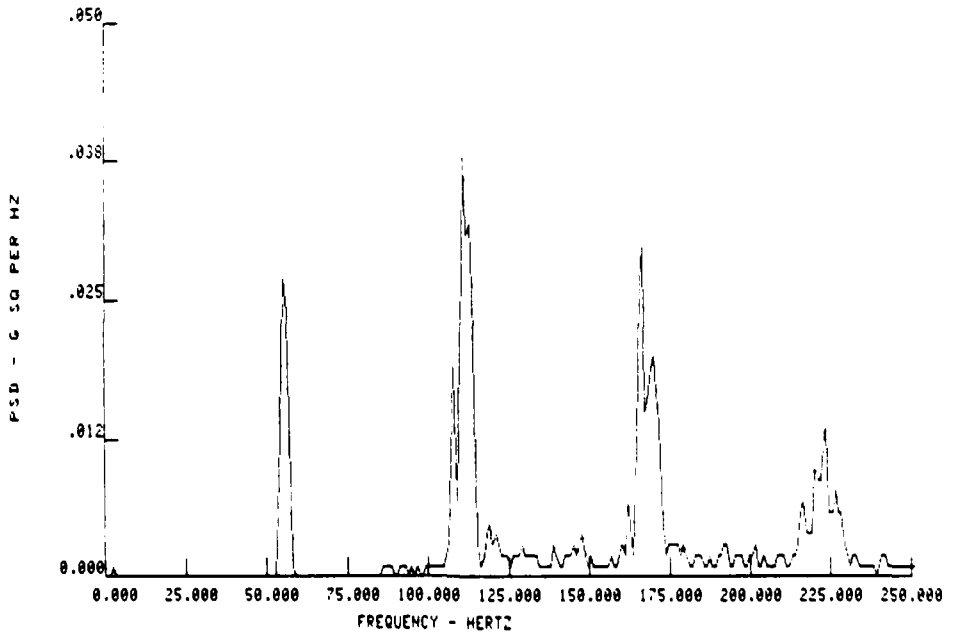

Figure 7. Typical Tracked Vehicle Spectrum.

```
6     NUMBER OF HARMONICS
 51.93     58.31     55.11       .38    .01112
107.83    114.22    111.02       .42    .02479
162.94    165.34    164.14       .25    .03538
217.25    222.04    219.65       .23    .01232
320.29    324.28    322.28       .15    .00635
325.88    334.66    330.27       .30    .01043
  1.1612  500.00      RMS OF RANDOM FLOOR,  UPPER FREQ
```

LOWER FREQ — UPPER FREQ — CENTER FREQ — RMS — PSD VALUE

Figure 8. Typical File of Periodics Created by the Program REMPR.

```
THE FOLLOWING DATA SETS WERE USED:
M1.PAVED, 6 MPH, 3PS, .EPT
M1.PAVED,10MPH,3PS,.EPT
M1.PAVED,12MPH,3PS,.EPT
M1.PAVED,14MPH,3PS,.EPT
      FREQUENCY   PSD VALUE      G(A,G)
                HARMONIC NUMBER: 1
         13.99        .00572
         21.96        .00921
                HARMONIC NUMBER: 2
         29.15        .00135
         39.94        .00181
                HARMONIC NUMBER: 3
         43.53        .00061
         65.10        .00128
                HARMONIC NUMBER: 4
         72.68        .00039
          0.00       0.00000
      50.78146        .10259     RMS, G SQ/HZ (5-500 HZ) OF RANDOM FLOOR
```

Figure 9. Typical File Created by the Program ACCPR.

```
                MASTER FILE FOR VIBRATION SCHEDULE CREATION
 FILE     PROGRAM      DATE              DESCRIPTION
$YD001    PSDFL     31 MAY 82     XM247 PAVED @ 6MPH  26 MAY 8
PKHUT     FNDPK     3JUN82        PK PSD,M1E1 B PACK,HULL,COMP
PkHUL     FNDPK     3JUN82        PK PSD,M1E1 B PACK,HULL,COMP
VSD02V    PKPSD     4 JUN 82      TR,VEH,M1,PAVED, 6MPH
VSD03V    PKPSD     4 JUN 82      TR,VEH,M1,PAVED, 8MPH
VSD04V    PKPSD     4 JUN 82      TR,VEH,M1,PAVED,10MPH
VSD05V    PKPSD     4 JUN 82      TR,VEH,M1,PAVED,12MPH
VSD06V    PKPSD     4 JUN 82      TR,VEH,M1,PAVED,14MPH
VSD07V    PKPSD     4 JUN 82      TR,VEH,M1,PAVED,16MPH
VSD08V    PKPSD     4 JUN 82      TR,VEH,M1,PAVED,18MPH
VSD09V    PKPSD     4 JUN 82      TR,VEH,M1,PAVED,20MPH
VSD10V    PKPSD     4 JUN 82      TR,VEH,M1,PAVED,22MPH
VSD11V    PKPSD     4 JUN 82      TR,VEH,M1,PAVED,24MPH
VSD12V    PKPSD     4 JUN 82      TR,VEH,M1,PAVED,26MPH
VSD13V    PKPSD     4 JUN 82      TR,VEH,M1,PAVED,28MPH
VSD14V    PKPSD     4 JUN 82      TR,VEH,M1,PAVED,30MPH
VSD16V    PKPSD     4 JUN 82      TR,VEH,M1,PAVED,32MPH
VSD17V    PKPSD     4 JUN 82      TR,VEH,M1,PAVED,34MPH
VSD18V    PKPSD     4 JUN 82      TR,VEH,M1,PAVED,36MPH
VSD19V    PKPSD     4 JUN 82      TR,VEH,M1,PAVED,38MPH
VSD21V    PKPSD     4 JUN 82      TR,VEH,M1,PAVED,40MPH
```

Figure 10. Typical Entry from VIBFIL.

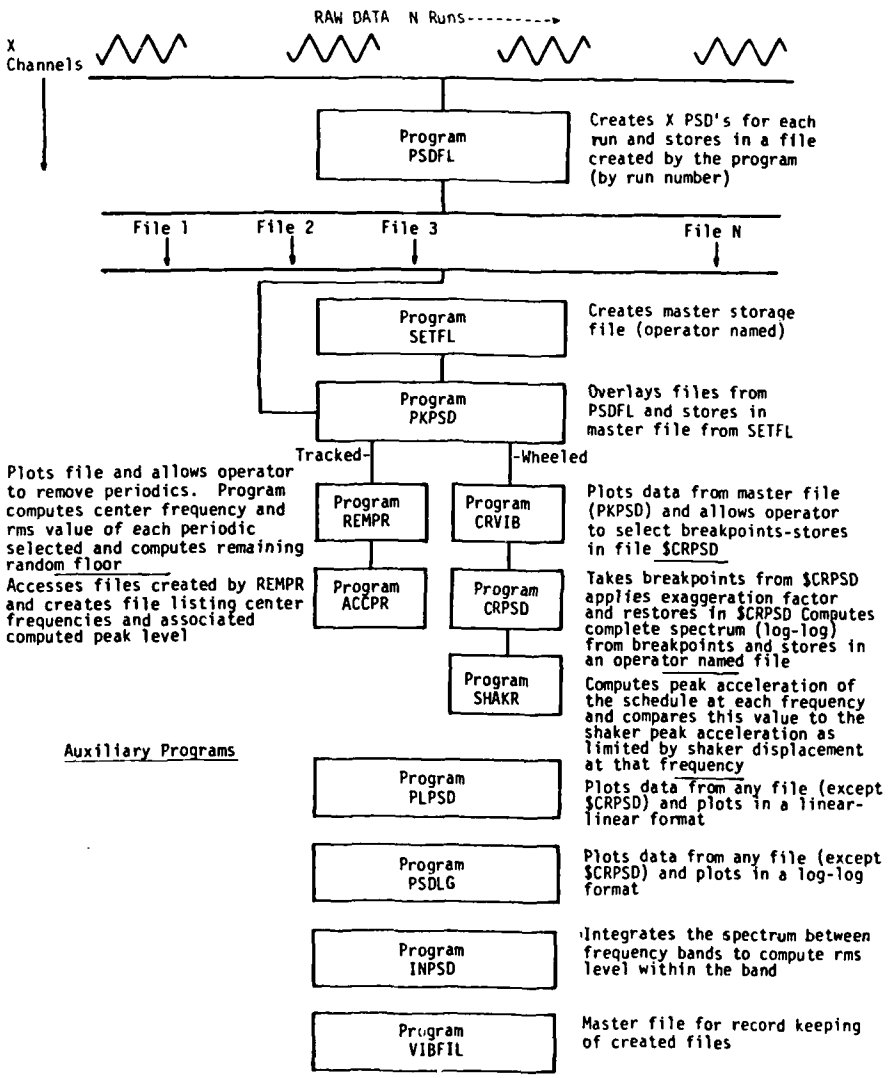

Figure 11. Summary of Vibration Schedule Development Procedure.

TESTING FOR SEVERE AERODYNAMICALLY INDUCED VIBRATION ENVIRONMENTS

H. N. Roos and G. R. Waymon
McDonnell Aircraft Company
McDonnell Douglas Corporation
St. Louis, Missouri

Aircraft structural vibration caused by separated aerodynamic flow is a condition commonly seen on high performance aircraft. Low speed wind tunnel and flight testing were conducted to evaluate F-15 vertical tail vibration response to excitation from separated airflow at high angles of attack. Good correlation was obtained between wind tunnel and flight vibration data. Flow visualization tests done in the wind tunnel determined that the separated flow affecting the tails comes from the mid-span leading edge of the wing. A special high-amplitude laboratory vibration exciter system was developed to duplicate the tail vibration level and to qualify all tail mounted equipment.

INTRODUCTION

The F-15 Eagle as shown in Figure 1 is a high performance fighter aircraft designed for the air superiority mission. Although both subsonic and supersonic capabilities were designed into the aircraft, most emphasis was placed on performance between 0.6 and 1.0 Mach number and 5000 to 30000 feet altitude. This is the part of the flight envelope where most high load factor maneuvers are performed. These maneuvers such as wind-up turns and pullups require that the aircraft be rotated to high angles of attack. This usually causes some airframe structural vibration from the resulting aerodynamic separated flow. The F-15 aircraft twin vertical tails exhibit a high vibration response when excited by turbulent aerodynamic flow. This paper deals with the comprehensive program of flight, wind tunnel, and laboratory testing conducted to determine the nature of this phenomenon.

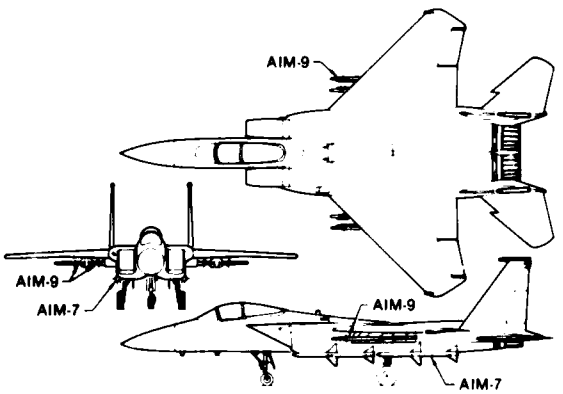

Fig. 1 - F-15 Air Superiority Configurations

FLIGHT TESTING

In order to explore the vibration response characteristics of the vertical tails, an F-15A aircraft was instrumented with accelerometers in the tail tip pod area. The two tails are asymmetric in that the left tail has a six-inch diameter tip pod and the right tail has a two-inch diameter pod. For this reason both tails were instrumented and the data were recorded using an onboard tape recorder. The transducers were located over the length of the tip pods as shown in Figure 2. Wind-up turn maneuvers were flown to evaluate the tail response levels in the presence of turbulent airflow. The maneuvers were performed by pulling and holding a limit load factor turn and as the airspeed bled off, the angle of attack was increased to 30 degrees. Wind up turn (WUT) maneuvers were flown in both left and right directions. The typical entry flight conditions for these maneuvers was 0.95 Mach at an altitude of 20000 feet.

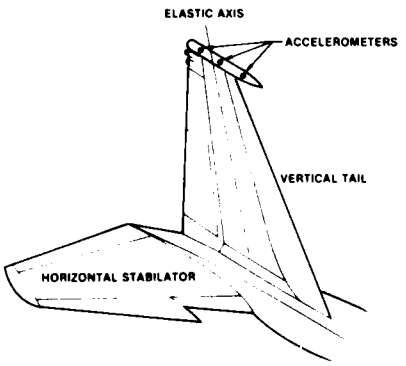

Fig. 2 - Flight Test Instrumentation

Vibration response data for these maneuvers were analyzed and compared with aircraft angle of attack (AOA). These results showed that tail vibration response levels increased with angle of attack to a peak at 22 degrees and then fell off sharply as AOA continued to increase. Figure 3 shows how RMS acceleration of the tail tip is affected by aircraft angle of attack for a typical maneuver.

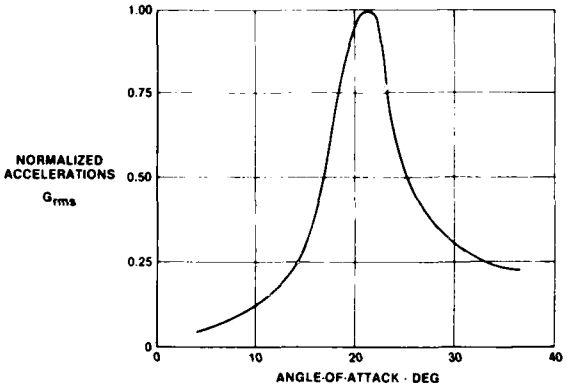

Fig. 3 - Tail Vibration vs Aircraft Angle-of-Attack

Data were also analyzed for frequency content using Power Spectral Density (PSD) techniques. This analysis shows that the peak response levels coincide with vertical tail resonant frequencies. The Figure 4 PSD frequency spectrum shows the fundamental bending mode at 10 Hz and the first tail torsion mode at 30 Hz. The torsion mode peaks at 22 degrees AOA and is the predominant response mode. The 10 Hz bending mode peeks at about 25 degrees AOA. This difference in AOA for the peak response of the various modes is due to a change in the frequency content of the flow impinging on the tail as the airframe rotates in the airstream.

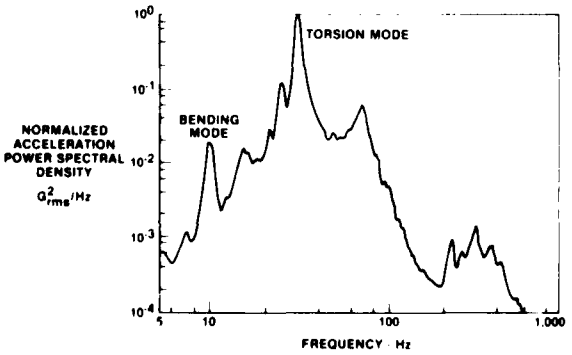

Fig. 4 - Tail Response Frequency Spectrum Flight Test Data

During the course of evaluating tail response characteristics, a large number of nominally identical maneuvers were flown. There turned out to be a wide variation in the maximum vibration levels for these maneuvers. This can be attributed to both pilot technique of flying the maneuver and the dynamic pressure at the time the AOA is 22 degrees. As the maneuver is flown the aircraft is gradually rotated to higher AOA. The angular rotation speed through 22 degrees AOA has an effect on the maximum vibration response levels. A slow angular rate through 22 degrees will result in high tail vibration levels while a fast rotation through 22 degrees does not allow time for the response to build up thus resulting in lower response levels. Dynamic pressure (q) is also responsible for variation in response levels. Maximum response levels were found to be a direct function of q. Data from several maneuvers are shown on the Figure 5 plot. This relationship was used in conjunction with aircraft performance limits to determine a theoretical maximum vibration response level for the flight envelope.

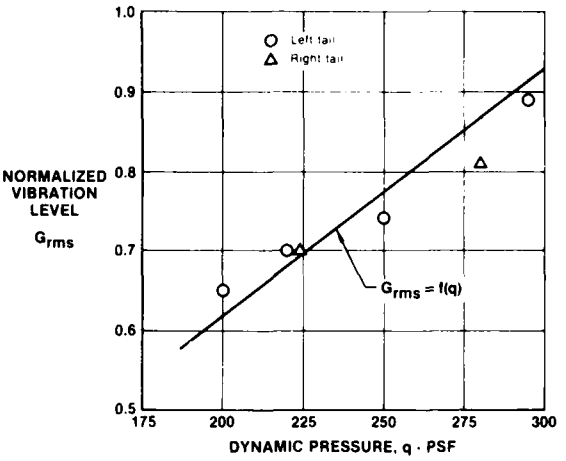

Fig. 5 - Vibration Level as a Function of Dynamic Pressure

WIND TUNNEL TESTING

Low speed wind tunnel testing was performed to determine if the vertical tail vibration response to separated airflow could be duplicated with an aircraft model. A 13 percent scale rigid F-15 aero model was used with a flexible vertical tail. The flexible tail was originally built for the F-15 flutter model. A photograph of this model installed in the wind tunnel is shown in Figure 6. Model test instrumentation consisted of lateral accelerometers at the forward and aft ends of the flexible tail tip pod as shown in Figure 7. Bending and torsion strain gage bridges were also used.

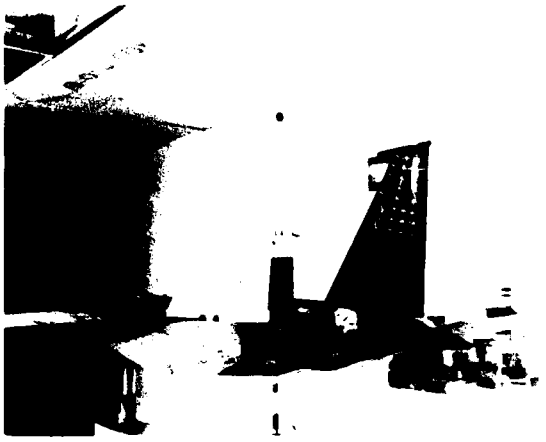

Fig. 6 - Model in Wind Tunnel

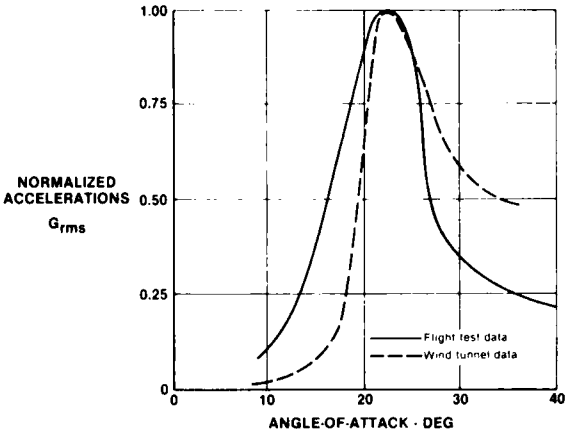

Fig. 8 - Tail Aft Pod Vibration as a Function of Aircraft Angle-of-Attack

Fig. 7 - Model Tail Instrumentation Locations

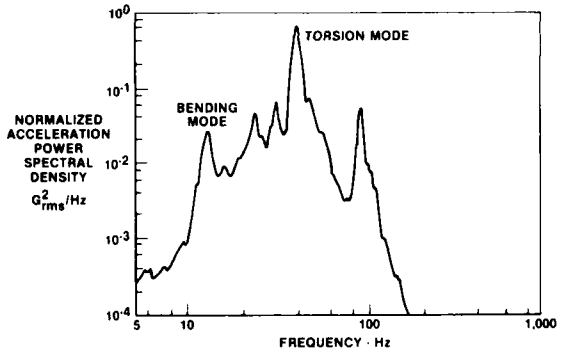

Fig. 9 - Tail Response Frequency Spectrum Wind Tunnel Data

The wind tunnel test procedure consisted of rotating the model from 0 through 35 degrees AOA at several tunnel airspeeds. Results from these tests showed good correlation with flight test results. The peak model tail response occurred at 22 degrees AOA as it did with the flight test data. A comparison of tail vibration response as a function of AOA is shown on Figure 8 for both flight and tunnel tests. The predominant vibration mode at the peak response condition was tail first torsion. A PSD frequency spectrum for model tail response at 22 degrees AOA is shown in Figure 9. The first bending mode at 13 Hz and the first torsion mode of 40 Hz are easily identified. Using the 1.346 ratio between flexible model frequencies and full scale aircraft frequencies, the correlation with flight test results of 10 Hz and 30 Hz for these modes is very good.

Response vibration data for the wind tunnel model were correlated with dynamic pressure for various AOA conditions. This correlation is shown for the 22 degree maximum response point on the Figure 10 plot. Correlation of the wind tunnel data with q is slightly better than was the Figure 5 flight data. This is to be expected considering the transient nature of the flight test maneuver.

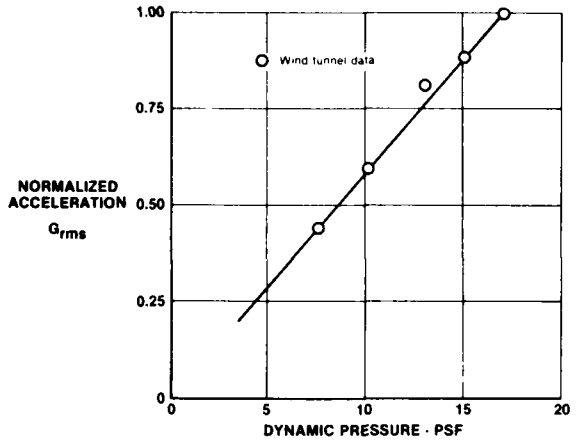

Fig. 10 - Vibration Level as a Function of Dynamic Pressure

In addition to obtaining model response data, the wind tunnel evaluation was useful in determining the source of the turbulent airflow which causes the tail vibration response. Flow visualization tests were conducted using mold-line tufts, fog, and hot wire anemometer techniques. The results of these efforts showed that at the peak tail response AOA of 22 degrees, the flow field consisted of unsteady, high velocity air eminating from the mid span of the wing leading edge. At this high AOA condition the flow separates and is pulled inboard by the low pessure region over the wide fuselage where it envelops the upper tail causing the high vibration response. This is shown on the Figure 11 sketch. From this testing it became apparent that below 22 degrees AOA the separated flow would affect only the lower part of the tail and at AOA's above 22 degrees, the separated flow went over the top of the tail. This explains why the peak response occurs at 22 degrees.

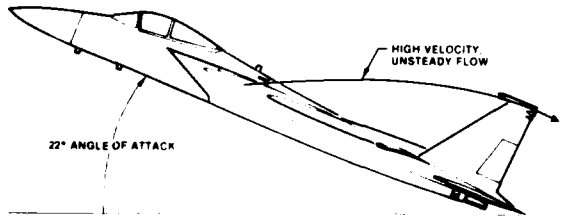

Fig. 11 - Flow Field Pattern

Response data from the wind tunnel test was quite repeatable due to the strict control over all the important parameters. Each test case in the wind tunnel could be judged on the basis of data from one run. The comparable flight test evaluations required several maneuvers to get a high confidence level in the measured data. Because of the excellent correlation between flight and wind tunnel test results there is good reason to use flexible model response data to identify high vibration response areas of the flight envelope due to separated airflow. Using model test results, new or modified aircraft designs can be evaluated prior to building flight hardware. Identification of high vibration response with a model test would provide an opportunity to consider alternate designs to reduce the vibration levels.

LABORATORY VIBRATION TESTING

Several equipment items consisting of navigation lights and electronic warfare antennas are located in the tail tip pod area as shown in Figure 12. These equipment items are exposed to the tail response vibration environment so a laboratory vibration qualification test was performed. After reviewing the tail response levels from the flight test evaluation, it was obvious that the equipment would have to be qualified to unusually high vibration levels.

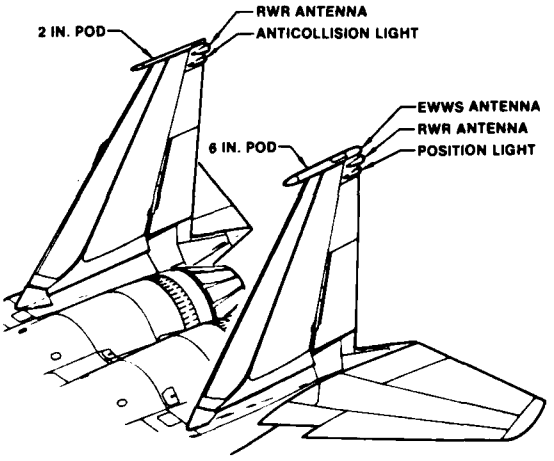

Fig. 12 - Vertical Tail Equipment

Vibration response data obtained from the Figure 2 measurands were reduced using one-third octave-band frequency analysis techniques. Vibration levels in each one-third octave-band for 15 high response maneuvers were combined using statistical methods. Mean plus three sigma levels were obtained for each frequency band. These levels were considered representative of the expected worst case that would be experienced by the equipment. From

these levels a vibration test curve was developed for laboratory qualification of the equipment. Vibration levels in the lateral axis were an order of magnitude greater than levels in the longitudinal and vertical axes. Because of this large difference, a separate test curve was formulated for the lateral axis. These curves are shown on Figure 13.

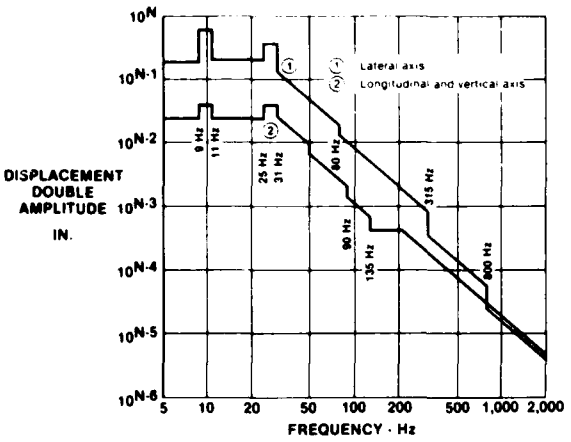

Fig. 13 - Vibration Test Curve for Tail Tip Equipment

After establishing the equipment test levels, it then became necessary to define a realistic test time. The high response levels are experienced on the aircraft during transient type maneuvers of which the occurrence is not easily predictable. Because the response level is dependent on angle of attack an estimate of aircraft operation in the AOA range from 20 to 25 degrees was made based on USAF usage data. Time history data for maneuvers causing the high level response levels were reviewed to determine the length of time at the highest levels compared with the time in the 20-25 degree AOA range. This exposure time per maneuver along with the usage projection were combined to obtain a realistic test time of 3 hours for each tail and equipment resonant frequency which would be representative of an aircraft lifetime.

Following a search for a suitable test facility it was determined that no equipment existed that had the capability to duplicate the required test curve levels. In order to fill this need a special high-amplitude vibration exciter system was developed and is described by Miller in Reference [1]. This system consists of a high output electromagnetic vibration shaker connected to a lever arm to magnify the shaker vibration output. This is shown on the Figure 14 schematic. Equipment items to be tested were mounted on the end of the lever arm for the high amplitude tests. This setup permitted the performance of vibration tests that had previously been beyond the capability of existing test equipment. Vibration qualification testing was successfully performed on all of the vertical tail equipment items to demonstrate their capability to survive in this high level environment.

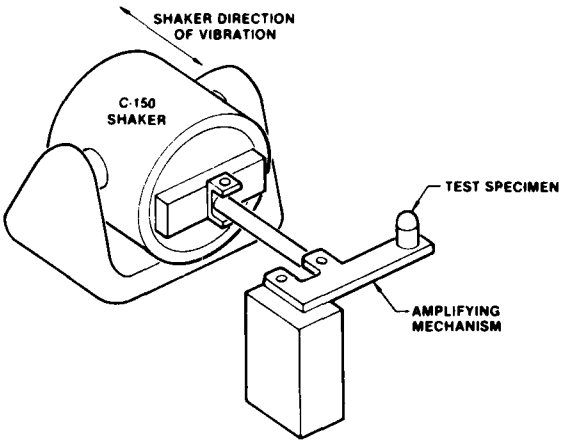

Fig. 14 - High Level Vibration Test Setup Schematic

CONCLUSION

Aircraft structural vibration response to excitation from separated aerodynamic flow during flight can be simulated in the low speed wind tunnel using a dynamically scaled flexible model. Both flight and wind tunnel test results confirmed the dependency of the peak vibration response on aircraft angle of attack and on dynamic pressure. Accelerometer and strain gage instrumentation on the wind tunnel model are adequate to define frequency and modal characteristics. Tufts, fog, and hot wire anemometer techniques are useful in determining the extent of the separated flow field causing structural vibration. The good correlation between flight and wind tunnel test results demonstrates the potential of using flexible model tests as a tool to define high vibration regions of the flight envelope due to separated air flow excitation. Wind tunnel results could be beneficial in evaluating new or modified aircraft configurations prior to building flight hardware.

High structural vibration response levels were beyond the capability of existing vibration exciter systems. A special high-amplitude exciter system was developed to perform laboratory qualification tests on equipment affected by the high response environment.

REFERENCE

1. R. M. Miller, "Development of High-Amplitude Vibration Exciter System", Proceedings - Institute of Environmetnal Sciences, April 1982.

EVALUATION OF MODAL TESTING TECHNIQUES FOR SPACECRAFT STRUCTURES

Kuniaki Shiraki and Hidehiko Mitsuma
National Space Development Agency of Japan
2-4-1, Hamamatsu-cho, Minato-ku, Tokyo 105, Japan

The paper describes a comparative study of modal testing techniques with a base excitation which are applicable to the development of spacecraft structures. Classical sine sweeps and random test methods based upon digital analysis techniques are compared by measuring transfer functions of a simple beam specimen. For the random test data, modal analyses were performed using two kinds of analyzers, for two steps of input levels, respectively. The modal parameters obtained by both analyzers were in good agreement. And the structural response non-linear characteristics due to the input level change were investigated. An example of the application of these techniques to the development of the Engineering Test Satellite-III is shown.

INTRODUCTION

The modal testing of spacecraft structures is performed as a part of the structural verification test. The primary objective of this test is to obtain fixed-free modal vibration data suitable for evaluating the math model of the spacecraft for use in the dynamic load analysis.

For the excitation technique of the structure, sine sweeps have been performed with a low level base excitation. Response data are analyzed using analog tracking filters in a form of transfer functions referenced to the base input acceleration such as, (1) Gain-Phase plot, (2) Co-Quad plot, and (3) Vector plot. And modal parameters such as the natural frequency, mode shape and damping factor are extracted from these plots.

Recently, the advent of mini-computers made the modal testing using digital techniques as an easily attainable tool in the spacecraft programs (Reference 1 and 2). The structure is excited by a random noise. The response data are digitized and generate transfer functions. Modal parameters are extracted using data curve fitting routines (Reference 3).

This paper reports results of a comparative study of these modal techniques with a review of the sine sweep testing. An experiment was performed using a beam model. The model was excited by the sinusoidal sweep and random noise, respectively. The test data were analyzed by an analog tracking filter system and FFT applied digital modal analysis systems, respectively.

For the sine sweep test data, the effects of sweep directions and sweep rates were investigated. And for the random test data, the modal analyses were performed using two kinds of modal extraction techniques, for two different input levels, respectively.

Finally, these techniques were applied to the modal testing of the Japanese Engineering Test Satellite-III (ETS-III).

BASE EXCITATION

Now, we consider a simple single degree of freedom (SDOF) system with a base excitation. For a linear, SDOF base-excited system, Figure 1, the Equation of motion is

$$\ddot{Z} + 2\zeta\omega_n\dot{Z} + \omega_n^2 Z = -\ddot{Y} \qquad (1)$$

where

Z = relative displacement (X-Y)

ω_n = undamped natural frequency ($\sqrt{k/m}$)

ζ = fraction of critical damping ($c/2\sqrt{mk}$)

Assuming harmonic motion, the linear transfer function between the acceleration of the mass and the acceleration of the base is

$$H(P) = \frac{1 + j2\zeta p}{1 - p^2 + j2\zeta p} \qquad (2)$$

where

$$p = \frac{\text{Excitation Frequency}}{\text{Natural Frequency, } \omega_n}$$

j = imaginary unit

In complex polar notation, Equation (2) can be expressed in terms of a gain factor $|H(P)|$ and a phase factor $\phi(P)$ as follows.

$$H(p) = |H(p)|\, e^{-j\phi(p)} \qquad (3a)$$

where

$$|H(P)| = \left\{ \frac{1 + (2\zeta p)^2}{(1-p^2)^2 + (2\zeta p)^2} \right\}^{\frac{1}{2}} \qquad (3b)$$

$$\phi(p) = \tan^{-1}\left[\frac{2\zeta p^3}{1- p^2 + (2\zeta p)^2} \right] \qquad (3c)$$

This particular function is called a Transmissibility or Transfer function. The Plot of $|H(p)|$ and $\phi(p)$ is called the Bode plot or Gain-Phase plot. Equation (2) also can be written in real and imaginary parts as

$$H(p) = \text{Re}\left[H(p)\right] + j\ \text{Im}\left[H(p)\right] \qquad (4a)$$

where

$$\text{Re}\left[H(p)\right] = \frac{1- p^2 + (2\zeta p)^2}{(1-p^2)^2 + (2\zeta p)^2} \qquad (4b)$$

$$\text{Im}\left[H(p)\right] = \frac{2\zeta p^3}{(1-p^2)^2 + (2\zeta p)^2} \qquad (4c)$$

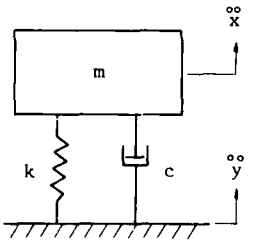

Figure 1. Base Excitation of SDOF System

The plot of real and imaginary parts is called the Co-Quad plot of a transfer function. Now at a modal resonance, i.e., p = 1, it is clear from the expression above that

$$\text{Re}\left[H(p)\right] = 1 \qquad (4d)$$

$$\text{Im}\left[H(p)\right] = \frac{1}{2\zeta} \qquad (4e)$$

If we put, Re H(p)=0 in equation (4b), we obtain

$$p = \frac{1}{\sqrt{1-4\zeta^2}} \quad (> 1, \text{ for } \zeta < \tfrac{1}{2}) \qquad (4f)$$

which is called the phase resonance.

The plot of Equation (2) in the Nyquist (or real vs. imaginary) plane is called the Vector plot or Argand plot. The modal resonance curve is close to a circle in the Nyquist plane. Usually, modal parameters at a resonance have been extracted from these plots (Reference 4, 5 and 6).

EXPERIMENTAL STUDY FOR A BEAM MODEL

To study the characteristics of modal techniques, a simplified beam model, combined three beams, was built and tested, Figure 2. The beam configuration was rigidly attached to a shaker and base excited. Figure 3 shows, in block diagram form, a typical test set-up. The specimen was instrumented with 9 accelerometers, one at the base, to measure the response and input levels.

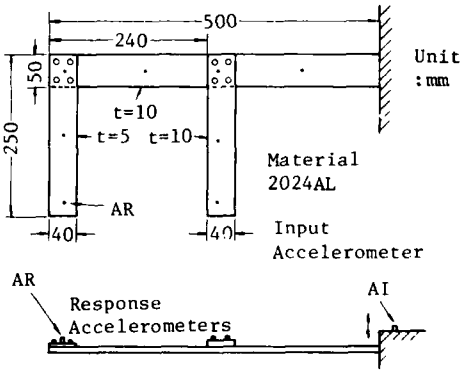

Figure 2. Beam Model Test Configuration

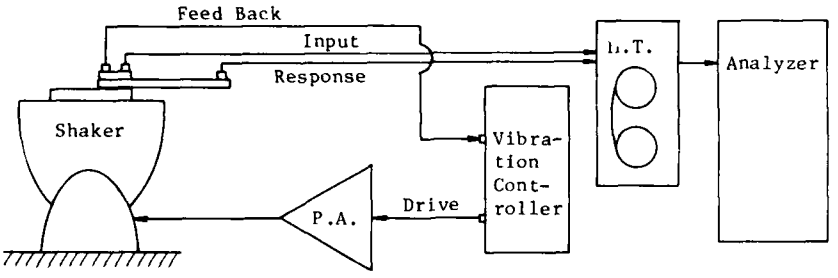

Figure 3. Test Set-up

The general procedure of data analysis is shown in a block diagram in Figure 4. The sine sweep data were analyzed using analog tracking filters in a form of the transfer function Gain-Phase plot. The random data were analyzed using digital analyzers applying FFT techniques. The digitized data were used to generate transfer functions, and the curve fitting techniques were applied to extract modal parameters. The transfer functions and mode shapes were hard copied.

plot for low level PSD input of $5 \times 10^{-4} G^2/Hz$ at a point AR in Figure 2, which corresponds to the sine sweep plot in Figure 5. Comparing both plots, we can observe for the 1st mode of 22.7 Hz, the sine sweep transfer function gives a higher build-up of the amplitude, and for the 4th mode of 183 Hz, the random test transfer function gives a higher amplitude. Although the sine sweep transfer function shows a small frequency shift to upper frequency, both plots are generally in good agreement.

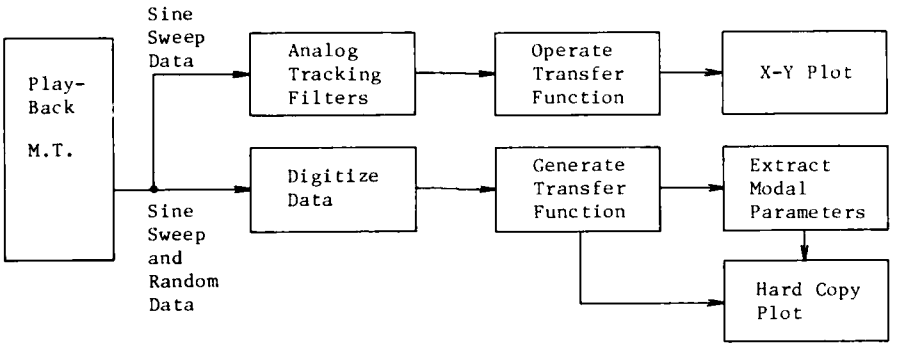

Figure 4. Data Analysis General Procedure

(1) Sine Sweep Tests

The sine sweep tests were performed with a constant base acceleration input level of 0.5 Go-p in the frequency range from 5 to 250 Hz. The logarithmic sweeps were applied because they are typical for spacecraft testings. Taking the sweep rate of 2 Oct/min with an increasing frequency, sweep up, as a reference test, the tests with different sweep rates of 1, 4, and 6 Oct/min and a decreasing frequency, sweep down test for 2 Oct/min rate were performed. A typical transfer function Gain-Phase plot for the 2 Oct/min sweep up test at a point AR in Figure 2, is shown in Figure 5. The configuration provided four modes in the frequency range from 5 to 200 Hz as indicated by the transfer function.

Table 1 compares the natural frequencies and Q-factors, the transmissibility at resonances, for different sweep directions and sweep rates. All data except the first column are expressed by factors for the 2 Oct/min sweep up test data. The table shows, the faster the sweep, the more the frequency shift and the lower the Q-factor. The sweep down data shows a smaller percentage of the frequency shift and a higher build-up of the resonance amplitude compared with the sweep up data.

(2) Random Tests

The random tests were performed with an equalized pure random excitation input in the frequency range from 5 to 200 Hz. Figure 6 shows a typical transfer function Gain-Phase

Table 1
Beam Model Sine Sweep Test, Comparison of Natural Frequencies and Q-factors for Different Sweep Directions and Sweep Rates

MODE		SWEEP RATE (Oct/min)				
		2 (up)	2 (down)	1 (up)	4 (up)	6 (up)
1	f1(Hz)	22.8*	0.97	0.98	1.03	1.04
	Q1	76	1.29	1.22	0.82	0.71
2	f2(Hz)	75	0.99	0.99	1.01	1.03
	Q2	19	1.32	1.16	0.89	0.74
3	f3(Hz)	95	1.00	0.99	1.02	1.03
	Q3	29	1.24	1.17	0.93	0.97
4	f4(Hz)	182	0.99	0.99	1.03	1.04
	Q4	38	1.84	1.32	0.92	0.74

fi : Amplitude Peak Frequency
Qi : Peak Amplitude of Gain Factor
* : Except the first column in Table 1, fi and Qi are given by factors for 2 Oct/min, sweep up data.

(3) Comparison of Random Techniques

To evaluate the modal extraction techniques applicable, two modal analysis systems, the Gen Rad TD 1923 (noted as Modal A) and the Hewlett Packard 5451C (noted as Modal B), were used to analyze the same random test data. The

tests were performed for two different input levels. The lower level is 5×10^{-4} G^2/Hz, and the higher level is 5×10^{-2} G^2/Hz in PSD, respectively. The comparison of modal parameters, i.e., the modal frequencies and modal damping extracted by these analyzers for two input levels is shown in Table 2. We can observe that both analyzers give almost the same results though the analyses were performed by different personnel. And also they are in good agreement with the sweep test natural frequencies in Table 1. However, we notice clear changes of modal parameters due to the increase of input level which will be discussed in the next section.

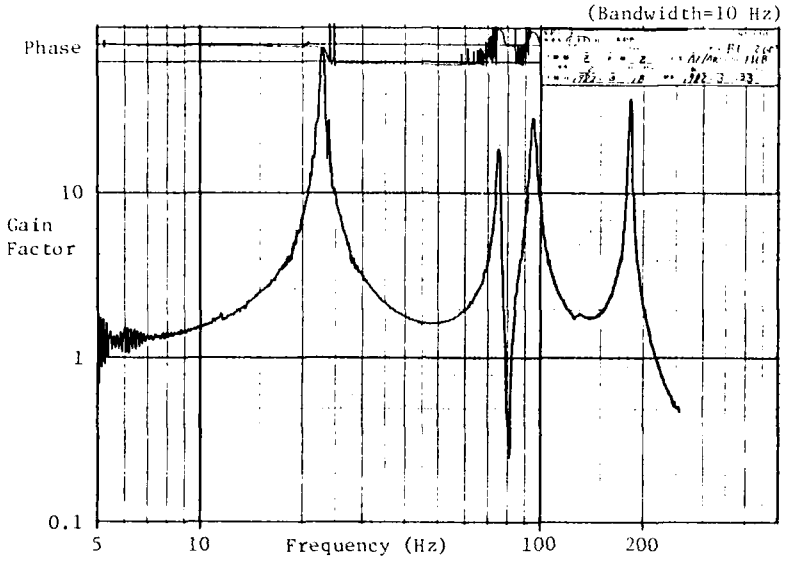

Figure 5. Beam Model Sine Sweep Test, Typical Transfer Function Gain-Phase Plot, AR/AI

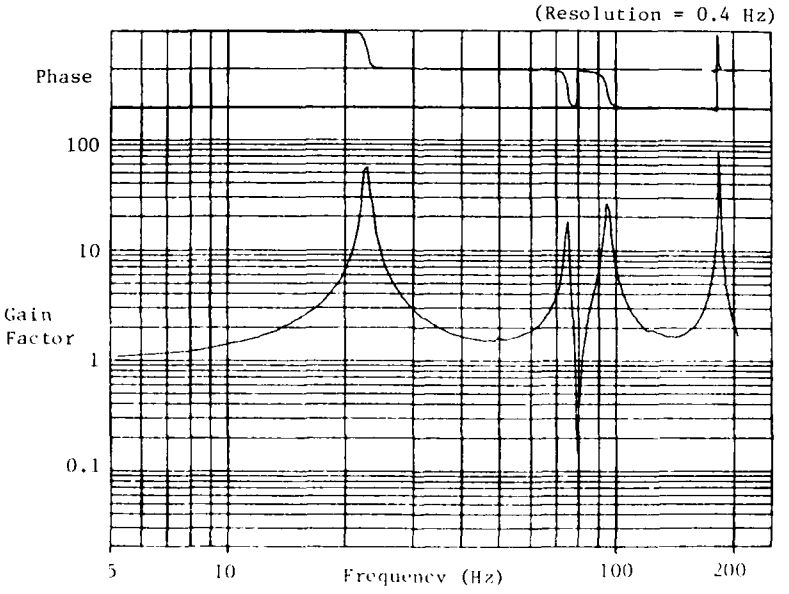

Figure 6. Beam Model Random Test, Typical Transfer Function Gain-Phase Plot, AR/AI

(4) Effects of Structural Non-linearity

As shown in Table 2, the increase of input level lowers the natural frequencies, and causes the modal damping changes depending upon the modes. These phenomena are clearly shown by the transfer function Co-Quad plots in Figures 7 and 8, and the vector plots in Figure 9, for the 3rd and 4th modes, respectively.

Table 2
Beam Model Random Test, Comparison of Measured Modal Parameters for Two Modal Extraction Systems and Two Excitation Levels

TEST CONDITON		INPUT LEVEL, PSD(G^2/Hz)			
		$5x10^{-4}$		$5x10^{-2}$	
Mode \ Analysis		Modal A	Modal B	Modal A	Modal B
1	f1(Hz)	22.74	22.67	22.47	22.39
	ζ1(%)	0.93	1.06	0.80	1.00
2	f2(Hz)	74.54	74.49	74.17	74.27
	ζ2(%)	0.76	0.72	1.55	1.29
3	f3(Hz)	94.80	94.54	93.75	93.67
	ζ3(%)	1.35	1.36	1.21	1.17
4	f4(Hz)	182.95	182.69	181.49	181.37
	ζ4(%)	0.20	0.25	0.50	0.54

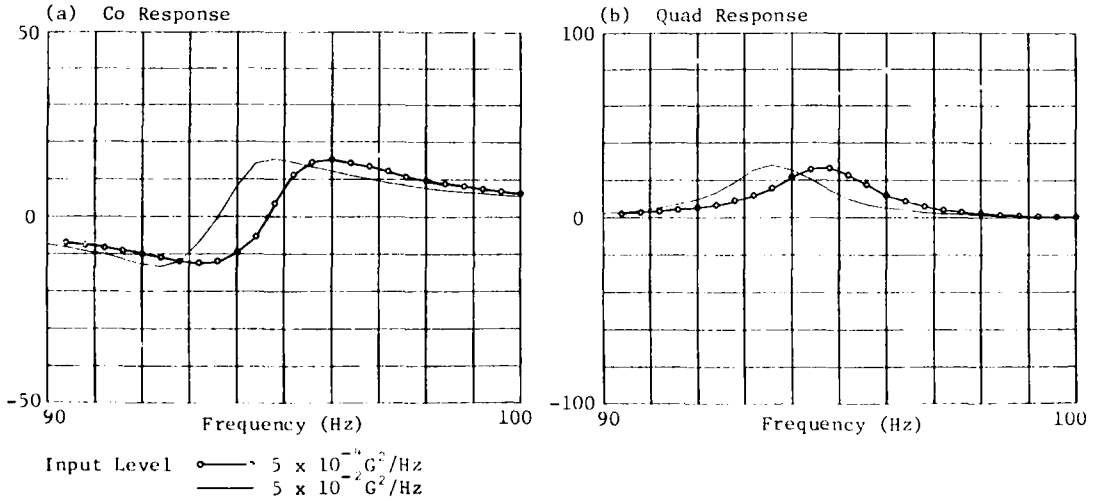

Figure 7. Beam Model Random Test, Transfer Function Co-Quad Response Plots Comparison for Different Excitation Levels, AR/AI (3rd Mode)

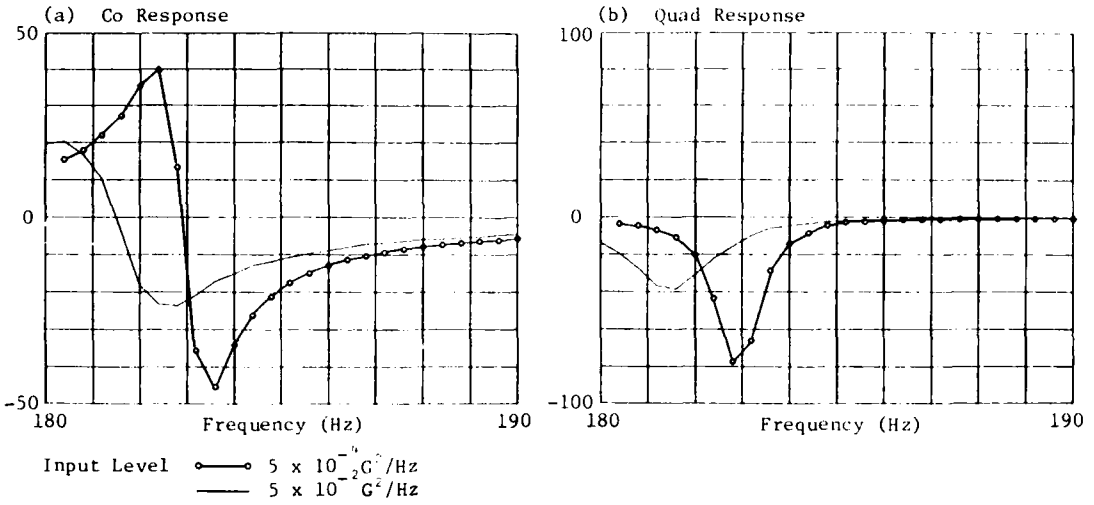

Figure 8. Beam Model Random Test, Transfer Function Co-Quad Response Plots Comparison for Different Excitation Levels, AR/AI (4th Mode)

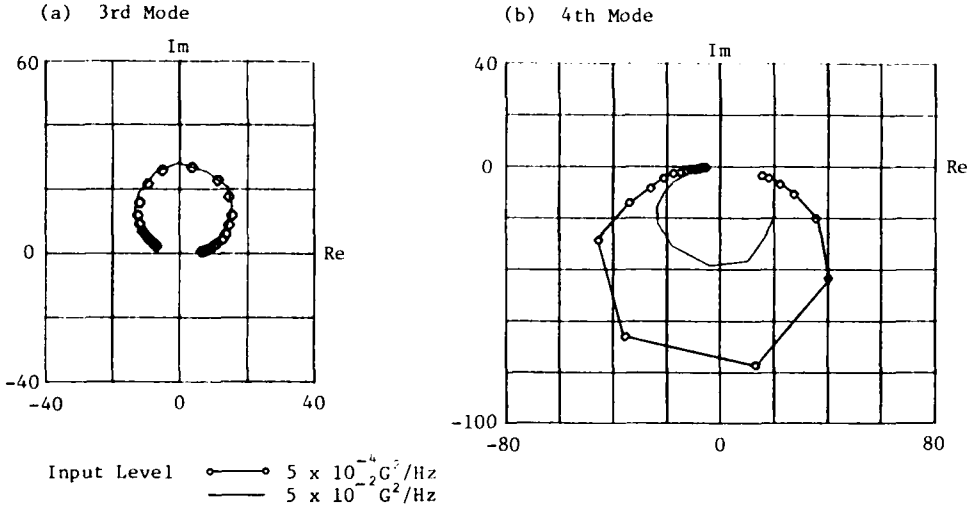

Figure 9. Beam Model Random Test, Comparison of Transfer Function Vector Plots for Two Different Excitation Levels, AR/AI (3rd and 4th Modes)

For both modes, the natural frequencies shift to lower frequencies with the increase of input level. However for the damping, though the 3rd mode shows almost no change, the 4th mode shows a remarkable change, about twice, with the increase of input level.

Those four modes are shown in Figure 10. The modes which cause a remarkable damping increase are the 2nd and the 4th modes that indicate fairly strong torsional mode of the longer beam in the configuration tested.

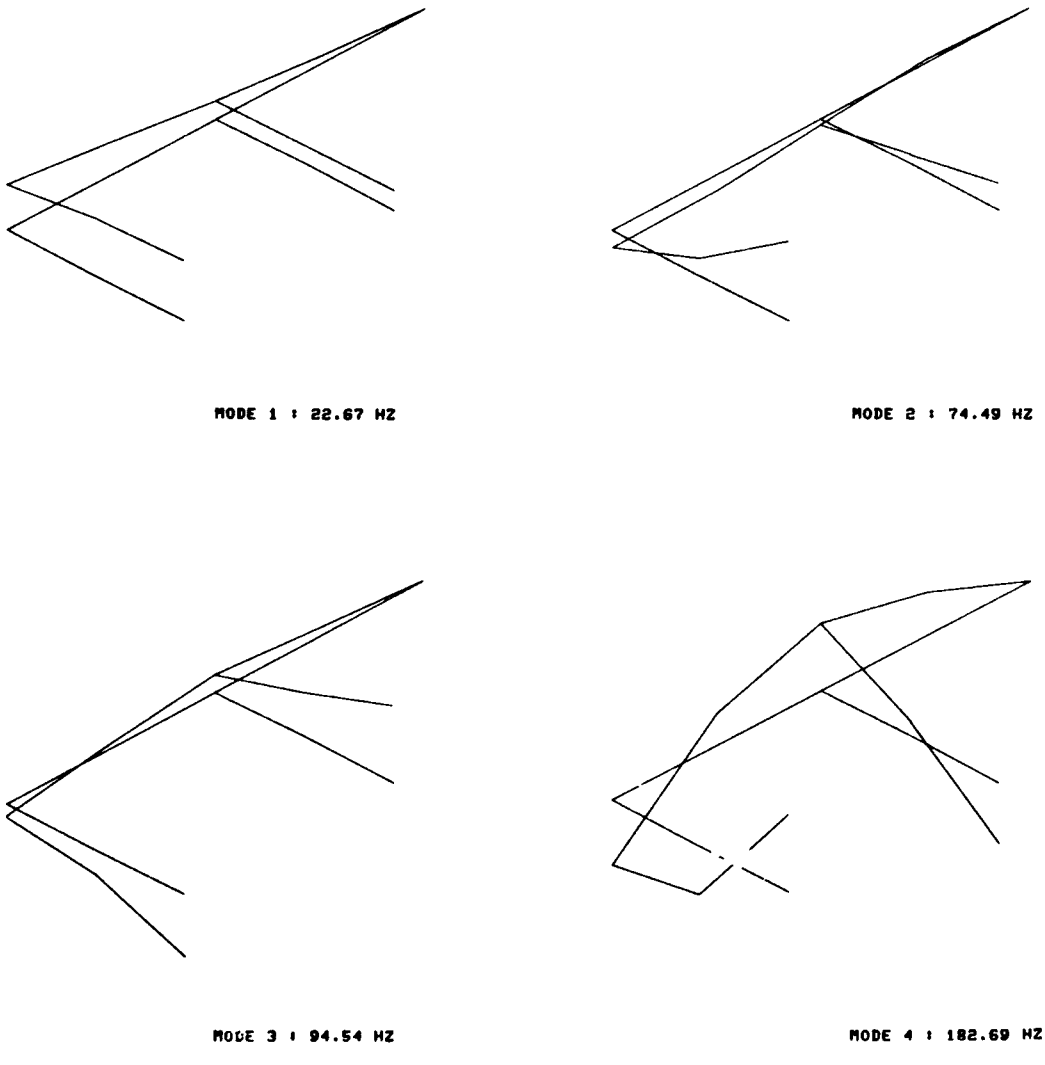

Figure 10. Beam Model Random Test, Mode Shapes for Excitation Level of $5 \times 10^{-4} G^2/Hz$

THE ETS-III SPACECRAFT MODAL TESTING

The modal survey test of the ETS-III structural dynamic model was conducted in order to determine the validity of the analytical model. The ETS-III shown in Figure 11 is the first three-axis-controlled spacecraft developed in Japan. It has a size of 1.1 m by 1.2 m and 2.1 m in height with launch weight of 383kg. The test set-up, shown in Figure 12 consisted of the spacecraft attached to the MDAC 3731A payload attach fitting (LVAF) on a shaker table. The low level sine sweep test, and the random test were performed in the direction of the spacecraft 3 perpendicular axes X, Y, and Z, respectively.

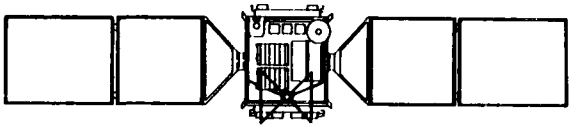

Figure 11. ETS-III Orbital Configuration (Top View)

For the sine sweep tests, the input level of 0.2 Go-p was controlled at the base of the LVAF in the frequency range from 5 to 200 Hz with the sweep rate of 2 Oct/min. Notching was imposed at the lowest lateral resonance to prevent overtesting of the spacecraft primary structure. For the random tests, the PSD input level of 5×10^{-4} G^2/Hz in the frequency range from 10 to 200 Hz, was equalized during 5 minutes of excitation. About 180 accelerometers were installed on the spacecraft to record the response.

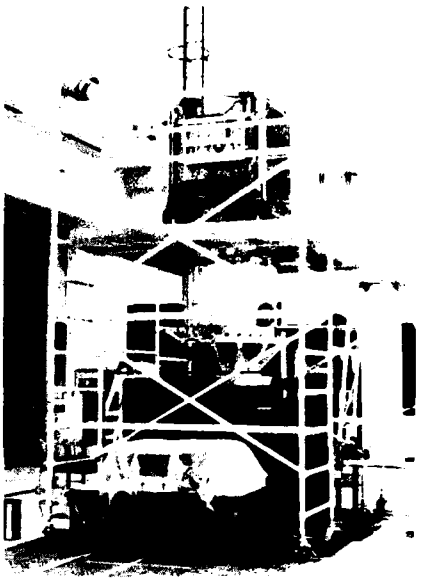

Figure 12. ETS-III Vibration Test Set-up

Figure 13 compares typical transfer function plots obtained by both the sine sweep and the random tests, respectively. It shows the same tendency as the case of the beam configu-

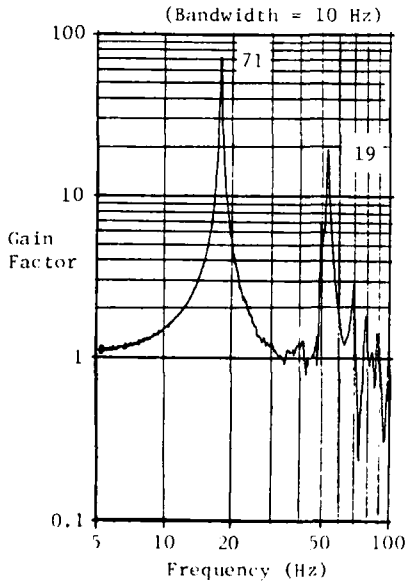

(a) Sine Sweep Test (Input Level=0.2 Go-p, Sweep Rate=2 Oct/min)

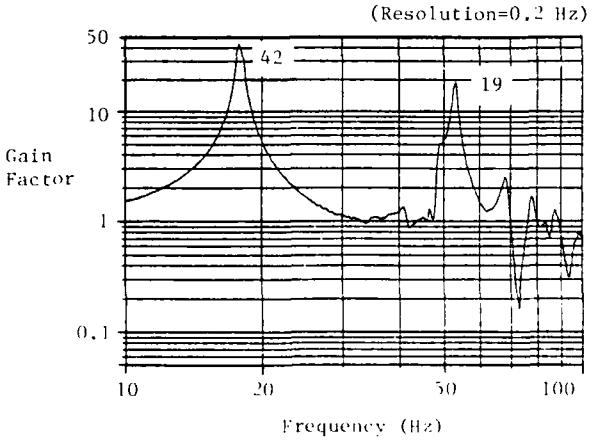

(b) Random Test (Input Level=5×10^{-4} G^2/Hz)

Figure 13. ETS-III Transfer Function Gain Factor Plots Comparison (Lateral Axis Response)

ration. The random test indicates a lower peak amplitude build-up compared with the sine test, at the 1st mode of 18 Hz due to the resolution problem.

For the random data, the modal analysis was performed using curve fitting techniques. The measured modes were compared with the predicted analytical modes. Table 3 contains the test and analysis comparisons for some of the correlated modes. Since the spacecraft structure was only excited in the spacecraft X, Y, and Z axes, not all of the spacecraft modes were excited. A total of 11 test modes were correlated with analytical predictions. Figure 14 illustrates measured 1st lateral mode.

To evaluate the adequacy of the measured modes, the orthogonality criteria was applied (Reference 2). The values of less than 0.2 for the off-diagonal matrix terms of the orthogonality matrix were obtained, and therefore, they were considered as acceptable.

Table 3
ETS-III Modal Test and Analysis Comparison

Mode	TEST		ANALYSIS
	Frequency (Hz)	Damping Factor (%)	Frequency (Hz)
1	17.9 X *	1.0	18.3
2	20.4 Y	1.1	21.2
3	29.0 Y	-	28.7
4	34.5 X	-	35.3
5	48.7 X	1.2	55.6
6	48.8 Y	1.3	55.6
7	53.1 X	1.1	52.0
8	54.1 Z	3.0	53.6
9	57.2 Y	-	51.2
10	64.0 Y	2.0	65.6
11	68.1 Z	-	66.2

* X and Y are Spacecraft Lateral Directions, and Z is Axial Direction

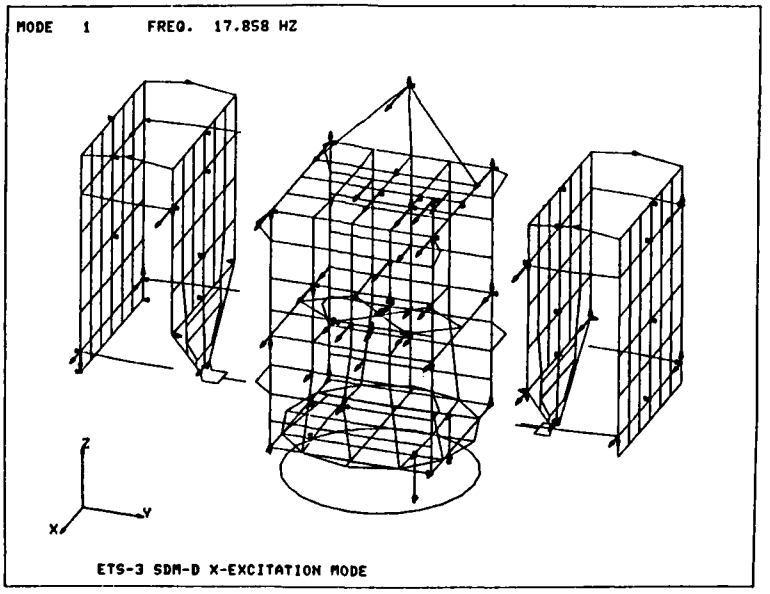

Figure 14. ETS-III 1st Lateral Mode Shape (X-axis)

CONCLUDING REMARKS

Classical sine sweep techniques still offer high resolution measurements for quick resonance survey over a wide frequency range, if the data are processed using analog tracking filters. Especially, the amplitude peak of major low frequency resonance can be resolved clearly. However, the difficulty to plot the transfer function in a variety of formats, gives limitations when identifying closely spaced modes. Although, the digital processing of the swept sine data which is not mentioned in this paper is possible, the data reduction time required is relatively long.

Digital transfer function measurements using steady random excitation can offer many kinds of transfer function formats easily, which is one of the great advantages of this

technique. Though the resolution problem exists in a lower frequency region when measuring the resonances over a wide frequency bandwidth simultaneously, the application of curve fitting techniques or zoom techniques over limited bandwidths (Reference 7), will allow very high resolution analysis. The capability to measure transfer functions of a structure with high resolution provides a tool to identify the non-linear characteristics of the structure.

The modal analysis using curve fitting techniques has high potential to identify the modal parameters accurately. For a simple beam configuration tested here, the measured mode did not show any differences between two analyzers used. However, to be implemented for spacecraft testings, more investigations are necessary to be confidently applied in the case when closely spaced modes exist.

It is felt that though the base excitation technique studied here is one of the convenient methods to measure structural modes, from the point of the test schedule and cost, because it can be performed in the process of dynamic environmental testings of a spacecraft, some modes are difficult to excite. Therefore, the use of single point force excitation techniques, changing the excitation point, will be necessary for the testing of future more complex structures.

ACKNOWLEDGEMENTS

The authors would like to express their thanks to Mr. Kuniyoshi Minami of National Space Development Agency of Japan and Mr. Fumihiro Kuwao of Toshiba Corporation who helped to conduct the experiment for this study.

REFERENCES

1. J.R. Fowler and E. Dancy, "Transfer Function Application to Spacecraft Structural Dynamics," The Shock and Vibration Bulletin, Bulletin 48, Part 1, pp. 93-101, September 1978.

2. M. Ferrante, C.V. Stahle, and D.G. Breskman, "Single-point Random and Multi-shaker Sine Spacecraft Modal Testing," The Shock and Vibration Bulletin, Bulletin 50, Part 2, pp. 191-198, September 1980.

3. M. Richardson, "Modal Analysis Using Digital Test Systems," Seminar on Understanding Digital Control and Analysis in Vibration Test Systems, Shock and Vibration Information Center Publication, U.S.A., pp. 43-64, May 1975.

4. C.C. Kennedy and C.D.P. Pancu, "Use of Vectors in Vibration Measurement and Analysis," Journal of the Aeronautical Sciences, Volume 14, Number 11, pp. 603-625, November 1947.

5. C.V. Stahle, Jr., "Phase Separation Technique for Ground Vibration Testing," Aerospace Engineering, pp. 56-57, 91-96, July 1962.

6. R.E.D. Bishop, and G.M.L. Gladwell, "An Investigation into the Theory of Resonance Testing," Phil. Trans. of the Royal Society of London, Series A, Volume 255, Mathematical and Physical Sciences, pp. 241-280, 1963.

7. H.W. McKinney, "Band-Selectable Fourier Analysis," Hewlett-Packard Journal, pp. 20-24, April 1975.

A FREE-FREE MODAL SURVEY SUSPENSION SYSTEM FOR LARGE TEST ARTICLES

Rick Webb
Martin Marietta Corporation
Denver, Colorado

The first assembly of a full-size, flight-weight MX missile was accomplished in February of 1982 for the purpose of conducting a modal survey test on a flight-configured test article. In order to approximate a free-free boundary condition simulating a missile in flight, a suspension system was required that would provide adequate separation ratios between lateral suspension frequencies and test article bending modes. A suspension system was developed that employed a large annular basering, to which the aft end of the first stage mounted, suspended vertically by three 200-inch long "pendulum" rods. The three-point suspension provided lateral stability even with a test article CG that was appreciably higher than the upper support point of the pendulum rods, while rod length was sufficient to allow rotational freedom of the missile base. A summary of the design and performance parameters is presented.

INTRODUCTION

The MX missile is a canister-launched four-stage ICBM that is designed to deliver up to twelve re-entry vehicles to independent targets. The missile is 92 inches in diameter, seventy feet long, and weighs almost 200,000 pounds at launch. The first three stages achieve nearly all of the required velocity necessary for intercontinental range through the burning of solid fuel propellants. The fourth stage, powered by storable hypergolics, remains attached to the re-entry system and controls post-boost vehicle maneuvers during the re-entry vehicle deployment portion of the mission. An on-board missile guidance and control set, housed within the fourth stage, initiates all events in the flight sequence from launch through RV deployment.

MODAL TEST REQUIREMENTS

The first total assembly of an MX missile was accomplished in February, 1982, for the purpose of performing modal survey testing to verify missile loads and guidance and control parameters. Modal test data were required for each of two flight configurations: all stages full at Stage I Start, and an empty first stage with all other stages full at Stage I Burnout.

In order to approximate a free-free boundary condition simulating a missile in flight, some means of suspending both missiles was required that would provide relatively unrestricted dynamic motion of all portions of the test articles. Since the test was intended to measure lateral missile bending modes only (no longitudinal modes), vertical low frequency test article isolation was not required beyond that necessary to preclude any rotational fixity of horizontal missile stations.

Restrictions unique to the MX program precluded some of the more obvious solutions to these suspension requirements. A horizontal test attitude was not possible due to the total lack of handling and mating equipment for horizontal stages.

Suspending a vertical missile from some point above its center of gravity was unsatisfactory because mechanical attachment to the missile would by necessity have to be at a stage-to-stage field joint, and the compliance in these joints was one of the major uncertainties in the analytical model. Masking any of these joints with test-peculiar attachments could easily invalidate the test results.

SUSPENSION SYSTEM DESCRIPTION

The suspension system that eventually evolved from these requirements and restrictions employed a large annular basering suspended at three (120°) points by "pendulum" rods(see Figures 1 and 2). The aft end of the first stage then interfaced with the top of this basering. The pendulum suspension rods were supported at their upper ends by rectangular crossbeams mounted on pairs of vertical columns. These columns were spaced so as to provide maximum clearance for stage installation and cross-braced for additional load capability. Pendulum rods were threaded on each end to accept special hex nuts that provided an adjustable pendulum length to accomodate basering leveling and fabrication tolerances.

PRELIMINARY ANALYSES

Once the basic concept of the missile suspension system had been solidified, it remained to be determined what detailed design parameters would best duplicate a missile in free flight. In order to minimize test-peculiar effects, it was decided to build a separate basering structure for each of the two test conditions in order to minimize their weights. Five percent of each test missile's weight was selected as a goal. This equated to a basering weight of about 10,000 pounds for the 195,000-pound Stage I Start configuration, and about half that for the 95,000-pound Stage I Burnout missile.

As a preliminary estimate of system behavior, rigid baserings of the above mass properties were analytically coupled to elastic missile models and attached to three pendulum links that incorporated the AE/L spring rates of 200-inch long, 2.25-inch diameter steel rods. Resulting missile mode shapes and frequencies were then compared to those of a free-free missile; these comparisons are shown in Figures 3 and 4. As can be seen from these figures, modal frequencies were very close to those of a free-flight missile, and modal amplitudes differed only slightly in the area of the missile aft end. The heavier test configuration, as expected, was far less effected by the test-peculiar mass addition in all modes.

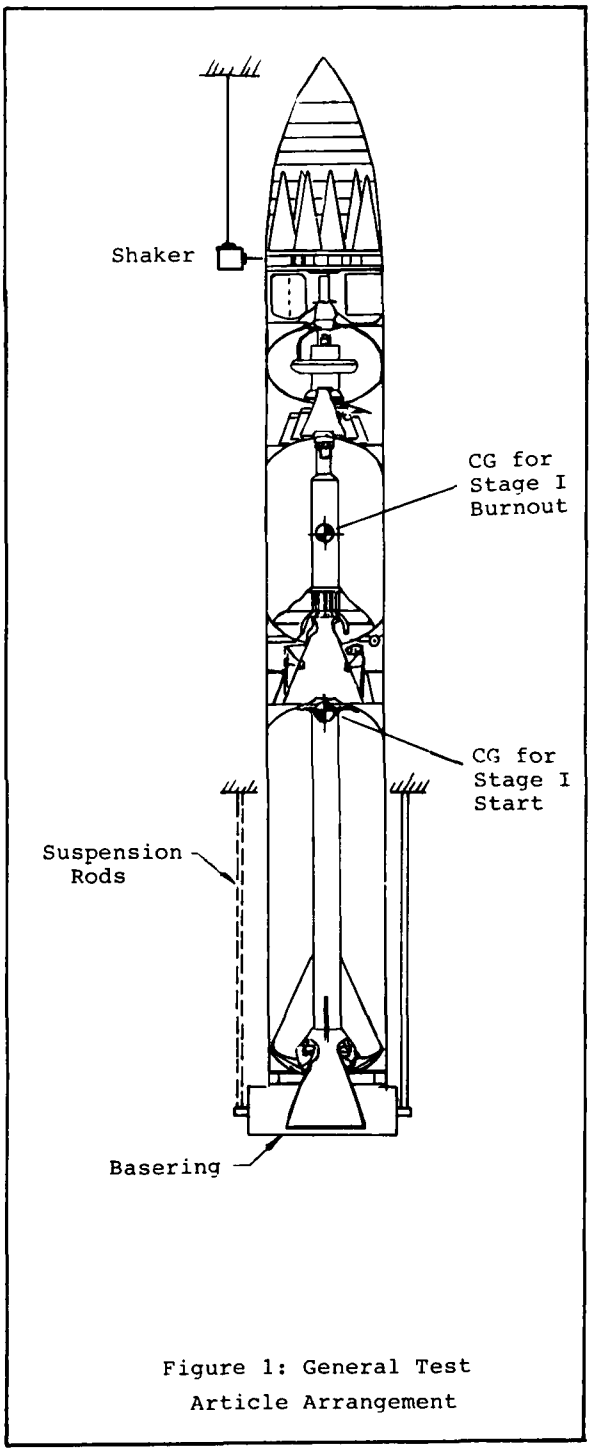

Figure 1: General Test Article Arrangement

Figure 2: MX Modal Survey
Suspension System

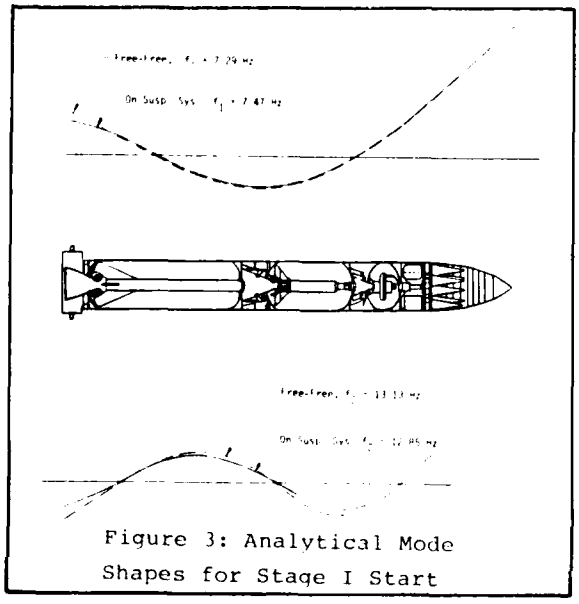

Figure 3: Analytical Mode
Shapes for Stage I Start

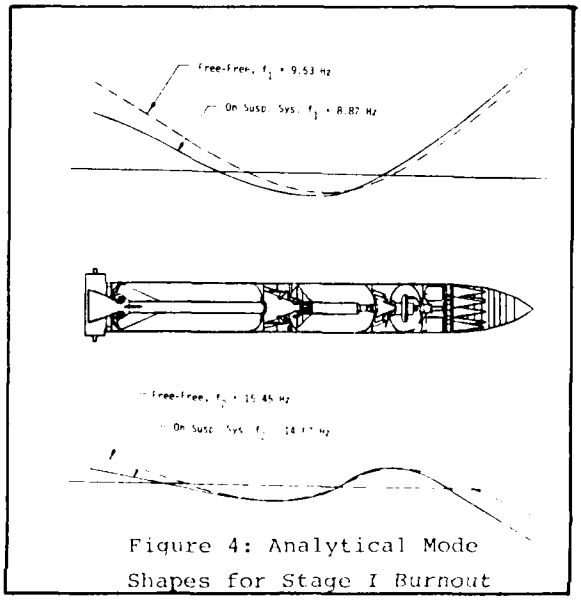

Figure 4: Analytical Mode
Shapes for Stage I Burnout

STABILITY ANALYSES

Once a modal analysis had demonstrated the dynamic suitability of the pendulum suspension system, it was then necessary to verify the system's static and dynamic stability. Instability, particularly of a non-symmetrically supported system, is not always obvious on inspection. In the particular case of a full MX missile, an analytical stability verification was obviously a prerequisite to any use of the system.

A simplified two-dimensional stability analysis was first performed based on Figure 5 by representing two of the pendulum support points at 60° on either side of the X-axis as a single point on the X-axis. Disturbing loads (P and M) were then applied at the CG of the test article and reaction loads in the suspension rods R_1 and R_2 were calculated from simple statics:[2]

$$R_1 = \frac{W}{2} + \frac{Ph + M}{2r}$$

$$R_2 = \frac{W}{2} - \frac{Ph + M}{2r} \qquad (1)$$

(Lateral reactions neglected)

Assigning K as the AE/L spring rate in pounds per inch of each suspension rod, we can then compute the extension of each rod due to W, P, and M as:

$$\zeta_1 = \frac{R_1}{K} \qquad \zeta_2 = \frac{R_2}{K} \qquad (2)$$

The deflected slope of the basering for this two-dimensional representation is then:

$$\theta_b = \frac{\zeta_1 - \zeta_2}{2r} \qquad (3)$$

This rotation then produces a rigid body deflection of the test article CG:

$$\zeta_{cg} = \theta_b h = \frac{(\zeta_1 - \zeta_2) h}{2r} \qquad (4)$$

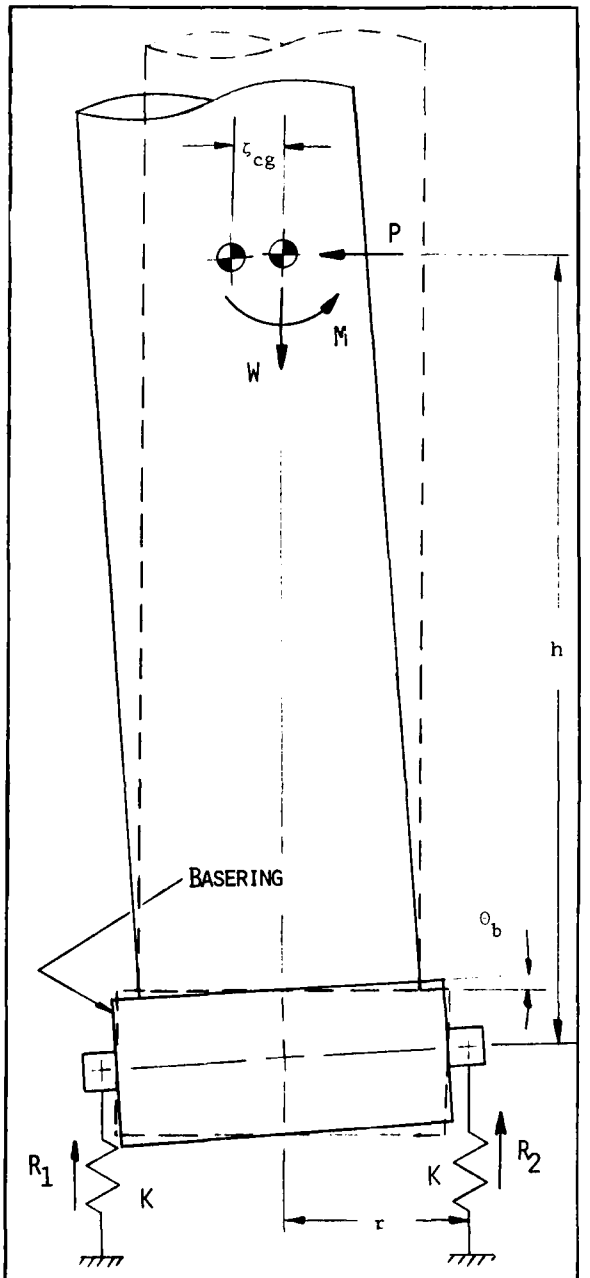

Figure 5: Stability Analysis Geometry

and the CG offset increments rod reaction loads R_1 and R_2 by an amount:

$$\Delta R_1 = \frac{W \zeta_{cg}}{2r} \qquad \Delta R_2 = -\frac{W \zeta_{cg}}{2r} \qquad (5)$$

The new rod loads are then:

$$R_1 = R_1 + \Delta R_1 = \frac{W}{2} + \frac{Ph + M}{2r} + \frac{W \zeta_{cg}}{2r}$$

$$R_2 = \frac{W}{2} - \frac{Ph + M}{2r} - \frac{W \zeta_{cg}}{2r} \qquad (6)$$

From these incremented rod loads, new rod deflections, basering rotations, CG offsets, etc. are re-computed in an iterative process. For a statically stable system the delta R's will decrease with each iteration and eventually become negligible. In an unstable system, of course, they will continually increase and no convergence will be reached.

For the steel suspension rods intended for this application (L=200 in, Dia=2.25 in), the AE/L spring rate of 6×10^5 lbs per inch indicated an ample stability margin (>50). As further verification, an expanded three-dimensional analysis was then performed using the full geometry of the system and expressing the rigid test article's potential and kinetic energies in terms of these geometric properties. The resulting stability margins were in close agreement with the simplified model predictions, thus confirming the system's stability.

It is interesting to note that the length of the three pendulum rods and their relationship to the missile CG did not enter into the final stability equations at all except as a term in the rods' axial stiffness. Intuition would lead to the conclusion that an upper pendulum pivot point well above the missile CG (see Figure 1) would be more stable than one far below the CG. Actually, just the opposite is true for a given rod diameter. The 200-inch rod length, then, was selected more to facilitate assembly and satisfy modal compatibility requirements than for any stability considerations.

DETAILED DESIGN

Detailed design of the two baserings was begun once the above analyses had indicated that the general suspension approach was valid. Each basering, while limited to 5% of the missile weight, would be required to support its respective test missile without inducing loads or deflections into the aft end of the first stage that exceeded allowable values.

A NASTRAN model of each basering was created as a means of verifying the above design constraints. A summary of the predicted loads and deflections at the aft end of the first stage is presented in Table I. These data were coordinated with the Stage I contractor (Thiokol Wasatch Division) to verify the ability of Stage I to safely react these loads.

Table I: Stage I Aft Skirt
Maximum Loads and Deflections

Location	Loads, lb.		Deflections, in.	
	Radial	Vertical	Radial	Vertical
1	-1357	13442	-7.68 E-3	-3.71 E-3
2	-961	6930	0.88	-7.30
3	-688	4020	7.81	-9.39
4	-961	6930	0.88	-7.30
5	-1357	13442	-7.68	-3.71
6	-961	6930	0.88	-7.30
7	-688	4020	7.81	-9.39
8	-961	6930	0.88	-7.30
9	-1357	13442	-7.68	-3.71
10	-961	6930	0.88	-7.30
11	-688	4020	7.81	-9.39
12	-961	6930	0.88	-7.30

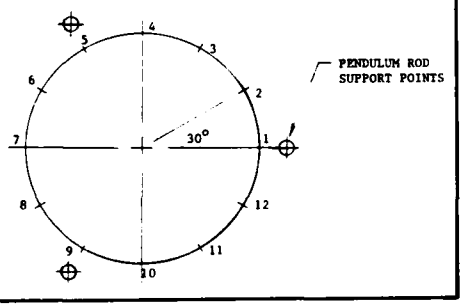

Output mass and stiffness matrices from this NASTRAN model were also used as input to a modal analysis to insure that no local basering modes were present below 150 Hz (three times the maximum test frequency) that could effect test data. This analysis resulted in several design changes that produced a heavier basering with a 189 Hz first mode and a lighter basering with a 176 Hz first mode.

The pendulum rods and their associated support structure were then designed in a manner consistent with the analytics. Rod ends were threaded to accept special 2¼-inch course thread nuts. No effort was made to approximate a ball/socket joint at either rod end, the rod length being more than sufficient to obviate any difference between a pin-ended beam and one that was fixed top and bottom.

Figure 6 depicts an additional design constraint that became apparent once detailed design had commenced. Note in the figure the effect that a "toed-in" suspension rod configuration would have on the attitude of the basering when it is displaced laterally. Although this consideration impacted both basering weight and test article installation clearances, the system was designed such that each suspension rod attached to the basering at a point directly below its upper support point on the cross-beam.

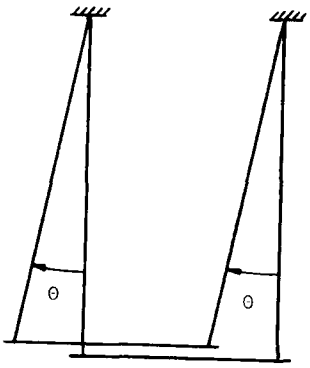

Vertical rods allow basering to remain horizontal during lateral test article displacements

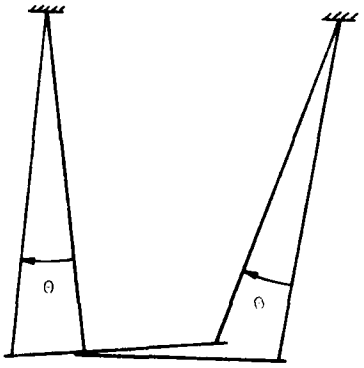

"Toed-in" suspension rods allow more clearance at top but cause basering to rotate with any lateral displacement

Figure 6: Effect of Non-Vertical Suspension Rods

Following design and fabrication of the suspension system, proof loading was accomplished to 150% of the predicted operating load. This proof loading was performed for three separate cases: the basering alone on the test cell floor (representing test article build-ups); the basering supported at three points by the hydraulic lifting jacks (representing the test article being raised); and the basering suspended by the three rods (representing modal test activities). All three proof loads were accomplished without incident.

Prior to modal test conduct, it was necessary to perform pre-test response analyses that would predict the dynamic behavior of the missile/suspension system in test and provide a baseline math model on which post-test corrections and modifications could be made to reflect actual test results. For these analyses the basering NASTRAN models were reduced to fifteen degrees of freedom (six at the CG and three translational at each of the three suspension rod attach points) and coupled to the two as-built missile mass/stiffness models. Each of these models was then analytically attached to the three 200-inch rods with AE/L longitudinal stiffnesses and a gravity vector acceleration to produce two mathmatical system models that predicted the behavior of each of the two dynamic systems under test. Table II presents a summary of these modal predictions.

Stage I Start:

Mode	Frequency	Description
1	0.245 Hz	Y Pendulum
2	0.245 Hz	Z Pendulum
3	0.551 Hz	Theta X (Missile Roll)
4	1.952 Hz	Theta Y (Missile Pitch)
5	1.952 Hz	Theta Z (Missile Yaw)
6	7.470 Hz	First Elastic Bending
7	9.590 Hz	X Displacement (Missile Long.)
8	12.86 Hz	Second Elastic Bending
9	16.00 Hz	Third Elastic Bending
10	32.70 Hz	Fourth Elastic Bending

Stage I Burnout:

Mode	Frequency	Description
1	0.268 Hz	Y Pendulum
2	0.268 Hz	Z Pendulum
3	0.582 Hz	Theta X (Missile Roll)
4	3.031 Hz	Theta Y (Missile Pitch)
5	3.031 Hz	Theta Z (Missile Yaw)
6	8.870 Hz	First Elastic Bending
7	13.31 Hz	X Displacement (Missile Long.)
8	14.70 Hz	Second Elastic Bending
9	23.50 Hz	Third Elastic Bending
10	26.33 Hz	Fourth Elastic Bending

Table II: Summary of Suspension System Predicted Frequencies

PERFORMANCE

Test article assembly was accomplished with the basering resting directly on the test cell floor and the pendulum rods unloaded. Once the test article had been completely assembled and was ready for test, the entire missile, including the basering, was raised using hydraulic jacks at the three suspension points. Half-inch spacers were then installed between the lower pendulum rod nuts and the basering suspension flanges. The jacks were then lowered, transferring the missile weight through the spacers and suspending the missile/basering from the three rods.

The dynamic behavior of the suspension system in test was almost exactly as predicted analytically. Once the test missile had been suspended, a low-frequency strain gage accelerometer was mounted to the basering and used to measure the lateral suspension frequency of the system. The measured value, 0.250 Hz, was close enough to the predicted 0.245 Hz that no effort was made to check rotational or vertical suspension frequencies.

A set of adjustable viscous dampers were designed and installed on the suspension rods to damp out any local rod modes that could feed energy back into the test article. It was found, however, that the modal test excitation levels were low enough (approx. 150# rms) that rod mode excitation and feedback were of no consequence. The dampers were therefore not used during modal testing.

Usage of the system in test was completely satisfactory. Raising and lowering of the missiles for suspension spacer installations was found to be an easily controllable operation, even with the limited sway space imposed by the personnel access platforms (see Figure 9). The test missile, once suspended, could be set into rigid body motion by little more than a light hand pressure. And the steel baserings made an excellent shaker attachment point, the local compliance being low enough to guarantee that all of the measured input vibration was indeed going into the test article (see Figure 7).

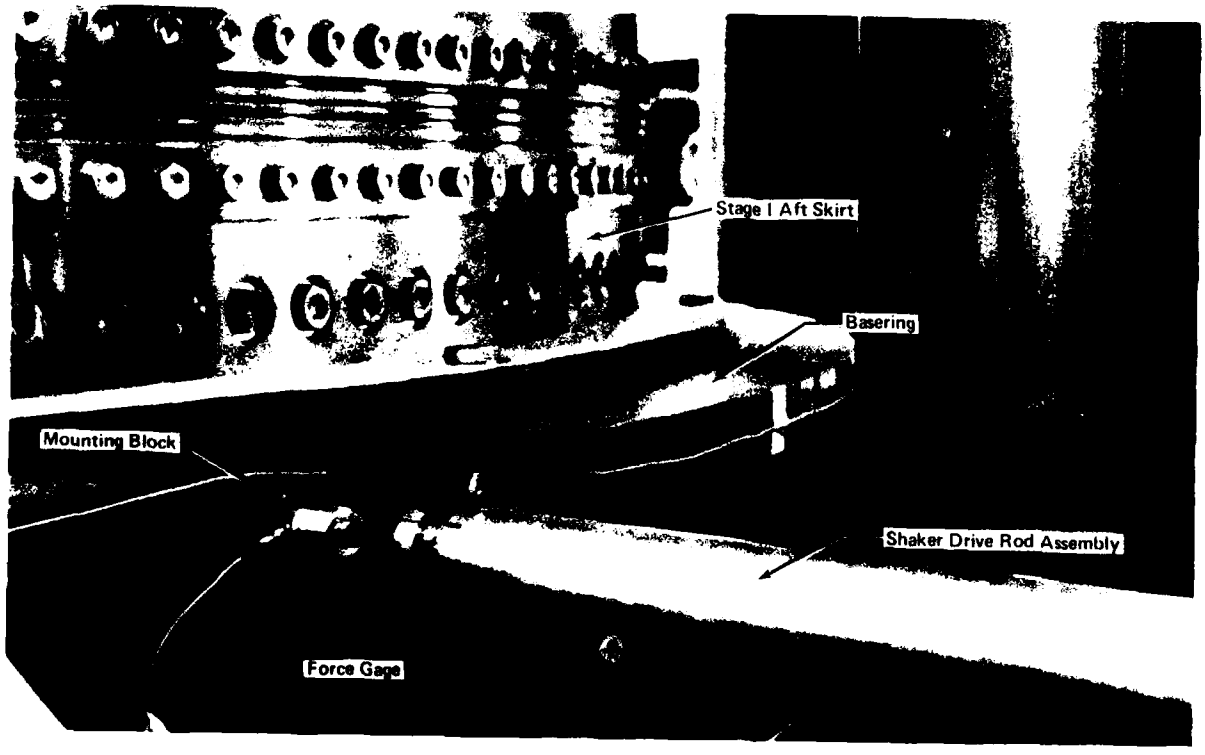

Figure 7: Shaker Attachment To The Basering

The resulting modal data, due to the nature of the test article, are classified SECRET and cannot be presented. Suffice only to say that any discrepancies between predicted and measured modal data were in no way attributable to the test suspension system.

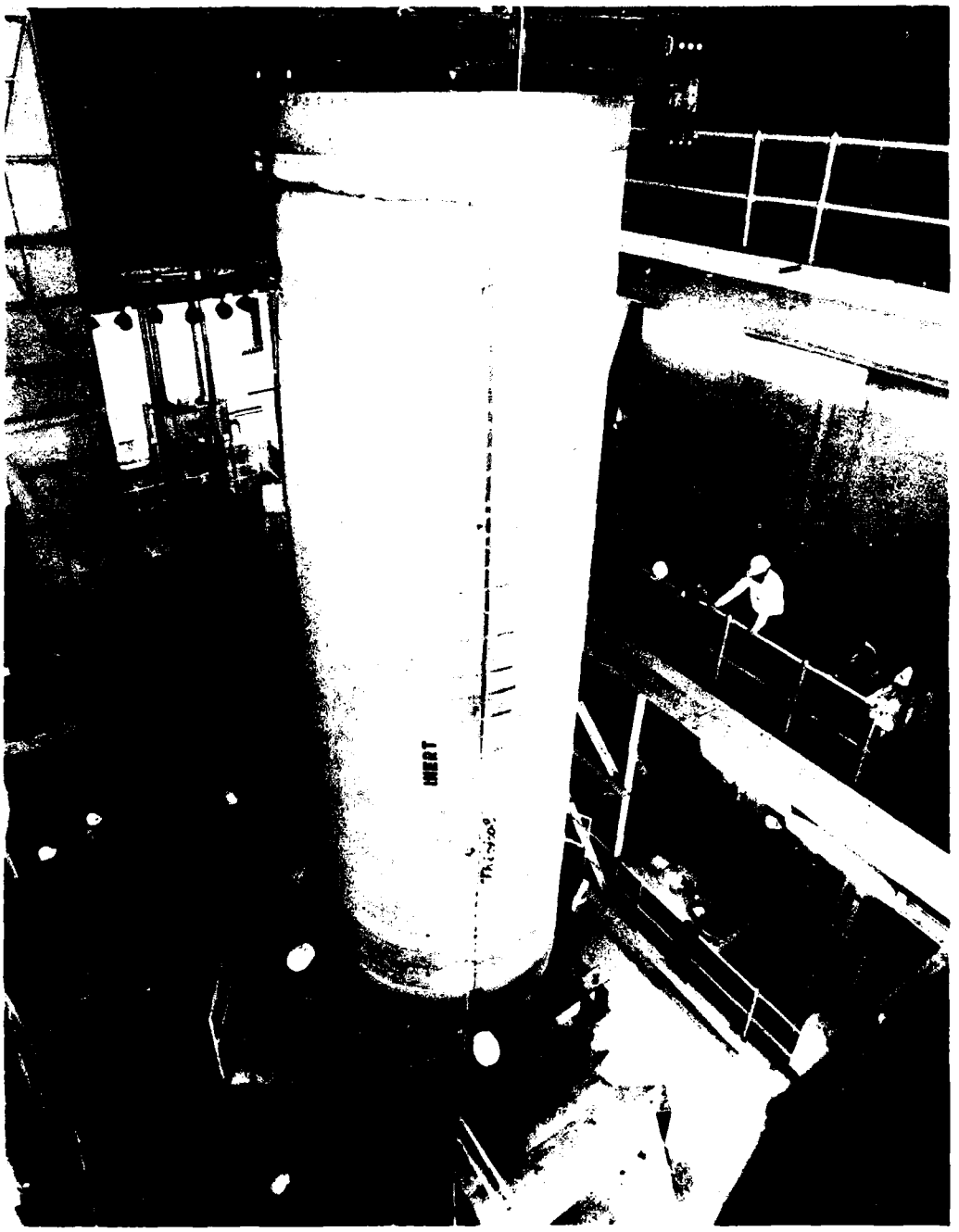

Figure 3: Installing Stage I in Suspension System

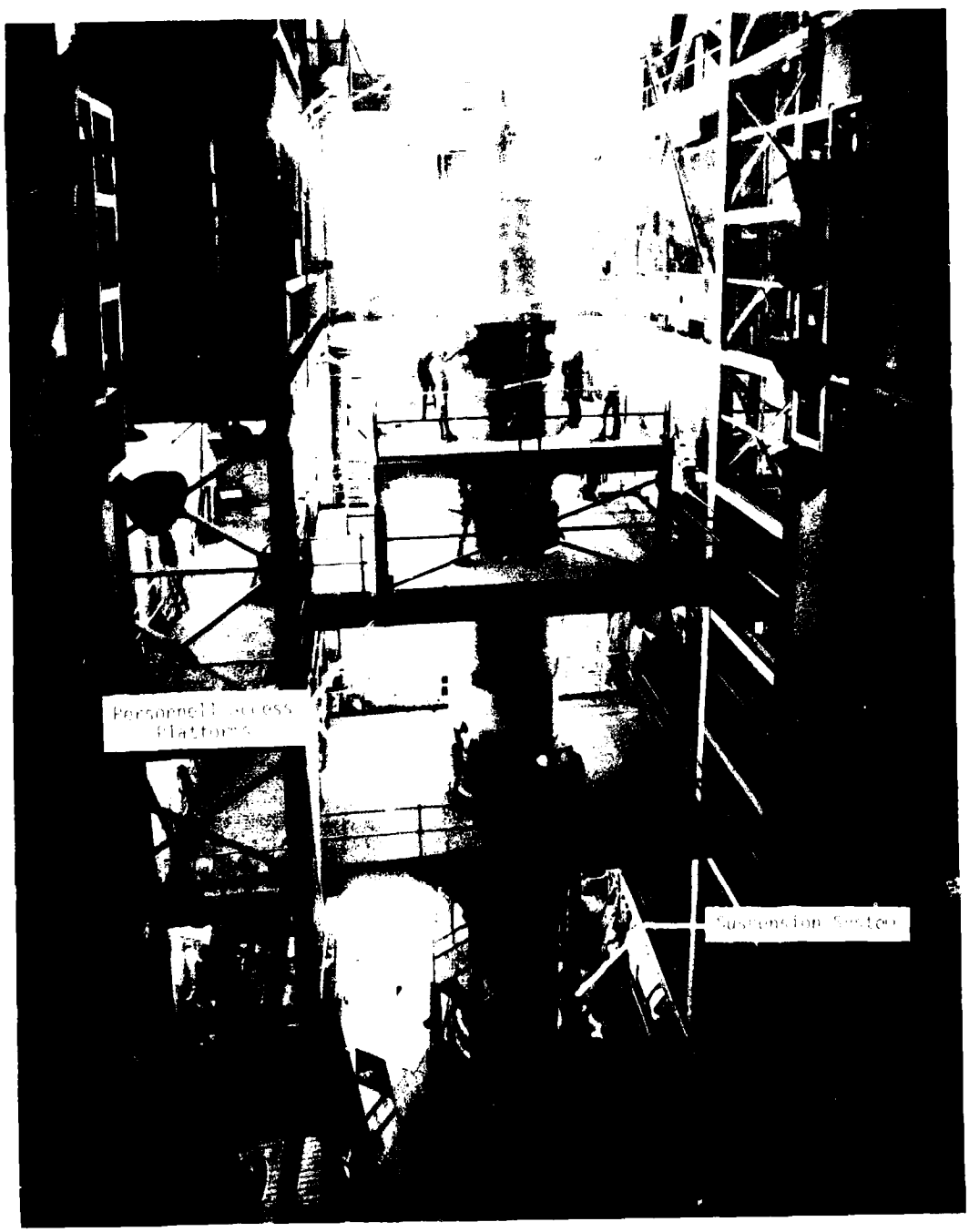

Figure 9: MX Missile
Completely Assembled in Test Cell